CROSS SECTION AND ANALYZING POWER MEASUREMENTS FOR NEUTRON SCATTERING FROM ^{27}AL AND ^{59}CO AND SPIN-SPIN CROSS SECTION CALCULATIONS

by

Mahmoud Mohamud Nagadi

Department of Physics
Duke University

Date: 7/14/92

Approved:

Richard L. Walter

Richard L. Walter, Supervisor

Dennis Toward

R. C. Pooles

Edward F. Bilpuch

Dissertation submitted in partial fulfillment of the requirements for the degree of Doctor of Philosophy in the Graduate School of Duke University

1992

ABSTRACT

CROSS SECTION AND ANALYZING POWER MEASUREMENTS FOR NEUTRON SCATTERING FROM ^{27}AL AND ^{59}CO AND SPIN-SPIN CROSS SECTION CALCULATIONS

by

Mahmoud Mohamud Nagadi

Department of Physics
Duke University

Date: 7/14/92

Approved:

Richard L Walter
Richard L. Walter, Supervisor

Warren Tornow

R. G. Palmer

Edward R. Bilpuch

Dissertation submitted in partial fulfillment of the
requirements for the degree of Doctor of
Philosophy in the Graduate School
of Duke University

1992

Abstract

Cross Section and Analyzing Power Measurements for Neutron Scattering from ^{27}Al and ^{59}Co and Spin-Spin Cross Section Calculations

by

Mahmoud Mohamud Nagadi

Differential cross sections and analyzing power data have been measured for ^{27}Al and ^{59}Co at 15.5 MeV. Cross section data was also measured for ^{59}Co at 10, 12, 14, 17, and 19 MeV using standard time-of-flight techniques at the Triangle Universities Nuclear Laboratory (TUNL). Absolute normalization of the $\sigma(\theta)$ data was performed using n-p scattering measurements. Both $\sigma(\theta)$ and $A_y(\theta)$ were corrected for finite geometry, attenuation, relative efficiency, and multiple scattering effects using Monte Carlo techniques.

A large data base was formed from our data and the existing data on ^{27}Al and ^{59}Co. This data base was used to develop a Dispersive Optical Model (DOM) and a Coupled Channels Model (CCM). The DOM model describes the data quite well above 8 MeV for ^{27}Al and ^{59}Co. However, for data below 8 MeV the model is not as satisfactory, perhaps because of angular momentum l -dependencies in the absorptive potential. The CCM improved the description of the data over the DOM, but still does not describe the data well at low energies.

The DOM and CCM for ^{27}Al and ^{59}Co were used to describe the spin-spin cross section data for ^{27}Al and ^{59}Co. We obtained a good fit for the spin-spin cross section with both the DOM and CCM with the spin-spin real surface parameters of V_{ss} = 0.80 MeV, r_{ss} = 1.00 fm and a_{ss} = 0.654 for both ^{27}Al and ^{59}Co. A surprising

relation between the spin-spin cross section and the derivative of the total cross section with respect to energy, was discovered:

$$\sigma_{ss} = c \frac{d\sigma_T}{dE}$$

where c is a constant related to the slope of the real central potential and spin-spin potential strength. This observation is not yet understood.

ACKNOWLEDGMENTS

My thanks and appreciation goes foremost to my advisor Dr. Walter for his encouragement, patience, and willingness to spend long hours teaching, discussing, and guiding, I am indebted to him for the completion of this work. I am grateful to Dr. Werner Tornow for his advice, help and availability no matter how busy he was. I also would like to thank Dr. Calvin Howell for his guidance and help with the experiments. A special thank you goes to Dr. J.P. Delaroche for the long days and nights we spent discussing and developing models for ^{27}Al and ^{59}Co. His theoretical background and thorough knowledge of the code ECIS enabled me to carryout my calculations successfully. I also would like to thank Dr. Edward G. Bilpuch for his care and continuous support. I thank Dr. Gary Weisel for reading the manuscript of this dissertation and discussing various aspects of this work. A special thank you goes to the rest of the time of flight group, Mohammad Al-Ohali, Ross Setze, and Richard Braun, and the visiting professors, J. Lambert and Z. Chen. I would like to extend my thanks to TUNL technical staff, Paul Carter, John Dunham, Sidney Edwards, and Patrick Mulkey. I thank Patty Atkinson for her excellent job typing this thesis. I thank Dr. A. Osman, my advisor at the Saudi Arabian Cultural Mission. I also would like to thank King Fahad University for Petroleum and Minerals for giving me this opportunity to pursue my graduate studies in the USA. I especially would like to thank Dr. Fahad Al-Dakhill the former Vice-Rector for his continuous support.

A deep gratitude goes to my parents for their love and support throughout my life. I greatly value my wife and children's patience and encouragement during this work. And last I thank Allah before and after for everything whether I know it or not.

TABLE OF CONTENTS

LIST OF FIGURES

LIST OF TABLES

CHAPTER 1

INTRODUCTION

Two main reasons motivated this study of the interaction of neutrons with the nuclei ^{27}Al and ^{59}Co. First was the need for a good nuclear model to describe measured data for the n + ^{27}Al and n + ^{59}Co total and differential cross section and analyzing power, in order to have a basis for interpreting the magnitude of the spin-spin cross section data for ^{27}Al and ^{59}Co. The second reason was to investigate the extension of the dispersion relation (DR) optical model to deformed nuclei.

The spin-spin interaction has been the subject of theoretical and experimental studies for the last four decades. The spin-spin potential and spin-spin cross section σ_{ss} for ^{59}Co have been estimated by Satchler [Sat71] and Fisher [Fis71a]. This cross section was measured by Nagamine *et al.* [Nag70] at 1.1 and 1.4 MeV, and by Fisher *et al.* [Fis71b] for E = 0.3-8.0 MeV. It was also measured later at E = 0.39-31.0 MeV by Heeringa *et al.* [Hee76 and Hee77]. For the energy range 0.39 to 31 MeV Heeringa *et al.* [Hee76, Hee77, and Hee83] tried to fit the available spin-spin cross section data for ^{59}Co but he was confronted with a difficulty fitting the data at low energy (< 5 MeV). The difficulty, which was connected to compound nucleus contributions to the cross section, was discussed by Thompson [Tho76].

In 1986 McAbee (a student of Thompson) [McA86] made a careful theoretical analysis of the nuclear spin-spin potential. His model, which was based on a phenomenological folding model, allowed him to estimate the spin-spin cross section for ^{27}Al and ^{59}Co. Subsequently, Gould *et al.* [Gou86] of TUNL measured the spin-

spin cross section for ^{27}Al using a polarized ^{27}Al target and polarized neutrons of energies 5-17 MeV. In order to fit the data they used a spin-spin potential that contained both real and imaginary volume terms. In 1987 Hnizdo *et al.* [Hni87] attributed the spin-spin effects seen in the ^{27}Al data of Gould *et al.* to the effect of the static quadrupole moment of a polarized ^{27}Al. This was contested by Gould *et al.* [Gou88] where they acknowledged the effect of the static deformation of ^{27}Al, but pointed out first that this quadrupole effect alone can not explain the measured σ_{ss} for ^{27}Al and secondly that this effect was included in their analysis through the imaginary term. Moreover, they pointed out that the quadrupole moment used in the calculation of Hnizdo *et al.* was too large by a factor of two. More recently, the σ_{ss} for ^{27}Al was measured by Heeringa *et al.* [Hee89] between 20 and 50 MeV. Heeringa *et al.* fit their data along with the Gould *et al.* data moderately well, but they only required a real surface spin-spin potential to do so.

Part of the problem that all these authors faced was the lack of a potential model designed specifically for the nucleus and energy range of interest. To approach this σ_{ss} study in a more logical way, one of the major goals of the present dissertation was to develop more complete and accurate models for neutron scattering for ^{27}Al and ^{59}Co. For both nuclei two models were developed; a dispersive optical model (DOM) and a coupled-channels model (CCM). A spin-spin potential was added to these models, and the strength of this term was investigated by comparing predictions from these models to the spin-spin cross section data for ^{27}Al and ^{59}Co.

A major part of the present work deals with the recent optical model developments stressed by Mahaux and coworkers. In this new approach the dispersion relation (DR) has been inserted into the conventional spherical OM. The DR relates the real and imaginary parts of the nuclear mean field as follows:

$$M(r, E) = V(r, E) + i\, W(r, E)$$

$$V(r, E) = V_{HF}(r, E) + \Delta V(r, E)$$

$$\Delta V(r, E) = (P/\pi) \int_{-\infty}^{\infty} [W(r, E') / (E' - E)]\, dE'$$

where W(r, E) is the usual absorptive potential containing a combination of a surface and a volume contribution. Here $V_{HF}(r, E)$ is the Hartree-Fock contribution and $\Delta V(r,E)$ is the dispersive contribution to the real part of the nuclear mean field V(r, E). The P denotes a principal value integral. Although the nuclear mean field V_{HF} has a simple monotonic energy dependence, the DR introduces a surface contribution to the real central potential V(r, E) that has a moderately strong variation with energy in the region below 10 MeV. So far, DR models for nucleon-nucleus scattering have been studied in detail mainly for the single-particle (SP) nuclei ^{208}Pb, ^{90}Zr, and ^{40}Ca.

While it is important in the development of the DR optical model to study "single-particle" SP nuclei in order to test the extension of the DOM to negative energies (SP bound states), it is also important to investigate the applicability of the DR to deformed nuclei, such as ^{27}Al and ^{59}Co. In a preliminary set of calculations we observed that the strength of the spin-spin potential that one obtains when describing the spin-spin data is sensitive to the inclusion of the dispersive terms. Because of this finding, and the fact that we were interested in studying the DR for deformed nuclei, we developed a spherical optical model for ^{27}Al and ^{59}Co with the DR as a constraint.

Although the DOM derived in the present work gives a qualitative description of σ_T data for $E_n > 9$ MeV, the data below 8 MeV are poorly described. This total cross section discrepancy is symptomatic of several DOM studies reported so far and the problem seems to be worse for the light nuclei. This fact is attributed in part to l -dependencies in the absorption and to reorientation effects. To further investigate the

problem of fitting the total cross section at low energies, a simple coupled-channels model was developed. This model only includes the coupling of the ground state to itself (called "reorientation effect") in order to study the effect of this important channel.

To assist in the development of these models, data for the differential cross section $\sigma(\theta)$ and analyzing power $A_y(\theta)$ from TUNL were used in addition to $\sigma(\theta)$ and σ_T data obtained from the National Nuclear Data Center at the Brookhaven National Laboratory. In order to further enhance the development of the models for ^{27}Al and ^{59}Co, we performed high accuracy $\sigma(\theta)$ and $A_y(\theta)$ measurements at TUNL at 15.5 MeV for both nuclei. In addition, $\sigma(\theta)$ data were obtained for ^{59}Co at 10, 12, 14, 17, and 19 MeV.

The $\sigma(\theta)$ data were obtained using the neutron time-of-flight spectrometer and the $^{2}H(d, n)^{3}He$ neutron source reaction. The $A_y(\theta)$ data were obtained using the same neutron source reaction, but in this case the reaction was initiated with polarized deuterons. We did not encounter any major difficulties in the measurements except for optimizing and determining the beam polarization. The latter is detailed in Chapter 2 along with a background of the $\sigma(\theta)$ and $A_y(\theta)$ data acquisition system and techniques. Chapter 3 reviews corrections and the reduction of the data. In Chapter 4 the compound nucleus calculations and corrections to the data base for ^{27}Al and ^{59}Co are presented. In Chapters 5 and 6, respectively, the Dispersive Optical Model (DOM) and Coupled Channels Model (CCM) analysis are presented. In Chapter 7 the DOM and CCM for ^{27}Al and ^{59}Co are used to estimate the size and shape of the spin-spin potential by comparing calculations to the available spin-spin cross sections for ^{27}Al and ^{59}Co. The last chapter of this thesis, Chapter 8, gives the summary and conclusion of this work.

CHAPTER 2

EXPERIMENTAL TECHNIQUE

2.1 Introduction

The differential cross section $\sigma(\theta)$ and analyzing power $A_y(\theta)$ for ^{27}Al and ^{59}Co were measured using the time-of-flight (TOF) facility at TUNL. This consist primarily of an ion source, the TUNL FN tandem Van de Graaff, a spectrometer, and a data acquisition system. The general layout of the facility is shown in Figure 2.1. The neutron time-of-flight spectrometer is located in the lower right-hand corner. Both $A_y(\theta)$ and $\sigma(\theta)$ measurements use the same apparatus except for the ion source. Some of the data acquisition techniques are also quite similar. Only general descriptions of the equipment and the data collection procedures will be given below since they have been already detailed in previous dissertations and publications as indicated below.

2.2 Neutron Beam Production

2.2.1 Cross Section Measurements

The neutron beam used for $\sigma(\theta)$ is produced using the $^{2}H(d, n)^{3}He$ reaction which produces a high intensity cone of monoenergetic neutrons centered around 0°. This reaction was chosen because it has a high cross section at 0° and because both the

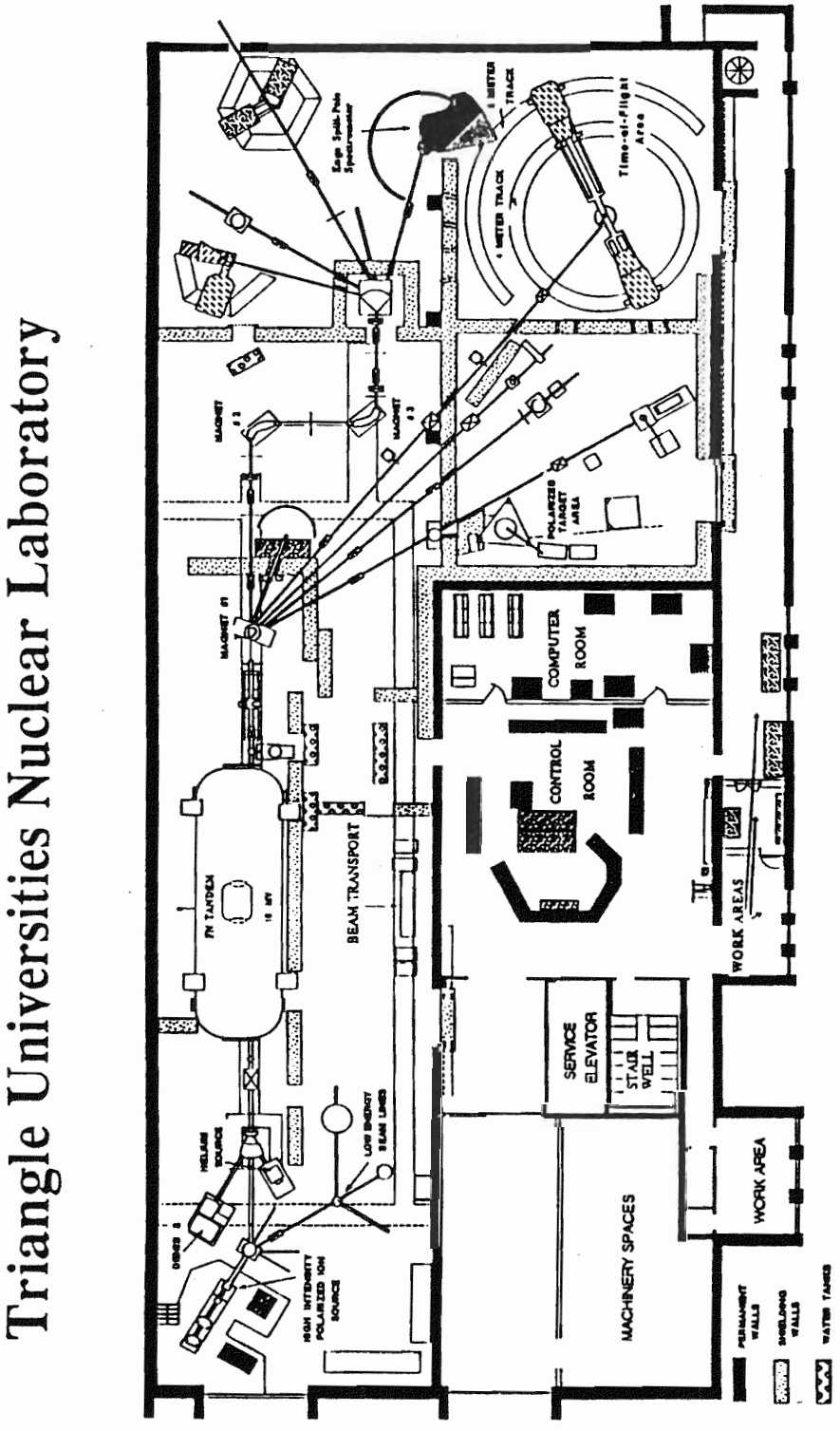

Figure 2.1. Floor plan of the accelerator facility at TUNL.

intensity and energy of these neutrons decreases rapidly away from 0°. This forward going cone of almost monoenergetic neutrons around 0° is very desirable because it reduces background events in the detectors which are located off to the side. Moreover, the $^{2}H(d, n)^{3}He$ with a Q-value of +3.27 MeV gives 5.5 MeV separation from breakup neutrons from the $^{2}H(d, np)^{2}H$ reaction. The deuteron beam was produced in DENIS-II, a negative ion source that uses the direct-extraction technique to produce 50 keV DC negative deuteron ions. This beam of D^- ions is chopped into pulses that are bunched prior injection into the tandem for acceleration. The chopping and bunching of the beam is essential for time-of-flight spectrometry since it changes the DC beam into compact packets of deuterons which are sufficiently separated in time. This separation allows the neutrons in one packet to interact at the target and to be detected before the arrival of the next packet. Knowing the time of arrival of deuterons at a certain reference point and then the detection of the neutrons at the neutron detector allows one to determine the energy of these neutrons.

Details of the chopping and bunching techniques and the recent improvements to the system are well described in [How84] and [Rob88]; a brief description of the technique is given here. The DC beam of deuterons passes through a set of horizontal deflection plates where a sinusoidal voltage is applied. This causes the beam to be chopped into packets of deuterons with a repetition rate that could be varied from 2 MHz to 31 kHz. Since the deuterons in these packets span a certain linear distance and have a nearly uniform velocity, the deuterons in the packet will arrive at the target over some relatively large time interval. This is not desirable for spectrometry. In order to make the ions in the packet arrive at the target at about the same time, these packets pass through a double-gap buncher which modulates the velocity of the ions in a way to compress the time spread when the packet arrives at the target. This is done by

applying a sinusoidal rf voltage which slows down the deuterons at the front of the packet and speeds up the ones in the rear.

After passing through the chopper and buncher the beam is accelerated by the upgraded FN tandem Van de Graaff which has a terminal voltage that can be varied between 0.65 MV and 9.1 MV. The accelerated beam is bent 38° off the axis of the accelerator toward the TOF target room with a momentum-analyzing magnet that has an NMR feedback system to maintain the desired field. This feedback system restricts the energy fluctuations in the deuteron beam to under 10 keV. However, because the analyzing angle is relatively small (38°) the calibration of the absolute energy of the beam is uncertain to about 60 keV. The analyzed beam passes through a set of magnetic lenses for focusing on the deuterium gas cell. For the cross section

Table 2.1

Gas pressure and beam energy loss for the cross section measurements.

Sample	Neutron energy (MeV)	Deuterium gas pressure (atm)	Energy loss in foil (MeV)	Energy loss in gas cell (MeV)
^{27}Al	15.5	4.0	0.214	0.160
^{59}Co	10.0	4.0	0.325	0.267
	12.0	4.0	0.272	0.214
	14.0	4.0	0.235	0.179
	15.5	4.0	0.214	0.160
	17.0	6.0	0.196	0.217
	19.0	7.8	0.177	0.251

experiments, the beam current was about 2.4 μA at the pulse repetition rate of 2 MHz, and a full width at half maximum of less than 2 ns. The deuteron beam enters the gas cell in a cylinder 0.8 cm in diameter and 3.16 cm long. This gas cell was used in both

$\sigma(\theta)$ and $A_y(\theta)$ experiments and was designed by G. Tungate. We used a 6.35 μm Havar foil which can sustain a gas pressure up to 15.2 bar. Table 2.1 lists the gas pressure and energy losses for the different incident deuteron energies for the cross section measurements.

2.2.2 Analyzing Power Measurements

During 1987 and 1988 the construction of a new Atomic Beam Polarized-Ion Source (ABPIS) was completed at TUNL (see Figure 2.2 and Clegg [Cle 90]). The new polarized ion source was installed and ready to use early in 1990. It consists of two sections. The first section has a dissociator and cooled nozzle followed by two sextupoles and radio-frequency transition units (see Figure 2.3). The second section is an electron-cyclotron-resonance (ECR) ionizer. Using this new source we were able to get a beam of 200-600 nA at the target. (Unfortunately, we were supposed to get 2 μA of pulsed beam with this new source. The low beam problem is caused by the fact that the ramping, bunching, and chopping techniques have not been optimized for this new polarized ion source. We were not able to use the ramp to pre-bunch the beam in order to increase our beam intensity. Detailed description of the ramping, bunching, and chopping techniques for $A_y(\theta)$ measurements are detailed in [How84] and [Rob88]). For the measurement reported in this dissertation, we only employed a 2.5 MHz chopper and a buncher to obtain deuteron pulses at the target with a 5 MHz repetition rate and a FWHM of about 2 ns. The pulsed deuterons enter a gas cell containing deuterium which is the same one used for our $\sigma(\theta)$ measurements. The Havar foil was 6.35 μm thick. The polarization of the neutrons was measured indirectly using

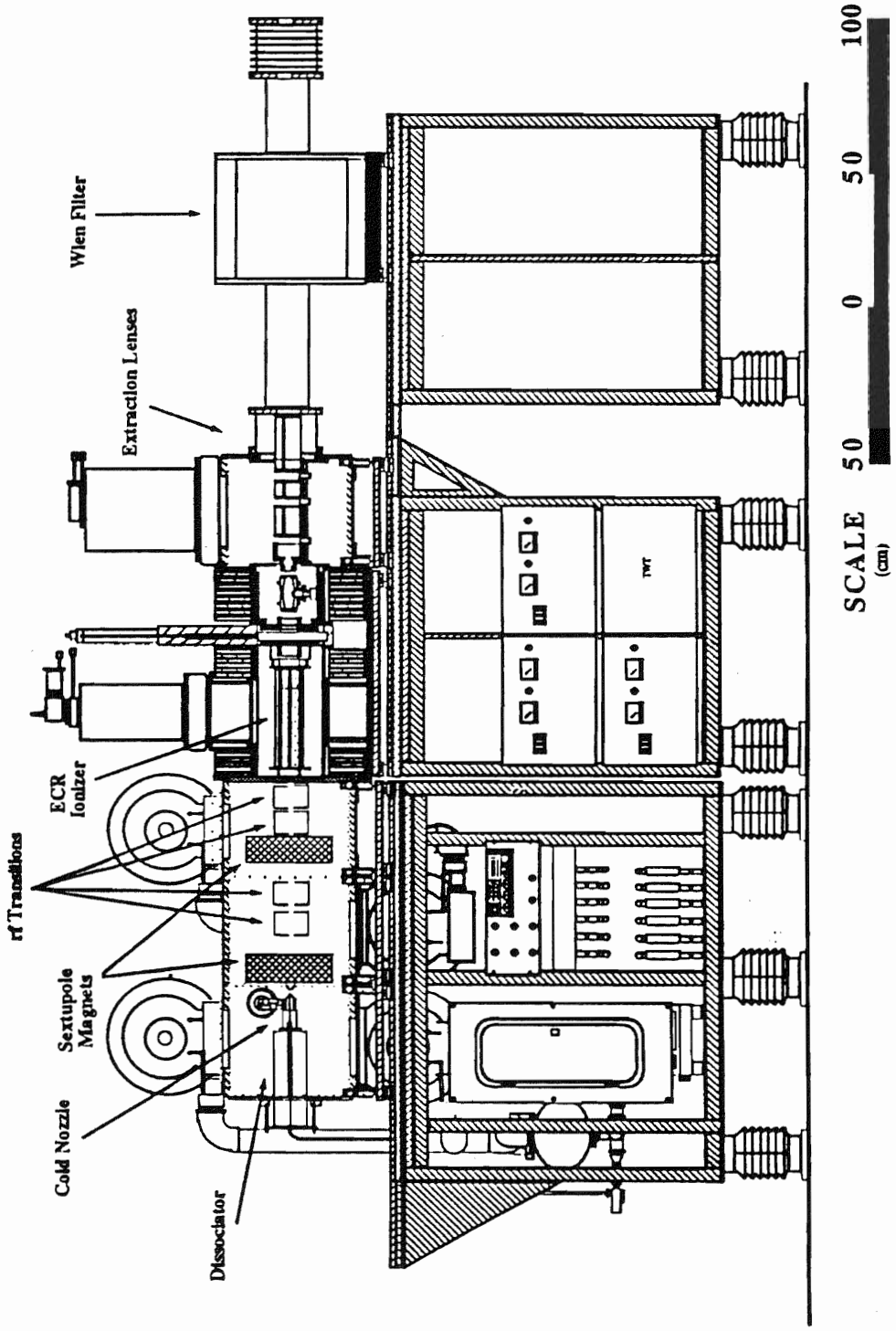

Figure 2.2. The new Atomic Beam Polarized-Ion Source.

ATOMIC TRANSITIONS

	SF1	WF1	SF2	WF2	STATES OBTAINED	POLARIZATION P_{Z}	POLARIZATION P_{ZZ}	FIGURES OF MERIT $P^2_Z I$	FIGURES OF MERIT $P^2_{ZZ} I$
Hydrogen									
a)			$2 \leftrightarrow 4$		1+4	+1		1	
b)				$1 \leftrightarrow 3$	2+3	- 1		1	
Deuterium									
a)				$1 \leftrightarrow 4$	2+3+4	-2/3	0	4/9	0
b)			$3 \leftrightarrow 6$		1+2+6	+2/3	0	4/9	0
c)		$1 \leftrightarrow 4$	$2 \leftrightarrow 6$	$3 \leftrightarrow 2$ $6 \leftrightarrow 5$	2+5	0	-2	0	8/3
d)		$1 \leftrightarrow 4$	$2 \leftrightarrow 6$		3+6	0	+1	0	2/3
e)	$3 \leftrightarrow 5$		$2 \leftrightarrow 6$		1+6	+1	+1	2/3	2/3
f)	$3 \leftrightarrow 5$			$1 \leftrightarrow 4$ $2 \leftrightarrow 3$	3+4	- 1	+1	2/3	2/3
g)	$3 \leftrightarrow 5$	$1 \leftrightarrow 4$			2	0	-2	0	4/3

Notes:

Hydrogyn $2 \leftrightarrow 4$ $\upsilon = 1485$ MHz, $B_0 \equiv 155$ G ($l_{mag} \equiv 0.9$ Å) 1000 turn coil

Deuterium $3 \leftrightarrow 5$ $\upsilon = 330$ MHz, $B_0 \equiv 85$ G ($l_{mag} \equiv 0.9$ Å) 500 turn coil
$3 \leftrightarrow 6$ $\upsilon = 400$ MHz, $B_0 \equiv 85$ G ($l_{mag} \equiv 0.45$Å) 1000 turn coil
$2 \leftrightarrow 6$ $\upsilon = 460$ MHz, $B_0 \equiv 85$ G ($l_{mag} \equiv 0.45$Å) 1000 turn coil

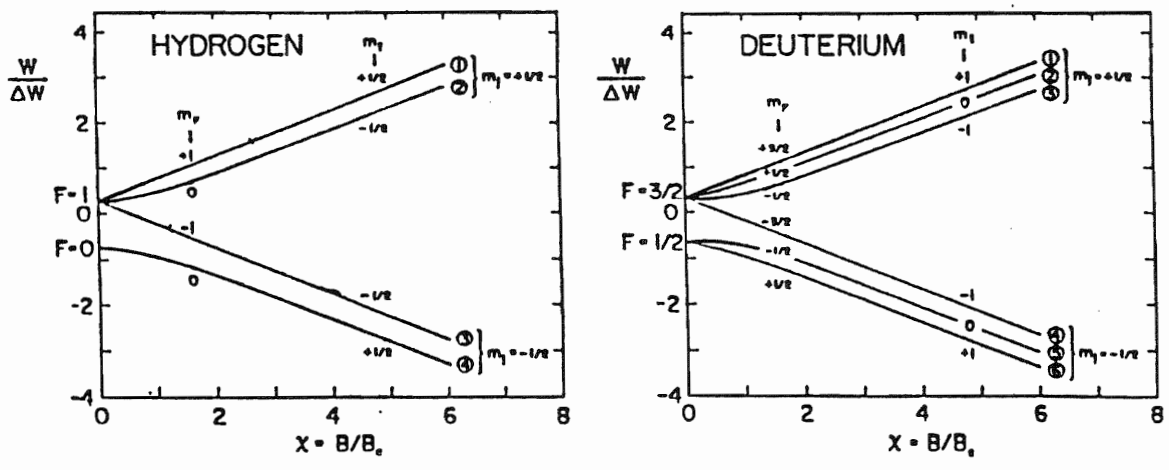

Figure 2.3. The atomic transitions available by the new ABPIS.

$^{12}C(n, n)$ reaction as will be explained later. Deuterium gas pressure and energy loss in the gas cell are detailed in Table 2.2.

Table 2.2

Gas pressure and beam energy loss for the cross section measurements.

Sample	Neutron energy (MeV)	Deuterium gas pressure (atm)	Energy loss in foil (MeV)	Energy loss in gas cell (MeV)
^{27}Al	15.5	4.0	0.214	0.160
	15.5	5.0	0.214	0.200
^{59}Co	15.5	7.8	0.214	0.312

2.3 Neutron TOF Spectrometer

The neutron time-of-flight spectrometer consists mainly of two parts; a capacitive pick-off unit with its electronics, and a set of neutron detectors and associated phototubes and electronics.

2.3.1 The Capacitive Pick-Off Unit

The pick-off unit is a cylindrical tube which is located in the evacuated beam pipe 46 cm away from the gas cell (see Figure 2.4). The cylinder is 1.9 cm in diameter and 6.35 cm long. As the positive beam pulse passes through the pick-off unit it produces a pulse at the output of the pre-amplifiers as shown in Figure 2.5. The amplitude of the pick-off signals is proportional to the beam intensity and related to the time structure of the deuteron beam pulse. The amplified pick-off signal is delayed by 500 ns and is fanned out to the TOF-TAC's to be used as a stop signal. Logically the pick-off signal should be used as a start signal since it signals the arrival of the deuteron pulse before the reaction takes place. However, because these signals arrive

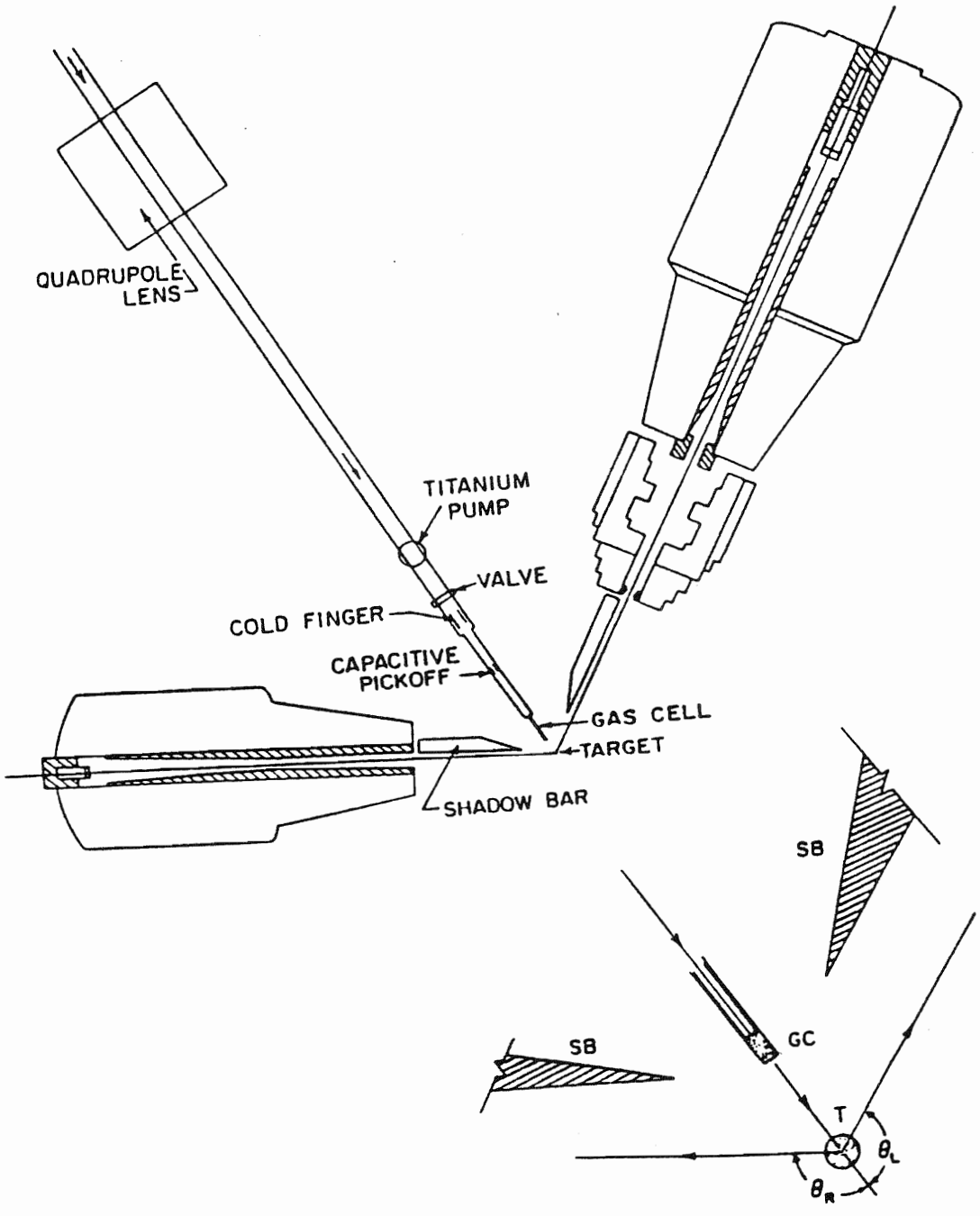

Figure 2.4. The layout of the neutron time-of-flight spectrometer facility.

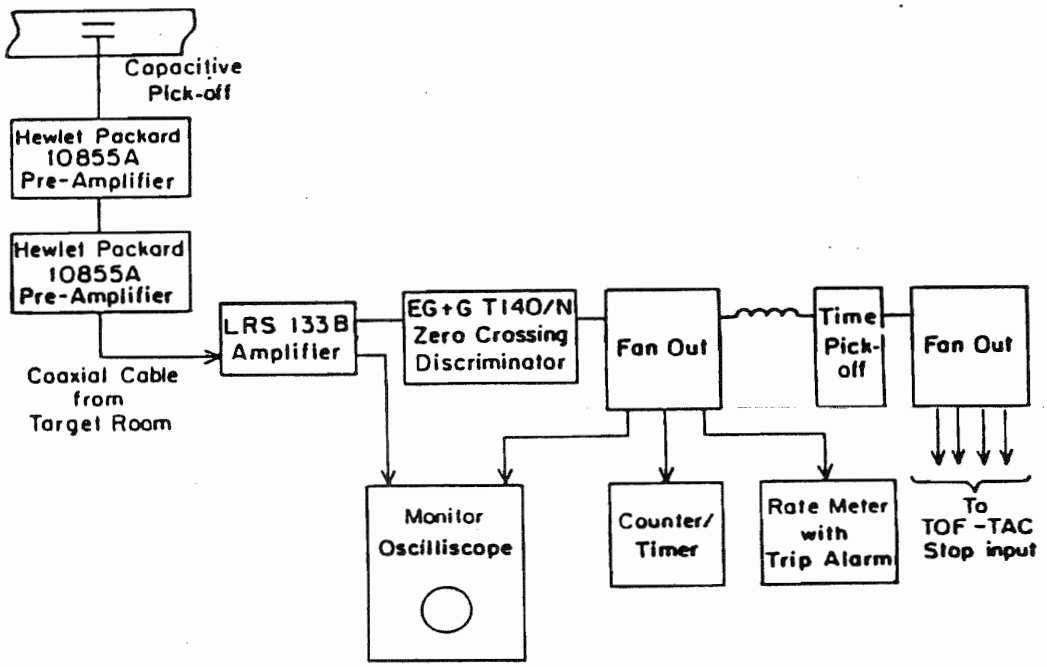

Figure 2.5. Block diagram of the beam pick-off electronics.

every 500 ns and would paralyze the TOF-TAC if used as a start signal, they were used as a stop-signal instead.

2.3.2 Neutron Detectors

For the cross section measurements four detectors were used. Two detectors, the so-called 4- and 6-meter detectors, were used to detect the flight time of the neutrons scattered from the sample. Both detectors are heavily shielded using copper, lead, paraffin, and lithium-carbonate, as shown in Figure 2.6. In addition to that shielding, a double truncated collimator inside both massive shields define acceptable neutron trajectories. The left detector (6-meter) has a large movable copper preshield (see Figure 2.4). To reduce the background from the neutrons coming directly from the $^{2}H(d, n)^{3}He$ source reaction a set of copper and tungsten shadow bars are used. Both detectors are mounted on carts that move on circular paths which span the angular range of 0°-160°. The left neutron detector (6-meter) is a cylinder 12.7 cm in diameter and 5.08 cm thick that contains the liquid organic scintillator NE213. The right detector is a cylinder of 8.8 cm in diameter and 5.08 cm thick that contains a liquid organic scintillator NE218. Both scintillators are coupled to photomultiplier tubes. The left detector has a flight path that can be varied from 3.76 to 5.7 m while the right detector has a flight path of 2.77 to 3.76 m.

The third detector is referred to as the ceiling monitor detector and is used for the normalization of $\sigma(\theta)$ data. This monitor is also a cylinder of the liquid organic scintillator NE218. The detector is suspended from the ceiling at 50° from the horizontal and looks directly at the gas cell with a flight path of 2 m. The ceiling monitor is shielded inside a thick cylinder of copper. The fourth detector is called the

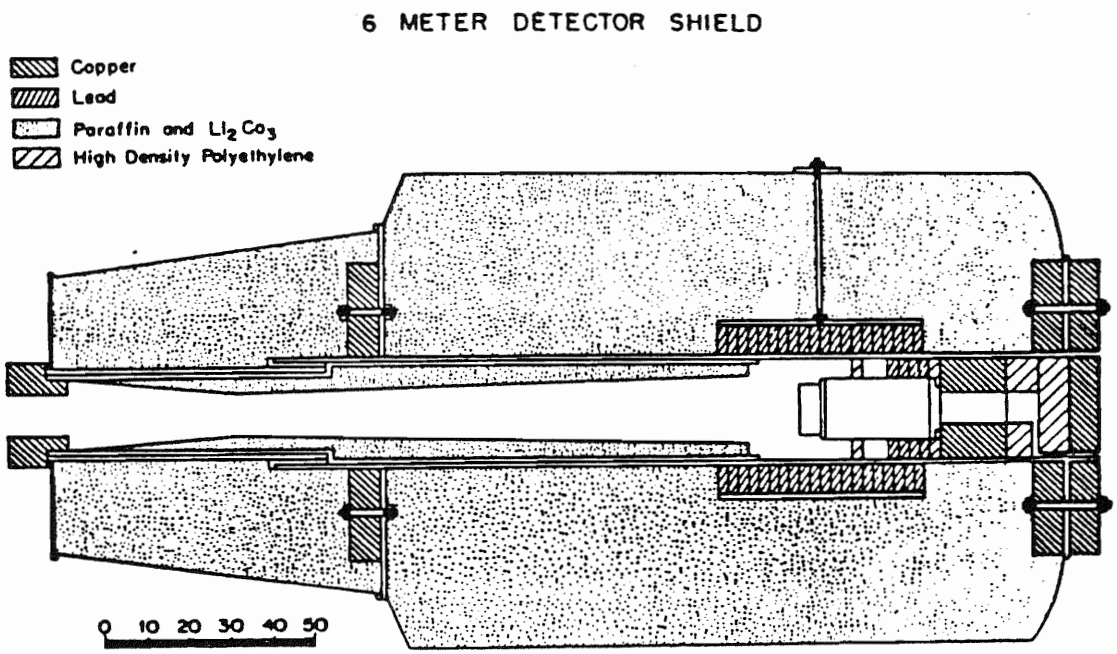

Figure 2.6. The shielding of the 6 m detector.

"zero-degree monitor" and is set at 0° with a flight path of about 3 m. This detector is not shielded since it is only used to monitor the time distribution of the neutrons emerging directly from the gas cell. The 0° monitor is also a cylinder of liquid organic-scintillator NE213.

All four detectors give a good pulse-shape discrimination between neutron and γ-ray events. The detection of neutrons in these detectors occurs when these neutrons transfer their energy to the scintillator nuclei (either ^{1}H or ^{12}C) which acquire a recoil energy that depends on the energy of the incident neutron and the angle through which the neutron was deflected. These recoiling nuclei deposit their energy through ionization or excitation. When the excited atoms decay back to their ground state they emit photons. The number of photons produced in the scintillator is proportional to the recoil energy. These photons are collected by the photomultiplier tube which produces an anode signal proportional to the number of photons. Figure 2.4 shows the layout of the four detectors.

For the analyzing power measurements only three detectors were used, the left and right detectors, and the 0° detector (pulse-timing detector). The ceiling monitor detector is not needed in the $A_y(\theta)$ measurements since these are relative measurements, and there is no need for absolute normalization.

2.3.3 Time-of-Flight Electronics

The time-of-flight electronics are designed to process the capacitive-pick-off signal and the anode signal from the detector's photomultipliers as shown in Figure 2.7. The signal processing for $\sigma(\theta)$ and $A_y(\theta)$ is similar. The electronics serves three purposes. First, it sets an energy bias below which no event is accepted. Second, it

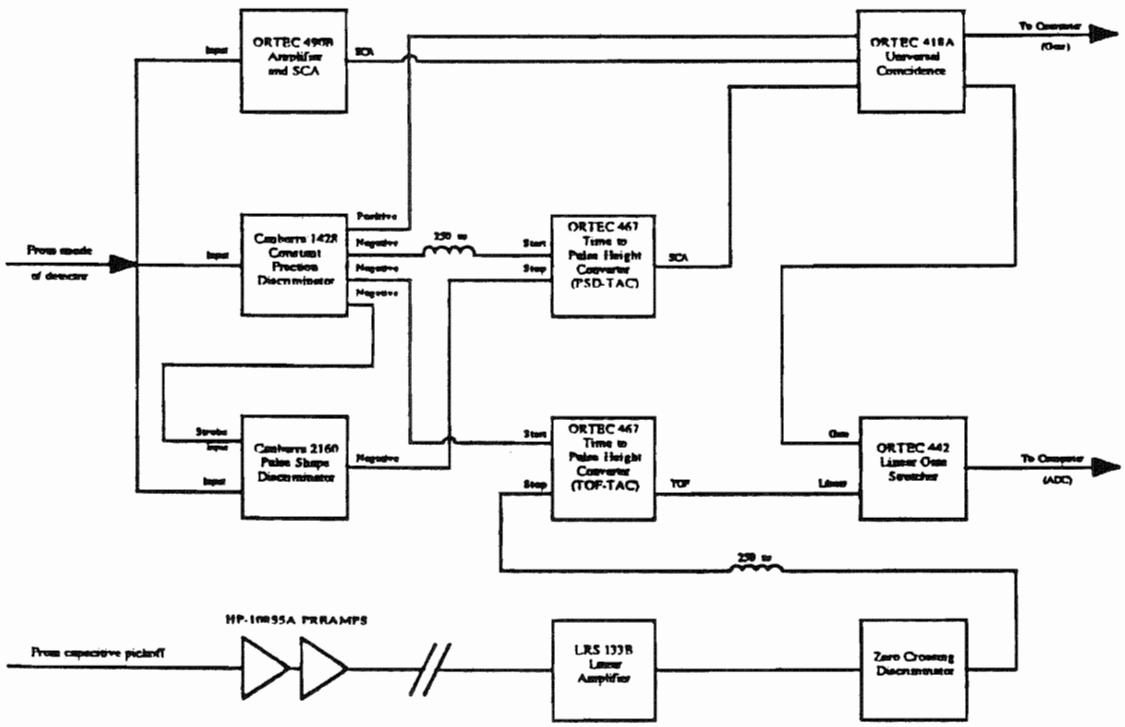

Figure 2.7. Block diagram of the electronics used in the TOF measurements.

discriminates between events caused by gamma-ray interaction and neutrons since the liquid organic scintillators are capable of detecting both. Third, it processes the signal and makes it ready to be used by our data acquisition system.

Following the two signals in Figure 2.7 will explain the function of the different modules of TOF electronics. The anode signal coming from the detectors in the target room is split three ways. One part goes to a linear amplifier with a single channel analyzer where a lower level threshold is set. Events lower than the threshold are rejected. To set this threshold a radioactive element (^{137}Cs) is used which produces γ-rays of 0.66 MeV. The γ-rays produce a Compton recoil spectrum in the organic scintillator. The energy bias is usually set at convenient values $1 \times$ Cs, $2 \times$ Cs, etc. where $1 \times$ Cs corresponds to the pulse height of the Compton edge. The light output for these Compton electrons correspond to the pulse height of a 1.6 MeV proton-recoil energy. Figure 2.8 shows a gated spectrum with a gate set at $1 \times$ Cs and an ungated spectrum for ^{137}Cs.

The other condition imposed on the signal is to be a neutron event, not a γ-ray event. This is accomplished by using the constant fraction module (CFD) and the pulse shape discrimination module (PSD). The pulses which are caused by a γ-ray are different in shape from the ones produced by neutrons (see Figure 2.9). The CFD produces a signal at the leading edge of the input signal while the PSD module produces a signal at the trailing edge of the input signal. These two signals are brought to a PSD-TAC which convert the time difference between the leading edge signal and the trailing edge signal to a voltage proportional to the time difference. Since the time difference for the neutrons is longer than that from electrons (caused by γ-rays) a lower level threshold is set using the SCA of the PSD-TAC so that all neutron events are accepted and most γ-rays events are rejected (see Figure 2.10).

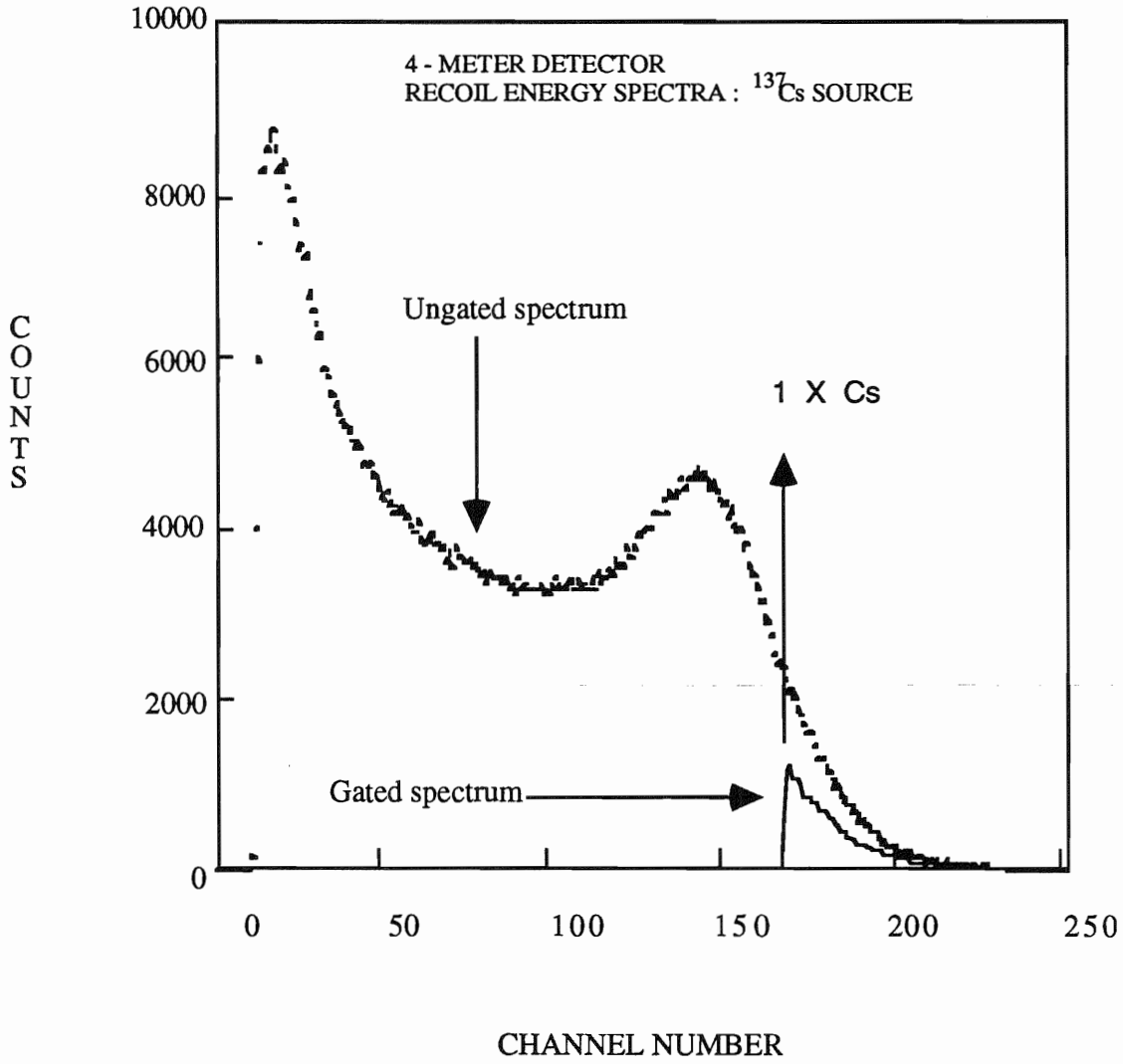

Figure 2.8. The 4-meter gated and ungated TOF spectra due to γ-rays from ^{137}Cs.

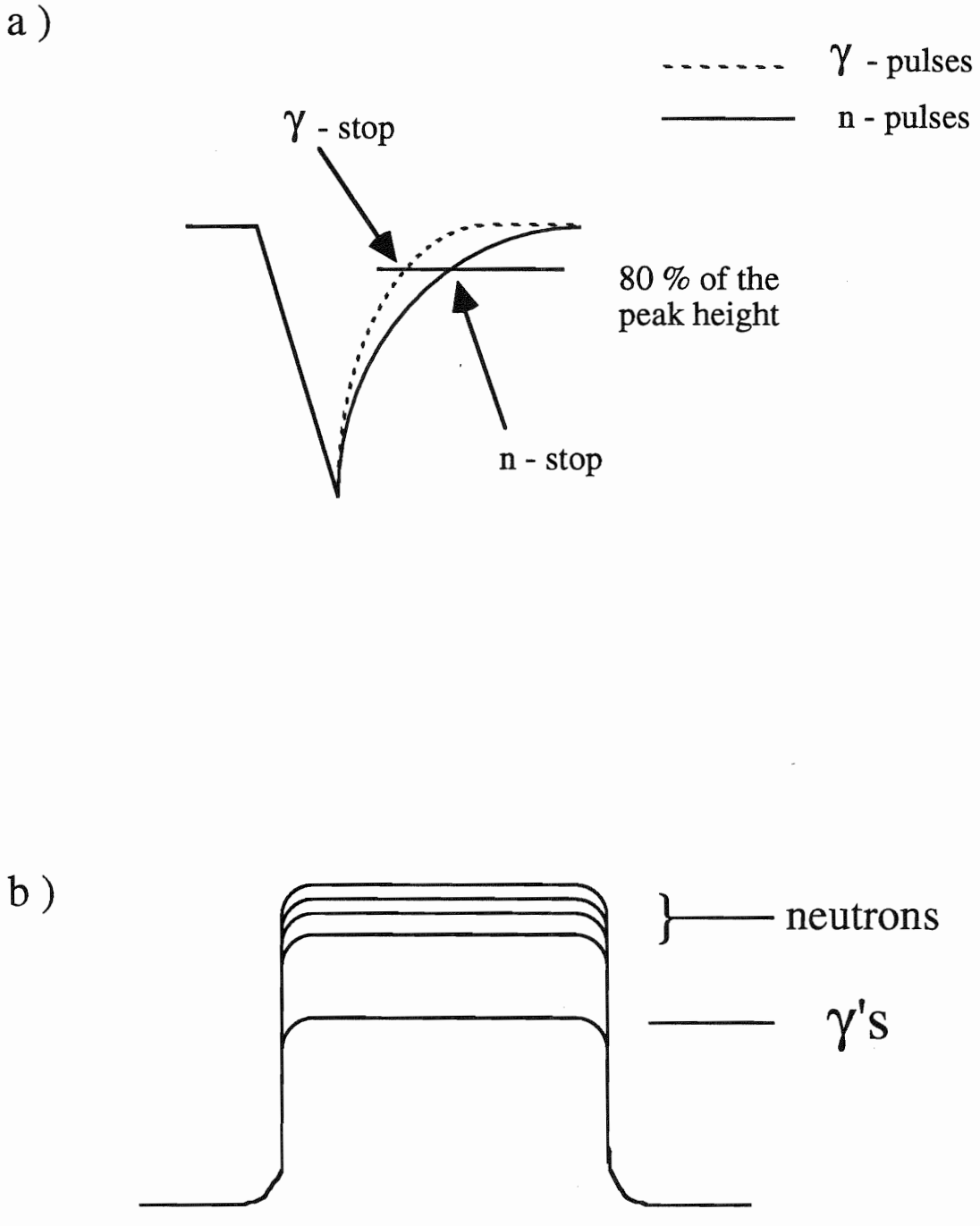

Figure 2.9. Anode signals from detector and output of PSD-TAC.

Time-of-flight spectra are produced in the TOF-TAC which gives signals that are proportional in amplitude to the time difference between the stop and start signal. The stop signal comes delayed from the capacitive pick-off and the start signal comes from the CFD. The TOF-TAC is fed to a linear gate stretcher which is gated by the universal coincidence (UC) module which gives signals only if the two conditions on the anode signal are satisfied, namely that it is a neutron event and larger than a certain bias level. The bias levels used in the various experiments depended on the neutron background and whether or not knowledge of the absolute efficiency was important. In general the bias was set at $1 \times$ Cs for $\sigma(\theta)$ and $2 \times$ Cs for $A_y(\theta)$ measurements. The gate signal from the UC and the analog signal from the TOF-TAC are taken to the computer interface to be processed by our data acquisition system.

2.4 Scattering Samples

Samples were suspended by a thin wire which can hold four samples. The wire is suspended from the ceiling either 8.8 or 11.4 cm away from the gas cell. The samples were very carefully aligned onto the axis of the incident deuteron beam by using a telescope at the end of the TOF target room. The neutron detectors are also carefully aligned with the scatterer. Changing the samples was accomplished by moving the sample wire up or down using a stepping motor which is controlled from outside the target room. All samples were cylindrical in shape and aligned coaxial with the vertical sample wire. As discussed below, the absolute cross section for ^{27}Al and ^{59}Co was obtained by normalizing the yields to yields obtained for scattering from hydrogen contained in a calibrated polyethylene sample. Table 2.3 gives the physical parameters for the scattering samples used in the $\sigma(\theta)$ and $A_y(\theta)$ experiments.

Table 2.3

The physical parameters of the scattering samples.

Sample	Experiment	Isotopic composition	Mass (g)	Radius (cm)	Height (cm)
^{59}Co	$\sigma(\theta)$, $A_y(\theta)$	99.9%	188.20	1.427	3.336
^{27}Al	$\sigma(\theta)$, $A_y(\theta)$	99.9%	19.60	0.955	2.546
Polyethylene	$\sigma(\theta)$	~66.6% ^{1}H ~33.3% ^{12}C	3.37	0.717	2.279
^{12}C	$\sigma(\theta)$	>99.0%	2.91	0.477	2.376
^{12}C	$A_y(\theta)$	>99.0%	42.012	1.429	3.810

2.5 Data Acquisition

2.5.1 Differential Cross Section Measurements

Data acquisition for $\sigma(\theta)$ was accomplished by processing the output signals from the TOF-TAC and universal coincidence modules. The signal was processed using CAMAC modules controlled by a Micro-programmed Branch Driver (MBD). The control of the hardware and data sorting was done with the XSYS software package using a 3200-MicroVax dedicated for data collection. For our on-line TOF $\sigma(\theta)$ measurements a group of programs were developed over the years and are contained in the package NTOF. These programs make it possible to carry out the collection and the sorting of the data into specific data areas, to set windows on certain peaks, and to do some on-line calculations.

Data were collected and spectra were stored for the angles between 18°-160° in steps of 4°. Spectra were taken with the sample IN and with the sample OUT for ^{27}Al and ^{59}Co. Measurements at the forward angles were conducted using both left and right detectors simultaneously set at the same nominal angle. By averaging the final

$\sigma(\theta)$ values for both detectors, slight misalignments that might arise from beam or sample positioning cancel. This cancellation is particularly important on the steep slope at the forward angles, where $\sigma(\theta)$ changes by 100% in 4°. Polyethylene measurements were done several times during the $\sigma(\theta)$ measurements at each energy, especially at the beginning, end, and whenever some experimental parameters were changed. The polyethylene scatterer provides an absolute normalization for our data since the n-p scattering cross section is very accurately known. The n-p yield at a certain angle and energy is obtained by subtracting the yield due to scattering from the carbon contained in the polyethylene $(CH_2)_n$ sample. To allow this subtraction for the polyethylene measurements the sample was considered OUT when we put a cylinder of ^{12}C that contains the same number of ^{12}C nuclei as the polyethylene sample. The scattering from polyethylene is measured at angles where good separation between both the elastic and inelastic carbon peaks from the hydrogen elastic peak is achieved. Normally, for the neutron energies in the present measurements the angle is chosen according to the following empirical equation

$$\theta = 42^\circ - \frac{1^\circ}{\text{MeV}} * E$$

where E is expressed in MeV.

2.5.2 Analyzing Power Measurements

The analyzing power data was acquired using basically similar hardware and software routines. The programs that are used for $A_y(\theta)$ data collection are called PTOF which enables us to display data areas and gates, and make some on-line calculations. For these measurements both the right and left detector are always set at the same angle and data are collected for four conditions in each detector. These conditions are sample-in spin-up, sample-in spin-down, sample-out spin-up and

sample-out spin-down. The spin-up and spin-down refers to the spin direction of the polarized neutron beam. These configurations are repeated many times for each angle in order to reduce instrumental asymmetry. The neutron beam polarization was calculated by observing the asymmetry for neutron scattering from ^{12}C at 50° as will be explained in Chapter 3.

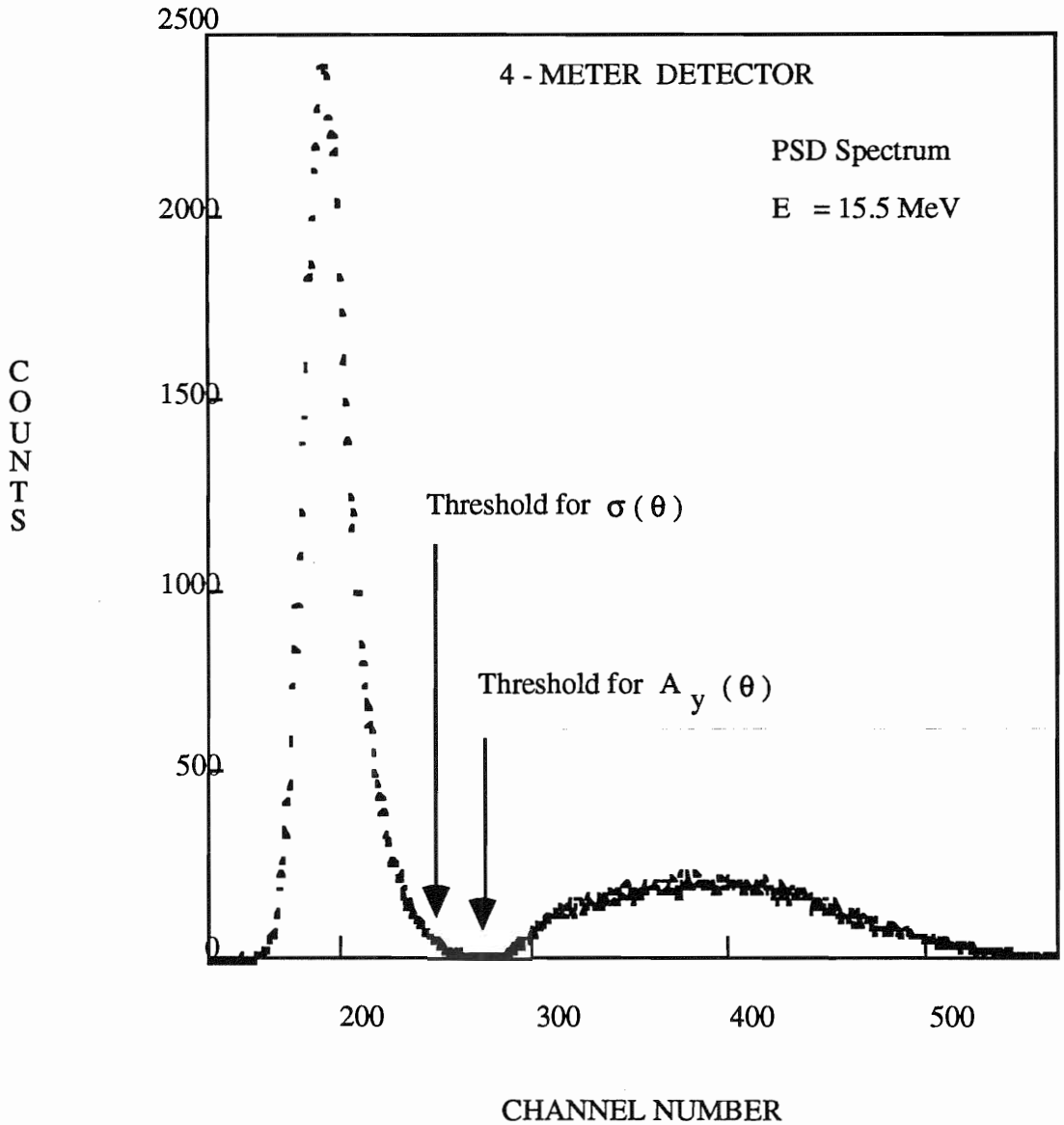

Figure 2.10. A PSD spectrum showing the threshold settings for the $\sigma(\theta)$ and $A_y(\theta)$ experiments.

CHAPTER 3

DATA REDUCTION AND CORRECTIONS

3.1 Introduction

A great deal of attention must be paid to the method of analyzing the data. Checking the stability of the beam, detectors, and electronics for any gradual or sudden changes is vital to the data analysis during a measurement of a complete angular distribution of the cross section. This is accomplished in part by carefully inspecting the ceiling-monitor yields and the zero-degree monitor yields for any changes over time. For an analyzing power measurement at a specific angle, the stability test was accomplished by observing the yields per accumulated beam-current-integrator (BCI) charge. Many tests were carried out to choose the correct window settings for the peaks of interest and as well as for obtaining good predictions of the background. Different background fits were tried in attempts to choose the best fit and to quantify the uncertainty in this determination. Early in the analyzing power analysis we found that for low background cases the least square fitting criterion, that is currently employed in the XSYS background fitting codes is not suitable. It consistently underestimates the background when it performs χ^2 fits to data having only one or two counts in some of the channels. The polarization of the background was an important issue in the $A_y(\theta)$ analysis since it affects the final result; this was carefully considered also.

3.2 Data Reduction

3.2.1 Cross Section Data

The NTOF spectra are the basic entities from which all of our information is extracted for $\sigma(\theta)$ and $A_y(\theta)$. For many of the angles, but particularly for forward angles where $\sigma(\theta)$ changes rapidly, both detectors were set at the same angles (on opposite sides of the incident beam axis). Time-of-flight spectra were accumulated for two configurations SAMPLE-IN and SAMPLE-OUT for each detector at every angle. These spectra were 1024 channels long with 0.18 ns per channel time calibration. The NTOF-OFF programs using XSYS software package were used to set gates, fit background (in some cases), and to perform different operations on spectra. Such spectra were used to provide the yields for the cross section data. (Similar spectra were used to obtain the normalization factor from n-p scattering to convert the yield to absolute cross sections). To do this, first the SAMPLE-OUT spectra in the 4- and 6-meter detectors were normalized to the SAMPLE-IN spectra and then subtracted from the SAMPLE-IN spectra to generate the DIFFerence spectra for each detector:

$$\text{DIFF} = \text{SAMPLE-IN} \; - \; \text{SAMPLE-OUT} \; \times \; \frac{\text{MON}_{\text{IN}}}{\text{MON}_{\text{OUT}}}.$$

The normalization factor $\frac{\text{MON}_{\text{IN}}}{\text{MON}_{\text{OUT}}}$ is obtained from the neutron-flux MONitor (ceiling monitor.) To obtain the MON_{IN} and MON_{OUT} yields, a very careful choice of the background in the monitor spectrum was done. Different polynomial fits and different window settings for the background were tested. Finally, for the neutron-flux monitor we ended up choosing a fifth-order polynomial to simultaneously fit to the background regions on the left and right sides of the peak of interest. Figure 3.1 shows the background fit for the neutron-flux monitor along with the windows settings used in

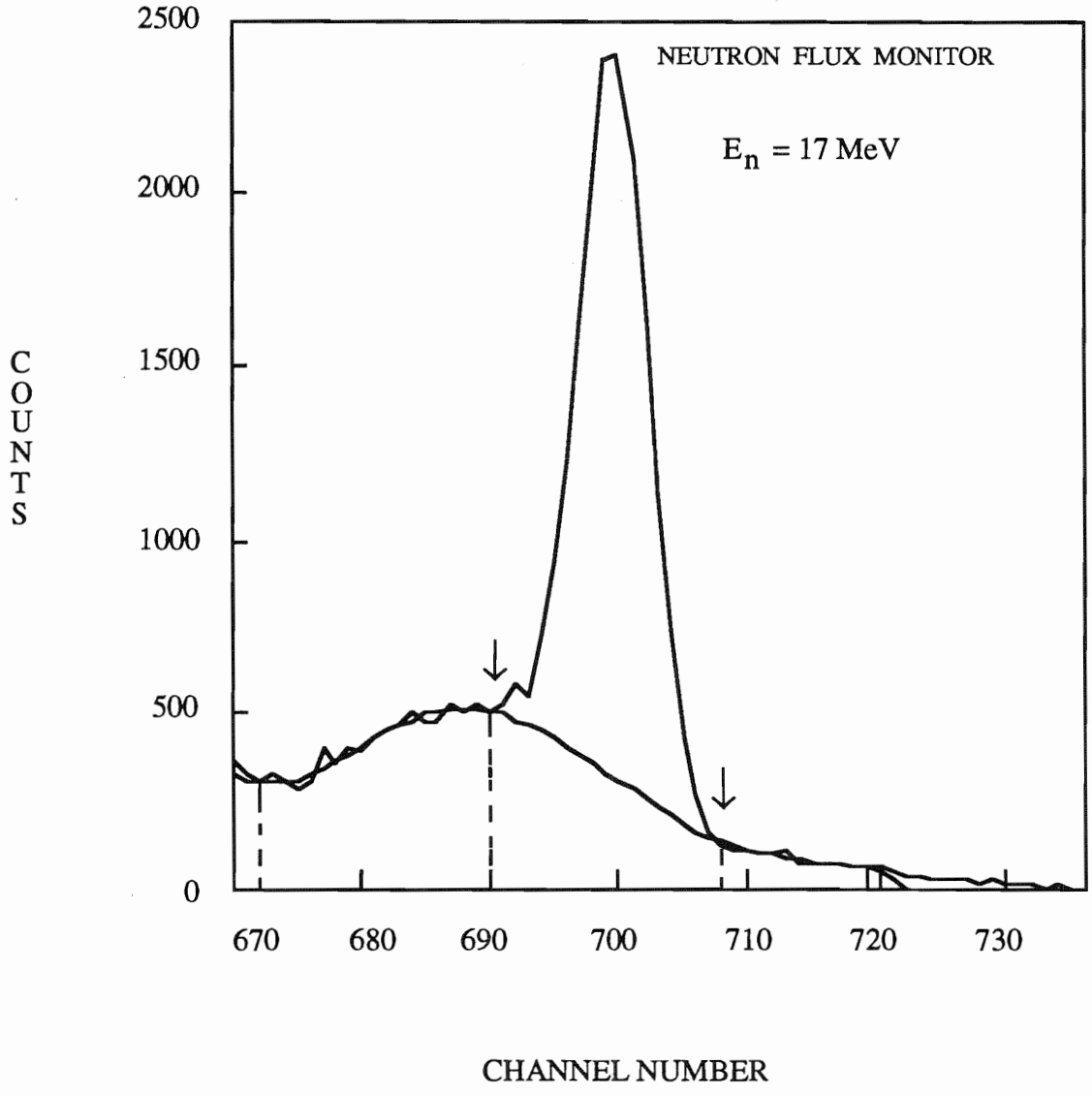

Figure 3.1. A TOF spectrum for the flux monitor at E_n = 17 MeV. The curve underneath the peak is the fit for the underlying background. The dashed vertical lines denote the regions used to fit the background; the arrows indicate the window used to sum the peak.

the background fitting procedure and the neutron peak coming from the $^2H(d, n)^3He$ ground-state reaction with a Q-value of 3.27 MeV. The flux monitor is located at a reaction angle of 50°. The large continuum of background is primarily due to neutrons from the breakup reaction $^2H(d, np)^2H$. This background is constant in time relative to the ground-state yield throughout the measurement at a single energy. Once the background fitting and windows settings were selected they were kept the same throughout the analysis for a single energy, including the n-p runs, in order to insure proper normalization. Window settings were only changed when there was a timing shift due to changing experimental parameters like the detector bias. In such cases, extra n-p runs were always conducted. After setting the appropriate windows and background the net MON_{IN} and MON_{OUT} yields were obtained by summing up the neutron events within the window of interest in the SAMPLE-IN and SAMPLE-OUT spectra.

Once the DIFF spectra for the 4- and 6-meter detectors are obtained they are used to extract the yields Y_s of the neutrons scattered from the sample. The DIFFerence spectra still has some background correlated to the presence of the scattering sample. This sample-correlated background must be subtracted before calculating the yields. An appropriate fit to this residual background was chosen, windows about the peaks of interest were drawn, and Y_s for the 4- and 6-meter detectors were obtained. These yields must then be normalized to the MON_{IN} yield for each angle:

$$Y'_s = \frac{Y_s}{MON_{IN}} = \frac{\text{SAMPLE-IN}}{MON_{IN}} - \frac{\text{SAMPLE-OUT}}{MON_{OUT}} - \frac{B_s}{MON_{IN}}$$

where B_s is the sample correlated background. Figure 3.2 shows a SAMPLE-IN, SAMPLE-OUT and a DIFFerence spectra.

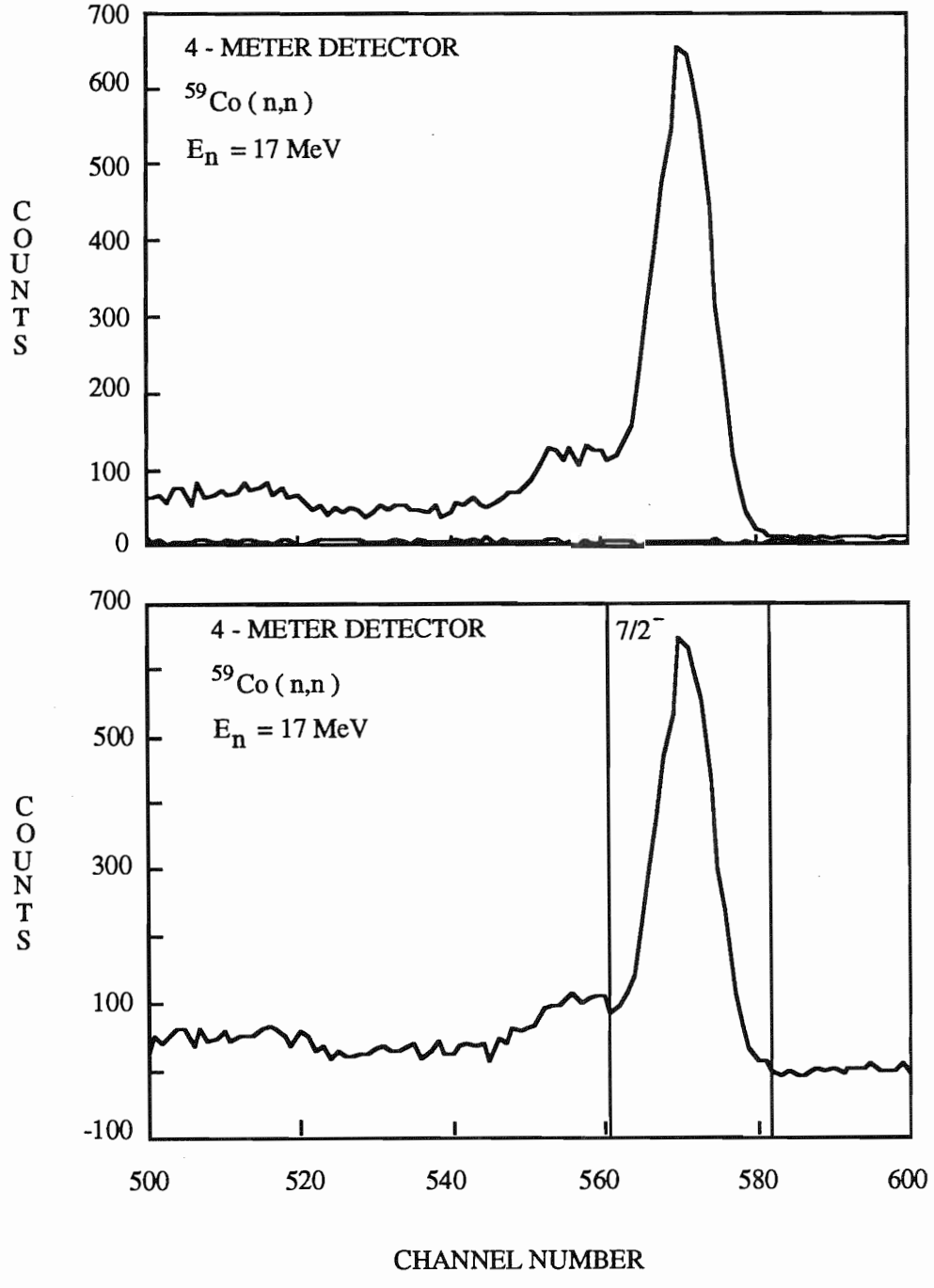

Figure 3.2. TOF spectra for the SAMPLE-IN, SAMPLE-OUT and DIFFerence spectra for the 4-meter detector at E_n = 17 MeV for ^{59}Co at $\theta_{lab} = 85°$. Note the zero-offset in the lower panel.

3.2.2 Analyzing Power Data

Both detectors were set at the same angle on opposite sides of the beam axis and time-of-flight spectra were taken at four configurations for each detector, SAMPLE-IN-UP, SAMPLE-IN-DOWN, SAMPLE-OUT-UP, AND SAMPLE-OUT-DOWN. These spectra were 512 channels long with 0.39 ns per channel time calibration. The PTOFOFF computer codes were used under XSYS to set gates, fit backgrounds, manipulate spectra, and make analyzing power calculations. These spectra were used to extract the yield at each configuration. Since $A_y(\theta)$ was a relative measurement no absolute normalization was necessary. For a relative value the data were normalized to the BCI. The DIFFerence spectra were calculated as follows:

$$\text{DIFF} = \text{SAMPLE-IN} - \frac{\text{BCI}_{\text{IN}}}{\text{BCI}_{\text{OUT}}} \times \text{SAMPLE-OUT}$$

Figure 3.3 shows a SAMPLE-IN, SAMPLE-OUT and a DIFFerence spectra.

Careful examination of the background remaining in the DIFFerence spectra was considered. First we had to decide whether to consider a polarized or unpolarized background. For this we set three gates (see Figure 3.4) on the right of the peak of interest and calculated the asymmetry of the counts within these gates over a wide range of angles. The asymmetry was found to be zero within the statistical error in most cases. The other consideration was the choice of the background level. For this, different background levels were chosen with polynomial fits of different orders. We noticed early in our analysis that due to the low level of background in the DIFFerence spectra, the least square method of the computer systems code XSYS to fit the background always underestimates the background when some of the channels contain only one or two counts. In order to overcome this problem we added 1000 counts to the counts in each channel in the spectrum and then fit the background with a constant level with a simple χ^2 routine. In this way the χ^2 fit will correspond to an average level

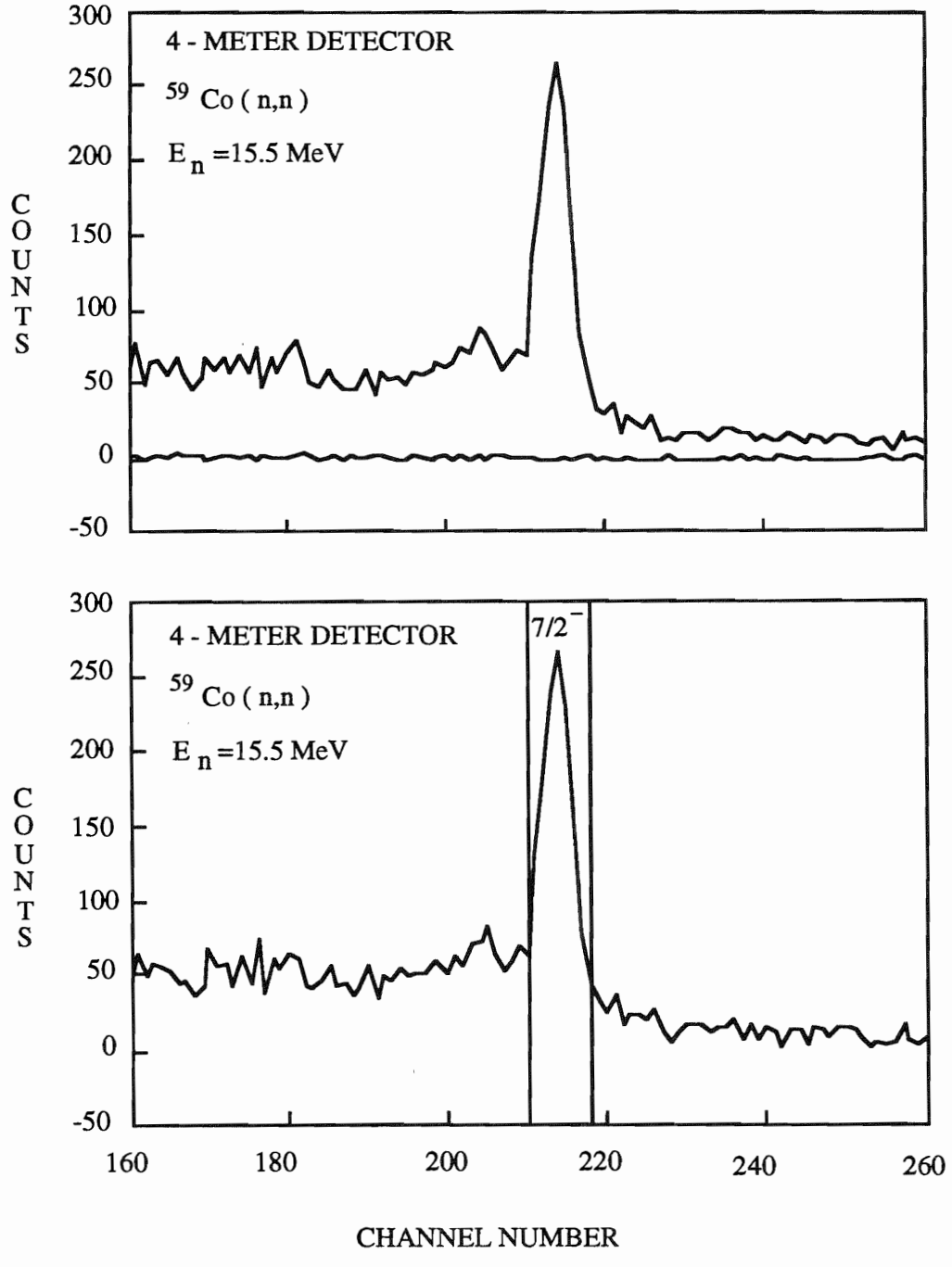

Figure 3.3. Polarized TOF spectra for the SAMPLE-IN, SAMPLE-OUT and DIFFerence spectra for the 4-meter detector at E_n = 15.5 MeV for ^{59}Co at $\theta_{lab} = 65^{\circ}$.

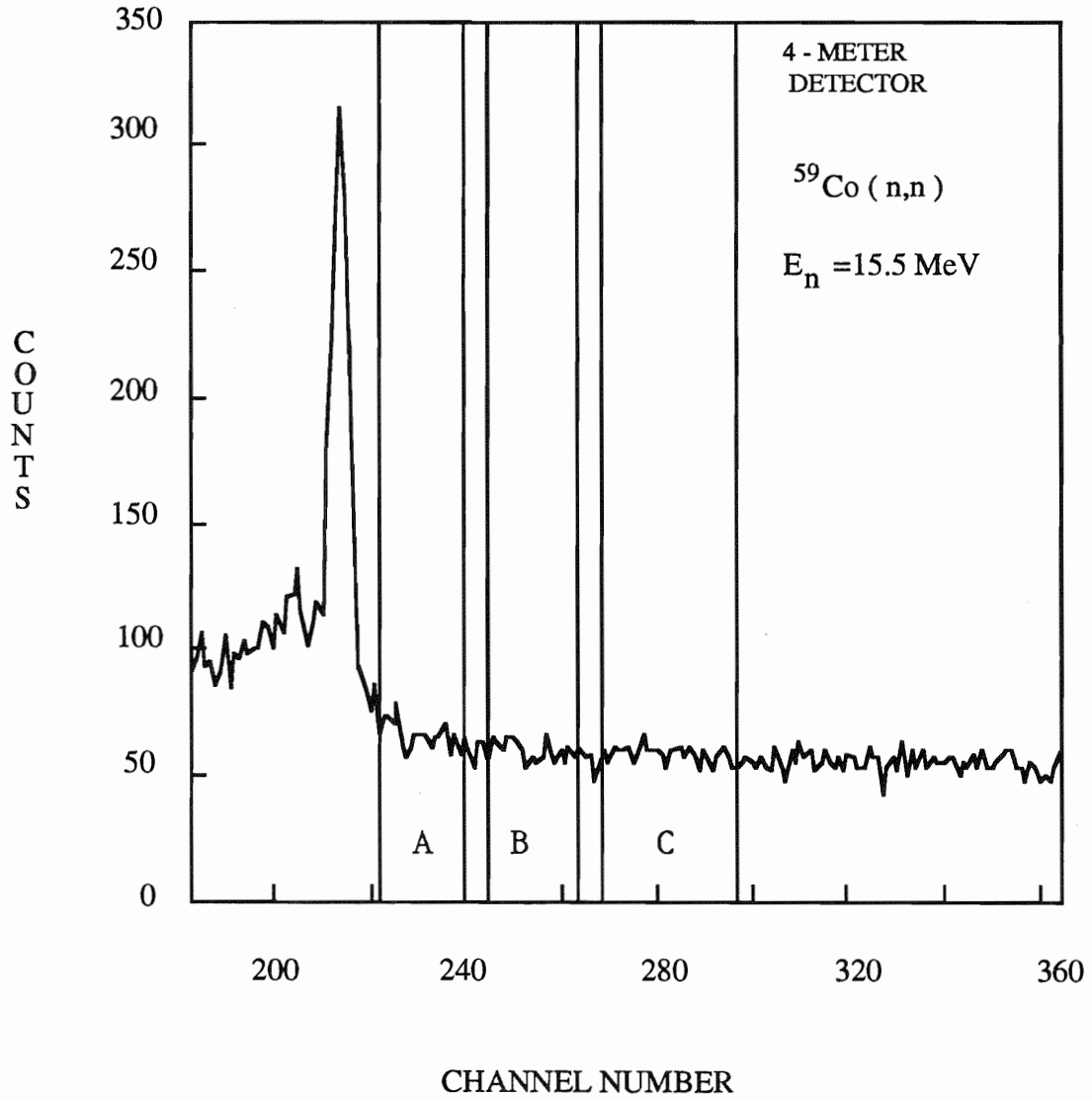

Figure 3.4. TOF spectra for the analyzing power measurements for E_n = 15.5 for ^{59}Co at θ_{lab} = 65°. The sharp peak is the peak due to elastic scattering, i.e., the peak of interest. The gates A, B and C that were set to test the background polarization are shown (see text).

of the background. Next, to obtain a relative measure of the counts in the neutron peak, three gates were set around the peak of interest at 10, 20, and 40% of the peak height. This helped to decide whether the level of background was correct. That is if the asymmetriescalculated using each of these three gates were equal, then the background level was considered to be proper. Figure 3.5 shows the DIFFerence spectra with the background level before adding 1000 counts to each channel.

At each angle four yields were extracted from the DIFFerence spectra, left-up (L↑), left-down (L↓), right-up (R↑), and right-down (R↓). From these yields the value of α was calculated:

$$\alpha = \sqrt{\frac{L\uparrow(\theta)R\downarrow(\theta)}{L\downarrow(\theta)R\uparrow(\theta)}} .$$

From this A_y was calculated:

$$A_y(\theta) = \frac{1}{P_n} \left[\frac{\alpha - 1}{\alpha + 1}\right]$$

where P_n is the neutron beam polarization.

To determine the beam polarization we used a ^{12}C scatterer as a target. We chose the laboratory scattering angle of 50°, an angle where the analyzing power is relatively large, and was previously measured at TUNL [Tor87]. From the TOF spectra for ^{12}C, the asymmetry ε was calculated according to the relation:

$$\varepsilon = \frac{\alpha - 1}{\alpha + 1} .$$

Since A_y is known for ^{12}C, then we obtain

$$P_n = \frac{\varepsilon(50°)}{A_y(50°)} .$$

This indirect method of determining the beam polarization required that we use the computer code JANE to calculate the effective analyzing power for the experimental

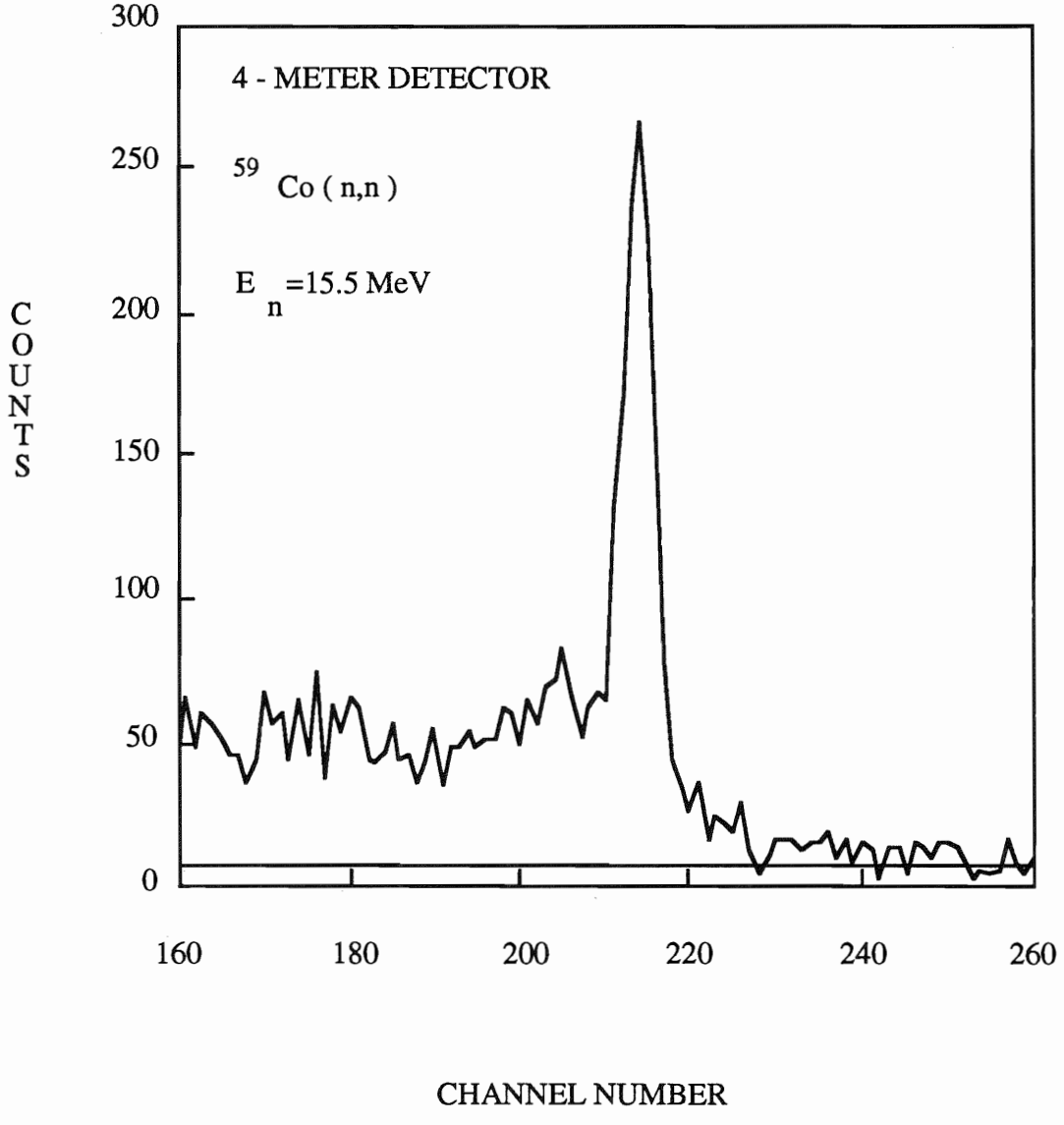

Figure 3.5. The analyzing power TOF DIFFerence spectrum before adding 1000 counts to each channel to improve the background estimate at E_n = 15.5 MeV for $\theta_{lab} = 65°$.

conditions, i. e. , $A_F^{exp}(\theta)$ for the finite geometry of the set up. From this the beam polarization was calculated:

$$P_n = \frac{\varepsilon_F^{exp}(50°)}{A_F^{exp}(50°)} .$$

3.3 Data Normalization

3.3.1 Cross Section Data

The next step in our process was to normalize the yields of the 6-meter detector and the 4-meter detector to n-p scattering. In doing this we assume that the efficiency curves of the two detectors are identical. This is true to within the accuracy of their calibration [Elk81, Ped86]. Absolute differential cross sections were calculated from yields according to the following equation:

$$\sigma(\theta_L, E_n) = \frac{Y_s'(\theta_L)}{Y_p'(\theta_p)} * \frac{n_H}{n_s} * \sigma_{np}(\theta_p, E_n) * \frac{1}{PCF(\theta_p)} .$$

This normalization process was done using the computer code DATANORM where

$Y_s'(\theta_L)$ = Yield for neutron scattering from sample normalized yield at the lab angle θ_L

$Y_p'(\theta_p)$ = Yield for neutron scattering from hydrogen normalized to the monitor yield at the lab angle θ_p where polyethylene measurements took place

n_H = Number of hydrogen nuclei in the polyethylene sample

n_s = Number of nuclei in sample

$\sigma_{np}(\theta_p, E_n)$ = Neutron cross section scattered from hydrogen at the energy E_n and angle θ_p.

The σ_{np} is obtained from a library of n-p cross sections based on the values reported by Hopkins and Breit [Hop71]. The normalization factor PCF(θ_p) is the polyethylene correction factor for relative efficiency, attenuation, finite geometry, and multiple scattering effects. This factor is obtained by running the computer code EFFIGY15 in the two element mode (i.e., for the mixture of carbon and hydrogen) for the experimental conditions under which the polyethylene measurement took place.

3.4 Data Corrections

3.4.1 Cross Section Data

Neutron experiments normally involve large samples and large detectors to enhance counting rates. The problem of low neutron counting rates stems from the fact that neutron scattering experiments involve two reactions, a neutron source reaction and the scattering reaction of interest. The other reason for low neutron counting rates is the fact that neutrons are neutral particles and they are only detected by nuclear reaction processes within the detectors. For energies above 8 MeV, typical detectors have an efficiency of 15% to 30%, depending on the neutron energy, the detector thickness and the bias settings. The combination of these facts lead to the use of large samples and large area detectors. In the ^{27}Al case, the full-width of the angle subtended by the scatterer as seen by the source is 8.5° and by the detector is 1.6°. For the ^{59}Co scatterer these angular acceptances were slightly larger. Since differential cross sections are defined for point samples and a definite scattering angle, the experimental data needs to be corrected accordingly.

Three types of corrections are applied to the data. First a finite geometry correction is applied because these detectors of finite size see a certain angular range of the (finite) sample. As the scattering cross section changes with angle, this causes an

angle shift between the mean angle of the scattering measurement and the nominal detector angle. Angle shifts range from 2°, for forward angles where the differential cross section slope is very steep, to near 0° for angles at the minima and maxima of the $\sigma(\theta)$. The second correction is the flux attenuation correction which causes a lowering of the observed events. This factor is almost the same over all angles. The third correction is due to multiple scattering. Since the scattering sample is finite, there is a chance for a scattered neutron to scatter a second, third or even more times within the scattering sample. The computer code EFFIGY15 revised by R.S. Pedroni [Ped86] is designed to apply these corrections to the normalized experimental $\sigma(\theta)$ data obtained from DATANORM. The code EFFIGY15 is a Monte Carlo routine which simulates the experimental data. This code uses an iterative procedure to calculate the correction to the data. To accomplish this the code starts with an initial library which contains the total and differential cross section data for the reaction of interest. Usually the initial $\sigma(\theta)$ library is built from the Legendre polynomial fits to the experimental data. In our case, we started with a library based on predictions from a preliminary coupled channels model for ^{27}Al and ^{59}Co. This library was updated after each iteration using a polynomial fit to the corrected experimental data. The input data set also contains the physical parameters of the experiment such as the gas cell, detector, and scattering dimensions. The code EFFIGY15 simulates experimental TOF spectra by following the individual neutron histories from their production at the gas cell through the scattering from the sample until they are detected. The code checks periodically for the convergence of the calculated yields to the experimental yields within a specified percentage. If convergence is not achieved, the cross section library is updated and the code is rerun again. Figures 3.6a, and 3.6b show the uncorrected data and the data corrected for finite geometry, neutron flux attenuation, and multiple scattering. Tables

of the corrected and uncorrected data are given in Appendix A. Note the angle shift due to the varying cross section over the combined angular spread subtended by the scatterer at the source and by the detector.

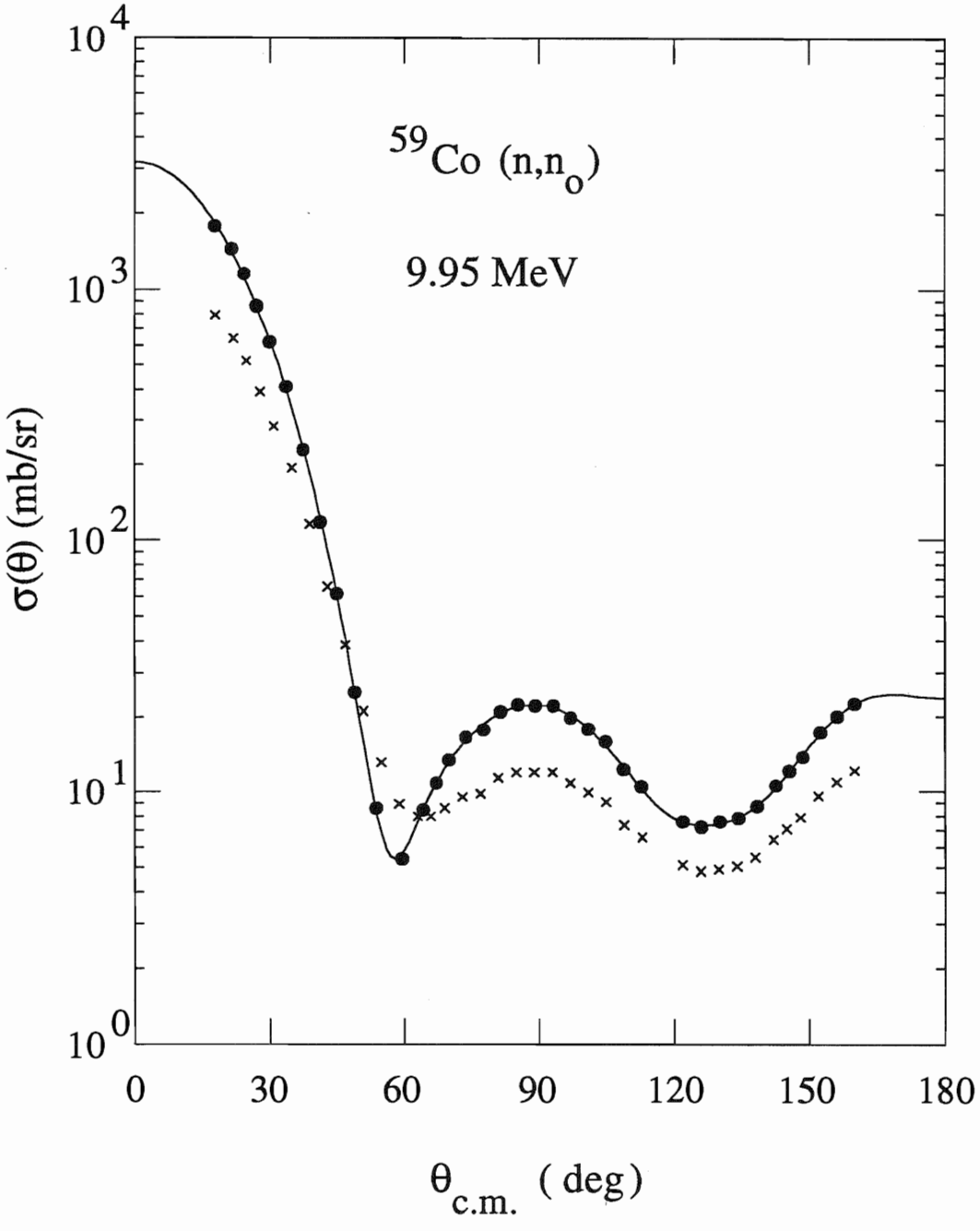

Figure 3.6a. Cross section data at E_n = 10.0 MeV for ^{59}Co before (crosses) and after (dots) correction for finite geometry, attenuation, and multiple scattering by EFFIGY15. The solid curve is the Legendre polynomial fit for the corrected data.

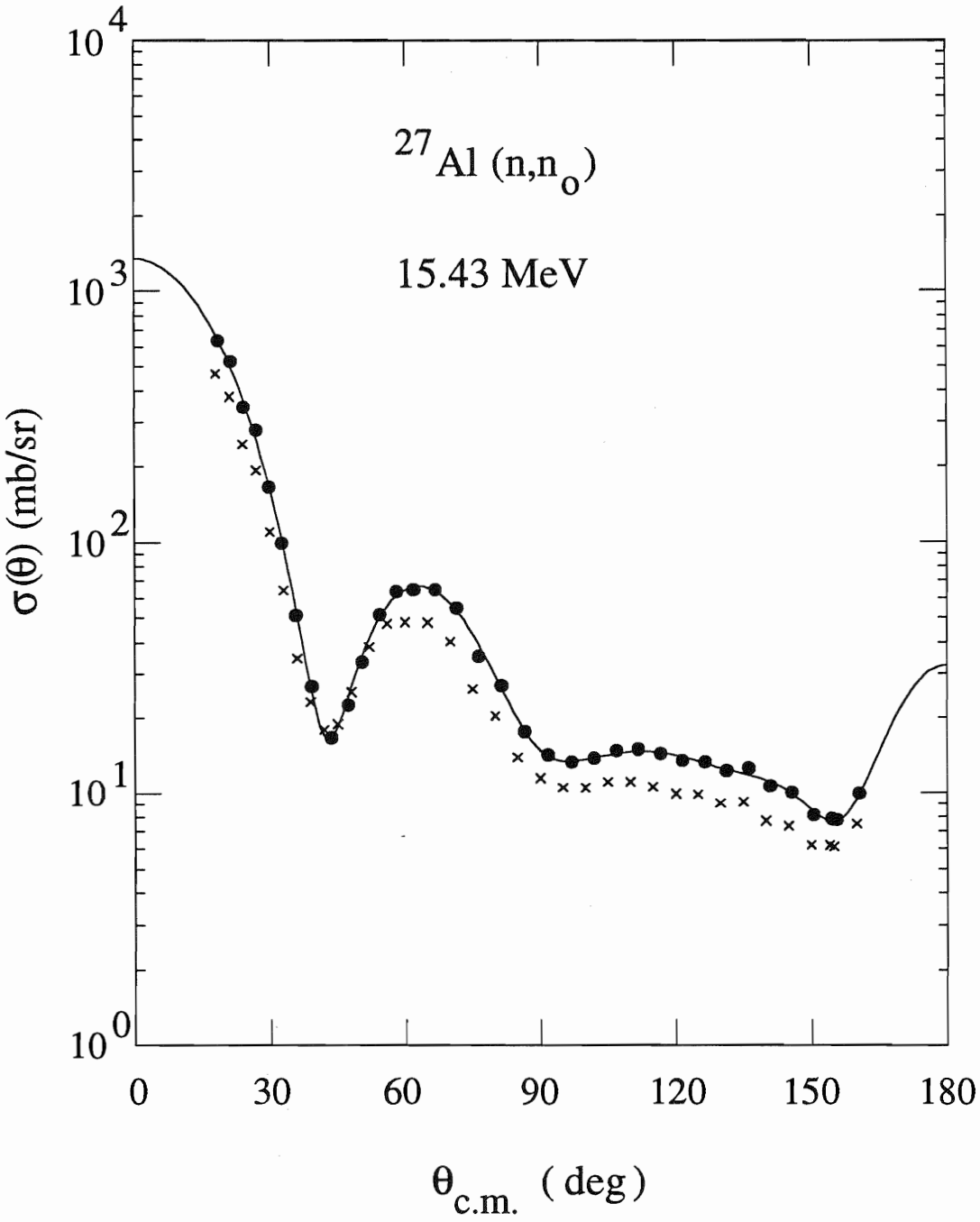

Figure 3.6b. Cross section data at E_n = 15.43 MeV for ^{27}Al before (crosses) and after (dots) correction for finite geometry, attenuation, and multiple scattering by EFFIGY15. The solid curve is the Legendre polynomial fit for the corrected data.

3.4.2 Analyzing Power Data

As for the $\sigma(\theta)$ data, analyzing power data need to be corrected for finite geometry, neutron flux attenuation, and multiple scattering effects. These corrections are done using the Monte Carlo code JANE. This code simulates the experiment in the lab the same way that EFFIGY15 does, except that JANE keeps track of the neutrons scattered to the left and those scattered to the right. This makes the correction procedure in JANE more complicated than in EFFIGY. This procedure is detailed by Guss [Gus82], Howell [How84], and Roberts [Rob88]. The code JANE uses a library of total and differential cross sections, along with the analyzing power in the energy region of interest. As in the $\sigma(\theta)$ case, this library was initially built in our case using our coupled channel model. After each iteration the library is updated with the newly corrected data. Only two iterations were required in order to reach convergence. Figures 3.7a and 3.7b show an example of the uncorrected data and the data as corrected by JANE. Appendix B has a tabulation of the corrected and uncorrected data.

3.5 Data Uncertainty

3.5.1 Cross Section Data

Cross section uncertainties can be grouped into two categories, relative uncertainties and normalization (scale) uncertainties. Relative uncertainties, which varied between 2-8% come from counting statistics, detector efficiencies, and Monte Carlo correction factors. Counting-statistics uncertainties which ranged from 1-7%, came from the statistical uncertainties in the neutron yields scattered from the sample and from the determination of the background underneath peaks of interest. Only the shape uncertainty of the efficiency curve enters into the relative uncertainty of $\sigma(\theta)$ since the

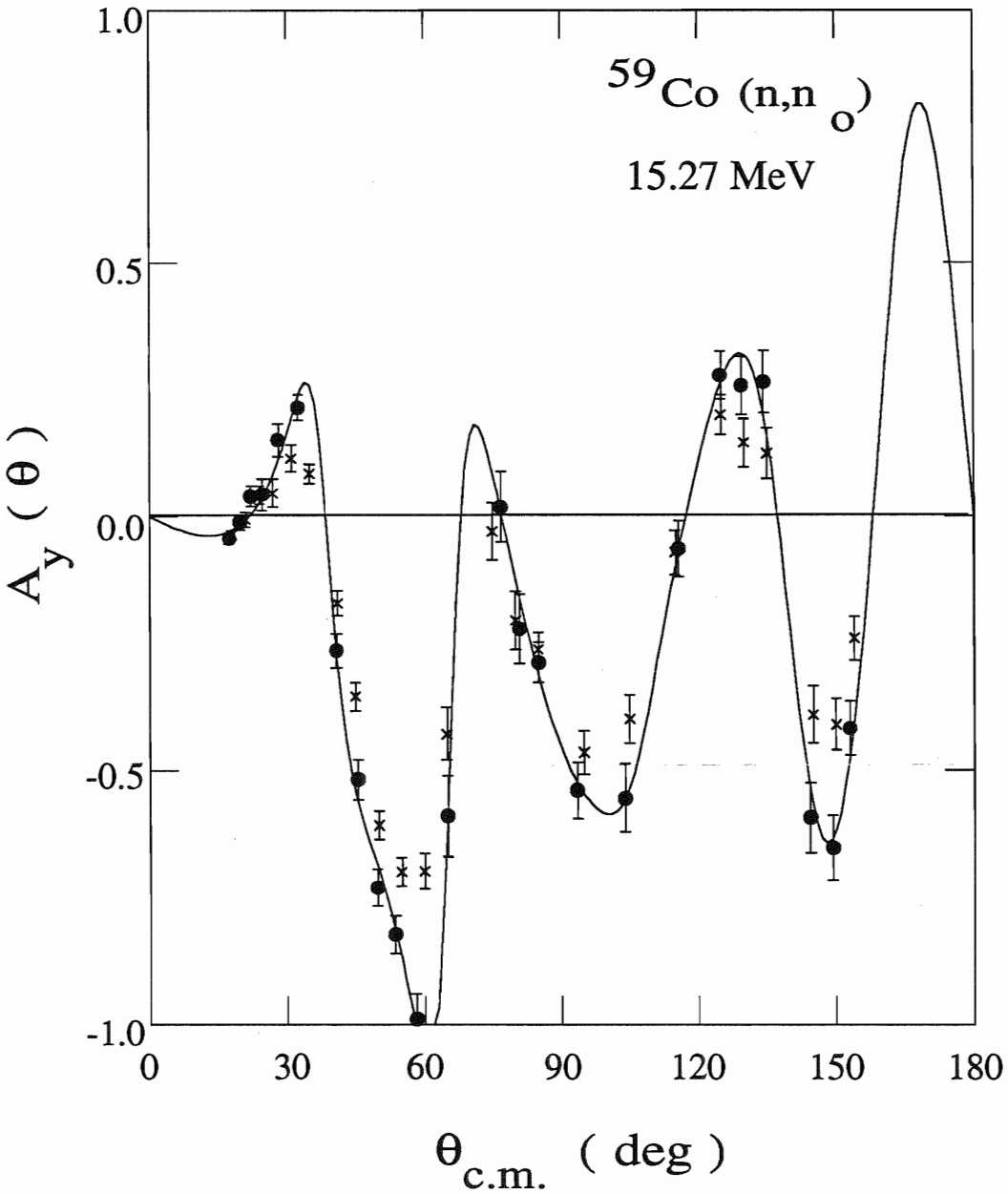

Figure 3.7a. Analyzing power data at E_n = 15.27 MeV for ^{59}Co before (crosses) and after (dots) correction for finite geometry, attenuation and multiple scattering by JANE. The solid curve is the associated Legendre polynomial fit for the corrected data.

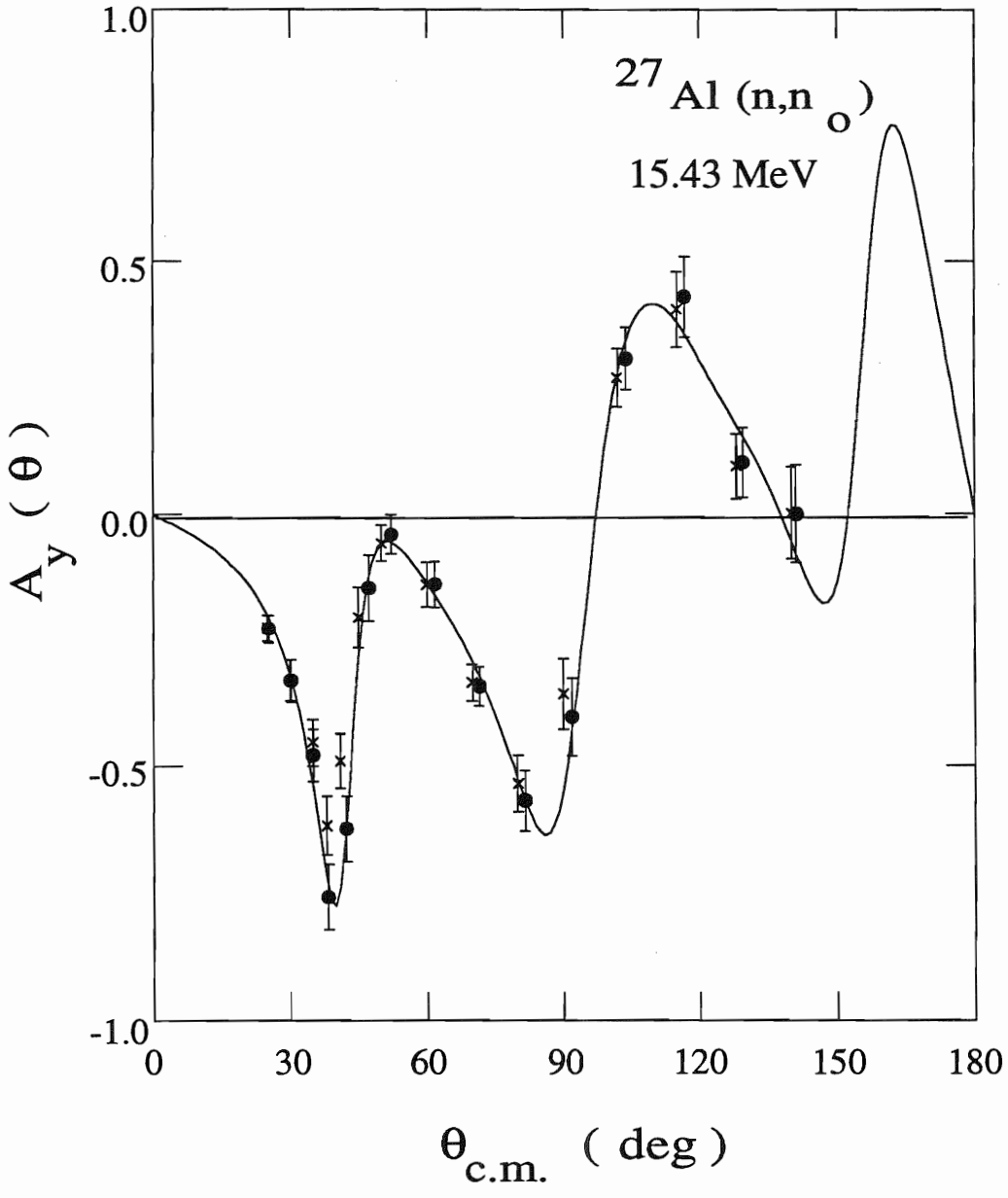

Figure 3.7b. Analyzing power data at E_n = 15.43 MeV for ^{27}Al before (crosses) and after (dots) correction for finite geometry, attenuation and multiple scattering by JANE. The solid curve is the associated Legendre polynomial fit for the corrected data.

absolute $\sigma(\theta)$ was measured relative to n-p scattering. This shape uncertainty is related to the narrow energy spread on the efficiency curve that covers the span of neutron energies caused by the kinematics from scattering through various angles by either the ^{59}Co or ^{27}Al sample. These errors were less than 2%, based on the efficiency calibration data reported by El-Kadi [Elk81]. Monte Carlo correction factors obtained from EFFIGY15 added 1% uncertainty to $\sigma(\theta)$ at most angles. However, this value does not include error enhancement from subtracting multiple scattering events from the measured yields. This process enhances the errors by a factor of 1.25 in the angular region of the minima of the elastic scattering cross section.

Normalization uncertainties include the following:

1. Statistical uncertainties from the n-p scattering yield that were used for normalization which ranged from 0.3%-0.9%.
2. Analytic corrections obtained with JANE that were applied to the n-p scattering yields to deduce σ_{np}. These corrections includes the finite geometry, and neutron flux attenuations for the scatterer.
3. Uncertainties in σ_{np} used in the EFFIGY15 library were about 0.5-1.0% as reported by Hopkins *et al.* [Hop71] in addition to the angle uncertainty of about 0.2°.
4. Dead time and electronic corrections (bias, PSD) were about 0.5%.
5. The number of hydrogen nuclei in the polyethylene sample plus the mass determination of the ^{59}Co and ^{27}Al samples combined to less than 1%.
6. The ratio of the detector efficiency for n - p scattering through about 28°(lab) to the efficiency for n - ^{27}Al or n - ^{59}Co scattering. This ratio is known to within 3% for $E_n < 14$ MeV and to within about 6% for higher E_n.

3.5.2 Analyzing Power Data

As in the case with $\sigma(\theta)$, the $A_y(\theta)$ uncertainties can be separated into relative and normalization uncertainties. The relative uncertainty averaged to about 5% of the $A_y(\theta)$ value. This size was caused mainly by counting statistics and Monte Carlo corrections. Normalization uncertainties came basically from the determination of neutron polarization which was measured to a statistical accuracy of about 2% and would enter in as a scale factor of 1.00± 0.02. In addition, there is an overall scale uncertainty of about 6% attributed to the uncertainty in the previously calibrated $A_y(50°)$ for $^{12}C(n, n)$. This latter error will be reduced in the near future in a new calibration measurement.

3.6 Data Presentation

3.6.1 Cross Section Data

The computer code MACRO was used to present the final corrected data with a Legendre polynomial fit of the following form:

$$\sigma(\theta, E) = \sum_{l=0}^{n} A_l(E) \times P_l(\cos\theta)$$

where $A_l(E)$ are the Legendre polynomial expansion coefficients calculated to minimize the total chi-square χ^2:

$$\chi^2 = \sum_{i=1}^{n} \left[\frac{\sigma^{exp}(\theta_i) - \sigma^{cal}(\theta_i)}{\Delta \sigma^{exp}(\theta_i)} \right]^2 .$$

Differential cross sections for ^{59}Co are shown in Figure 3.8. Figure 3.9 shows $\sigma(\theta)$ for ^{27}Al at 15.5 MeV. The error bars shown represent the relative uncertainties only; they

do not include the scale (normalization) errors which give a scale factor of about 1.00±0.03.

3.6.2 Analyzing Power Data

The code MACRO was also used to fit the analyzing power data of ^{27}Al and ^{59}Co at 15.5 MeV using an associated Legendre polynomial fit to the product of $A_y(\theta) \times \sigma(\theta)$. This expression has the form

$$A_y(\theta, E) \times \sigma(\theta, E) = \sum_{l=1}^{n} B_l(E) \times P^1_l(\cos\theta)$$

where $B_l(E)$ are the associated Legendre polynomial expansion coefficients for the neutron energy E. Figures 3.10 and 3.11 show the corrected $A_y(\theta)$ data for ^{59}Co and ^{27}Al, respectively, with the corresponding fits. The error bars shown represent only the relative uncertainties; there is a scale factor of about 1.00 ± 0.06 as discussed above.

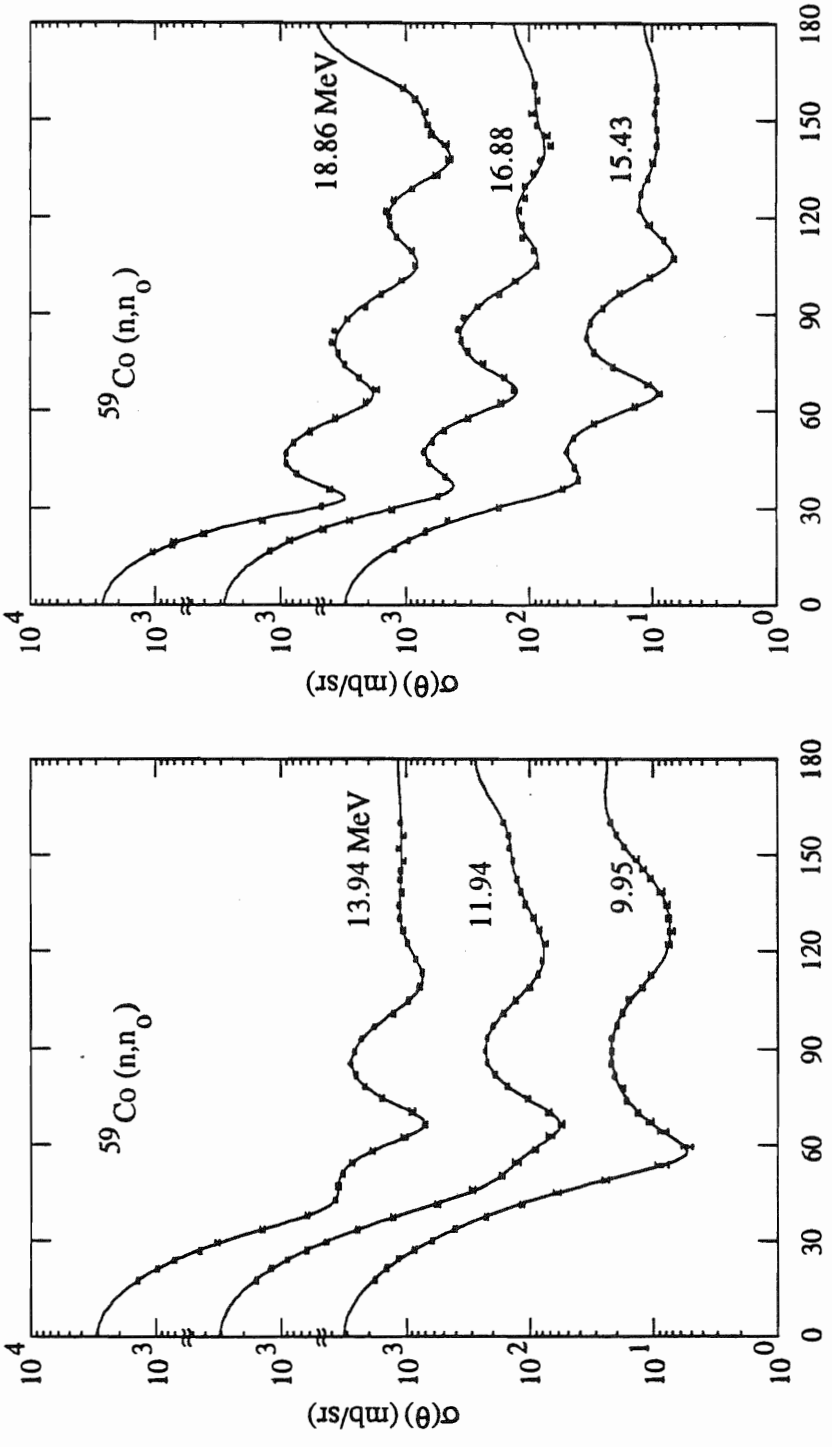

Figure 3.8. The differential cross section data for ^{59}Co. Curves are Legendre polynomial fits.

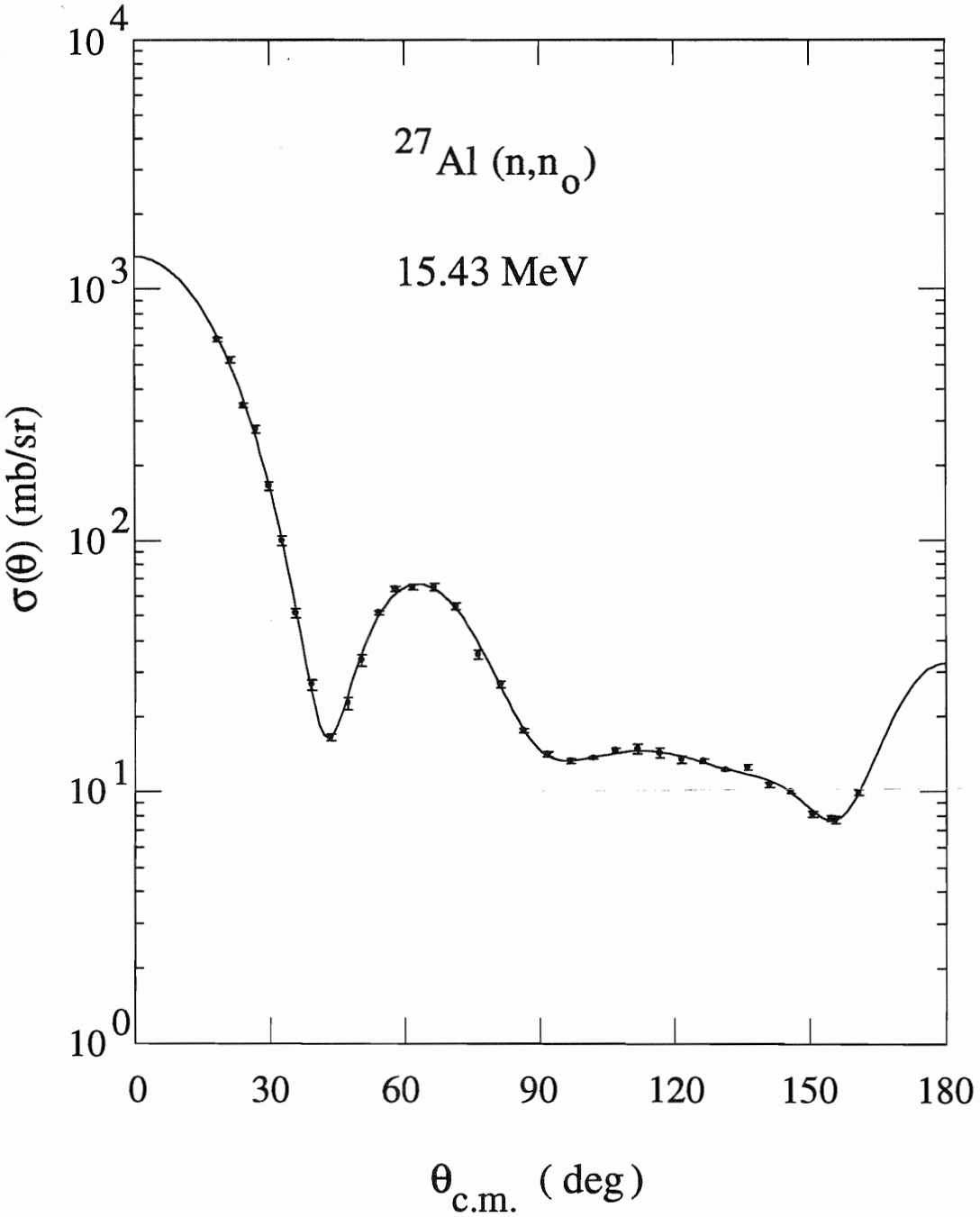

Figure 3.9. The differential cross section data for ^{27}Al at 15.5 MeV. The curve is a Legendre polynomial fit.

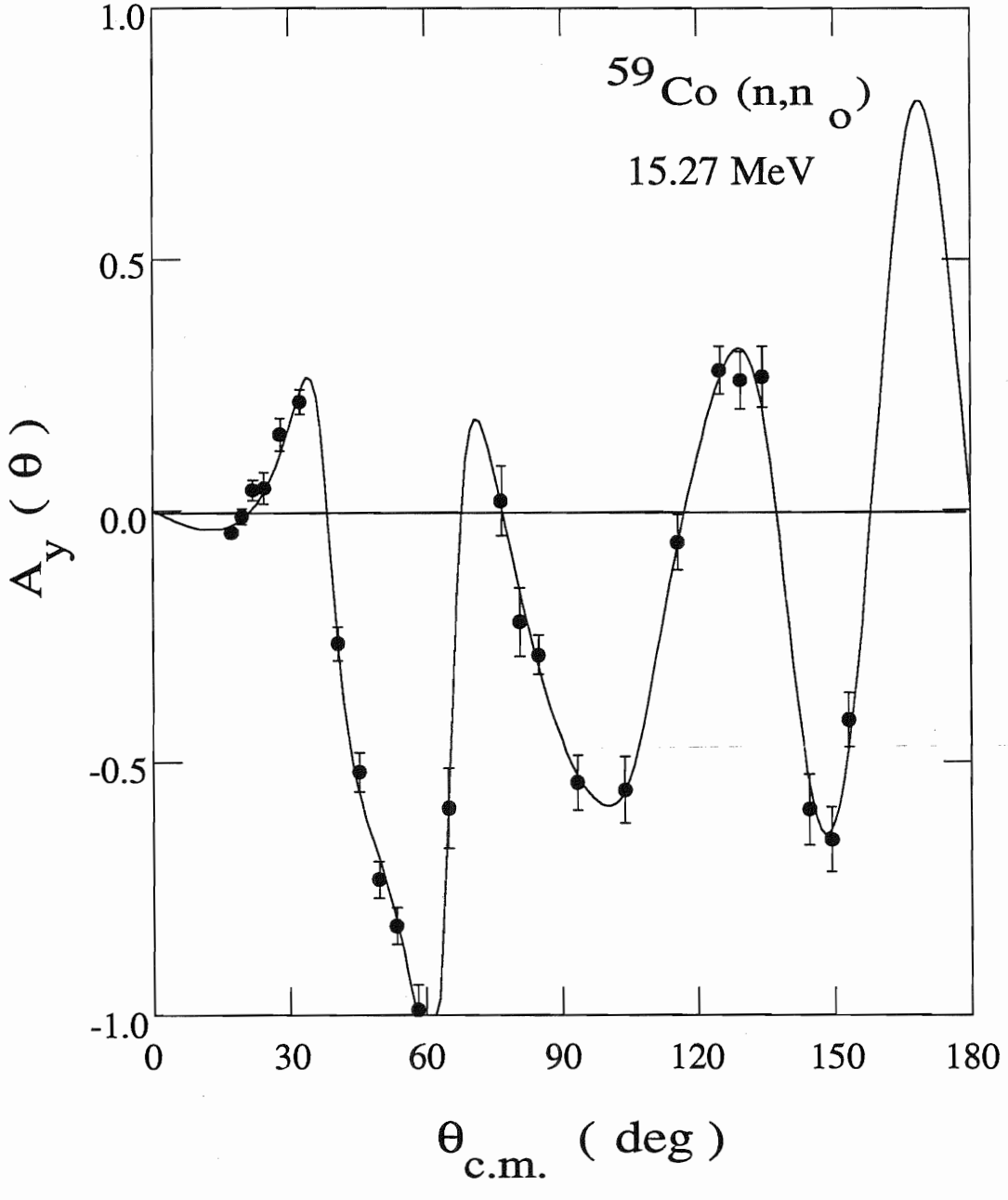

Figure 3.10. The analyzing power data for ^{59}Co at E_n = 15.27 MeV. The curve is the associated Legendre polynomial fit.

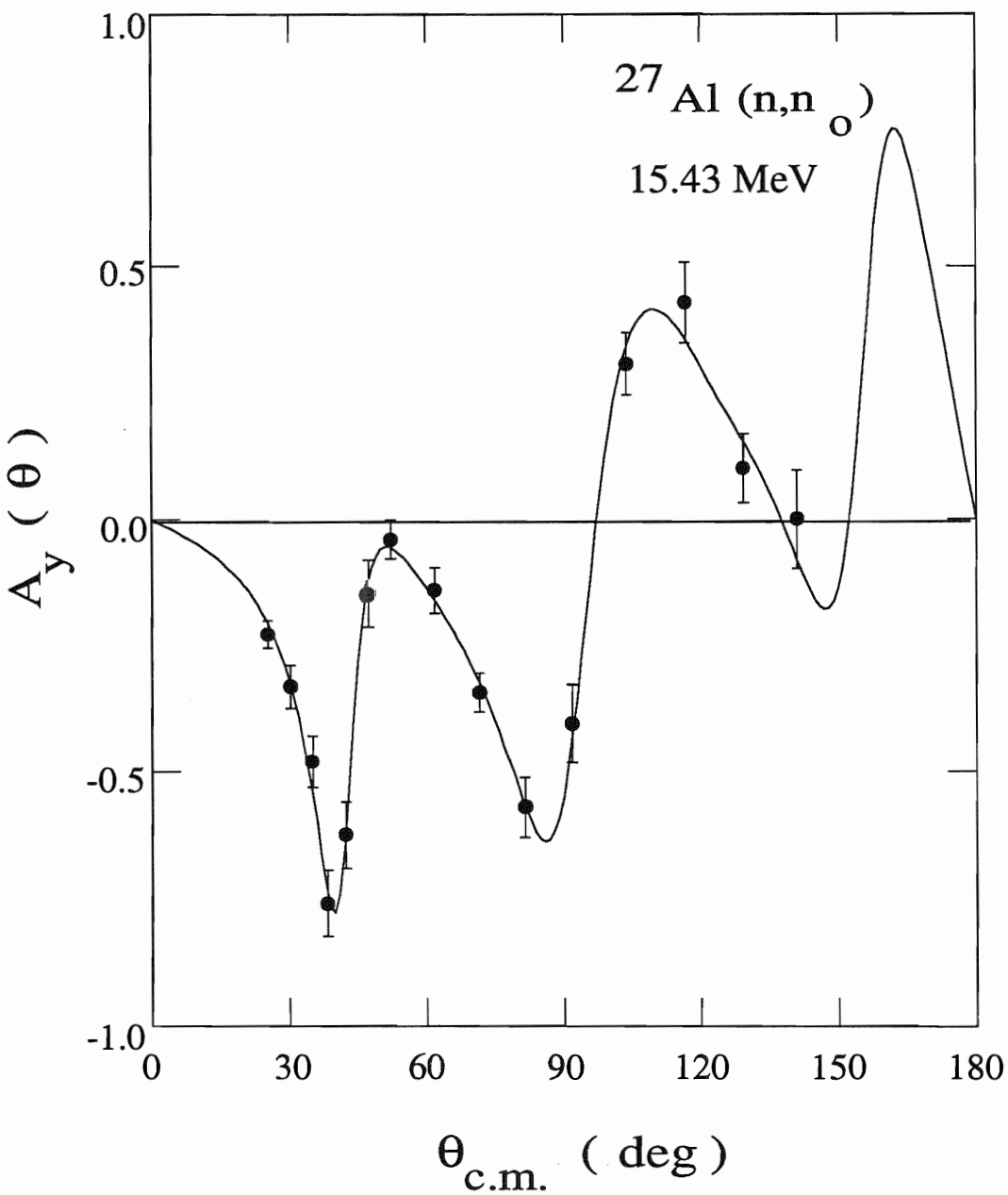

Figure 3.11. The analyzing power data for ^{27}Al at E_n = 15.43 MeV. The curve is the associated Legendre polynomial fit.

CHAPTER 4

DATA BASE AND COMPOUND NUCLEUS CALCULATIONS

4.1 Introduction

Two extremes are recognized when two nuclear systems collide. First they may coalesce to form a compound nucleus(CN) in an excited state. The compound nucleus lives long enough (~10^{-16} s) for its excitation energy to be shared by all its nucleons. Then this new compound system decays through one or more channels:

$$A + a \rightarrow C^* \rightarrow B^* + b \ .$$

The other extreme is the direct reaction process where the two nuclear systems interact with each other very quickly (10^{-24} s) and proceed directly from initial to final states without forming an intermediate compound state:

$$A + a \rightarrow B^* + b \ .$$

Between these two extremes other intermediate processes take place that do not fall into either category and are referred to as pre-equilibrium reactions. These processes are less important except for reactions between heavy nuclei.

In our neutron experiments the two extremes, i.e., the compound nucleus reactions and direct reactions, compete and depending on the neutron energy and mass number of the target nucleus one of them predominates. Figure 4.1 shows the competition between the two processes as a function of neutron energy for the ^{56}Fe (n, n') reaction [Kin70]. The figure shows the compound nucleus reaction predominates at low energy and becomes negligible at about 8 MeV.

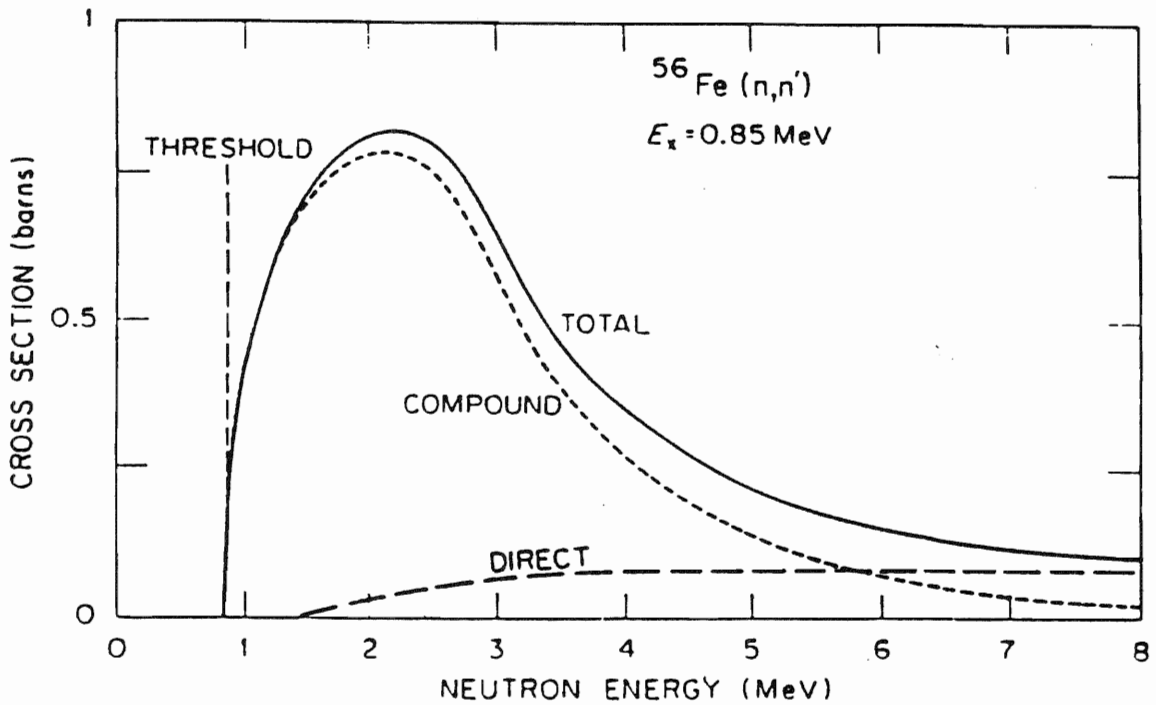

Figure 4.1. Excitation functions for exciting the lowest excited state of ^{56}Fe. The figure shows the competition between the CN and direct reactions.

In our models developed later we are only concerned with direct elastic scattering processes, sometimes called shape elastic processes. But compound nucleus elastic processes contribute to the observed elastic cross section, especially at low energy

$$\sigma_{el}(\theta) = \sigma_{CE}(\theta) + \sigma_{SE}(\theta) .$$

Here σ_{CE} is the compound elastic cross section and σ_{SE} is the shape elastic cross section. Experimentally the shape elastic and compound elastic contributions are indistinguishable, so we have to resort to calculation to subtract the compound elastic cross section from the observed elastic cross section to determine the "observed" shape elastic cross section.

Compound nucleus contributions are usually calculated through a statistical model since there is a large number of possible exit channels. The statistical model used conventionally is due to Hauser and Feshbach [Hau52] and is outlined in the next section.

4.2 Hauser-Feshbach Statistical Model

Three assumptions constitute Hauser-Feshbach theory about CN formation:

i) That flux is conserved.

ii) That the CN decay is independent of its mode of formation.

iii) That time-reversal invariance holds.

From the independence assumption *ii*) we can write the CN cross section $\sigma^{CN}_{\alpha\beta}$ as follows:

$$\sigma^{CN}_{\alpha\beta} = \sigma^{CN}_{\alpha} P_{\beta} \qquad 4.1$$

where σ^{CN}_{α} is the cross section for forming the compound nucleus from the entrance channel α and P_{β} is the probability of decaying through a particular exit channel.

The fact that the energy spread ΔE in the experiment is wide enough to contain a large number of resources, that is, for a resonance of spacing D, $\Delta E >> D$. Then, using assumption *i*) we obtain for the formation of the CN the relation [Mar71]:

$$\sigma_{\alpha}^{CN} = \frac{\lambda_{\alpha}^2}{4\pi} T_{\alpha} \qquad 4.2$$

where T_α is the transmission coefficient for the incident channel. So

$$\sigma_{\alpha\beta}^{CN} = \frac{\lambda_{\alpha}^2}{4\pi} T_{\alpha} P_{\beta} \qquad 4.3$$

from the time reversal assumption *iii*) we have

$$\sigma_{\beta\alpha}^{CN} = \left(\frac{\lambda_B}{\lambda_a}\right)^2 \sigma_{\alpha\beta}^{CN} \qquad 4.4$$

from 4.3 and 4.4

$$T_\alpha P_\beta = T_\beta P_\alpha. \qquad 4.5$$

Then

$$\frac{P_\alpha}{T_\alpha} = \frac{P_\beta}{T_\beta} = \text{constant} = a \qquad 4.6$$

$$P_\beta = a\, T_\beta$$

So summing over all channels we get

$$\sum_i P_i = \sum_i a T_i = a \sum_i T_i \ .$$

However,

$$\sum_i P_i = 1$$

so

$$\sum_i T_i = 1/a = \frac{T_\beta}{P_\beta} \ . \qquad 4.7$$

Substituting 4.7 in 4.3, we obtain

$$\sigma_{\alpha\beta}^{CN} = \frac{\lambda_{\alpha}^2}{4\pi} \frac{T_\alpha T_\beta}{\sum_i T_i} \ . \qquad 4.8$$

Detailed derivation which includes spin and gives explicit expressions for $\sigma(\theta)$ is

lengthy and more involved. One can refer to Hodgson 1971 [Hod71] for more complete information.

The assumption that the outgoing channels do not know about the incoming channels, *e.g.*, the amnesia assumption, is only partially true. To account for this correlation between entrance and exit channels a correction factor $W_{\alpha\beta}$ is introduced into each reaction channel. The approach that we used in our CN calculations is due to Moldauer [Mol64] and the width-fluctuation factor $W_{\alpha\beta}$ has the form

$$W_{\alpha\beta} = \left\langle \frac{\Gamma_\alpha \Gamma_\beta}{\sum_i \Gamma_i} \right\rangle \frac{\left\langle \sum_i \Gamma_i \right\rangle}{\langle \Gamma_\alpha \rangle \langle \Gamma_\beta \rangle} \qquad 4.9$$

where Γ_α and Γ_β are the resonance widths of the α and β channels. Putting $W_{\alpha\beta}$ in eq. 4.8, the $\sigma_{\alpha\beta}^{CN}$ becomes

$$\sigma_{\alpha\beta}^{CN} = \frac{\lambda_\alpha^2}{4\pi} \frac{T_\alpha T_\beta}{\sum_i T_i} W_{\alpha\beta} \ .$$

4.3 Level Densities

The notation α or β for the entrance and exit channels, respectively, represent the total angular momentum, parity, and excitation energy of the residual nucleus. This information may be known for the states up to a few MeV of excitation energy, and is used in the CN calculation. However for higher excitation energies many unresolved or uncharacterized exit channels become available and a modeling for the continuum of the excited states becomes necessary. Two forms of the level density $\rho(E)$ are used to estimate the number of excited states available to the scattering system at $E = E_x$. The first formula is the constant temperature formula which is used for excitation energies below 10 MeV. For higher excitation energies the Fermi gas formula is used. For our

CN calculations for both ^{27}Al and ^{59}Co we used the constant temperature formula

$$\rho(E) = N(E)/T \qquad 4.10$$

where

$$N(E_X) = \exp\left[\frac{(E_x - E_0)}{T}\right] = \text{number of states}$$

E_X = excitation energy

E_0 = pairing energy

T = nuclear temperature.

Figures 4.2 and 4.3 show the plots of $N(E_X)$ versus E_X for ^{27}Al and ^{59}Co. From the least square fit of $N(E_X)$ for ^{27}Al and ^{59}Co one can determine the parameters E_0 and T. For ^{27}Al, the E_0 = -0.664 MeV and T = 0.482 $(MeV)^{-1}$. For ^{59}Co, the E_0 = 0.049 MeV and T = 0.889 $(MeV)^{-1}$.

4.4 Compound Nucleus Estimates for ^{27}Al + n and ^{59}Co + n

Our $\sigma(\theta)$ and $A_y(\theta)$ measurements were done at neutron energies where the CN contribution was negligible. For ^{27}Al the CN contribution is only appreciable below 10 MeV while for ^{59}Co it is below 7 MeV. However, we needed to carry out CN calculations to correct $\sigma(\theta)$ and $A_y(\theta)$ of our database for ^{27}Al and ^{59}Co, since these databases covered the energy range below these energies. In our database listed in Tables 4.1 and 4.2 that we used to develop our DOM and CCM models, we have $\sigma(\theta)$ data as low as 1 MeV for ^{59}Co and 2 MeV for ^{27}Al. At these low energies CN becomes appreciable and correction for it becomes crucial for the development of our models.

In our CN calculations only important exit channels were considered. For ^{27}Al these channels were

Reaction	Q-value
$^{27}Al + n \rightarrow {}^{27}Al + n$	0.0 MeV
$\rightarrow {}^{27}Mg + p$	-1.830 MeV
$\rightarrow {}^{27}Na + \alpha$	-3.129 MeV

Table 4.1

^{27}Al data base used to develop DOM and CCM

Data	Energy (MeV)	Author	Ref.
$\sigma(\theta)$	3.0, 3.49, 4.0, 4.56 6.09, 7.05, 8.05	B. Holmquist *et al.*	R - AE - 366 (1969)
$\sigma(\theta)$	7.62	G. Schreder *et al.*	Phys. Rev. C39,1768 (1989)
$\sigma(\theta)$	9.0	D. E. Velkley	Phys. Rev. C9,2181 (1974)
$\sigma(\theta)$	10.16	G. Boerker *et al.*	PTB-N-1 (1989)
$\sigma(\theta)$	11	C.S. Whisnant *et al.*	Phys. Rev. C30,1435 (1984)
$\sigma(\theta)$ and $A_y(\theta)$	14, 17	C.S. Whisnant *et al.*	Phys. Rev. C30,1435 (1984)
$\sigma(\theta)$ and $A_y(\theta)$	15.43	Present Work	
$\sigma(\theta)$	18, 20, 22, 25, 26	J. S. Petler *et al.*	Phys. Rev. C32, 673 (1985)
$\sigma(\theta)$	21.6	N. Olsson *et al.*	Nucl. Phys. A472, 237(1987)
σ_T	0.20 - 49.0	F. G. Perey *et al.*	ORNL- 4823 (1972)
σ_T	2.0 - 81.0	D. C. Larson *et al.*	ORNL- 5787(1981)
σ_T	0.5 - 32.0	S. Cierjacks *et al.*	KFK-1000 (1968)

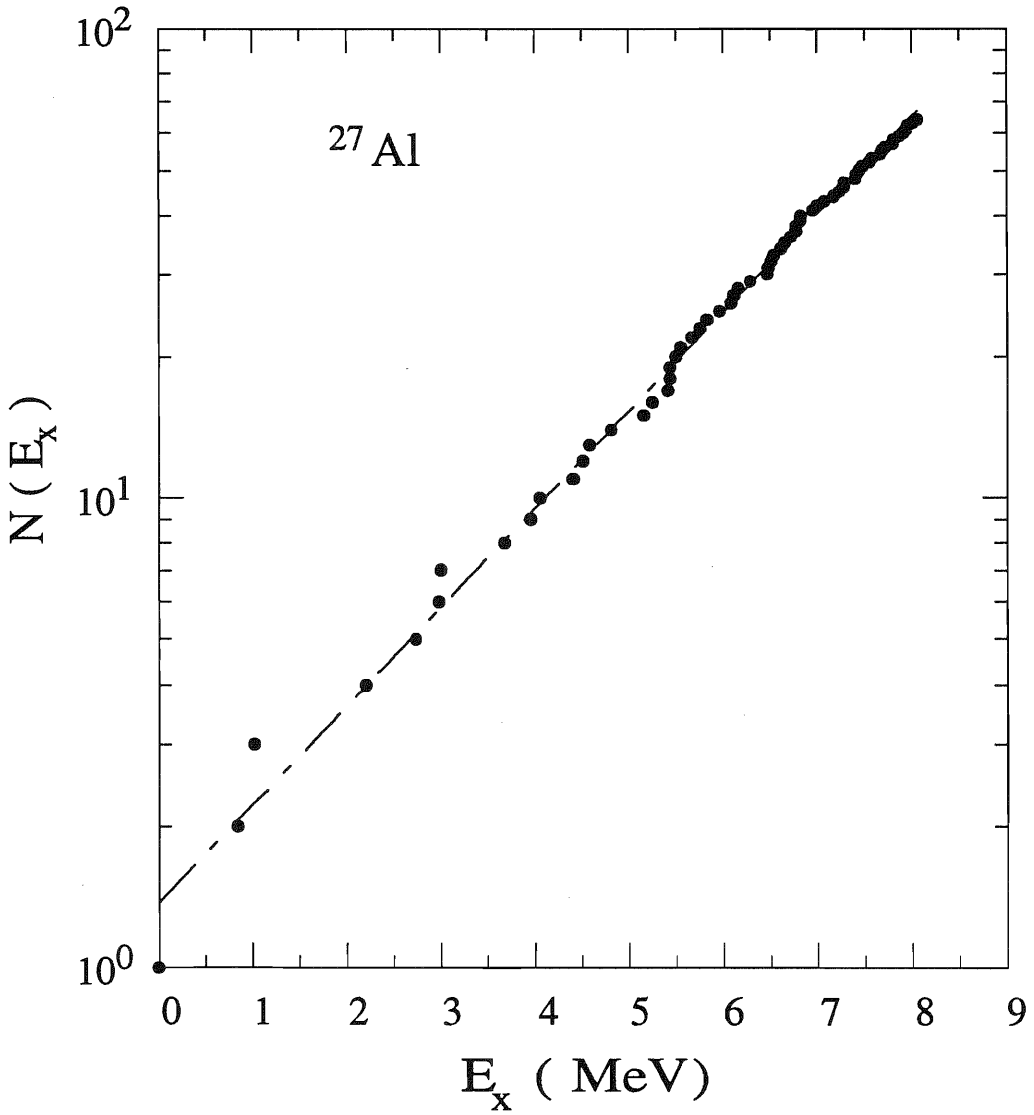

Figure 4.2. A plot of $N(E_x)$ versus E_x for ^{27}Al.

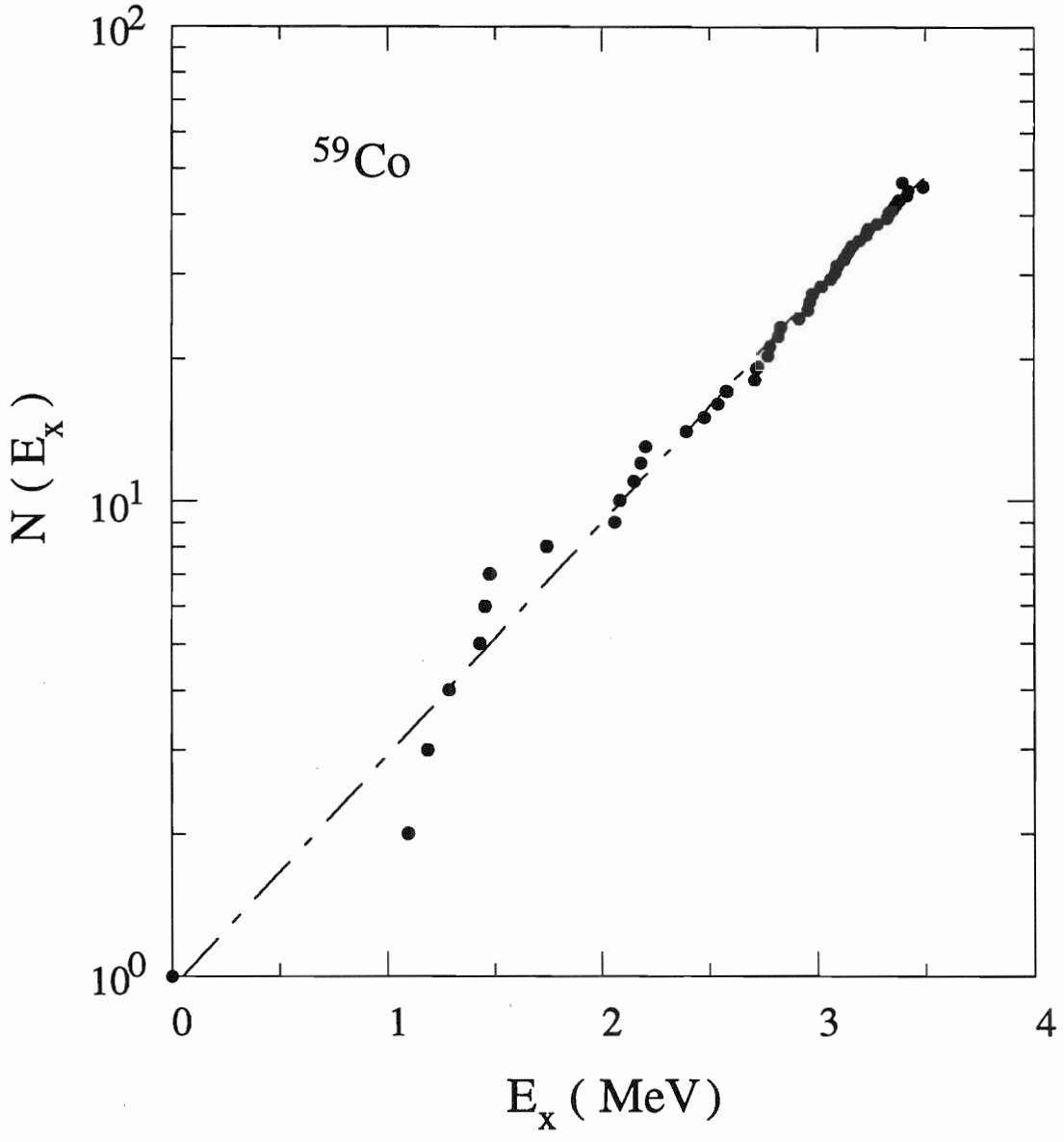

Figure 4.3. A plot of $N(E_x)$ versus E_x for ^{59}Co.

Table 4.2

^{59}Co data base used to develop DOM and CCM

Data	Energy (MeV)	Author	Ref.
$\sigma(\theta)$	1.57, 2.07, 2.58, 3.04, 3.55, 4.5, 5.0, 5.5, 5.9, 6.5, 7.14, 7.5, 8.03, 8.4, 9.06, 9.5, 9.99	A. B. Smith *et al.*	Nucl. Phys. A483, 50(1988)
$\sigma(\theta)$	4.0	P. T. Guenther *et al.*	NSE 54, 273 (1974)
$\sigma(\theta)$	8.97	D. E. Velkley	Phys. Rev. C9, 2181 (1974)
$\sigma(\theta)$	9.95, 11.94, 13.94, 16.88, 18.86	Present Work	
$\sigma(\theta)$	11.01	J. C. Ferrer	Nucl. Phys. A275, 325(1977)
$\sigma(\theta)$,and $A_y(\theta)$	15.43	Present Work	
$\sigma(\theta)$	21.6	N. Olsson *et al.*	Nucl. Phys. A472, 237(1987)
$\sigma(\theta)$	23.0	S. T. Lam	Phys. Rev. C32, 76 (1985)
σ_T	.04 - 32.0	J. A. Harvey	W. Harvey (1986)
σ_T	0.5 - 32.0	S. Cierjacks *et al.*	KFK-1000 (1969)
σ_T	26.0 - 80.0	D. C. Larson *et al.*	Bul. Am. Phys. Soc. 25, 543 (1980)

The (n, α) channel opens at about E_n = 5.2 MeV while the (n, p) channel opens at E_n = 2.4 MeV. The (n, γ) channel is negligible since it only contributes less than 0.5 mb at E_n = 0.5-14 MeV. The two-particle channels (n, 2n), (n, np) were neglected due to their large negative Q-values and small contribution below 14 MeV, e.g., about 0.1 mb at E_n = 14 MeV for the 2n-channel.

For ^{59}Co the only dominant exit channel is the neutron channel. For example, at E_n = 6 MeV the $\sigma_{n,n'}$ = 1500 mb while $\sigma_{n,\gamma}$ = 2.5 mb, $\sigma_{n,p}$ = 15 mb and $\sigma_{n,\alpha}$ = 1 mb. The two particle channels (n, 2n) and (n, np) are also neglected due to their high negative Q-value.

4.5 Correction of the Data Base

Correction for CN contribution of our data base was done using a special version of the computer code OPSTAT which includes the DOM parameterization for ^{27}Al and ^{59}Co. The measured elastic cross section can be expressed as the incoherent sum of the direct and compound nucleus cross sections,

$$\sigma_{el}(\theta) = \sigma^{SE}(\theta) + \sigma^{CE}(\theta)$$

while the analyzing power can be expressed as the weighted sum of the direct and compound nucleus analyzing powers

$$A_y^{el} = \frac{\sigma^{SE}(\theta)}{\sigma_{el}(\theta)} A_y^{SE}(\theta) + \frac{\sigma^{CE}(\theta)}{\sigma_{el}(\theta)} A_y^{CE}(\theta)$$

since we assume $\Delta E >> D$, the CE contribution produces no analyzing power. That is,

$$A_y^{CE}(\theta) = 0 \ .$$

Then we can write:

$$A_y^{el} = \frac{\sigma^{SE}(\theta)}{\sigma_{el}(\theta)} A_y^{SE}(\theta) \ .$$

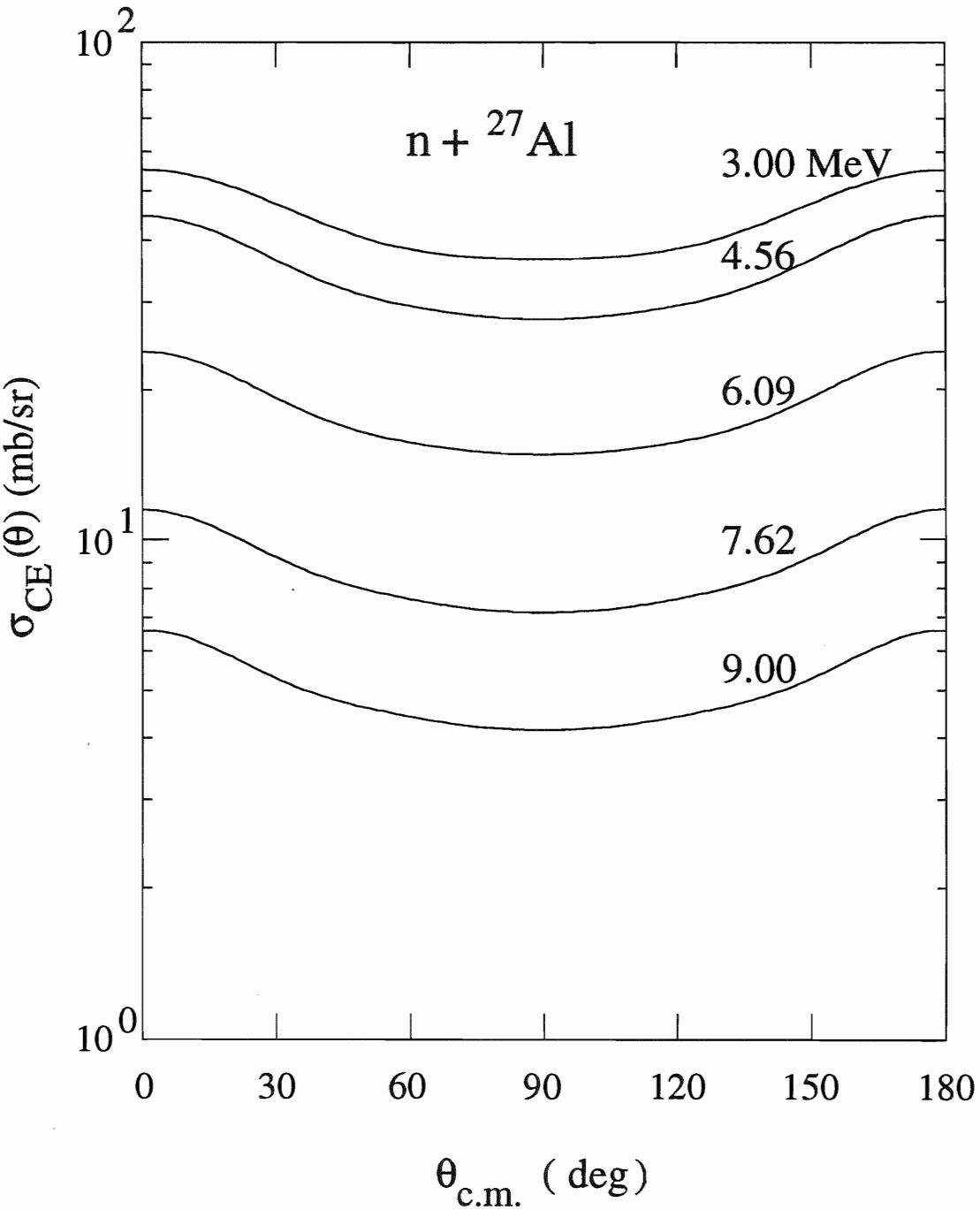

Figure 4.4. Compound Nucleus Calculations for ^{27}Al.

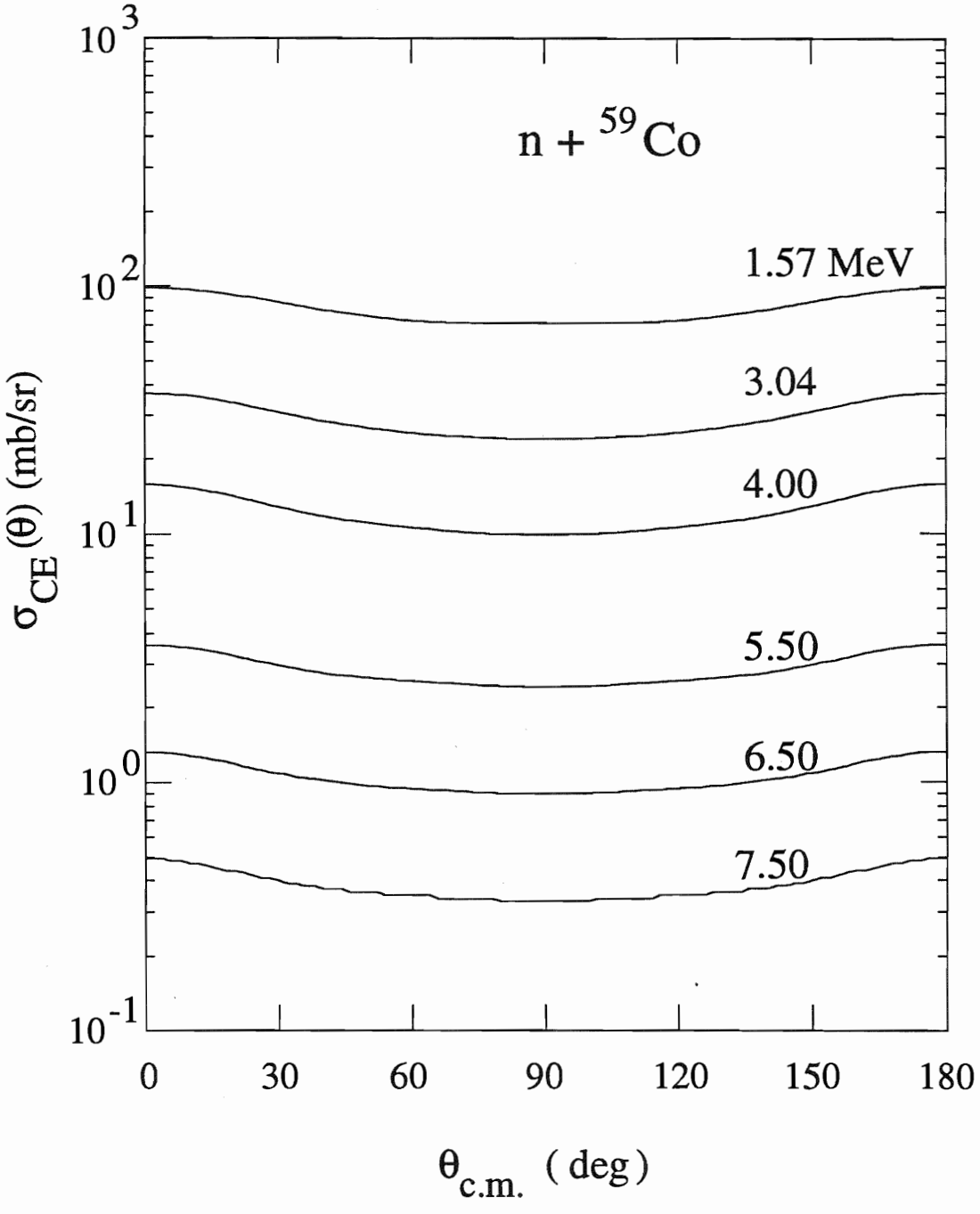

Figure 4.5. Compound Nucleus Calculations for ^{59}Co.

Tables 4.3 and 4.4 give the CN contribution at energies used in our data base and figures 4.4 and 4.5 show a sample of these calculations for ^{27}Al and ^{59}Co, respectively.

Table 4.3

^{27}Al compound nucleus contribution at energies used in our data base.

Ang	Energy (MeV)										
(deg)	1.95	2.47	3.0	3.49	4.00	4.56	6.09	7.05	7.62	8.0	9.0
0	64.8	46.5	55.2	49.7	49.5	44.6	23.9	15.1	11.5	9.6	6.6
5	64.6	46.3	54.9	49.4	49.1	44.3	23.7	14.9	11.4	9.5	6.5
10	64.0	45.6	54.1	48.6	48.2	43.4	23.1	14.6	11.1	9.3	6.4
15	63.1	44.6	52.8	47.3	46.7	42.0	22.3	14.0	10.7	9.0	6.1
20	61.8	43.2	51.2	45.6	44.9	40.2	21.4	13.4	10.2	8.5	5.8
25	60.3	41.7	49.2	43.8	42.9	38.3	20.3	12.7	9.7	8.1	5.5
30	58.7	40.1	47.2	41.9	41.0	36.4	19.3	12.0	9.2	7.7	5.3
35	56.9	38.5	45.3	40.1	39.1	34.6	18.4	11.4	8.8	7.4	5.1
40	55.1	37.0	43.4	38.4	37.4	33.1	17.6	11.0	8.4	7.1	4.9
45	53.4	35.7	41.7	37.0	36.0	31.9	16.9	10.6	8.2	6.9	4.7
50	51.8	34.6	40.3	35.8	34.9	30.8	16.4	10.2	7.9	6.7	4.6
55	50.3	33.7	39.2	34.9	34.0	30.0	16.0	10.0	7.8	6.5	4.5
60	49.0	33.1	38.3	34.2	33.3	29.4	15.7	9.8	7.6	6.4	4.4
65	47.9	32.6	37.6	33.6	32.7	28.9	15.4	9.6	7.5	6.3	4.3
70	46.9	32.2	37.2	33.2	32.2	28.5	15.2	9.4	7.4	6.2	4.3
75	46.2	32.0	36.9	32.8	31.9	28.1	15.0	9.3	7.3	6.1	4.2
80	45.6	31.9	36.7	32.6	31.6	27.9	14.9	9.2	7.2	6.1	4.2
85	45.3	31.8	36.6	32.5	31.5	27.7	14.9	9.2	7.2	6.0	4.2
90	45.2	31.8	36.6	32.4	31.4	27.6	14.8	9.2	7.2	6.0	4.2
95	45.3	31.8	36.6	32.5	31.5	27.7	14.9	9.2	7.2	6.0	4.2
100	45.6	31.9	36.7	32.6	31.6	27.9	14.9	9.2	7.2	6.1	4.2
105	46.2	32.0	36.9	32.8	31.9	28.1	15.0	9.3	7.3	6.1	4.2
110	46.9	32.2	37.2	33.2	32.2	28.5	15.2	9.4	7.4	6.2	4.3
115	47.9	32.6	37.6	33.6	32.7	28.9	15.4	9.6	7.5	6.3	4.3
120	49.0	33.1	38.3	34.2	33.3	29.4	15.7	9.8	7.6	6.4	4.4
125	50.3	33.7	39.2	34.9	34.0	30.0	16.0	10.0	7.8	6.5	4.5
130	51.8	34.6	40.3	35.8	34.9	30.8	16.4	10.2	7.9	6.7	4.6
135	53.4	35.7	41.7	37.0	36.0	31.9	16.9	10.6	8.2	6.9	4.7
140	55.1	37.0	43.4	38.4	37.4	33.1	17.6	11.0	8.4	7.1	4.9
145	56.9	38.5	45.3	40.1	39.1	34.6	18.4	11.4	8.8	7.4	5.1
150	58.7	40.1	47.2	41.9	41.0	36.4	19.3	12.0	9.2	7.7	5.3
155	60.3	41.7	49.2	43.8	42.9	38.3	20.3	12.7	9.7	8.1	5.5
160	61.8	43.2	51.2	45.6	44.9	40.2	21.4	13.4	10.2	8.5	5.8
165	63.1	44.6	52.8	47.3	46.7	42.0	22.3	14.0	10.7	9.0	6.1
170	64.0	45.6	54.1	48.6	48.2	43.4	23.1	14.6	11.1	9.3	6.4
175	64.6	46.3	54.9	49.4	49.1	44.3	23.7	14.9	11.4	9.5	6.5
180	64.8	46.5	55.2	49.7	49.5	44.6	23.9	15.1	11.5	9.6	6.6

Table 4.4

^{59}Co compound nucleus contribution at energies used in our data base.

Ang	Energy (MeV)										
(deg)	1.57	2.07	2.58	3.55	4.00	4.50	5.00	5.50	6.50	7.14	8.03
0	98.7	75.4	48.5	27.1	15.8	9.3	5.8	3.6	1.3	0.7	0.3
5	98.3	75.0	48.2	26.9	15.6	9.2	5.7	3.6	1.3	0.7	0.3
10	97.1	74.1	47.5	26.3	15.3	9.0	5.6	3.5	1.3	0.7	0.3
15	95.1	72.5	46.3	25.4	14.8	8.7	5.4	3.4	1.2	0.7	0.3
20	92.6	70.6	44.9	24.3	14.1	8.3	5.2	3.2	1.2	0.6	0.3
25	89.7	68.4	43.2	23.1	13.5	8.0	5.0	3.1	1.1	0.6	0.2
30	86.6	66.0	41.6	21.9	12.8	7.6	4.7	3.0	1.1	0.6	0.2
35	83.5	63.7	40.0	20.8	12.3	7.3	4.6	2.9	1.0	0.6	0.2
40	80.7	61.6	38.5	19.9	11.8	7.0	4.4	2.8	1.0	0.5	0.2
45	78.1	59.7	37.3	19.2	11.4	6.8	4.3	2.7	1.0	0.5	0.2
50	76.0	58.1	36.2	18.5	11.1	6.7	4.2	2.6	1.0	0.5	0.2
55	74.3	56.8	35.4	18.0	10.8	6.5	4.1	2.6	1.0	0.5	0.2
60	73.1	55.8	34.7	17.6	10.6	6.4	4.1	2.6	0.9	0.5	0.2
65	72.3	55.0	34.1	17.2	10.4	6.3	4.0	2.5	0.9	0.5	0.2
70	71.8	54.5	33.7	16.9	10.2	6.2	4.0	2.5	0.9	0.5	0.2
75	71.6	54.1	33.4	16.7	10.1	6.1	3.9	2.5	0.9	0.5	0.2
80	71.5	53.9	33.1	16.5	9.9	6.1	3.9	2.5	0.9	0.5	0.2
85	71.5	53.8	33.0	16.3	9.9	6.0	3.8	2.4	0.9	0.5	0.2
90	71.5	53.7	33.0	16.3	9.9	6.0	3.8	2.4	0.9	0.5	0.2
95	71.5	53.8	33.0	16.3	9.9	6.0	3.8	2.4	0.9	0.5	0.2
100	71.5	53.9	33.1	16.5	9.9	6.1	3.9	2.5	0.9	0.5	0.2
105	71.6	54.1	33.4	16.7	10.1	6.1	3.9	2.5	0.9	0.5	0.2
110	71.8	54.5	33.7	16.9	10.2	6.2	4.0	2.5	0.9	0.5	0.2
115	72.3	55.0	34.1	17.2	10.4	6.3	4.0	2.5	0.9	0.5	0.2
120	73.1	55.8	34.7	17.6	10.6	6.4	4.1	2.6	0.9	0.5	0.2
125	74.3	56.8	35.4	18.0	10.8	6.5	4.1	2.6	1.0	0.5	0.2
130	76.0	58.1	36.2	18.5	11.1	6.7	4.2	2.6	1.0	0.5	0.2
135	78.1	59.7	37.3	19.2	11.4	6.8	4.3	2.7	1.0	0.5	0.2
140	80.7	61.6	38.5	19.9	11.8	7.0	4.4	2.8	1.0	0.5	0.2
145	83.5	63.7	40.0	20.8	12.3	7.3	4.6	2.9	1.0	0.6	0.2
150	86.6	66.0	41.6	21.9	12.8	7.6	4.7	3.0	1.1	0.6	0.2
155	89.7	68.4	43.2	23.1	13.5	8.0	5.0	3.1	1.1	0.6	0.2
160	92.6	70.6	44.9	24.3	14.1	8.3	5.2	3.2	1.2	0.6	0.3
165	95.1	72.5	46.3	25.4	14.8	8.7	5.4	3.4	1.2	0.7	0.3
170	97.1	74.1	47.5	26.3	15.3	9.0	5.6	3.5	1.3	0.7	0.3
175	98.3	75.0	48.2	26.9	15.6	9.2	5.7	3.6	1.3	0.7	0.3
180	98.7	75.4	48.5	27.1	15.8	9.3	5.8	3.6	1.3	0.7	0.3

CHAPTER 5

THE DISPERSIVE OPTICAL MODEL

5.1 Introduction

The Dispersive Optical Model (DOM) has been the framework of many current optical model analysis. The DOM simply relates the real and imaginary parts of nuclear mean field using the Dispersion Relation (DR) as a constraint. Although it was introduced in physics by Kramers and Kronig in 1926 in their analysis of the scattering of light, only recently [Mah83, Mah86, Mah87] the dispersion analysis was fully developed and used to obtain the gross features of the energy dependence of the real part of the average potential for nucleon-nucleus scattering and the main properties of the bound single-particle states. Basically, ^{40}Ca and ^{208}Pb were used as testing grounds for this new technique [Joh87, Joh88, Rob91, Tor90] where the DOM enjoyed a great success.

The DR constraint proved to be very useful to connect between the scattering states ($E > 0$) where the optical model applies and the bound states ($E < 0$) where the shell model applies. In the framework of the nuclear mean field with the DR as a constraint we obtain a smooth continuous function which relates the positive (scattering) states and negative (bound) states. Although the DR reduces the number of adjustable parameters in the optical model analysis it was shown to give a better prediction of the scattering data than the standard Optical Model Potential (OMP). Delaroche and Tornow [Del88] demonstrated for ^{40}Ca that the description of analyzing power data, which is sensitive to surface interactions, have been improved considerably

by the introduction of a real surface term to the real central potential via the dispersion relation. The DR also includes effects associated with the coupling of the single particle degrees of freedom to collective excitations which give rise to a characteristic energy dependence of the potential radius near the Fermi energy [Mah90]. The introduction of the dispersive volume and surface real terms to the central potential as a result of using the DR relation helped in solving what is known as the "Fermi surface anomaly". This anomaly was introduced in the discussion about the inability of the standard OMP to account for the need to raise the potential strength at low energies [Rap78] in order to describe scattering data in the n + ^{208}Pb system. However this rise in potential at low energies was accounted for by the dispersive terms [Joh87], thus solving this relatively long-standing problem.

So far ^{40}Ca [Joh88, Tor90], ^{208}Pb [Mah87, Joh87, Rob91], and ^{90}Zr [Del89] have been studied extensively using the DOM technique with great success. Other nuclei, such as ^{93}Nb [Smi86] and ^{209}Bi [Das90, Wei92], were also studied with success.

While it is important in the development of the DR optical model to study "single-particle" SP nuclei in order to test the extension of the DOM to negative energies (SP bound states), it is also important to investigate the applicability of the DR to deformed nuclei, such as ^{27}Al and ^{59}Co. In our first attempt of the latter nuclei we made a set of preliminary calculations which shows that the strength of the spin-spin potential that one obtains when describing the spin-spin data is sensitive to the inclusion of the dispersive terms. Because of this finding and the fact that we were interested in studying the DR for deformed nuclei, we developed a spherical optical model for ^{27}Al and ^{59}Co with the DR as a constraint.

5.2 The Optical Model Potential and Dispersion Relation

It is helpful to review the OMP briefly before introducing the DOM. The OMP is a sum of a central potential and a spin-orbit potential where the central potential is a complex quantity defined as

$$V(r,E) = V(r,E) + iW(r,E) \tag{5.1}$$

where

$$V(r,E) = -V(E) f(r,R_v,a_v) \tag{5.2}$$

and

$$W(r,E) = 4a_s W_s(E) \frac{d}{dr} f(r,R_W,a_W) - W_v(E) f(r,R_w,a_w)\ . \tag{5.3}$$

Here $f(r,R,a)$ is a Woods Saxon form factor

$$f(r,R,a) = \frac{1}{1+\exp\left(\frac{r-R}{a}\right)} \tag{5.4}$$

where $R_i = r_i A^{\frac{1}{3}}$ is the nuclear radius and a is the diffuseness. The real part of the potential V(r,E) represents the average potential energy of an incoming nucleon with energy E in the field of the target nucleus. The imaginary part models all the nuclear reactions (excluding the shape elastic scattering) that take place between the incoming nucleon and the nucleus. The surface term W_S of the imaginary potential is introduced to take into account the fact that for low incoming projectile energies, nuclear reactions take place mostly at the surface.

In addition to the central part of the OMP, the mean field contains a spin-orbit component which is given by the standard Thomas form

$$V_{so}(r,E) = \left(\frac{\hbar}{m_\pi c}\right)^2 V_{so}(E) \frac{1}{r} \frac{d}{dr} f(r,R_{so},a_{so}) \vec{\ell} \cdot \vec{\sigma}\ \ .$$

In the general case the $V_{so}(E) \rightarrow V_{so}(E) + i\, W_{so}(E)$ with the addition of the imaginary term $W_{so}(E)$ to cover the case of spin-orbit dependent absorption. In a global

representation other terms are added to the mean field such as the isospin term. The isospin term is added to parameterize the difference between X(n,n), X(p,p), and X(p,n) scattering to account for differences between the fundamental nucleon-nucleon interactions. For charged particle scattering, a term due to the Coulomb field is necessary.

The importance of the DR comes from the fact that it relates the real and imaginary part of the nuclear mean field of eq. 5.1. The main difference between the OMP and the shell model potential is the imaginary part. While it was not previously possible to reliably extend the real part of the OMP to the negative energies (bound states), however, this can now be accomplished very successfully through the dispersion relation. In the framework of the Dispersive Optical Model the real part is constrained by the imaginary part through the dispersion relation. Since the imaginary part is closely related to the internal structure of the nucleus, a real potential obtained through the DR will reflect or will be influenced by the internal structure of the nucleus. This fact, which allows for a valid parameterization of V(r, E) for all energies, explains the ability to extend the real part to the negative energies smoothly and reliably.

The dispersion relation relates the real and imaginary part of the mean nuclear field through the following integral relation

$$M(r,E) = V(r,E) + iW(r,E) \tag{5.5}$$

$$V(r,E) = V_{HF}(r,E) + \Delta V(r,E) \tag{5.6}$$

$$\Delta V(r,E) = \frac{P}{\pi}\int_{-\infty}^{\infty} \frac{W(r,E')}{E'-E}\, dE' \tag{5.7}$$

where $V_{HF}(r,E)$ is the Hartree-Fock contribution, and $\Delta V(r,E)$ is the dispersive contribution to the real part of the nuclear mean field. The P denotes a principal value

integral. Although the nuclear mean field V_{HF} has a simple monotonic energy dependence, the DR introduces a surface contribution to the real central potential V(r,E) that has a moderately strong variation with energy at low energies. For a detailed derivation of the dispersion relation from Schrödinger wave equation and a causality constraint see [Mah86].

5.3 Dispersive Optical Model (DOM)

The nuclear mean field can be written as

$$M(r,E) = V(r,E) + iW(r,E) \qquad 5.5$$

where in the context of the DOM model

$$V(r,E) = V_{HF}(r,E) + \Delta V(r,E) \qquad 5.6$$

and

$$\Delta V(r,E) = \frac{P}{\pi}\int_{-\infty}^{\infty} \frac{W(r,E')}{E'-E}\,dE' \cdot \qquad 5.7$$

The Hartree-Fock potential V_{HF} is the local equivalent of a non-local energy independent potential $V_{HF}(r,r')$ where the energy dependence is introduced because of the replacement of a non-local potential with a local one. Hartree-Fock potential could be defined from eqs. 5.6 and 5.7 if we set W(r,E) = 0 in eq. 5.7. This gives from eq. 5.6

$$V(r,E) = V_{HF}(r,E)\ .$$

In other words, Hartree-Fock potential can be defined as the mean field when there are no nuclear reactions other than elastic scattering. The parameterization of $V_{HF}(r,r')$ was postulated by Perey and Buck [Per62] as follows:

$$V_{HF}(r,r') = V(r)\exp(-|r-r'|^2/\beta^2) \qquad 5.8$$

with a local equivalent potential where they assumed a Gaussian shape for the non-locality of $V_H(r,r')$ and β is the non-locality range. This can be rewritten as

$$V_{HF}(E) = V_{HF}(0)\exp[-\alpha V_{HF}(0)]\exp[-\alpha(E - V_{HF}(E))] \qquad 5.9$$

where

$$\alpha = \left(\frac{m}{2\hbar^2}\right)\beta^2 \quad .$$

From eq. 5.9 $V_{HF}(E)$ can be approximated by

$$V_{HF}(E) = V_{HF}(0)\exp(-\alpha E) \qquad 5.10$$

for E < 150 MeV [Joh87]. The V(r,E) is assumed to be a Woods-Saxon type:

$$V_{HF}(r,E) = V_{HF}(E)\, f(r, R_{HF}, a_{HF}) \qquad 5.11$$

where $f(r, R_{HF}, a_{HF})$ is the Woods-Saxon form factor defined in eq. 5.4. The geometrical parameters R_{HF} and a_{HF} are independent of energy.

Contrary to V_{HF} the energy dependence of $\Delta V(r,E)$ is local and arises through the DR of eq. 5.7. Due to the definition of $\Delta V(r,E)$ of eq. 5.7, $\Delta V(r,E)$ consists of two terms, a dispersive volume term and a dispersive surface term since W(r,E) consists of a volume and a surface term. Hence,

$$\Delta V(r,E) = \Delta V_v(r,E) + \Delta V_s(r,E) \qquad 5.12$$

The real part of the mean field can be rewritten as

$$V(r,E) = V_{HF}(r,E) + \Delta V_v(r,E) + \Delta V_s(r,E) \quad . \qquad 5.13$$

The imaginary part of the nuclear mean field is defined by

$$W(r,E) = W_v(r,E) + W_s(r,E) \qquad 5.14$$

where

$$W_v(r,E) = W_v(E)\, f(r, R_v, a_v) \qquad 5.15$$

and

$$W_s = -4a_s\, W_s(E)\frac{d}{dr} f(r, R_s, a_s) \quad . \qquad 5.16$$

Since the mean field is real at Fermi energy then

$$W(r, E_F) = 0 \quad .$$

The Fermi energy is ideally defined as the average of the energy of the last occupied and the energy of the first occupied shell. (However, see sect. 5.4.4). The imaginary potential W(r, E) is assumed to be symmetric around E_F:

$$W(r,E+E_F)=W(r,E-E_F) \quad . \tag{5.17}$$

It is desirable to represent the functions $W_S(E)$ and $W_V(E)$ in forms suitable for the DOM analysis. The schematic model of Jeukenne *et al.* [Jeu83] provides such forms which are

$$W_s(E)=A_s\frac{(E-E_F)^4}{(E-E_F)^4+B_s^4}\exp[-C_s(E-E_F)] \tag{5.18}$$

and

$$W_v=A_v\frac{(E-E_F)^4}{(E-E_F)^4+B_v^4} \quad . \tag{5.19}$$

In our analysis we did not restrict ourselves to power 4 only, but we rather tried a combination of powers 2, 4, and 6 for W_V and W_S.

The assumption that $W_q(r, E)$, where q stands for v or s, is symmetric around E_F (eq. 5.17) and that

$$\Delta V_q(r,E)=\frac{P}{\pi}\int_{-\infty}^{+\infty}\frac{W_q(r,E')}{E'-E}dE' \tag{5.20}$$

$$=\frac{2}{\pi}(E_F-E)\int_0^{\infty}\frac{W_q(r,E'+E_F)\,dE'}{(E-E_F)^2-E'^2} \tag{5.21}$$

leads to the fact that ΔV_q is skew symmetric around E_F. That is,

$$\Delta V_q(r,E_F+E)=-\Delta V_q(r,E_F-E). \tag{5.22}$$

We can rewrite ΔV_S (r,E) and ΔV_V (r,E) as

$$\Delta V_v(r,E)=\Delta V_v(E)f(r,R_v,a_v) \tag{5.23}$$

and

$$\Delta V_s(r,E)=4a_s\Delta V_s(E)\frac{d}{dr}f(r,R_s,a_s) \tag{5.24}$$

where

$$\Delta V_q(E) = \frac{p}{\pi}\int_{-\infty}^{\infty} \frac{W_q(E')}{E'-E} dE' \quad . \qquad 5.25$$

Finally, after summing all the terms and making the assumption that $r_{HF} = r_V$ and $a_{HF} = a_V$, we can rewrite the central DOM as follows:

$$U(r,E) = -[V_{HF}(E) f(r,R_v,a_v) + \Delta V_v(E) f(r,R_v,a_v) - 4a_s \Delta V_s(E) \frac{d}{dr} f(r,R_s,a_s)] \qquad 5.26$$
$$+ i[4a_s W_s(E) \frac{d}{dr} f(r,R_s,a_s) - W_v(E) f(r,R_v,a_v)] \; + \; U_{so}(r,E)$$

where U_{so} has the standard Thomas form

$$U_{so} = \left[\frac{\hbar}{m_\pi c}\right]^2 V_{so}(E) \frac{1}{r} \frac{d}{dr} f(r,R_{so},a_{so}) \vec{\ell} \cdot \vec{\sigma} \, . \qquad 5.27$$

5.4 Dispersive Optical Model Search and Results

The data bases described in Chapter 4, which consists of differential cross sections, analyzing powers, and total cross section data, were employed in the analyses. For ^{27}Al the search for the DOM started with Martin [Mart87] OM for 2s-1d nuclei. For ^{59}Co the search started with Pedroni ^{58}Ni OMP [Ped88]. To speed up the search and reach convergence fast, two search methods were used, the grid search method as a first stage, and then the global search method (i.e., global in energy) as a second stage. Both methods, which are explained below, were carried out using a version of the computer code GENOA that includes the relativistic correction and the recent formulation of the DOM. The reasoning behind using the two search methods is that with the grid search we could first study the behavior of the various parameters of the DOM individually and select a near optimum form or value for each parameter. The global search was used to fine tune the model. By using this method we hoped to avoid getting trapped at a certain minimum in the multi-dimensional χ^2-space while there is a deeper minimum (a better solution) somewhere else in that multi-dimensional space.

The other problem that this two-stage method addresses is the fact that the code may not search a wide enough range for the parameters to find the optimum values for the parameters.

5.4.1 Grid Search Techniques

The grid search method is also called the single-energy search since optimum values for parameters are chosen based on minimizing the χ^2 between the data and the fit at only one energy. These optimum values for the parameters are then plotted and the behavior of that parameter is studied carefully. However, the search was carried out in a systematic way. First the geometry parameters were fixed and a single energy search was done on the potential depths V_{HF}, W_S, and W_V. Then the volume parameters a_V and r_V were searched using the optimized potential depths V_{HF}, W_S and W_V. The surface geometry parameters r_S and a_S were searched by fixing the rest of the parameters. This process was carried out in an iterative fashion by starting all over again with the new optimized set of parameters. At certain points in the search some parameters were forced to have some chosen fixed values in order to investigate new regions of the χ^2-space. Another way to carry out the grid search, which we also investigated, was to study each parameter individually and step its values until an optimum value is reached. The range of values lies between a physically acceptable maximum and minimum values. For example, the acceptable physical values for r_V for ^{27}Al were conducted to be between r_V = 1.10 and 1.30 fm, so we stepped r_V in that range in increments of 0.01 fm. The quality of the fit for $\sigma(\theta)$, $A_y(\theta)$, and σ_T is studied and an optimum value for r_V is chosen. Then we move to another parameter. After reaching an optimum set of values this process is repeated in an iterative way but with narrower range of values (*i.e.*, r_V = 1.15-1.25). Although this process was tedious and

lengthy, it gives an assurance that the χ^2-space is well searched and all possible minima in that space are investigated.

5.4.2 Global Search Technique

This method is based on minimizing the χ^2-value between the experimental data and the fit of $\sigma(\theta)$, $A_y(\theta)$, and σ_T at all energies at the same time where

$$\chi^2 = \sum_{i=1}^{N_s} \left| \frac{\sigma^{\exp}(\theta_i) - \sigma^{cal}(\theta_i)}{\frac{\Delta\sigma^{\exp}(\theta_i)}{W_\sigma}} \right|^2 + \sum_{i=1}^{N_a} \left| \frac{A_y^{\exp}(\theta_i) - A_y^{cal}(\theta_i)}{\frac{\Delta A_y^{\exp}(\theta_i)}{W_A}} \right|^2 + \left| \frac{\sigma_T^{\exp} - \sigma_T^{cal}}{\Delta\sigma_T^{\exp}} \right|^2$$

where N_s and N_a are the numbers of data points of differential cross section and analyzing power data, respectively, at a certain energy E_n. The W_σ and W_A are the weights given to that set of data. Weights on σ_T were adjusted by changing $\Delta\sigma_T^{\exp}$ accordingly. The search is carried globally on all data sets at all energies simultaneously. First V_{HF} and W_S parameters were optimized and then V_{HF} and W_V parameters were optimized. In both cases the geometry obtained from our grid search was fixed. Then the geometry parameters along with V_{HF} parameters were optimized. This process was carried out in an iterative fashion checking the χ^2-values and the quality of the fit each time. The problem of this technique is that one could miss a good set of parameters by getting trapped at a certain minimum in the χ^2-space while there is a better set of parameters at a deeper χ^2 minimum somewhere else. By using the grid search technique at the first stage of the search we avoided such problems and the final set of parameters obtained by the grid search was only fine tuned.

5.4.3 Recent Developments in the DOM Search

Recently and while we were working on the DOM models for ^{27}Al and ^{59}Co some new developments were suggested by Mahaux *et al.* [Mah91a]. These developments, which turned out not to be drastic nor to change our analysis in a critical way, were to be incorporated in the computer code GENOA after the first stage of the DOM analysis. The first point was that W_S and W_V were forced to be zero not only at Fermi-energy but in the neighborhood of E_F. The range of the neighborhood was defined by Mahaux and Sartor [Mah91a] to be the average energy of the particle states

$$E_p = \frac{1}{N}\sum_{i=0}^{N} E_i$$

where N is the number of single particle states. This change was incorporated in GENOA by Weisel [Wei92] by defining an "offset energy" E_{off} as follows:

$$E_p = E_{off} + E_F$$

and redefining W_S and W_V of eqs. 5.18 and 5.19 as follows:

$$W_v = W_s = 0 \qquad (E_F < E < E_p)$$

and

$$W_v = A_v \frac{(E-E_p)^n}{(E-E_p)+B_v^n} \qquad (E > E_p) \qquad 5.28$$

and

$$W_s = A_s \frac{(E-E_p)^m}{(E-E_p)^m + B_s^m} \exp[-C(E-E_p)] \quad (E < E_F)\,. \qquad 5.29$$

Also, the symmetry was maintained:

$$W(E+E_F) = W(E_F - E)\ . \qquad 5.17$$

The offset effect was checked in our analysis with artificial offsets for ^{59}Co and ^{27}Al because of insufficient data on the single particle states and the fact that these two nuclei are deformed. Values up to E_p=3.0 MeV were studied and no improvement of

the fits to the data base were apparent. For simplicity, in our final model we have chosen an offset of zero for ^{27}Al and ^{59}Co, as in the early models of Mahaux.

The second point suggested by Mahaux and Sartor [Mah86] was the fact that the symmetry of W around E_F is only true for a limited energy range E given by

$$(E_F - E_0) < E < (E_F + E_0)$$

The E_0 was chosen to be 60 MeV for ^{40}Ca [Mah91b] and ^{208}Pb [Mah91a]. The reason for this asymmetry of W_v and W_s is due to non-local effects, which make the imaginary potential increase at large positive energies and decrease at large negative energies [Mah91a]. The surface part is due to surface excitations of the core and becomes negligible for large |E| in conventional optical model formulations. The form we used in the DOM (see eq. 5.18) drops to zero exponentially and presents an automatic correction for the non-locality effects. Therefore, W_s was not changed from the above models. (See [Mah91a] who did the same for ^{40}Ca [Mah91a]). However, the volume absorption is large at large |E| according to eq. 5.19 and must be considered. If we define $\Omega_v(E)$ as the new volume absorption function and W_v is the symmetric volume absorption then for large negative energy $W_v(E)$ must approach zero and increase for large positive energy (see [Mah91a]). This behavior was parameterized by Mahaux and Sartor for large negative E as

$$\Omega_v(E) = W_v(E) - W_v(E_1)\frac{(E-E_1)^2}{(E-E_1)^2+\rho_1^2}\,\theta(E-E_1)$$

where $\theta(E - E_1)$ is a step function, $E_1 = (E_F - 60)$ MeV and $\rho_1 = 60$ MeV. For large positive E the behavior of $\Omega_v(E)$ depends upon the short range behavior of the nucleon-nucleon interaction. For a dilute hard sphere Fermi-gas, the high energy behavior is the following [Sar80]:

$$\Omega(E) \sim \alpha E^{\frac{1}{2}}$$

where

$$\alpha = \frac{2}{\pi} k_F (k_F C)^2 / m^{\frac{1}{2}}$$

where k_F is the Fermi momentum and C is the hard core radius. So the volume absorption $\Omega_v(E)$ was parameterized as follows for positive energy

$$\Omega_v(E) = W_v(E) + \alpha \left(E^{\frac{1}{2}} + \frac{E_0^{\frac{3}{2}}}{2E} - \frac{3}{2} E_0^{\frac{1}{2}} \right) \theta(E - E_0).$$

This new change was also incorporated in GENOA by Weisel [Wei92]. We tested the importance of these modifications to W_V, also using ρ_1 = 60 MeV. The modifications did not affect the quality of our fits. Because of the uncertainties in the parameters α and ρ_1 for our nuclei and because there is no good bound-state information (see below) to assist in their determination, the models reported here use the forms 5.18 and 5.19 unaltered to explicitly account for absorptive potentials.

5.4.4 Bound state Calculations

The computer code BSEAUTO was used in the calculation of the single particle and hole states from our DOM model. This is a modified version of the original program BOUNDSTATE obtained from C.H. Johnson of ORNL [Joh90]. There is no suitable experimental information on the particle and hole states of ^{27}Al and ^{59}Co because of the deformation of these nuclei which causes these states to be very fragmented. So in order to obtain a Fermi energy for ^{27}Al and ^{59}Co, we used the separation neutron energy S_N. Then the Fermi energy is defined as

$$E_F = \tfrac{1}{2}[S_N(N) + S_N(N+1)] \ .$$

For ^{27}Al,

$$E_F = \tfrac{1}{2}[S_N(^{27}Al) + S_N(^{28}Al) \ = \tfrac{1}{2}[-13.058 - 7.726] = -10.392 \text{ MeV} \ .$$

For ^{59}Co

$$E_F = \tfrac{1}{2}[S_N(^{59}Co) + S_N(^{60}Co)] = \tfrac{1}{2}[-10.460 - 7.492] = -8.976 \text{ MeV} \ .$$

This method is very consistent with the reported values for ^{40}Ca, ^{208}Pb, and ^{209}Bi, for instance. For ^{208}Pb it gives E_F = -5.653 MeV compared with the reported value of -5.65 MeV [Wei92] calculated from the experimental particle and hole states of ^{208}Pb. [Joh87, Joh88, Wei92]. Therefore in order to check the predictive power of our DOM, we used the available experimental [Fru84] data on the deeply bound 1s particle-states for ^{27}Al and ^{58}Ni for the ^{59}Co model. The values reported in [Fur68] are proton single-particle states which were adjusted for neutron single-particle states by adding the Coulomb energy difference. This energy difference was calculated to be -3.9 MeV for ^{27}Al and -5.6 MeV for ^{58}Ni. So, from this approach, we estimate the 1s neutron (single-particle) state to be at -61±5 MeV for ^{27}Al and at -67.5±5 MeV for ^{58}Ni.

5.5 DOM Parameters and Results for ^{27}Al

Table 5.1 shows the final parameters of our search; notice that our analysis favored a power of 6 for W_S and a power of 4 for W_V. The solid circles in Figure 5.1 illustrate the optimum value for the Hartree-Fock strength obtained in the single-energy searches at each energy when the other parameters were held fixed at those in Table 5.1. The data base only includes total cross section data above 26 MeV and the excursions of the solid circles in the range 26 MeV < E < 55 MeV reflects this fact. Figures 5.2 and 5.3 show the behavior of the absorptive potentials W_S and W_V along with dispersive real surface and volume terms ΔV_S and ΔV_V derived from the absorptive potentials through the dispersion relation. These final parameters were used to calculate σ_T, $\sigma(\theta)$, $A_y(\theta)$ and the spin-spin cross section σ_{ss}, the latter of which will be explained in Chapter 7. Figure 5.4 shows the DOM calculations for σ_T along with the experimental data averaged over 50 keV intervals below 10 MeV and over 200 keV or more intervals above 10 MeV. It can be seen in Figure 5.4 that the DOM

calculations are good between 10-20 MeV and 50-80 MeV. In the region 30 MeV< E < 40 the model underpredicts σ_T by about 2.0%. Below 10 MeV the DOM calculations overestimate σ_T. This is a common problem with DOM calculations in this energy range in particular for the lighter nuclei ^{28}Si and ^{40}Ca [AlO92, Tor90]. This problem gets worse for lighter systems and it may be due to l -dependencies in the absorption. We did try (see sect. 5.6) to solve this problem in the next chapter by coupling the ground state to itself (reorientation effect) this has a profound effect on σ_T at low energies, but not enough to eliminate the problem.

From Figures 5.5 and 5.6 we see that the DOM describes $\sigma(\theta)$ data quite well above 8 MeV except for a small discrepancy at the backward angles at some energies like 15.4, 18, and 26 MeV. For energies below 8 MeV the model overestimated $\sigma(\theta)$ at the forward angle by as much as 60%. This region (below 8 MeV) is where the model overestimates σ_T also. Our new $\sigma(\theta)$ data at 15.43 MeV is predicted well by the DOM except at the backward angles where the model underestimates $\sigma(\theta)$.

As for the analyzing power, Figures 5.7 and 5.8 shows the DOM predictions at 14.0, 17.0, and 15.4 MeV. The model predicts $A_y(\theta)$ at all angles except in the region between 65° - 90° where it overpredicts $A_y(\theta)$ consistently at all three energies. Except for the region 65° - 90° and the datum at 140° our measurement of $A_y(\theta)$ at 15.43 is well predicted by the DOM within the error bars.

In general our DOM predicts the data quite well except for energies below 8 MeV. Extension of the calculation to negative energies was successful by predicting the deeply bound 1s state as shown in Figure 5.1.

Table 5.1. Dispersive optical model parameters[a] for ^{27}Al.

$V(r,E) = V_{HF}(r,E) + \Delta V(r,E)$

$V_{HF} = V_{HF}(E)\ f(r)$

$V_{HF}(E) = V_{HF}(E_F) \exp[-\alpha\ (E - E_F)/V_{HF}(E_F)]$

$f(r) = [1+\exp((r-R_{HF})/a_{HF})]^{-1}, \qquad R_i = r_i\ A^{1/3}$

$V_{HF}(E_F) = 51.163, \quad \alpha = 0.310, \quad r_{HF} = 1.190, \quad a_{HF} = 0.660$

$W_V(E) = A_v\ (E - E_F)^4 / [(E - E_F)^4 + B_v^4]$

$A_v = 9.13, \quad B_v = 50.00, \quad E_F = -10.39$

$W_S(E) = A_s (E - E_F)^6 \exp(-C_s (E - E_F)) / [(E - E_F)^6 + B_s^6]$

$A_s = 10.413, \quad B_s = 12.98, \quad C_s = 0.0186$

$r_s = 1.280, \quad a_s = 0.550$

$V_{so} = 5.700, \quad r_{so} = 1.000, \quad a_{so} = 0.410$

[a] Potential depths are given in MeV and geometries in fm.

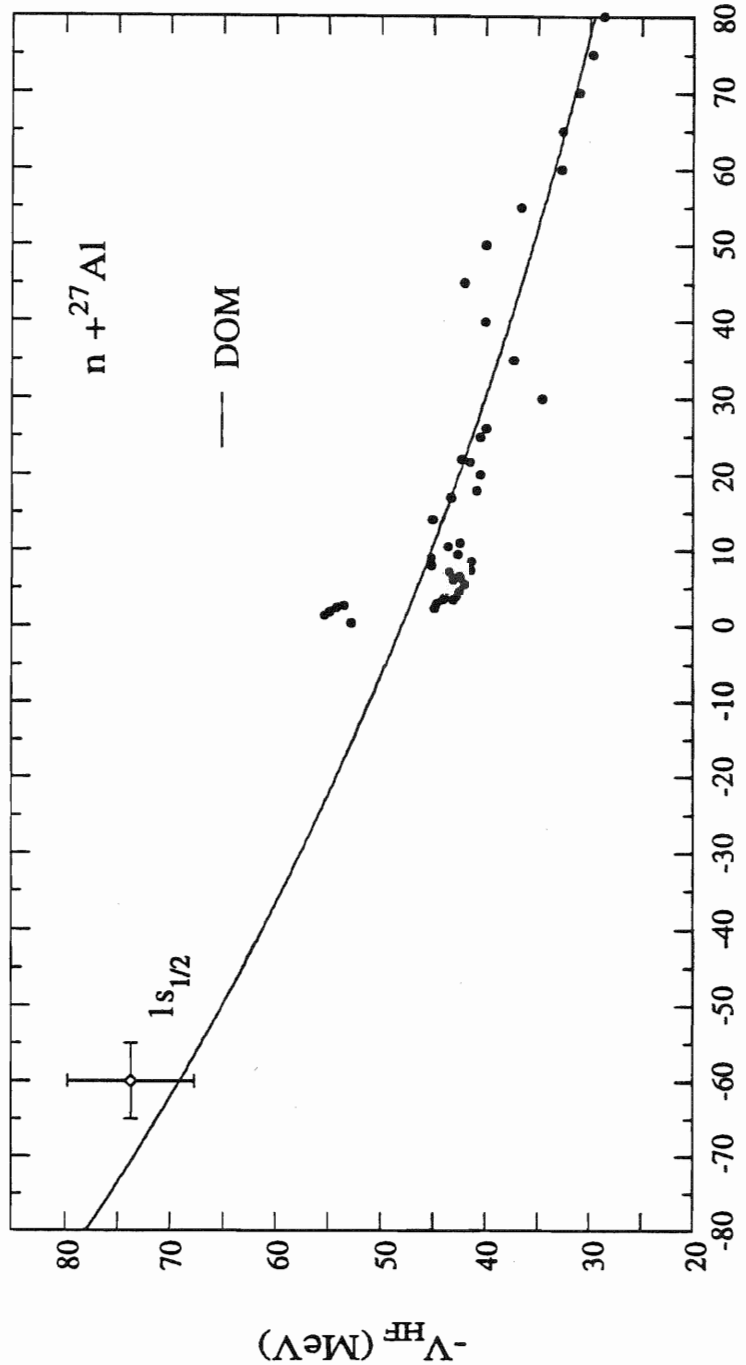

Figure 5.1. The strength of the Hartree-Fock potential V_{HF}. Dots show the optimum V_{HF} strength obtained in single-energy searches.

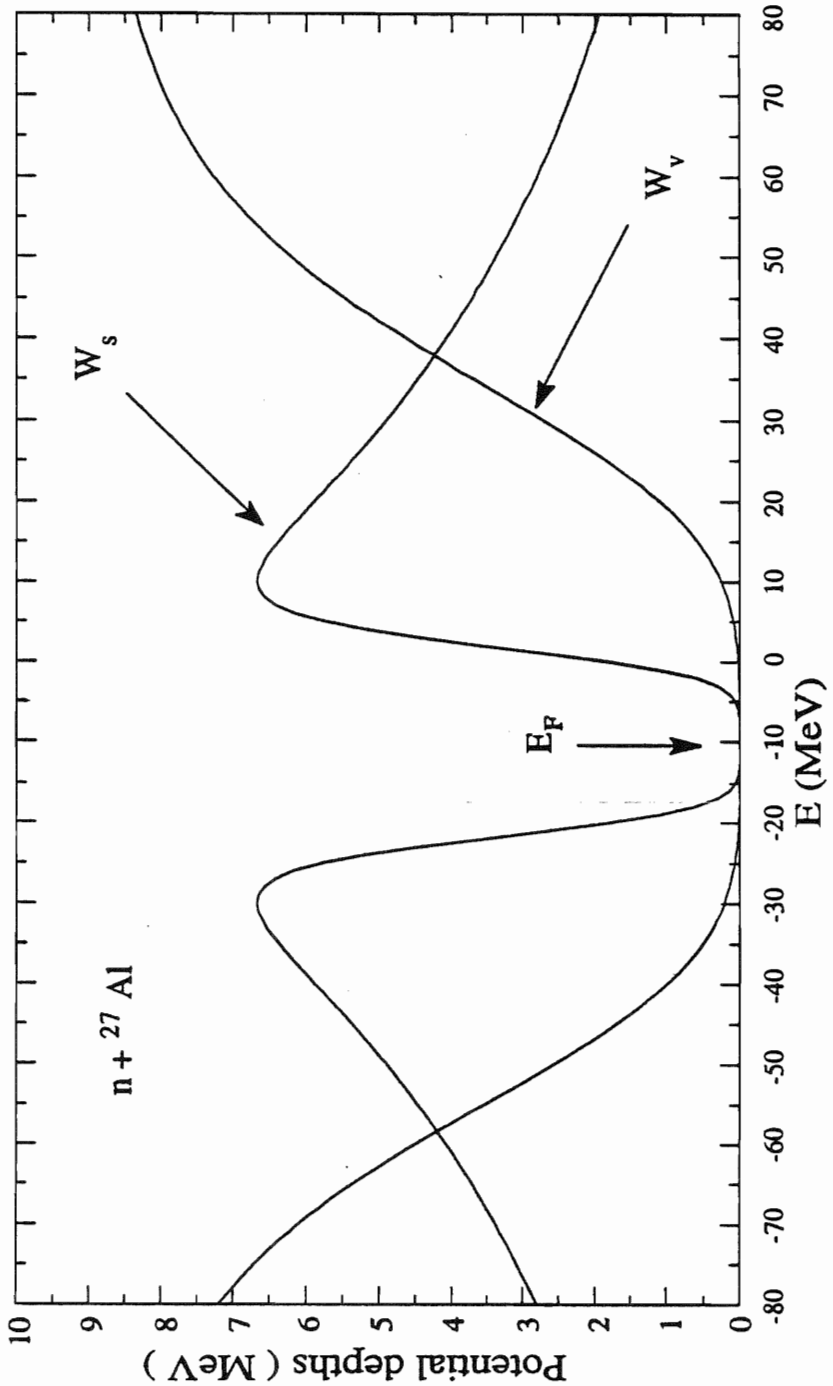

Figure 5.2. Energy dependencies of the strength of the imaginary volume (W_v) and surface (W_s) terms.

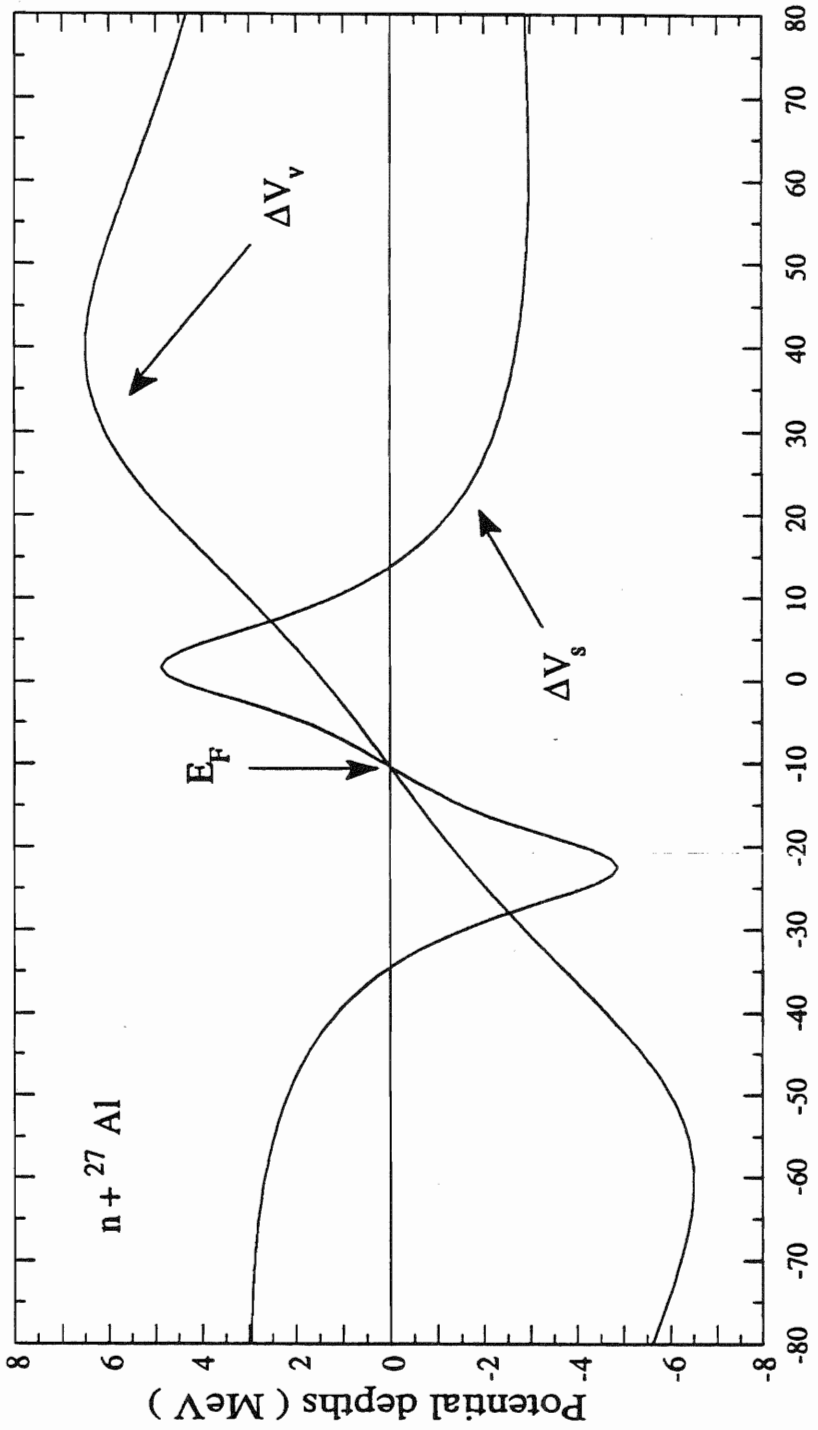

Figure 5.3. The strength of the dispersive volume (ΔV_v) and surface (ΔV_s) terms.

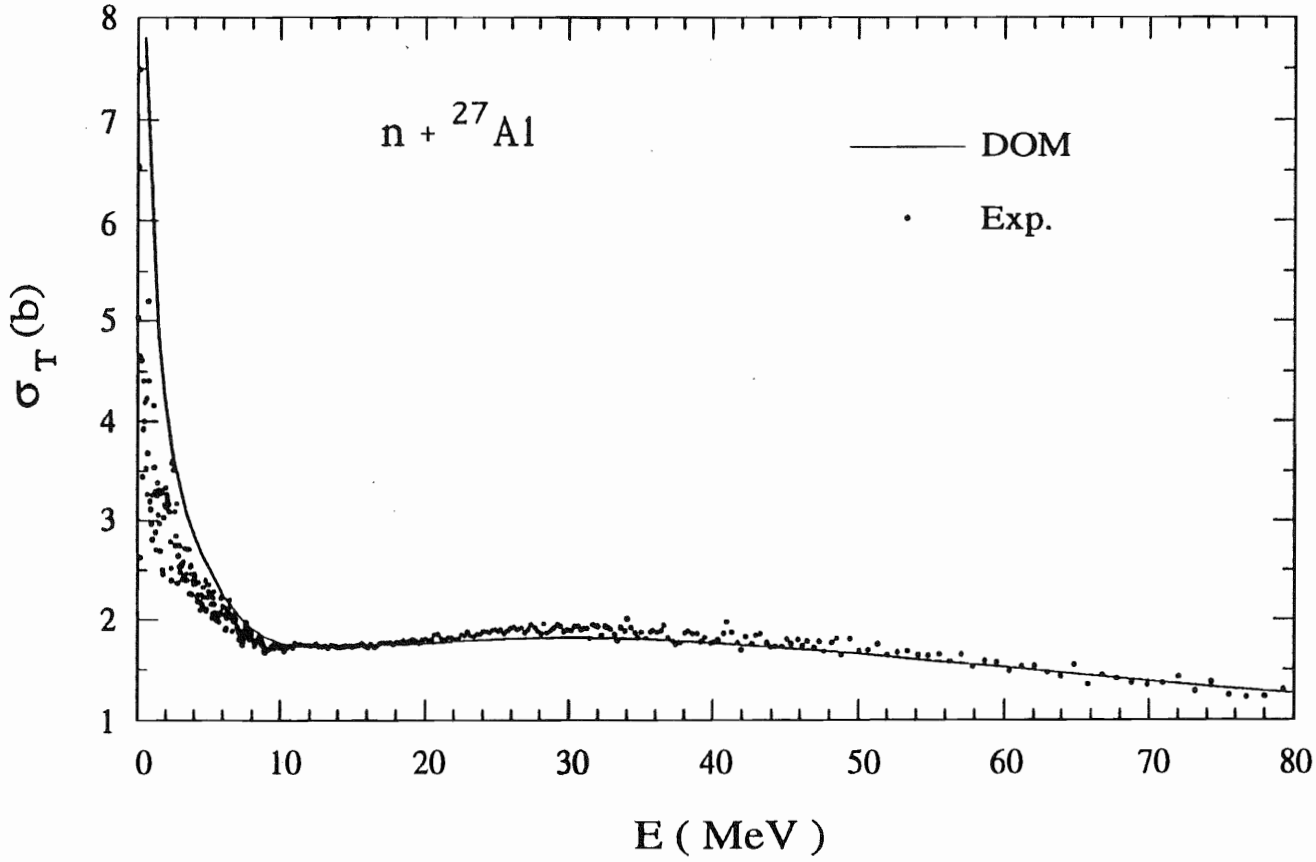

Figure 5.4. DOM calculation of σ_T compared to measurements. Data below 10 MeV are the averaged σ_T over 50 keV intervals. Above 10 MeV the average is over 200 keV or more intervals.

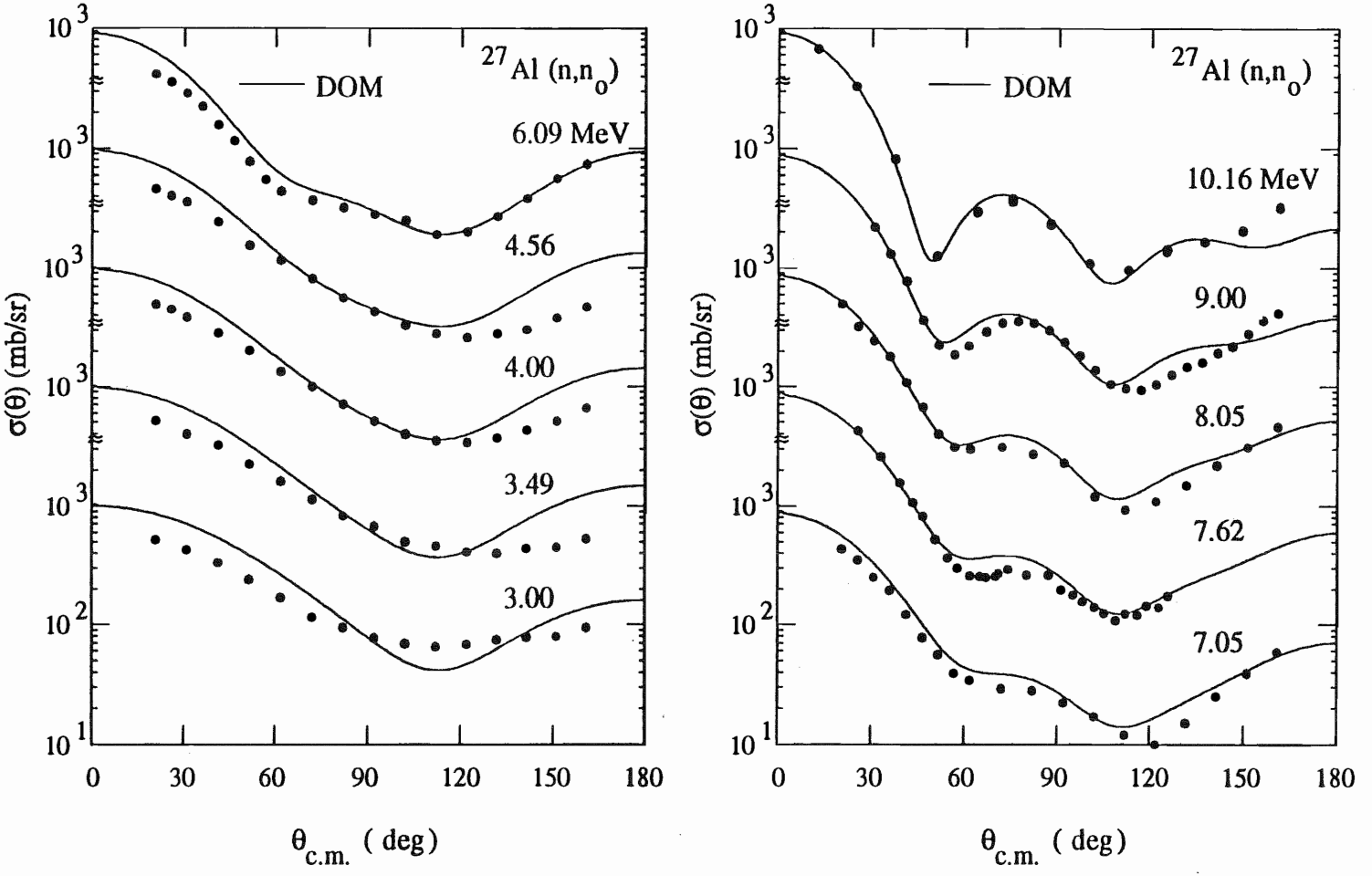

Figure 5.5. DOM calculations for σ(θ) compared to measurements. Compound nucleus contribution is added to the calculation below 11 MeV.

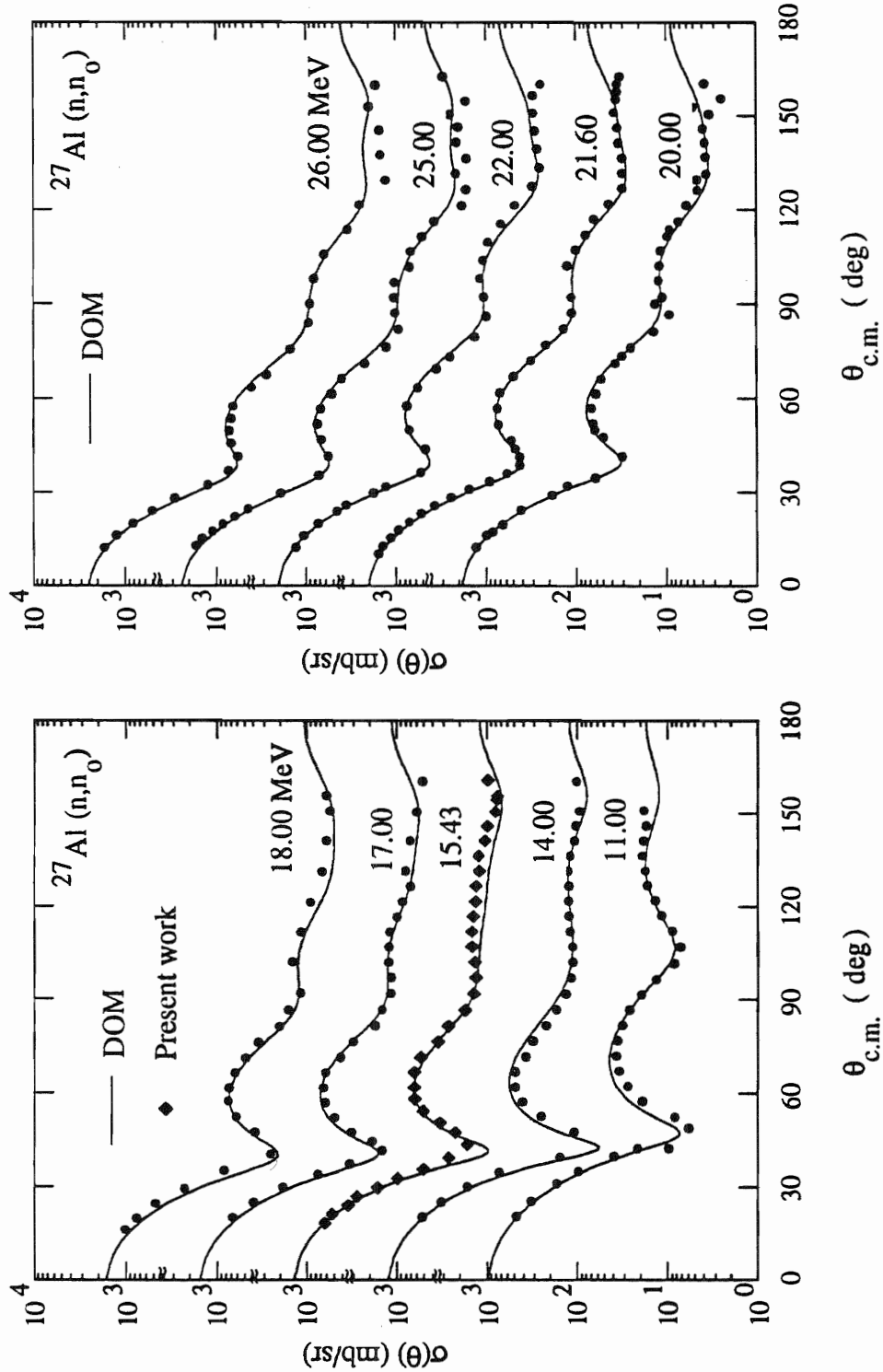

Figure 5.6. DOM calculations for σ(θ) compared to measurements.

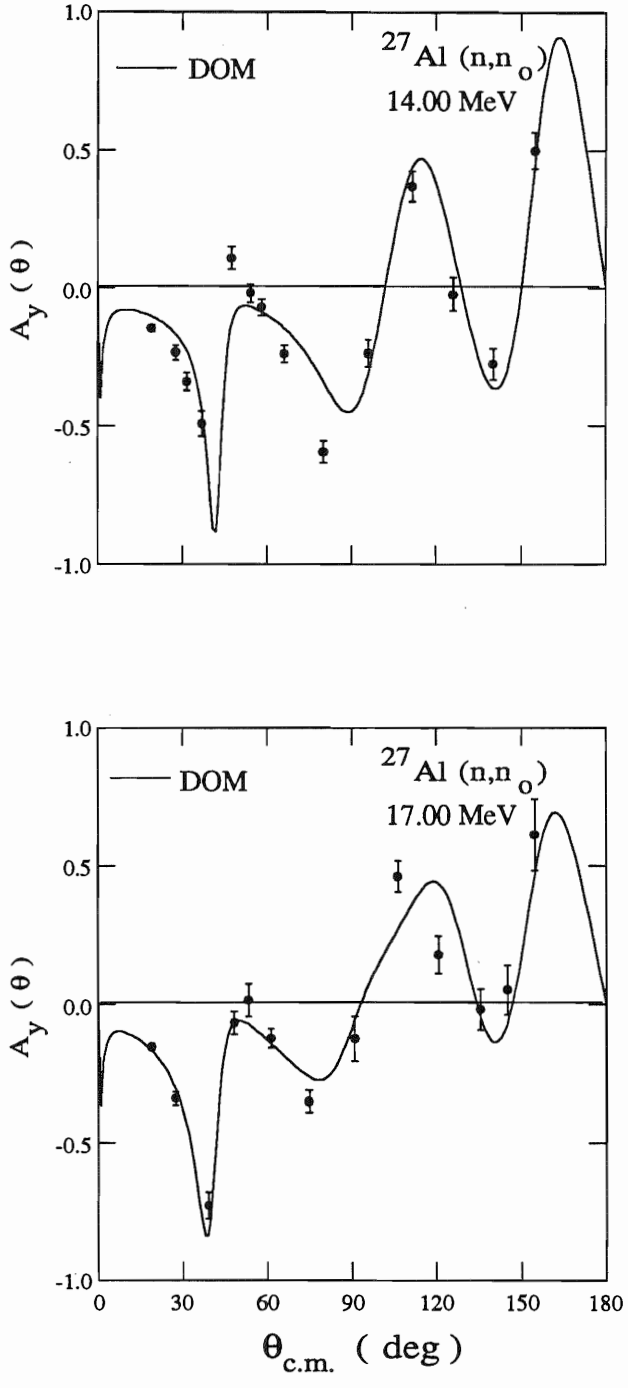

Figure 5.7. DOM calculations for $A_y(\theta)$ compared to measurements at 14 and 17 MeV.

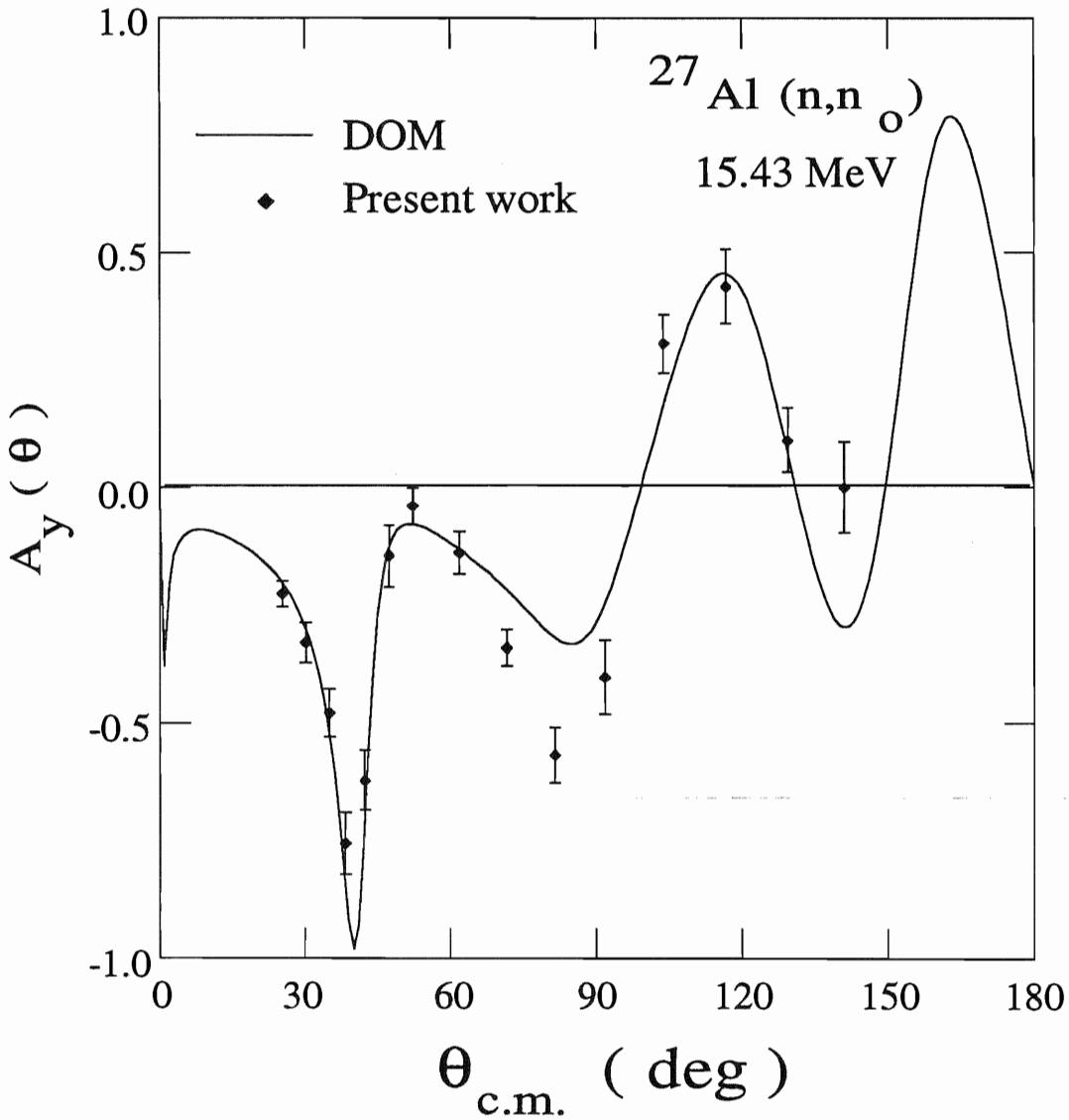

Figure 5.8. DOM calculations for $A_y(\theta)$ compared to measurements at 15.43 MeV.

5.6 DOM Parameters and Results for ^{59}Co

Table 5.2 shows the final parameters for our DOM model. Note that for ^{59}Co the power of 4 gave the best representation of the data. Figure 5.9 shows the Hartree-Fock potential V_{HF} along with the single-energy search for the optimum V_{HF} at each energy. No data is available for ^{59}Co above 32 MeV. Figures 5.10 and 5.11 show the behavior of W_V, W_S, ΔV_V and ΔV_S. Figure 5.12 shows the DOM calculations for σ_T. Here again the DOM overpredicts σ_T below 10 MeV as in the case of ^{27}Al. The data points are the experimental data for ^{59}Co below 32 MeV; they have been averaged over 50 keV intervals below 10 MeV, and over 200 keV or more intervals above 10 MeV. Data points above 32 MeV are for ^{58}Ni and shown there for comparison.

Figures 5.13 - 5.15 show the DOM calculations of $\sigma(\theta)$. Above 6 MeV the model does quite well predicting the data except at 11.01 MeV where we believe that the data are not as accurate as reported. The model also predicted $\sigma(\theta)$ quite well between 1.5 - 6 MeV except for the angular region between 60° - 100° where there is some discrepancy between the prediction and the data. Our new data at 9.95, 11.94, 13.94, 15.43, 16.88, and 18.86 MeV is very well predicted by the model except for a small discrepancy at the backward angle at 15.43, 16.88, and 18.86 MeV. Figure 15.16 shows the DOM calculations at 15.27 compared to our $A_y(\theta)$ data. The data is generally well predicted by the model except below 30° where the model overpredicts $A_y(\theta)$. The model also overpredicts the data between 90° and 105°.

In general our DOM calculations predict $\sigma(\theta)$ and $A_y(\theta)$ quite well except for a small discrepancy between the data and the calculations at backwards angles at some energies. We successfully extended the model to negative energies by predicting the

deeply bound 1s-state for ^{58}Ni which was used due to lack of information on bound states for ^{59}Co. The prediction is quite satisfactory (see Figure 5.9).

Table 5.2. Dispersive optical model parameters[a] for ^{59}Co.

$V(r,E) = V_{HF}(r,E) + \Delta V(r,E)$

$V_{HF} = V_{HF}(E)\ f(r)$

$V_{HF}(E) = V_{HF}(E_F) \exp[-\alpha\ (E - E_F)/V_{HF}(E_F)]$

$f(r) = [1+\exp((r-R_{HF})/a_{HF})]^{-1}, \qquad R_i = r_i\ A^{1/3}$

$V_{HF}(E_F) = 51.910, \quad \alpha = 0.430, \quad r_{HF} = 1.210, \quad a_{HF} = 0.660$

$W_V(E) = A_v\ (E - E_F)^4 / [(E - E_F)^4 + B_v^{\ 4}]$

$A_v = 8.612, \quad B_v = 52.589, \quad E_F = -8.98$

$W_S(E) = A_S\ (E - E_F)^4 \exp(-C_S\ (E - E_F))\ /[(E - E_F)^4 + B_S^{\ 4}]$

$A_S = 8.584, \quad B_S = 9.935, \quad C_S = 0.0110$

$r_S = 1.261, \quad a_S = 0.593$

$V_{so} = 6.200, \quad r_{so} = 1.017, \quad a_{so} = 0.600$

[a] Potential depths are given in MeV and geometries in fm.

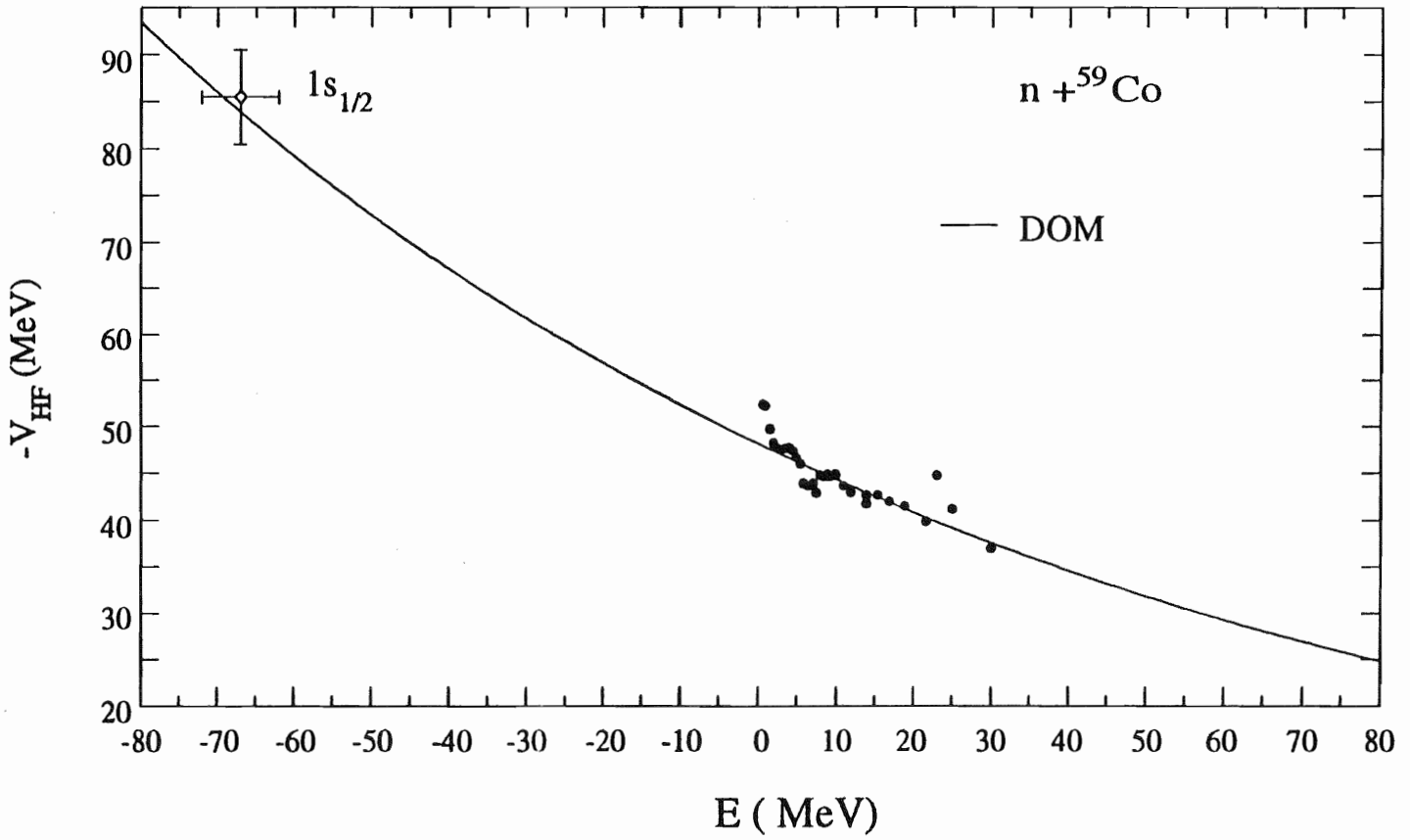

Figure 5.9. The strength of the Hartree-Fock potential V_{HF}. Dots show the optimum V_{HF} strength obtained in single-energy searches.

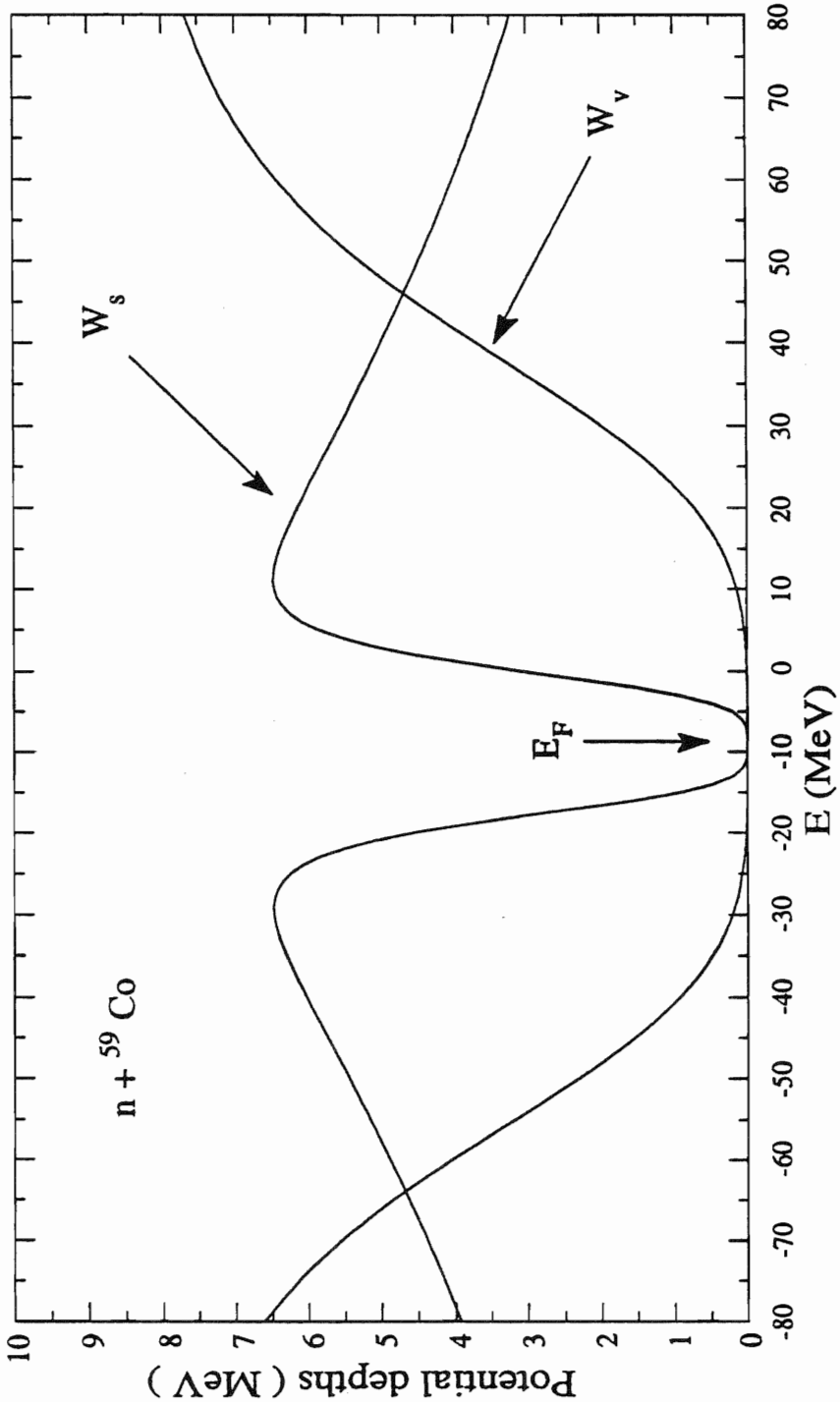

Figure 5.10. Energy dependencies of the strength of the imaginary volume (W_v) and surface (W_s) terms.

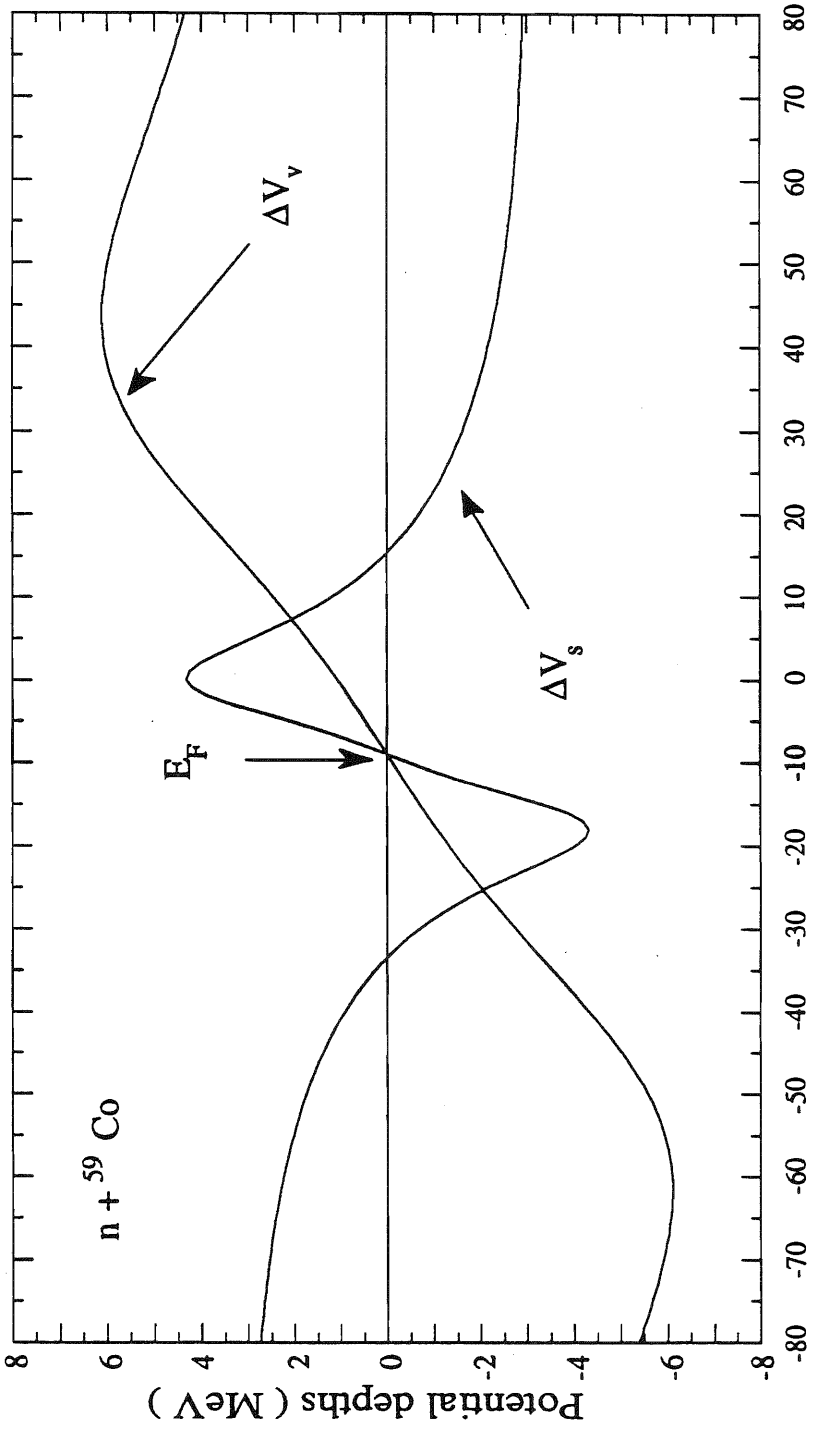

Figure 5.11. The strength of the dispersive volume (ΔV_v) and surface (ΔV_s) terms.

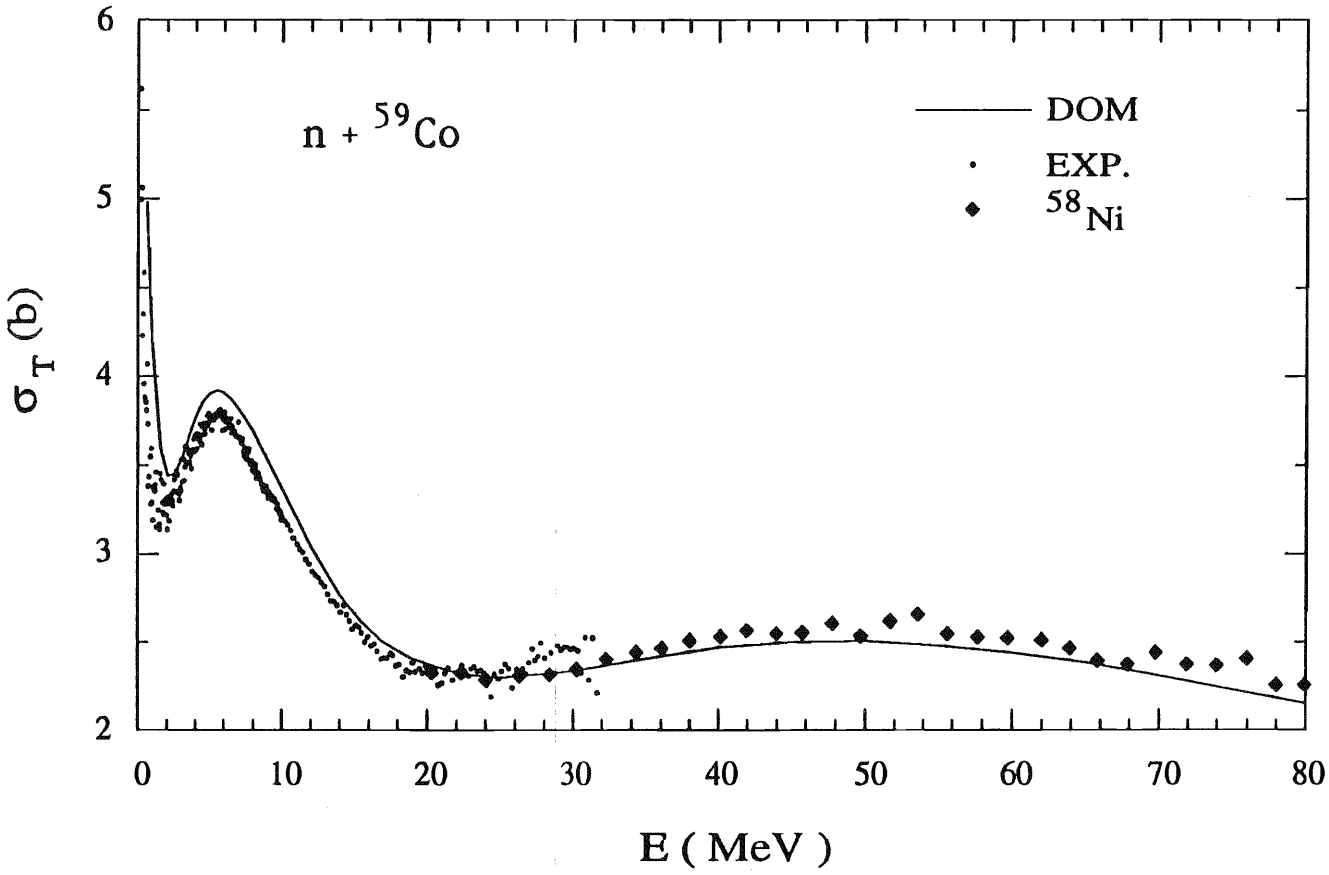

Figure 5.12. DOM calculation of σ_T compared to measurements. Data below 10 MeV are the σ_T averaged over 50 keV intervals. Above 10 MeV the average is over 200 keV or greater intervals. Data above 32 MeV are for ^{58}Ni.

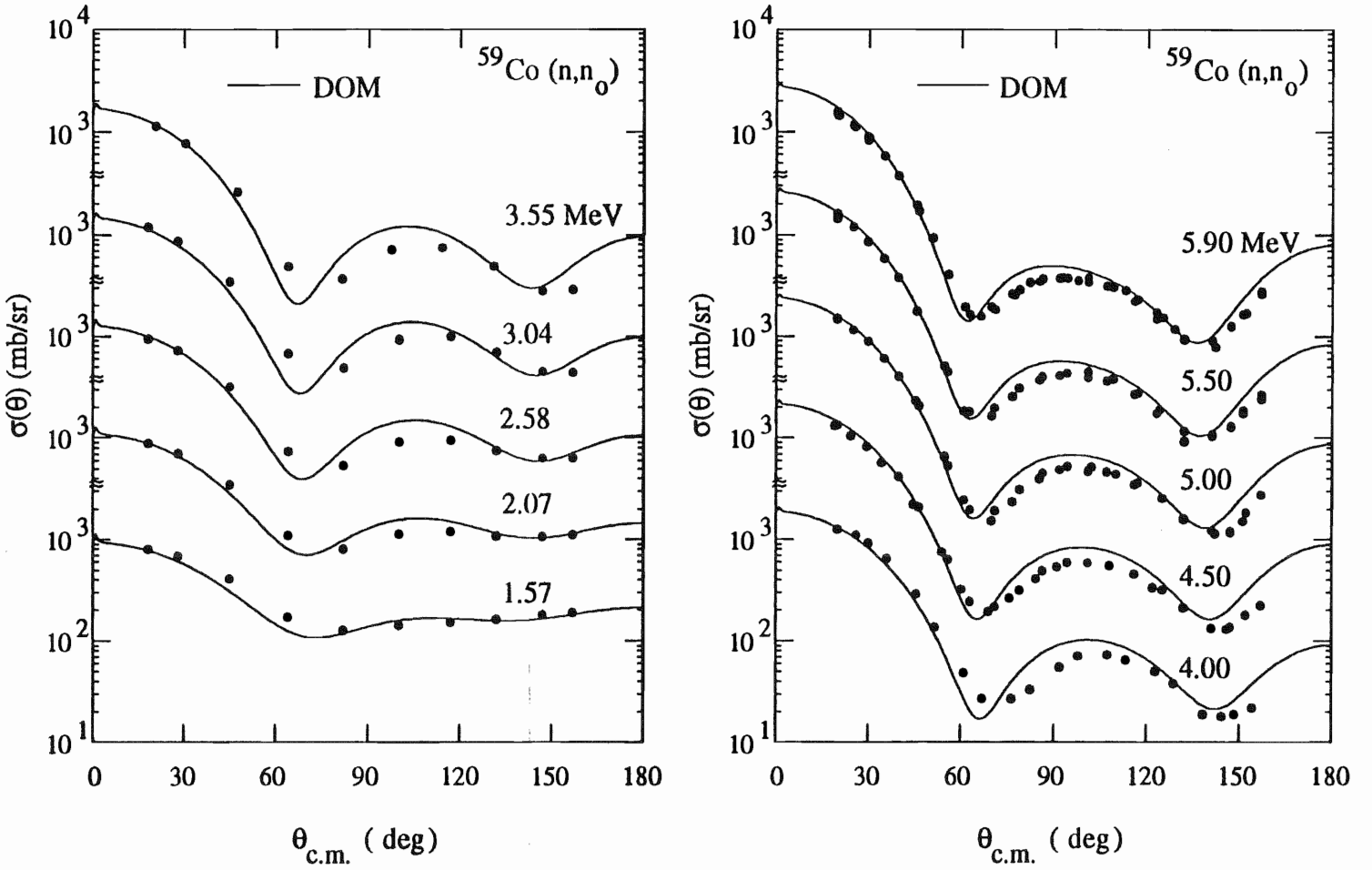

Figure 5.13. DOM calculation for σ(θ) compared to measurements. Compound nucleus contribution is added to the calculations below 8 MeV.

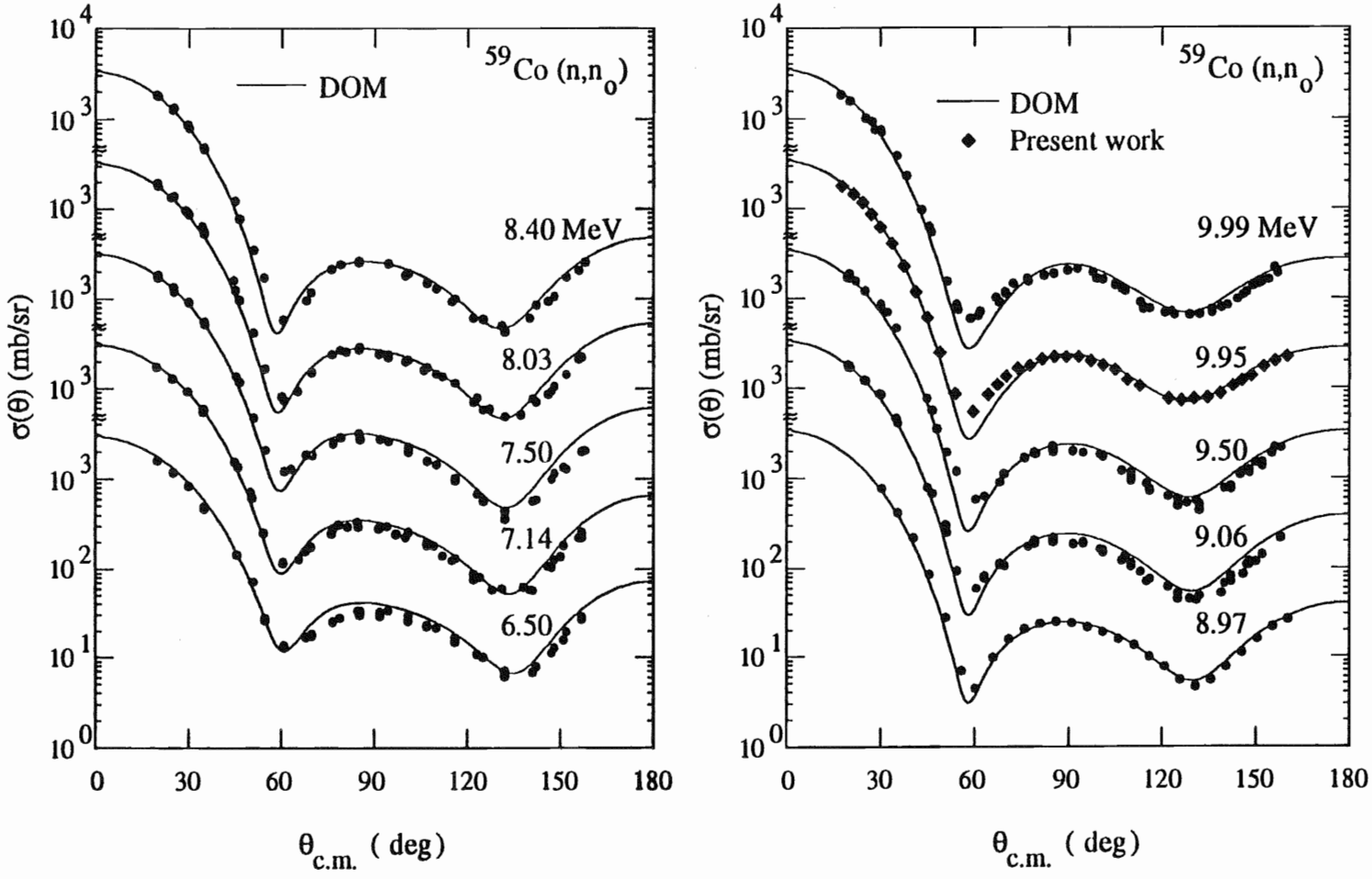

Figure 5.14. DOM calculation for $\sigma(\theta)$ compared to measurements. Compound nucleus contribution is added to the calculations below 8 MeV.

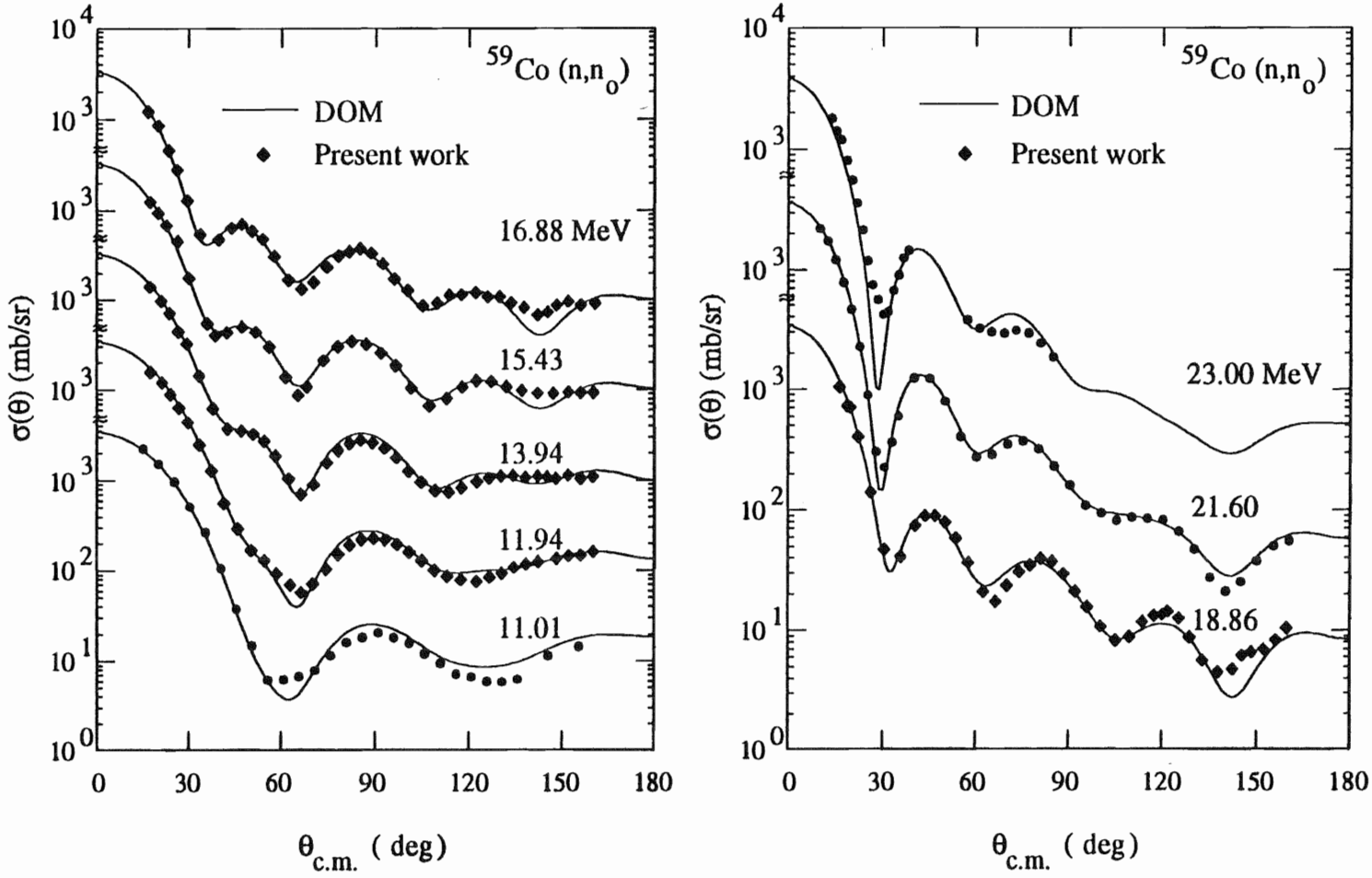

Figure 5.15. DOM calculation for σ(θ) compared to measurements. Compound nucleus contribution is added to the calculations below 8 MeV.

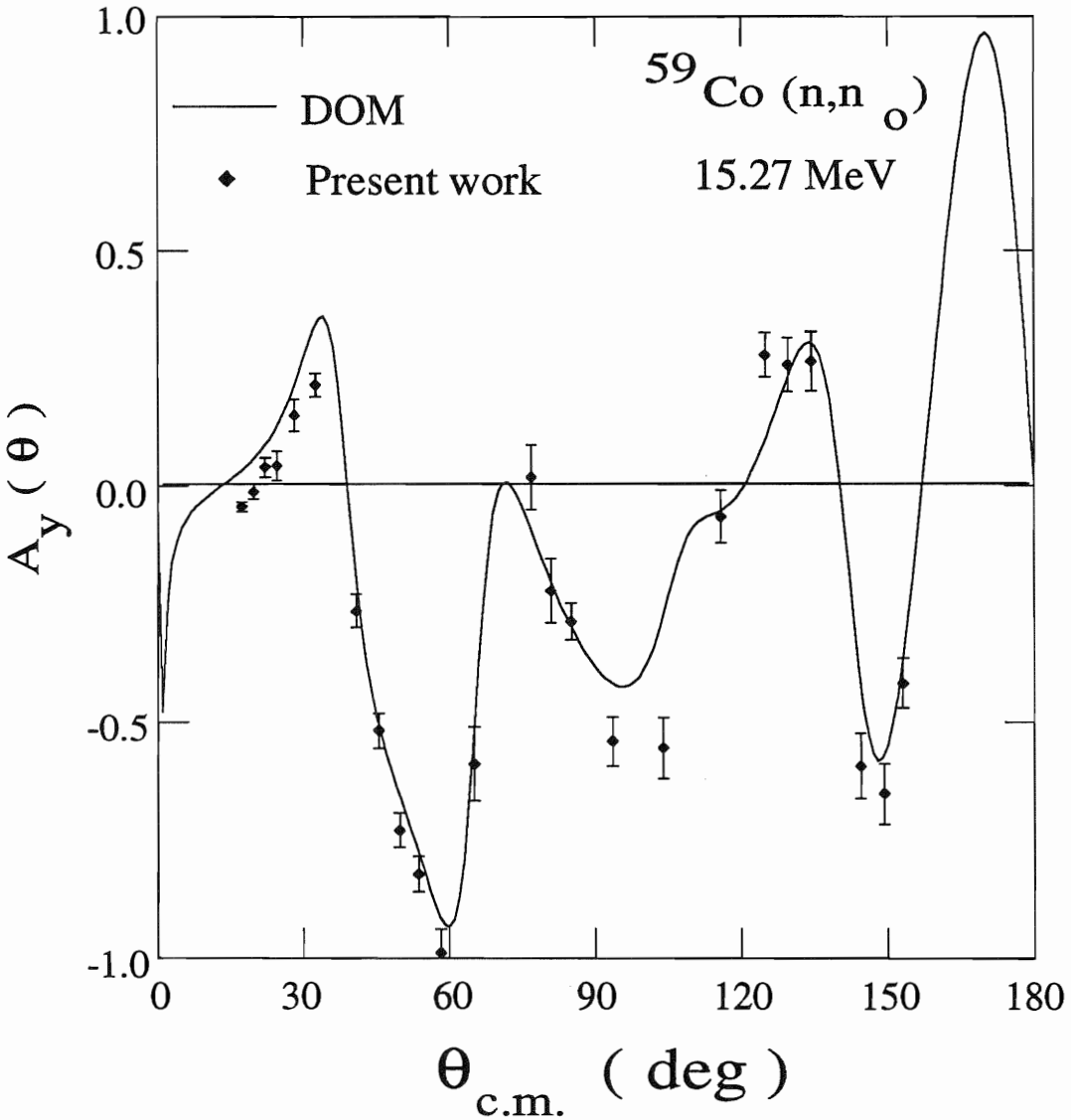

Figure 5.16. DOM calculation for $A_y(\theta)$ compared to measurements at 15.27 MeV.

CHAPTER 6

THE REORIENTATION EFFECT

6.1 Introduction

Although the DOM fit for the total cross section gives a reasonable description for the data at $E_n > 9$ MeV for ^{27}Al and at $E_n > 8$ MeV for ^{59}Co, the fit to data below 8 MeV is not as good in both cases (see Figures 5.4 and 5.12). This total cross section discrepancy is symptomatic of many DOM studies so far; for example, see the DOM studies of ^{90}Zr by Delaroche *et al.* [Del89] and of ^{40}Ca by Johnson and Mahaux [Joh88]. This problem seems to be exacerbated for the light, deformed nucleus ^{27}Al. The problem is attributed partially to l -dependencies of the absorptive interaction that are not accounted for in our DOM and to reorientation effects, which are not treated explicitly in the DOM. The reorientation effect is simply the coupling of the ground state to itself as we explain in detail below. So, in order to examine the problem of describing the total cross section at low energy, we developed a simple coupled channels model (CCM) for neutron scattering from ^{27}Al and ^{59}Co. The aim of the study in this chapter then is to carry out a study of the effect on the total cross section that coupling of the ground state ($J^{\pi} = 5/2^{+}$ for ^{27}Al and $7/2^{-}$ for ^{59}Co) to itself produces, meanwhile avoiding a complete coupled channels analysis. As shown below, we found that the reorientation effects have a profound effect on the total cross section at low energies ($E_n < 6$ MeV), and a negligible effect at higher energies.

6.2 The Reorientation Effect

In order for a populated state μ_i (see Figure 6.1) to decay to a final state μ_f it can either decay through a direct first order process $\mu_i \rightarrow \mu_f$ or by a second order process involving an intermediate state μ' which then decays to μ_f (that is $\mu_i \rightarrow \mu' \rightarrow \mu_f$). For instance, an initial state of J = 0 ($\mu_i = 0$) would decay to a state of J = 2 and μ_j = -1 (out of the possible projections μ_j = -2, -1, 0, +1, +2) either directly (that is 0 → -1) or through an intermediate substate μ' of μ_j = -2 (for example) so $\mu_i \rightarrow \mu' \rightarrow \mu_f$ or 0 → -2 → -1. The process $\mu' \rightarrow \mu_f$ (-2 → -1) where a sub-state decays to another substate of the same state is called a REORIENTATION EFFECT. This latter process is actually a coupling of the state to itself.

6.3 The Collective Model of the Nucleus

Elastic nucleon scattering from spherical nuclei can be well described using a simple spherical optical model; however, for non-spherical nuclei or for inelastic scattering, it was observed that data are not well described with the shell model wave functions. In 1958 Cohen and Rubin [Coh58] attributed the discrepancy between the experimental and calculated inelastic cross section to the collective motion of the nucleus. This motion, which is of two types, depends on the nucleus being studied. For nuclei with Z or N close to the magic numbers the incident particle will excite the nucleus into vibrational states where the nucleus undergoes a collective vibrational motion about a spherical axis. This motion is represented in terms of the nuclear radius R where

$$R(\theta, \phi) = R_0 \left[1 + \sum_{\lambda \mu} \alpha_{\lambda\mu} \, Y_{\lambda\mu} \, (\theta, \phi)\right]$$

for the vibrational nuclei. The angular coordinates θ and ϕ are space-fixed coordinates and $R_0 = r_R \, A^{1/3}$ is the equilibrium radius. The variables $\alpha_{\lambda\mu}$ are operators that either

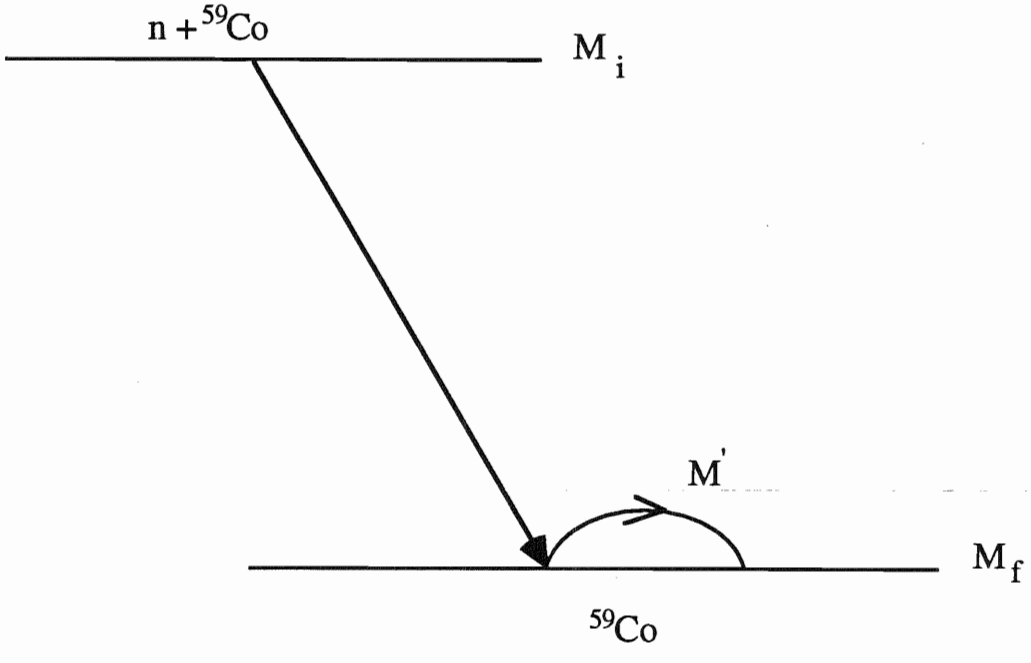

Figure 6.1. The reorientation effect.

create or annihilate single phonons of angular momentum λ, projection μ, and parity $(-1)^{\lambda}$. For vibrational nuclei these operators are related to the coupling strengths β_{λ} as defined by Tamura [Tam65].

For nuclei that are permanently deformed, such as ^{27}Al and ^{59}Co, the nucleus is excited into rotational states where the nucleus is treated as a rotating ellipsoid with a deformation parameter β. For oblate deformed nuclei (pancake shape) β is negative, and for prolate nuclei (cigar shape) β is positive. For these permanently deformed nuclei the nuclear surface is also described by the nuclear radius $R(\theta')$ where

$$R(\theta') = R_0 \left[1 + \sum_{\lambda} \beta_{\lambda} Y_{\lambda 0} (\theta')\right]$$

where θ' is the body-fixed angular coordinate and β_{λ} is the permanent deformation of the nucleus.

The radial wave functions for vibrational and rotational states are given by the coupled equations

$$\left[\frac{d^2}{dr^2} - \frac{\ell(\ell+1)}{r^2} + k_{\alpha}^2 - W_{\alpha\alpha}(r)\right] u_{\alpha}(r) = \sum_{\alpha' \neq \alpha} W_{\alpha\alpha'}(r) u_{\alpha'}(T)$$

where

$$W_{\alpha\alpha'}(r) = \frac{2m}{\hbar^2} \sum_{\ell m} \int Y^*_{\ell' m'} (\theta, \phi)\, V_{\alpha\alpha'}(r)\, Y_{\ell m}(\theta, \phi) d\Omega$$

and

$$V_{\alpha\alpha}(r) = \int \chi^*_{\alpha}(\varepsilon)\, V(r, \xi)\, \chi_{\alpha'}(\varepsilon) d\varepsilon$$

where $\chi_{\alpha}(\varepsilon)$ are the nuclear states and ε are the nuclear coordinates for the vibrational or rotational states. The interaction $V(r, \xi)$ is the optical-model potential.

In our coupled channels calculations we used the computer code ECIS79 of Raynal [Ray79] which uses an iterative method to solve the above coupled equations.

Unfortunately the code does not search on parameters globally as with the code GENOA. In fact, we varied the parameters one at a time and then compared the resulting calculations of $\sigma(\theta)$, $A_y(\theta)$, and σ_T qualitatively with the available experimental data at each energy individually. This is a time-consuming process which took several weeks to complete since the data base was very large.

6.4 The Coupled Channels Calculation for n + ^{27}Al

For our coupled channels calculation for n + ^{27}Al we started the search using a preliminary DOM parameterization of W_S and W_V as starting parameters. For the real central potential geometry parameters and deformation parameters we started with those of Howell *et al.* [How88] from their CCM of ^{28}Si. In our search we used the same data base that we used in our DOM calculations of Chapter 5. Our primary goal was to account for the large σ_T discrepancy at low energy, so we only considered the coupling of the ground state to itself, since this is the dominant coupling. We started by optimizing the real central potential V_R and its geometrical parameters r_R and a_R. Then we searched W_S especially at energy regions where $W_V \cong 0$. We searched on the rest of the parameters in an orderly fashion, each time comparing the calculated values for $\sigma(\theta)$, $A_y(\theta)$, and σ_T to the experimental data. We proceeded in the search in an iterative way; after optimizing some subset of parameters, we started since the optimum parameter at a certain point of the search may not l value at another point. In our analysis we started with the deformatio and β_4 of ^{28}Si and optimized them for ^{27}Al. For our CCM we only de and imaginary part of the central potential. Table 6.1 shows the parameters, and Figure 6.2 illustrates these parameters. Note that V

(Basically) Used def. parms of ^{28}Si. Quadrupole Hexadecapole Optimized for ^{27}Al $\beta_4 = +0.20$ $\beta_2 = -0.35$

Table 6.1. The coupled channels model parameters [a] for $^{27}Al + n$

$V(r,E) = V_R(E)\ f(r)$
$V_R(E) = 53.61 - 0.29 * E$
$f(r) = [1+\exp((r-R_v)/a_v)]^{-1}$
$r_v = 1.150, \quad a_v = 0.650$
$\beta_2 = -0.35, \quad \beta_4 = +0.20, \quad R_i = r_i\ A^{1/3}$
$W_v(E) = a\,(E - E_F)^4 / [(E - E_F)^4 + b^4]$
$a = 9.13, \quad b = 50.00, \quad E_F = -10.39$
$W_s(E) = g\,(E - E_F)^6 \exp(-c\,(E - E_F)) / [(E - E_F)^6 + h^6]$
$g = 10.413, \quad h = 12.98, \quad c = 0.0186$
$r_s = 1.250, \quad a_s = 0.580$
$V_{so} = 6.00, \quad r_{so} = 1.010, \quad a_{so} = 0.500$

[a] Potential depths are given in MeV and geometries in fm.

and W_v and W_s contain powers of 4 and 6, respectively. The spin-orbit parameters of Howell *et al.* [How88] were used as they give a better fit to the data than our DOM spin-orbit parameters. Figures 6.3 and 6.4 show the CCM predictions of $\sigma(\theta)$ compared to the experimental data. The CN contribution is added to the coupled channels calculations below 10 MeV. We can see quite an improvement in the prediction of $\sigma(\theta)$ over the DOM especially at low energy for forward angles although the CCM still overpredicts the data there. There is also an improvement in the prediction of the first minimum at all energies. Figures 6.6 and 6.7 show the calculated $A_y(\theta)$ at 14, 17, and 15.43 MeV using the CCM and the DOM where we can see that the predictions of both models are comparable. Figure 6.5 shows the prediction of σ_T using CCM and DOM; clearly the CCM gives a much better prediction of σ_T below E_n

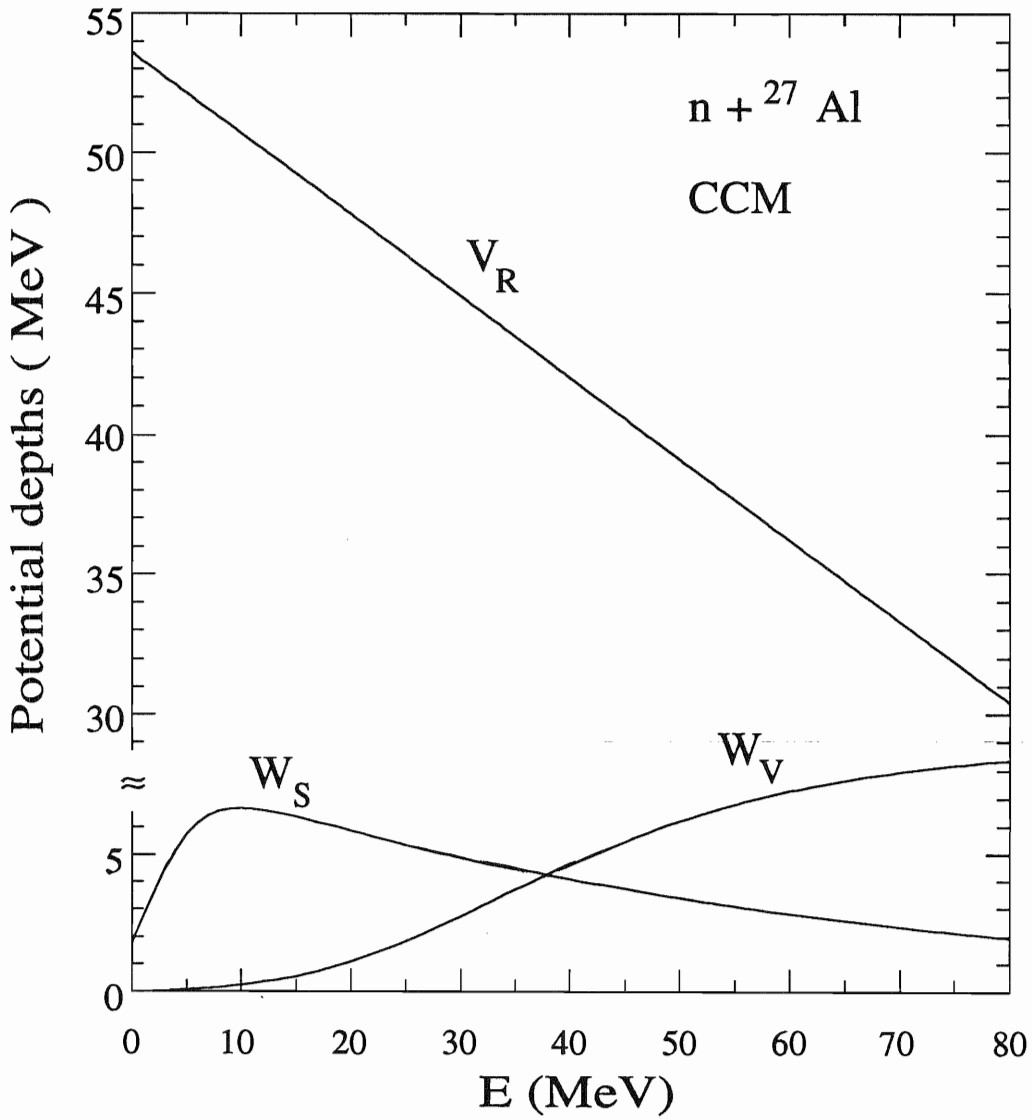

Figure 6.2. The CCM parameters for ^{27}Al + n.

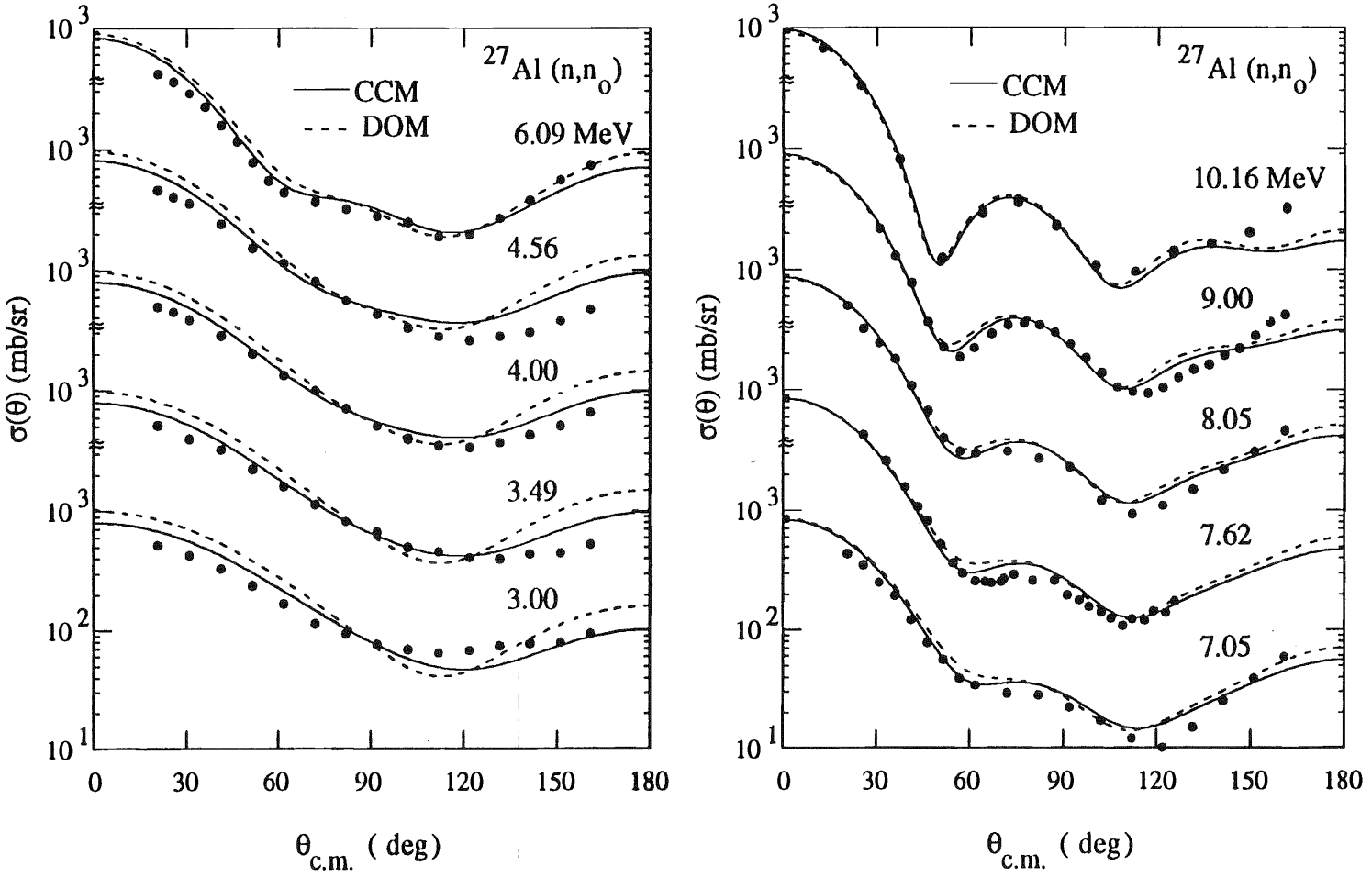

Figure 6.3. Coupled channels and DOM calculations of σ(θ) for ^{27}Al compared to data and to DOM calculations.

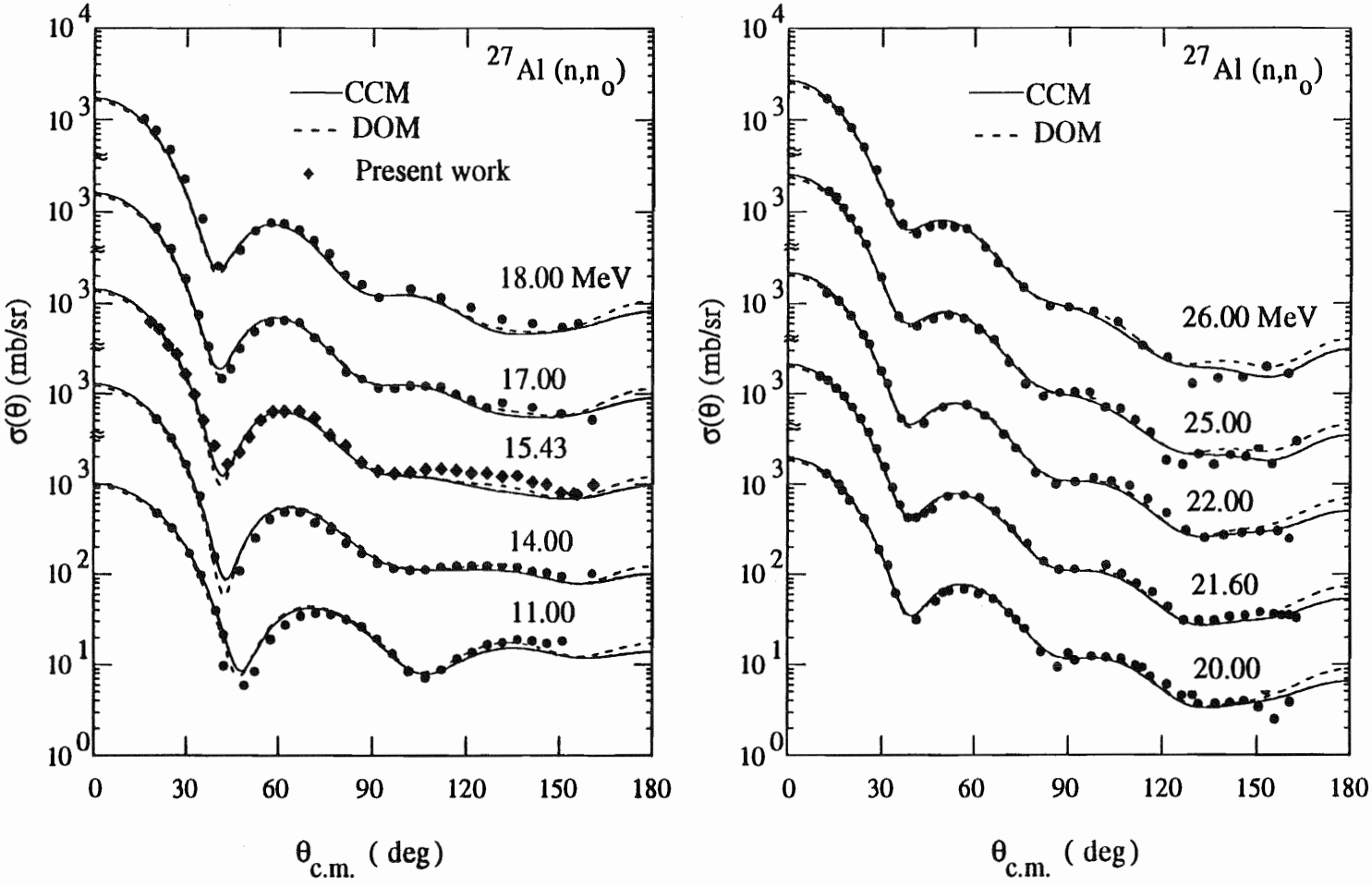

Figure 6.4. Coupled channels and DOM calculations of σ(θ) for ^{27}Al compared to data and to DOM calculations.

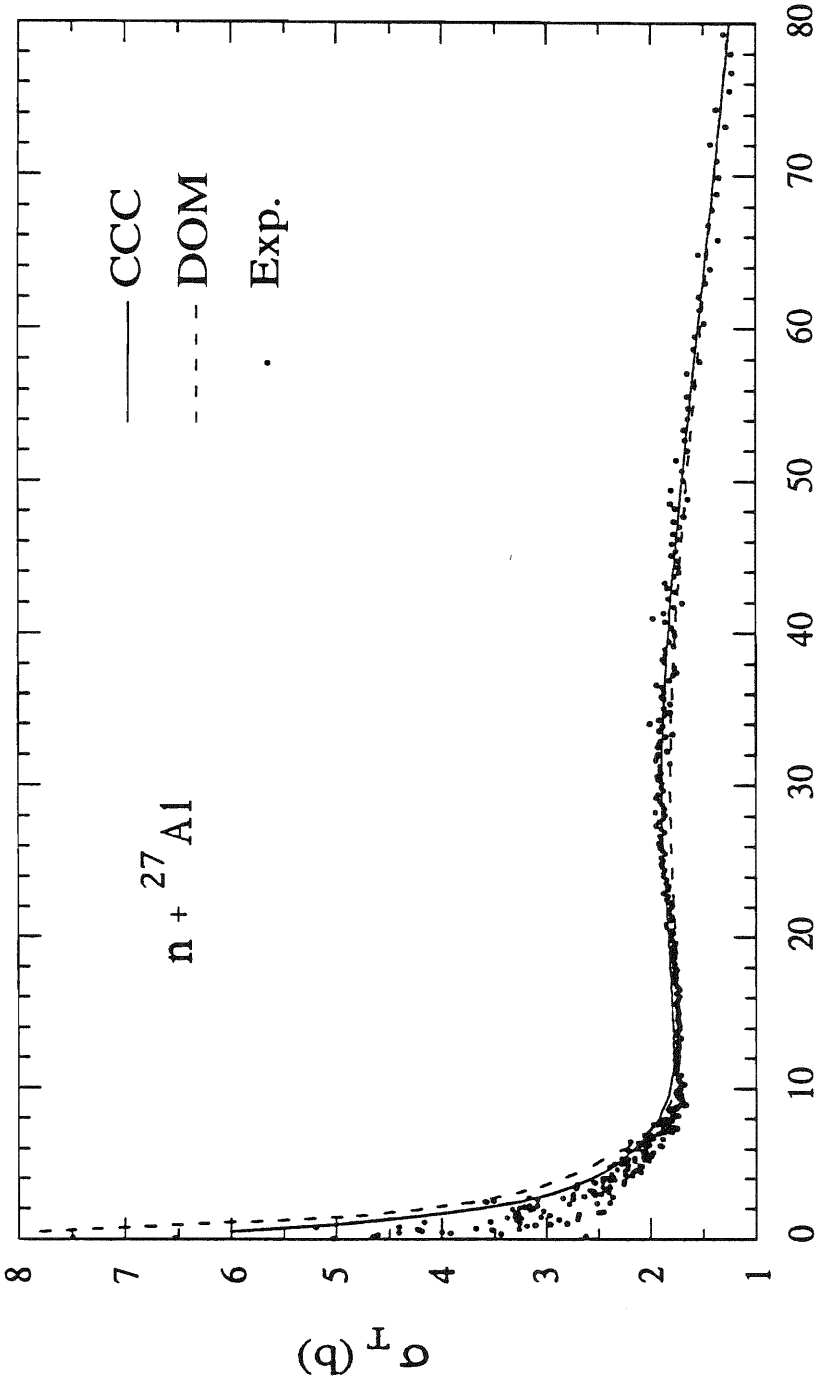

Figure 6.5. Coupled channels calculations of σ_T for ^{27}Al compared to data and to DOM calculations.

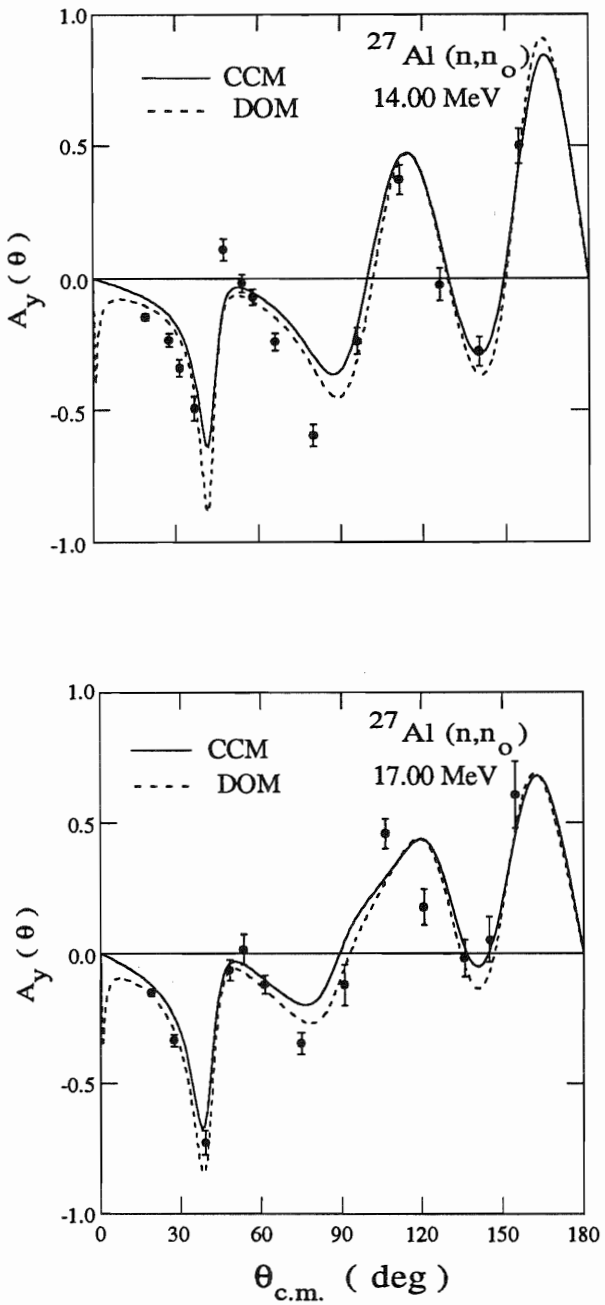

Figure 6.6. Coupled channels calculations of $A_y(\theta)$ for ^{27}Al at 14 and 17 MeV compared to data and to DOM calculations.

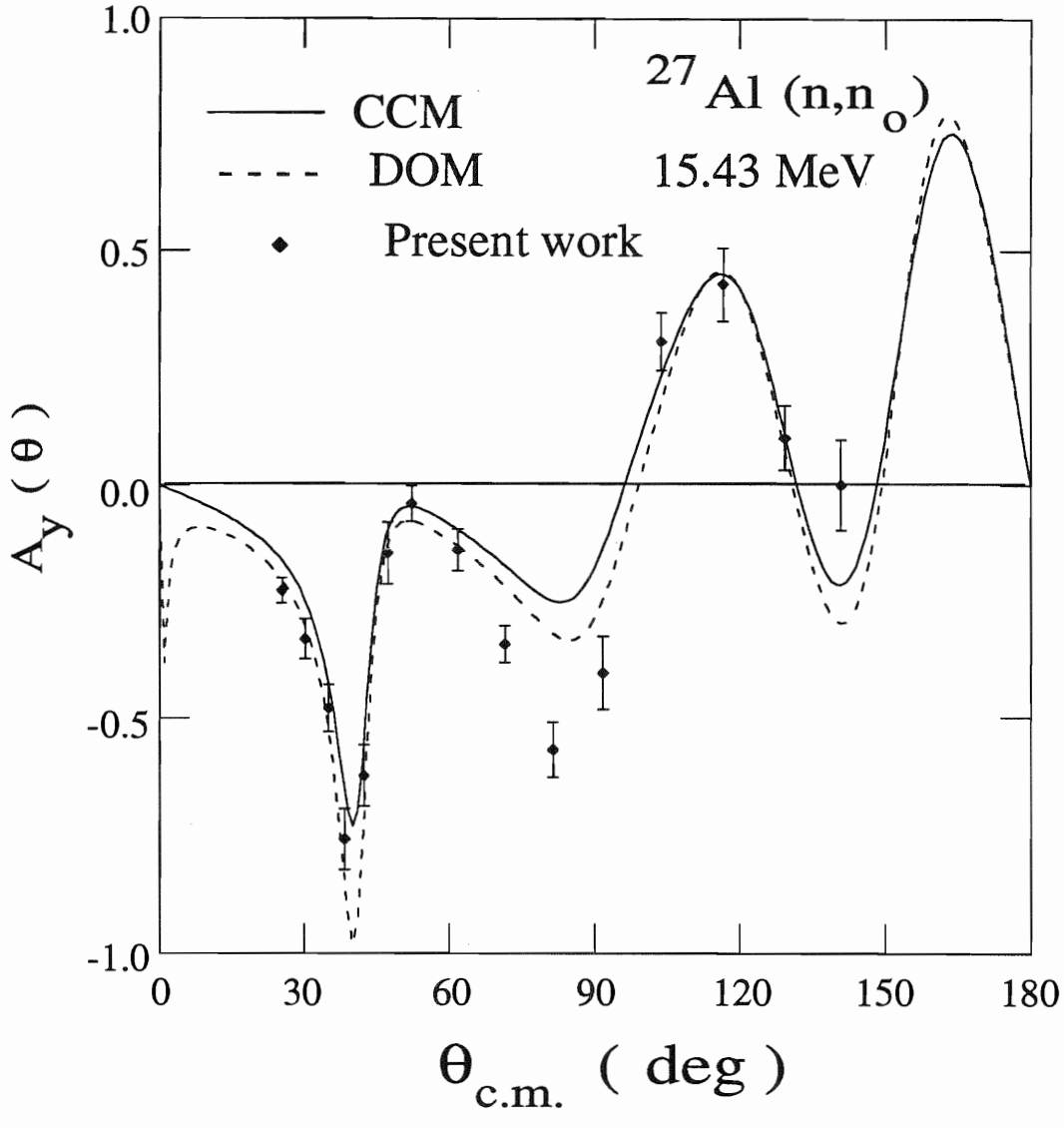

Figure 6.7. Coupled channels calculations of $A_y(\theta)$ for ^{27}Al at 15.43 MeV compared to data and to DOM calculations.

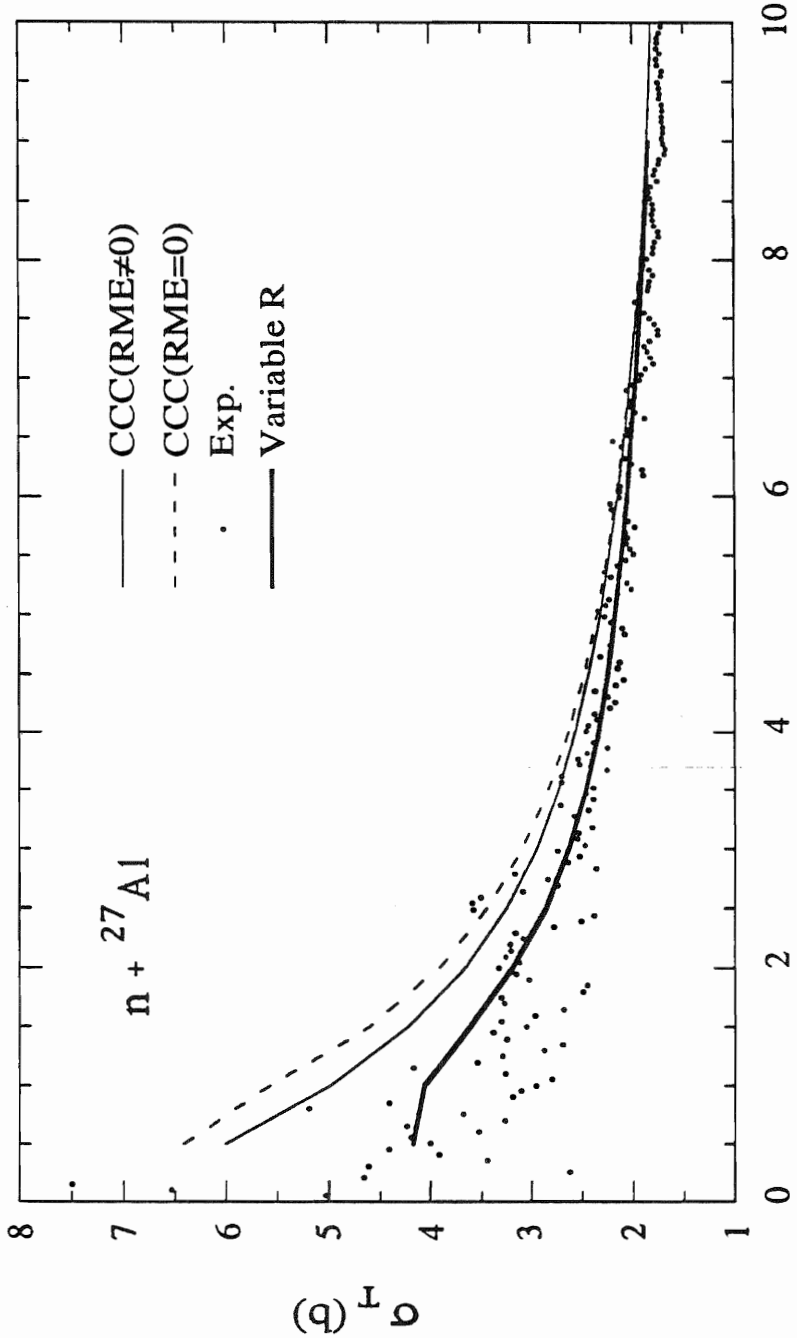

Figure 6.8. The impact of turning off the reorientation on σ_T for ^{27}Al and the effect of introducing a linearly varying energy dependent radius for the real central potential.

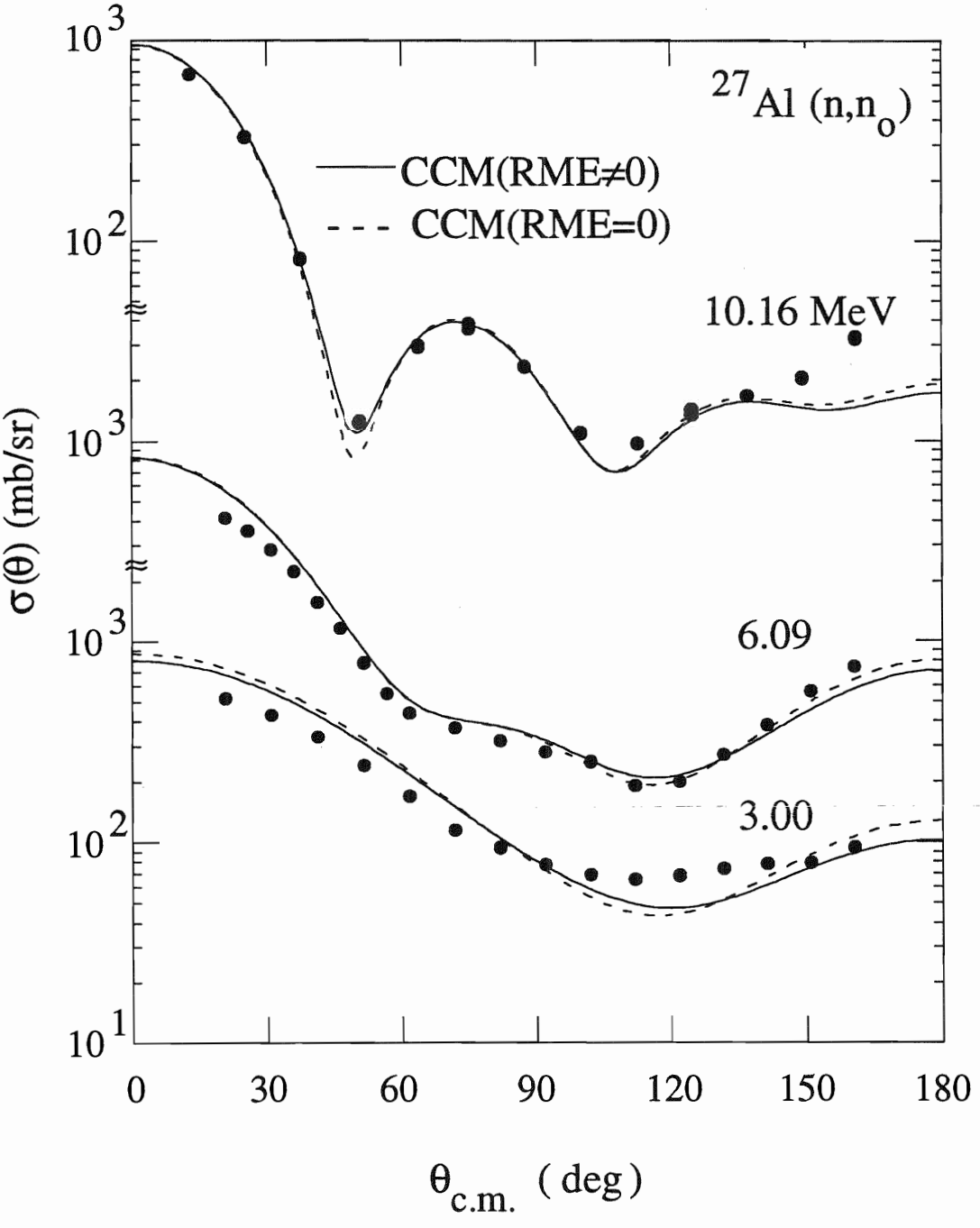

Figure 6.9. The impact of turning off the reorientation on σ(θ) for ^{27}Al.

= 9 MeV. We also looked at the effect of turning off (by setting the Reorientation Matrix Elements (RME) to zero) the reorientation effect on σ_T (Figure 6.8), $\sigma(\theta)$ (Figure 6.9), and $A_y(\theta)$ (Figure 6.10 and Figure 6.11). Above 5 MeV the coupling to this reorientation channel is nearly insignificant for σ_T and $\sigma(\theta)$, although at 10 MeV the first minimum in $\sigma(\theta)$ does fill in by about 30%. However, at 14 and 15.43 MeV the effect on $A_y(\theta)$ is quite sizable around 40°, the angle near the first minimum in $\sigma(\theta)$. Figures 6.8 and 6.12 show the effect of using a variable radius r_R below 10 MeV in order to improve the description of σ_T and $\sigma(\theta)$ respectively. We settled upon the following simple energy dependent radius below 10 MeV:

$$r_R = 1.07 + 0.008 * E .$$

Clearly this energy dependent radius helped to improve the fit of σ_T and $\sigma(\theta)$ at low energies but we have no explanation for this phenomenological energy dependent radius. This dependence is much larger than one would normally attribute to dispersive corrections.

6.5 The Coupled Channels Calculation for n + ^{59}Co

For the coupled channels calculation of n + ^{59}Co we followed the same procedure we used in the case of n + ^{27}Al. We initiated the search using our preliminary DOM parameters. For the real central potential, geometry parameters, and deformation parameters we started with those of Pedroni *et al.* [Ped88] from their CCM work on ^{58}Ni and ^{60}Ni. We used in our search the same data base as in the ^{59}Co DOM of Chapter 5. The same procedure used in developing the CCM for ^{27}Al was used for ^{59}Co; that is, only coupling the ground state to itself via the reorientation matrix. Calculated $\sigma(\theta)$, $A_y(\theta)$ and σ_T were compared with experimental values qualitatively. The deformation parameter β_2 of ^{60}Ni was initially used and then optimized for ^{59}Co.

Table 6.2. The coupled channels model parameters for ^{59}Co + n.

$V(r,E) = V_R(E)\ f(r)$

$V_R(E) = 54.85 - 0.428 * E + 0.00224 * E^2$

$f(r) = [1+\exp((r-R_v)/a_v)]^{-1}$

$r_v = 1.165, \quad a_v = 0.630$

$\beta_2 = +0.21, \quad \beta_4 = 0.00, \quad R_i = r_i\ A^{1/3}$

$W_v(E) = a\,(E - E_F)^4 / [(E - E_F)^4 + b^4]$

$a = 8.612, \quad b = 52.589, \quad E_F = -8.980$

$W_s(E) = g\,(E - E_F)^4 \exp(-c\,(E - E_F)) / [(E - E_F)^4 + h^4]$

$g = 8.53, \quad h = 10.231, \quad c = 0.0108$

$r_s = 1.261, \quad a_s = 0.593$

$V_{so} = 6.200, \quad r_{so} = 1.017, \quad a_{so} = 0.600$

a) Potential depths are given in MeV and geometries in fm.

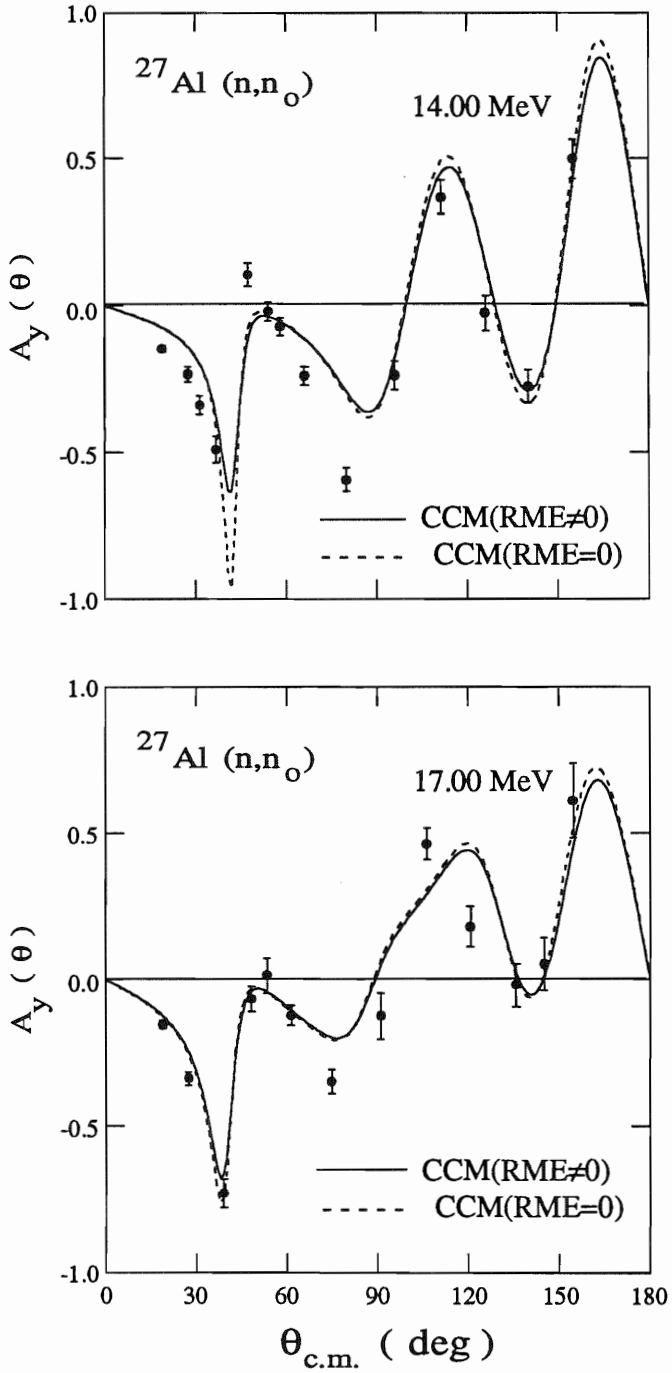

Figure 6.10. The impact of turning off the reorientation on $A_y(\theta)$ for ^{27}Al.

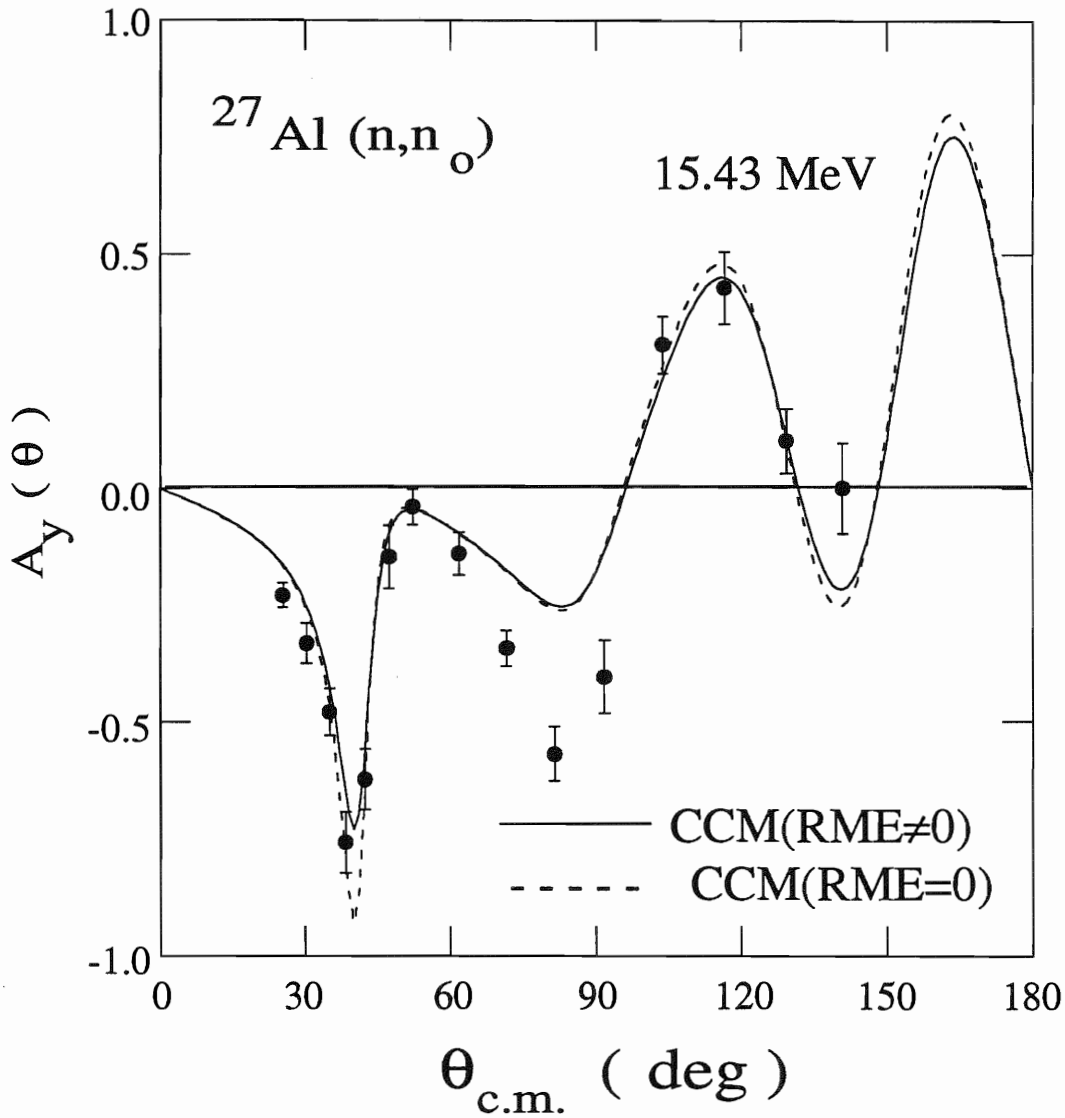

Figure 6.11. The impact of turning off the reorientation on $A_y(\theta)$ for ^{27}Al.

Only the real and imaginary central potentials were deformed. Table 6.2 summarizes our final set of parameters and Figure 6.13 shows a plot of these parameters. Note that in order to obtain a reasonable fit to the data, it was necessary to adopt a parabolic energy dependence for $V_R(E)$. For this nucleus the power of 4 was used for $W_V(E)$ and $W_S(E)$. For the spin-orbit potential we have the same parameters as those of Pedroni *et al.* [Ped88] except we use an energy-independent V_{so}. Figures 6.14 - 6.16 illustrates the CCM predictions of $\sigma(\theta)$. The CN nucleus contribution was added to these calculations below $E_n = 8$ MeV. The CCM gives a better prediction of $\sigma(\theta)$ data than the DOM. Note that the CCM gives a shallower minimum than the DOM in the vicinity of the first diffraction minimum away from 0°. Clearly the data favor this shallower minimum. Figure 6.17 shows the prediction of σ_T using CCM and DOM. Again the CCM gives a better prediction of the data. Following some sensitivity tests of σ_T to the strength of $V_R(E)$ a new relationship was produced in order to improve σ_T below 4 MeV. The following energy dependence for V_R was settled upon:

$$V'_R = 56.57 + 0.17 * E + 0.086 * E^2 - 0.23 * E^3 + 0.040 * E^4 .$$

This helped to improve σ_T below 4 MeV as shown in Figure 6.18. Figure 6.19 show the calculated $A_y(\theta)$ for the CCM compared to the DOM prediction, where although the CCM does a better job than the DOM at forward angles it overpredicts $A_y(\theta)$ between 45° - 60° and 75° - 105°. Figures 6.18, 6.20, and 6.21 show the effect of turning off the reorientation effect on σ_T, $\sigma(\theta)$, and $A_y(\theta)$, respectively, it produces deeper minima as the spherical DOM did for $\sigma(\theta)$. This sensitivity test shows the significance of the reorientation effect and its ability to produce the shallower minima evidenced in the data.

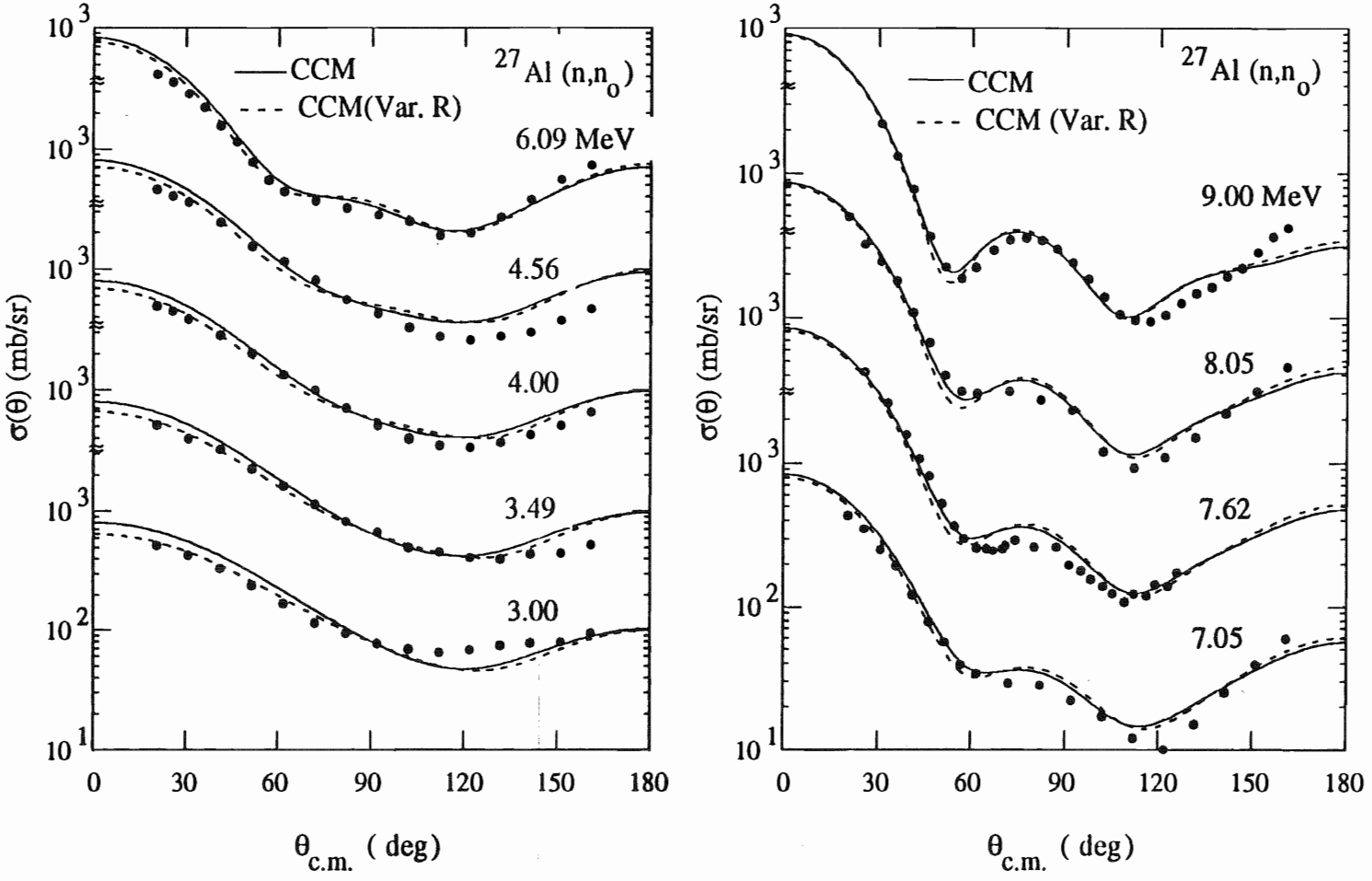

Figure 6.12. The effect of using a variable radius for E < 10 MeV on σ(θ) for ^{27}Al.

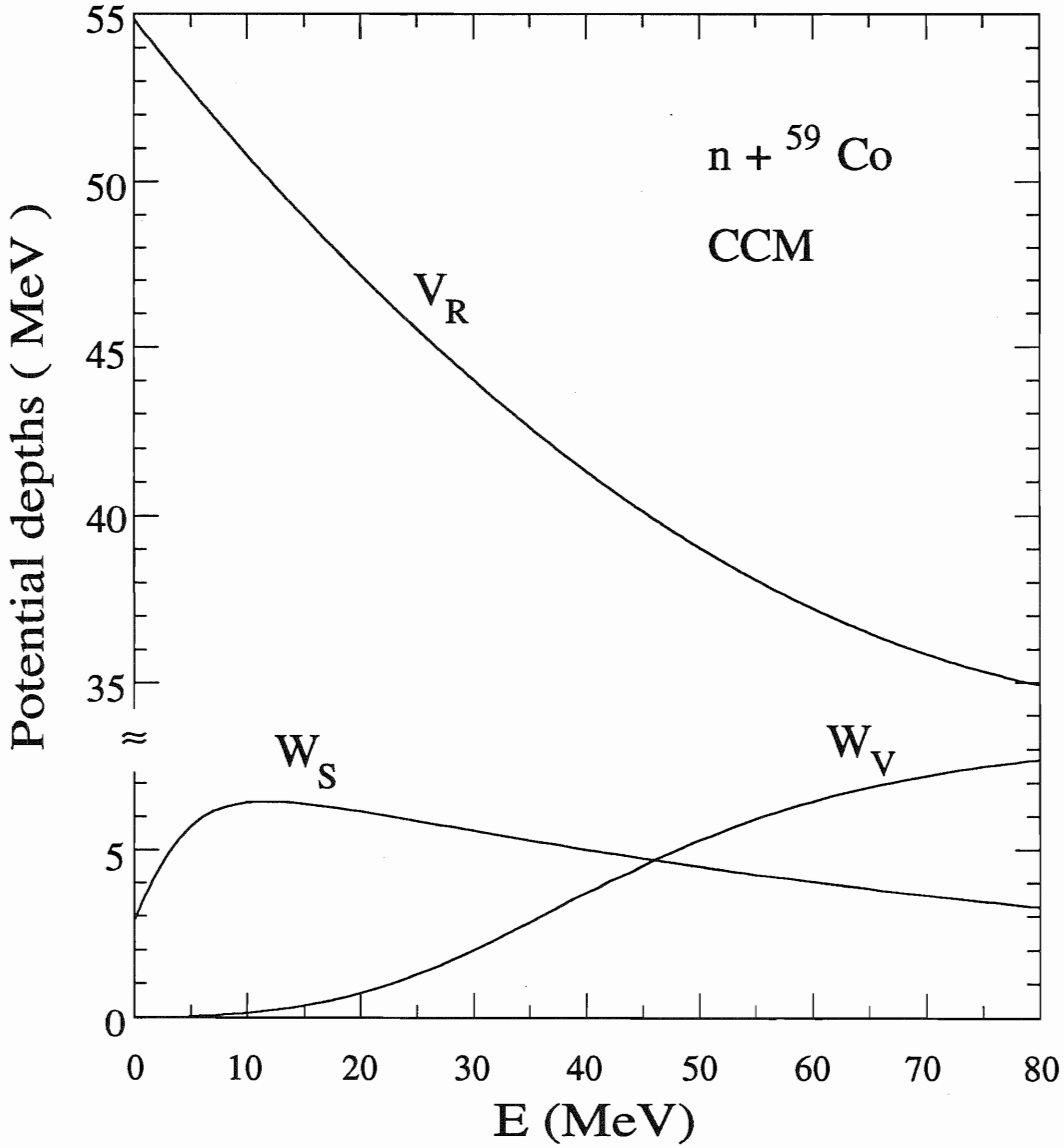

Figure 6.13. The CCM parameters for n + ^{59}Co .

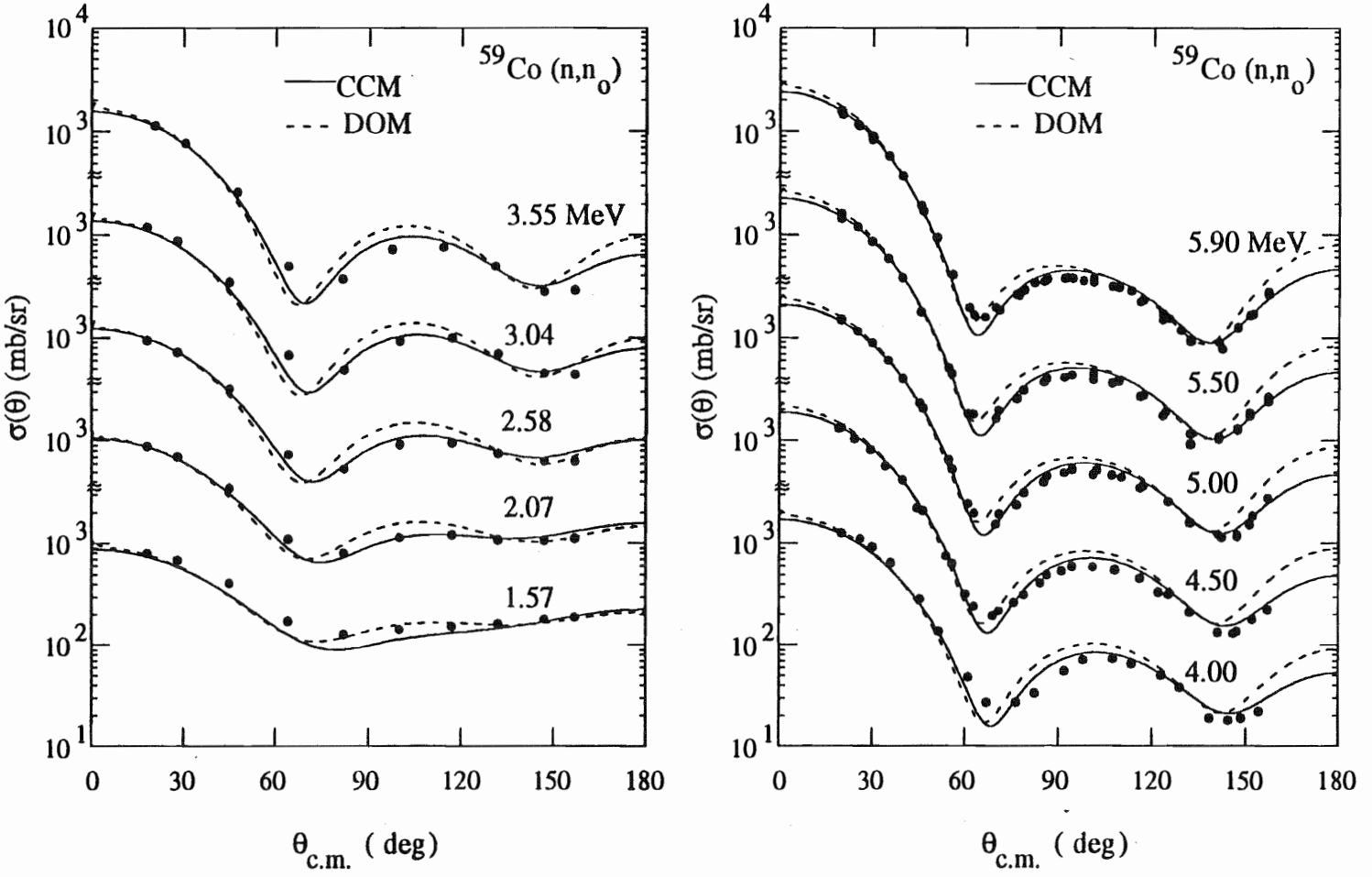

Figure 6.14. Coupled channels calculations of σ(θ) for ^{59}Co compared to data and to DOM calculations.

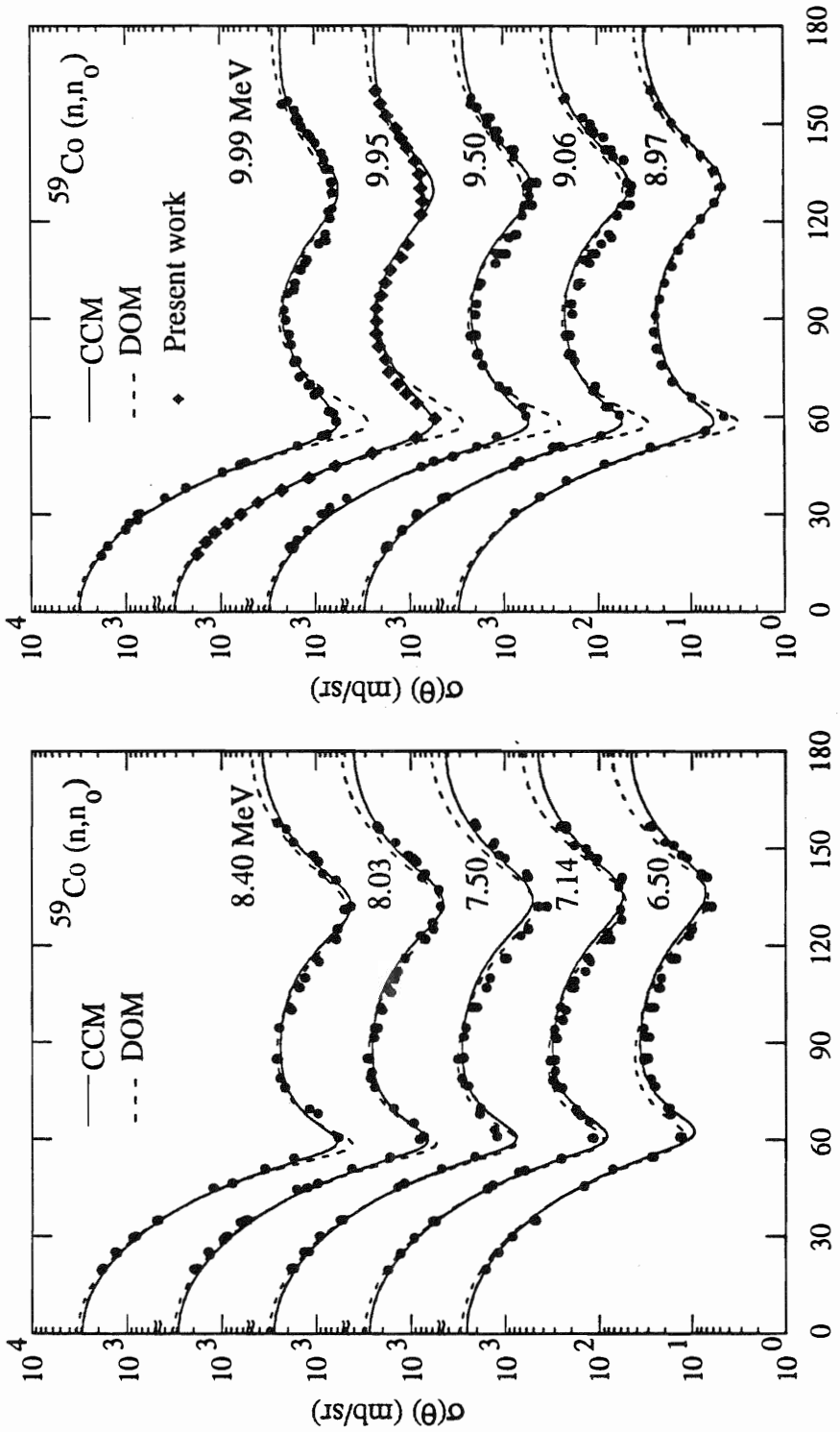

Figure 6.15. Coupled channels calculations of σ(θ) for ^{59}Co compared to data and to DOM calculations.

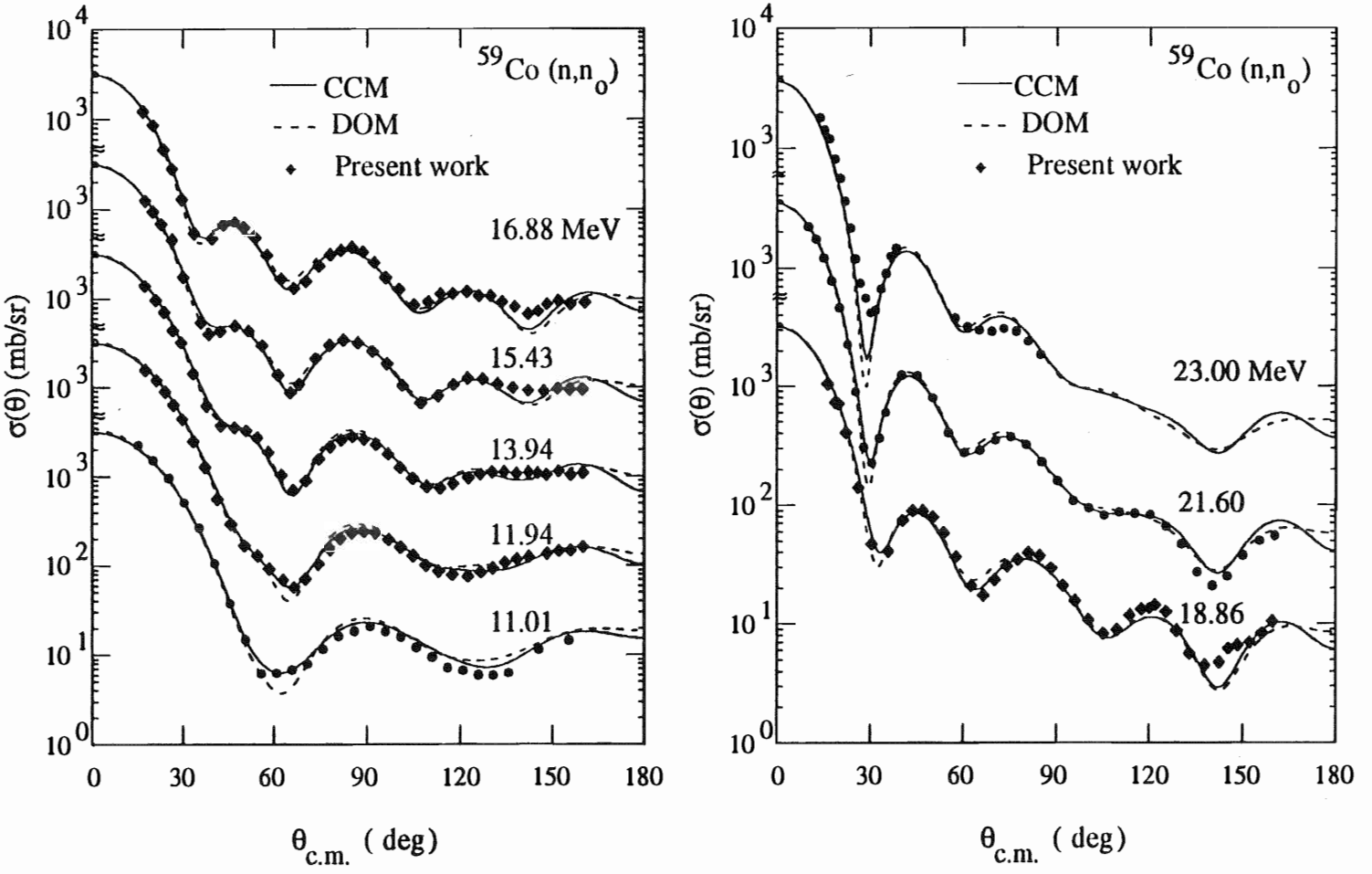

Figure 6.16. Coupled channels calculations of σ(θ) for ^{59}Co compared to data and to DOM calculations.

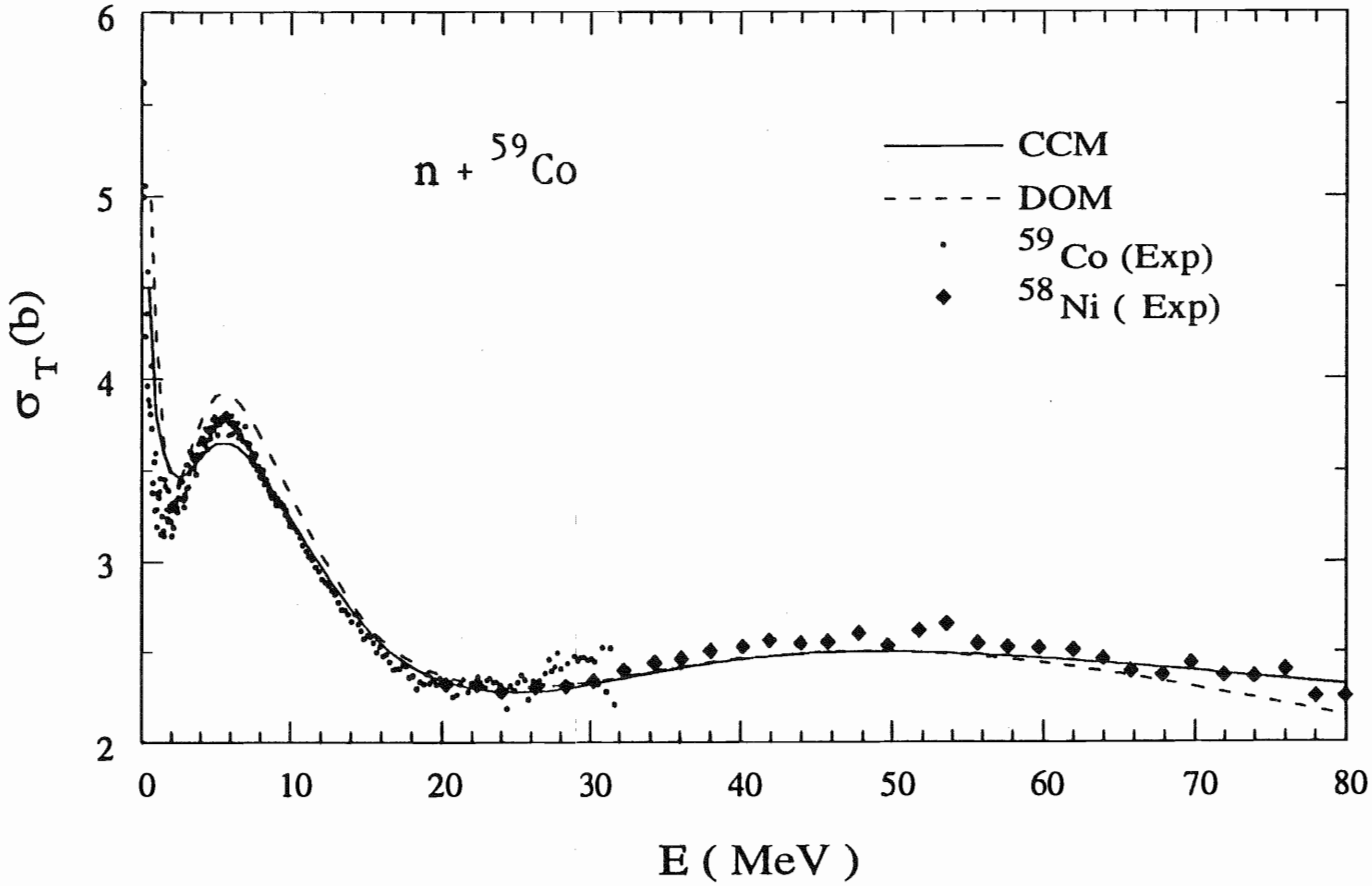

Figure 6.17. Coupled channels and DOM calculations of σ_T for ^{59}Co compared to data and to DOM calculations.

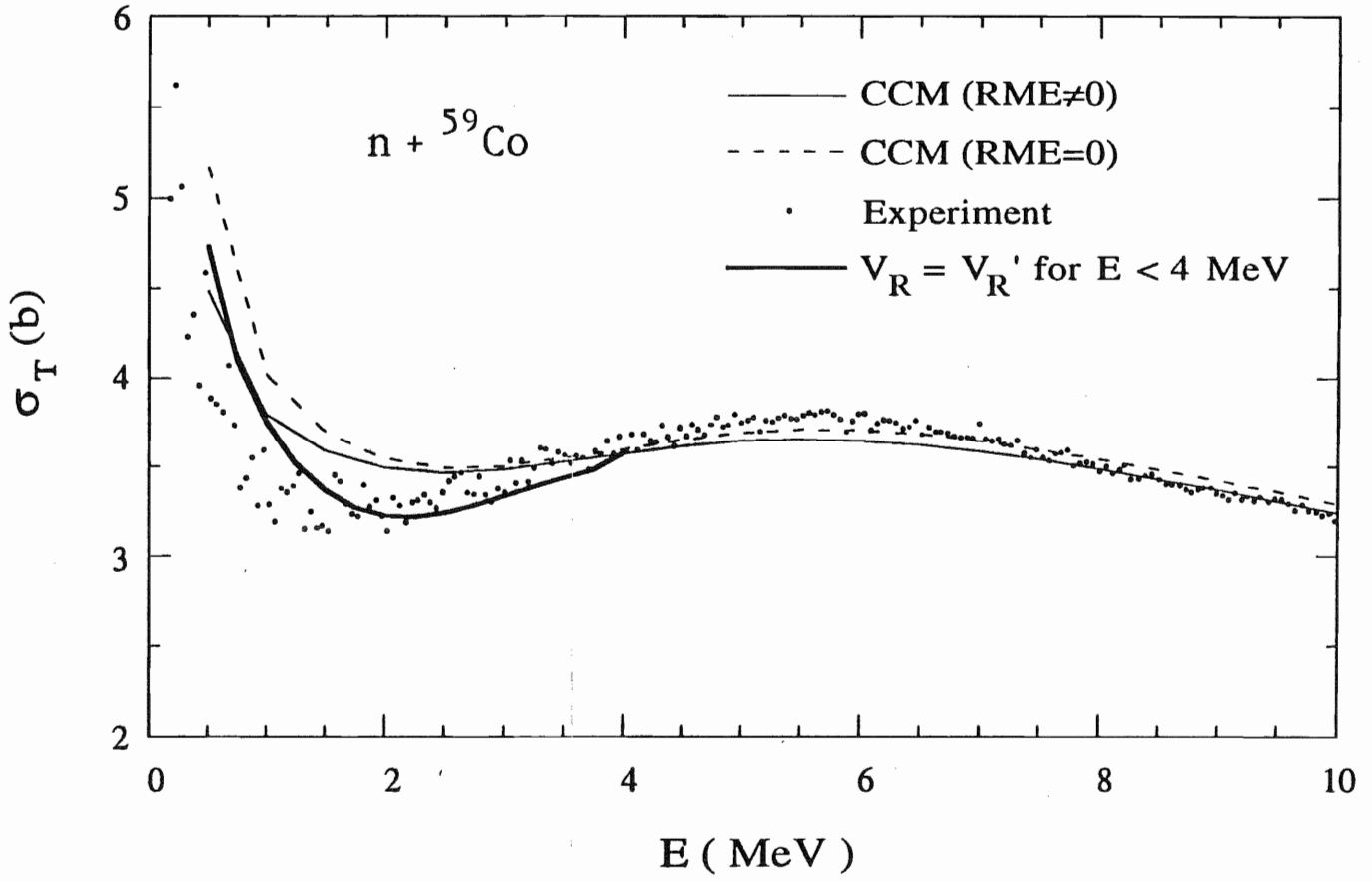

Figure 6.18. Coupled channels calculations of σ_T using V'_R for E< 4 MeV for ^{59}Co, the figure also shows the impact of turning off the reorientation.

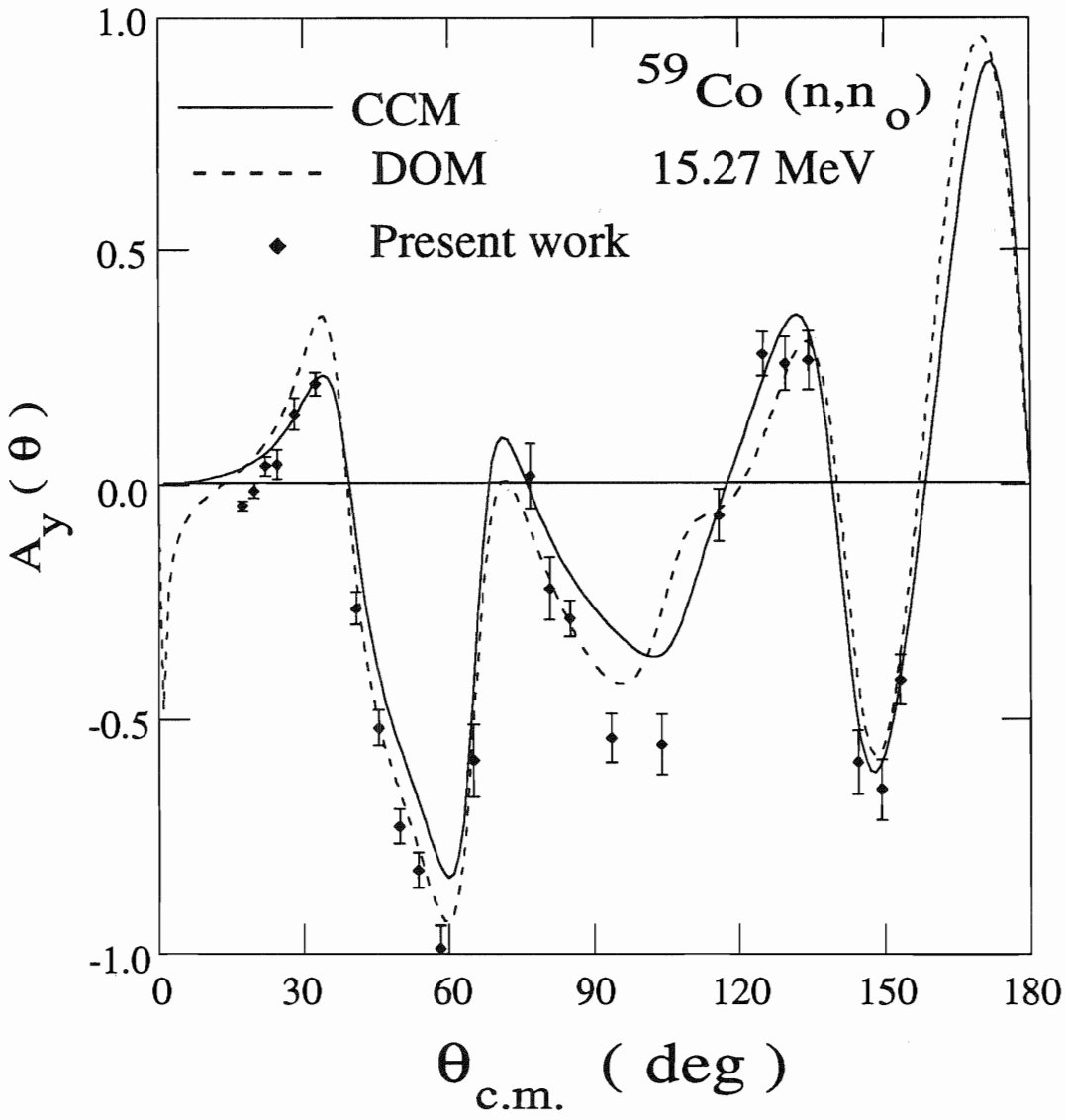

Figure 6.19. Coupled channels and DOM calculations of $A_y(\theta)$ for ^{59}Co compared to data and to DOM calculations.

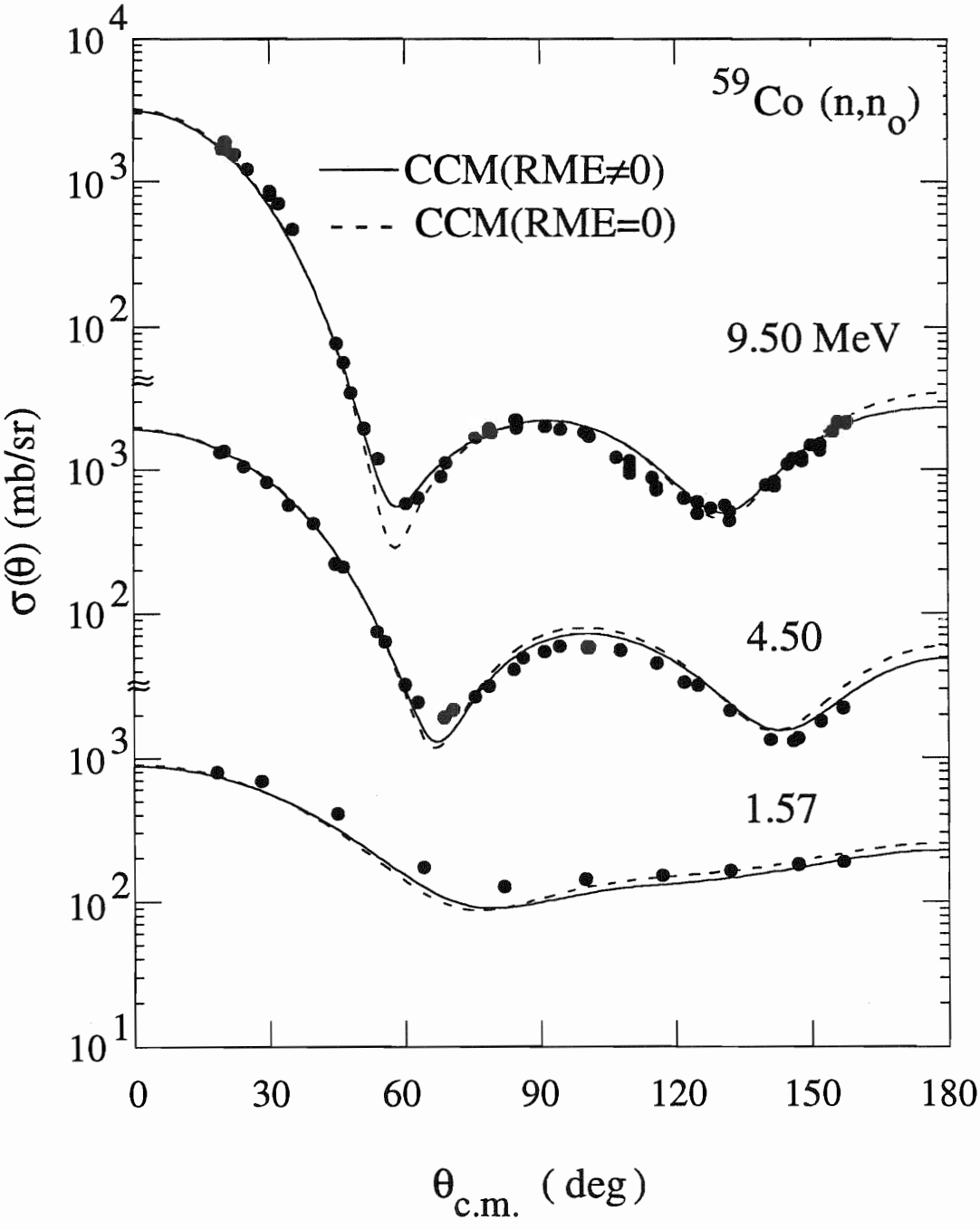

Figure 6.20. The impact of turning off the reorientation on σ(θ) for ^{59}Co.

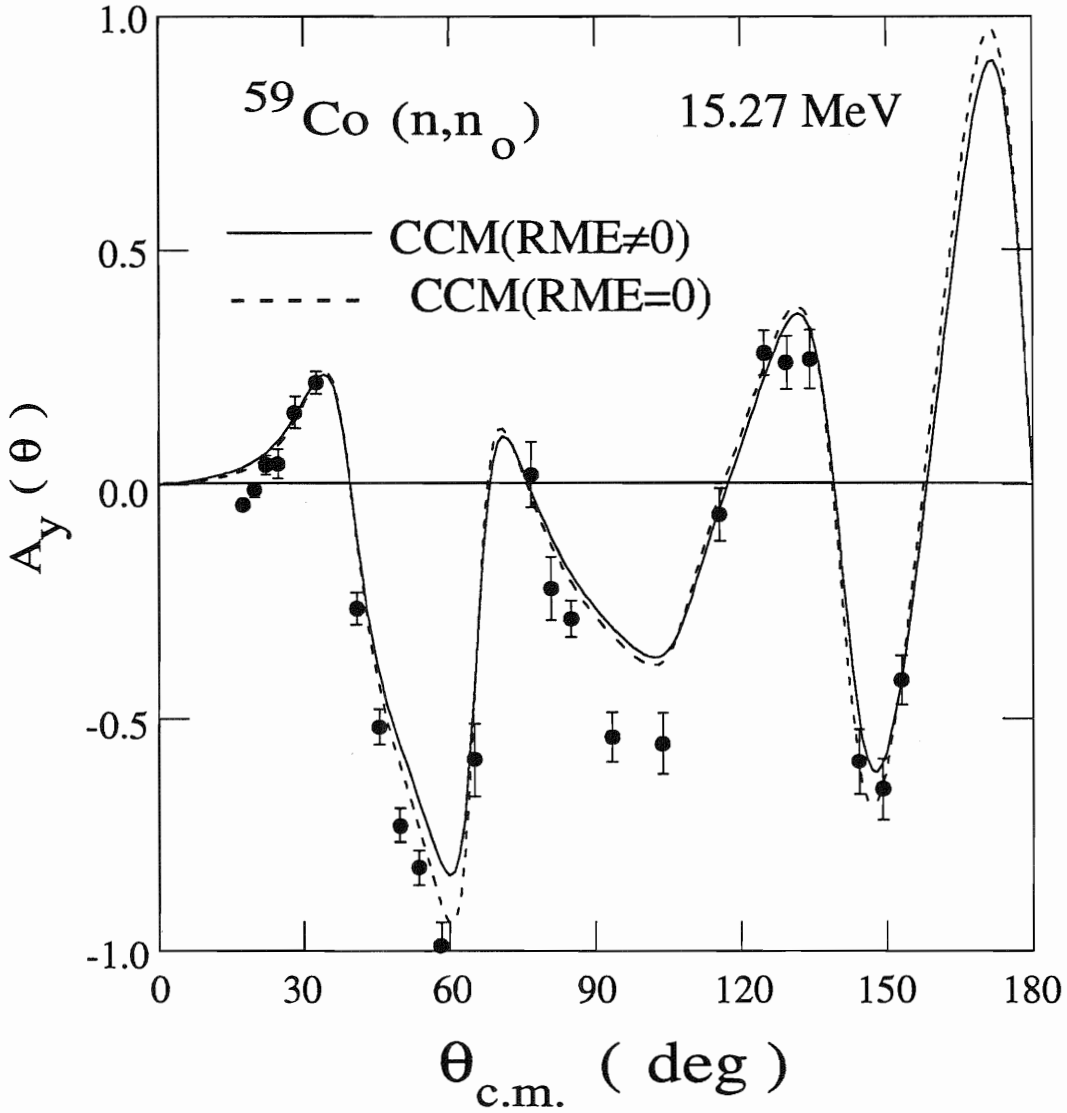

Figure 6.21. The effect of turning off the reorientation effect on A_y (θ) for ^{59}Co.

CHAPTER 7

SPIN-SPIN CROSS SECTION CALCULATIONS

7.1 Introduction

Since the introduction of the spin-spin term in the optical potential by Feshbach [Fes58] in 1958, many theoretical and experimental studies have been made to determine the properties of this term. Early theoretical studies described the spin-spin potential using a spherical and a nonspherical first-rank tensor terms. The interaction between a polarized nucleon and a polarized target can be approached either macroscopically or microscopically. In the macroscopic approach spin dependent terms are introduced in the optical model potential. These terms are a spherical term and a tensor term. The spherical term has the form

$$U_{10}(r) = -V_{10} f_{10}(r) \frac{\vec{\sigma} \cdot \vec{I}}{I} \qquad 7.1$$

where $\vec{\sigma}$ is the Pauli spin vector of the projectile, $\vec{I}$ is the spin of the target nucleus, V_{10} is the potential strength, and $f_{10}(r)$ is the radial form factor. The '10' notation follows the convention of Brink and Satchler [Bri71] for reduced matrix elements where '1' indicates the rank of the tensor and ' 0' corresponds to the order of the angular dependence of the Legendre polynomial. The tensor term has the form

$$U_{12}(r) = -V_{12}\ f_{12}(r) \frac{3(\vec{\sigma} \cdot \vec{r})(\vec{I} \cdot \vec{r}) - \vec{\sigma} \cdot \vec{I}}{2I}. \qquad 7.2$$

In the microscopic approach the initial and final nuclear states are represented by shell-model configurations, and the interaction between the projectile and the nucleus is described by a two-nucleon potential where the nucleus is assumed to be a

core of spin zero and an extra nucleus. The latter approach was used recently by McAbee [McA86]. The important finding of McAbee's work is that for nuclei with $I \geq 3/2$ the contribution of the higher tensor term U_{32}, which was usually neglected in the previous microscopic studies, is more than U_{12}. In his work McAbee considered nuclei with a core of zero spin and one extra valence nucleon. Theoretical studies predict a potential strength for the spin-spin spherical term of magnitude as high as 3 MeV [Nag70] to a potential strength as low as a few hundreds of keV's [Fis69]. For the tensor term the prediction of the potential strength is in the vicinity of 2 MeV [Hee77].

Experimentally many spin-spin studies were carried out using a wide spectrum of nuclei as targets. Most of these studies predict a spin-spin cross section which is consistent with zero except at low energies. However, the nuclei ^{165}Ho, ^{59}Co, ^{93}Nb, and ^{27}Al, show an appreciable spin-spin cross section at higher energies. Two different experimental methods were used to study the spin-spin interaction:

(*i*) measurements of the transmission of a beam of polarized neutrons through a polarized target using a transverse or longitudinal geometry (see Figure 7.1).

(*ii*) measurements of the depolarization of polarized nucleons scattered by un-polarized nuclei.

Transmission experiments are preferred over depolarization experiments because the extraction of a spin-spin term from depolarization measurements is complicated by other mechanisms, such as the quadrupole spin-flip and compound-elastic scattering. Transmission measurements for transverse and longitudinal geometries give the same magnitude for σ_{ss}; this indicates that the contribution of the tensor terms is small.

Many transmission experiments have been performed using ^{59}Co in the transverse and longitudinal geometries. Kobayashi *et al.* [Kob67] measured σ_{ss} at 7.9 ,

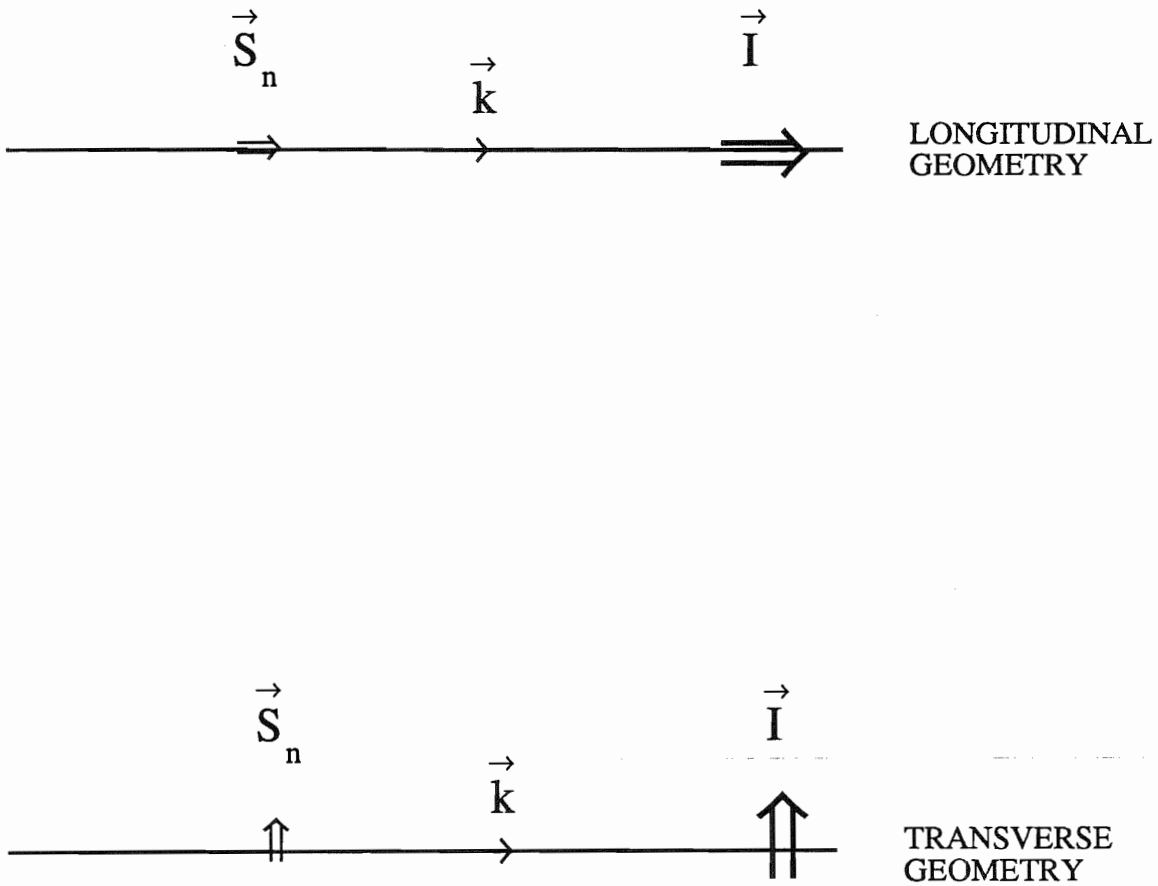

Figure 7.1. Longitudinal and transverse geometry for spin-spin cross section measurements. Here S_n represents the polarization orientation of the nucleon beam, k is the incident momentum and I is the spin orientation of the target nucleus.

MeV using a transverse geometry and predicted a spin-spin potential that has a real volume form and a strength of +1.75 MeV. Nagamine *et al.* [Nag70] measured σ_{ss} at 1.1 and 1.4 MeV using a transverse geometry and could only establish an upper limit on the potential strength V_{10} of 3.5 MeV(for a real, volume form). Fisher *et al.* [Fis72] measured σ_{ss} at E_n = 0.3 to 8.0 MeV using a longitudinal geometry predicting a potential strength V_{10} between -2.5 and 1.4 MeV(for a real, volume form). In 1976 and 1977 Heeringa *et al.* made measurements on ^{59}Co [Hee76, Hee77] using a transverse geometry between E_n = 0.39 to 7.88 MeV and E_n = 8.2 to 30.6 MeV the data were fitted using a surface spin-spin potential of -1.2 MeV in magnitude. Model predictions [Hee76, Hee77] for ^{59}Co σ_{ss} at low energy were much lower than the measured σ_{ss}. Thompson [Tho76] showed that the main reason why the models underpredicted σ_{ss} was because of the neglect of the compound nucleus spin-spin contribution.

In 1986 McAbee [McA86] undertook a careful theoretical analysis of the nuclear spin-spin potential. His model, which was based on a phenomenological folding model, allowed him to estimate the spin-spin cross section for ^{27}Al and ^{59}Co. Subsequently, Gould *et al.* [Gou86] measured the spin-spin cross section for (polarized) ^{27}Al using polarized neutrons of energies 5-17 MeV at TUNL. In order to fit the data they used a spin-spin potential that contained both a real and an imaginary volume term. In 1987 Hnizdo *et al.* [Hni87] attributed the spin-spin effects seen in the ^{27}Al data of Gould *et al.* to the effect of the static quadrupole moment of a polarized ^{27}Al on the total cross section for polarized neutrons. This was contested later by Gould *et al.* [Gou88] where they acknowledged the effect of the static deformation of ^{27}Al, but pointed out first that this quadrupole effect alone can not explain the measured σ_{ss} for ^{27}Al and secondly that this effect was taken into consideration in their

analysis by the imaginary term. Moreover, they pointed out that the quadrupole moment used by Hnizdo *et al.* was too large by a factor of two. More recently σ_{ss} for ^{27}Al was measured by Heeringa *et al.* [Hee89] between 20 and 50 MeV. Heeringa *et al.* developed a model to fit their data along with the Gould *et al.* data, but the model only required a real surface V_{ss} potential (a strength of 0.850 MeV).

Part of the problem that these authors faced was the lack of a suitable nucleon-nucleon potential designed specifically for the nucleus and energy range of interest. To approach this σ_{ss} study in a more logical way, one of the major goals of the present dissertation was to develop more complete and accurate models for neutron scattering for ^{27}Al and ^{59}Co. For both nuclei two models were developed; a dispersive optical model (DOM) and a coupled channels model (CCM). A real spin-spin potential of a surface form was added to each of these models, and the strength of this term was investigated by comparing predictions from these models to the spin-spin cross section data for ^{27}Al and ^{59}Co.

7.2 Spin-Spin Cross Section σ_{ss}

For a beam which is alternately polarized along the +z-direction (parallel to the target polarization $\uparrow\uparrow$) and -z-direction (antiparallel to the target polarization $\downarrow\uparrow$) Ohlsen [Ohl72] showed that

$$\sigma_{LR}^{\uparrow\uparrow}(\theta) = \sigma_o(\theta)\,[1 + P_p P_t\, C_{z,z}(\theta)] \qquad 7.3$$

and

$$\sigma_{LR}^{\uparrow\downarrow}(\theta) = \sigma_o(\theta)\,[1 - P_p P_t\, C_{z,z}(\theta)] \qquad 7.4$$

where $\sigma_{LR}(\theta)$ is the sum of the left and right cross sections at an angle θ, P_p is the projectile polarization and P_t is the target polarization. The term $C_{z,z}(\theta)$ is defined as follows:

$$C_{z,z} = \frac{Tr[M\sigma_z(p)\sigma_z(t)M^+]}{Tr(MM^+)} = \sigma_{ss}/\sigma_o \qquad 7.5$$

where M is the scattering Matrix, and $\sigma_z(p)$ and $\sigma_z(t)$ are the Pauli spin matrices for the projectile and the target, respectively. If expressions 7.3 and 7.4 are integrated over the solid angle and using eq. 7.5, we obtain for the total cross section:

$$\sigma^{\uparrow\uparrow} = \sigma_o + P_p P_t \sigma_{ss} \qquad 7.6$$

and

$$\sigma^{\uparrow\downarrow} = \sigma_o - P_p P_t \sigma_{ss} \quad . \qquad 7.7$$

So from 7.6 and 7.7

$$\sigma_{ss} = \frac{1}{2P_p P_t}(\sigma^{\uparrow\uparrow} - \sigma^{\uparrow\downarrow}) . \qquad 7.8$$

Experimentally what is measured in the lab are the yields $N^{\uparrow\uparrow}$ and $N^{\uparrow\downarrow}$ for the beam transmitted through the target. These are related to the total cross sections $\sigma^{\uparrow\uparrow}$ and $\sigma^{\uparrow\downarrow}$ as follows:

$$N^{\uparrow\uparrow} = N_0 \exp(-n_o \times \sigma^{\uparrow\uparrow}) \qquad 7.9$$

and

$$N^{\uparrow\downarrow} = N_0 \exp(-n_o \times \sigma^{\uparrow\downarrow}) \qquad 7.10$$

where N_0 is the count rate when the target is removed from the beam, n_o is the density of the target nuclei and x is the target thickness. Let the quantity ε be defined as

$$\varepsilon = \frac{N^{\uparrow\uparrow} - N^{\uparrow\downarrow}}{N^{\uparrow\uparrow} + N^{\uparrow\downarrow}} \quad . \qquad 7.11$$

Then from 7.9 and 7.10

$$\varepsilon = \frac{N_0 \exp(-n_o \times \sigma^{\uparrow\uparrow}) - N_0 \exp(-n_o \times \sigma^{\uparrow\downarrow})}{N_0 \exp(n_o \times \sigma^{\uparrow\uparrow}) + N_0 \exp(-n_o \times \sigma^{\uparrow\downarrow})} .$$

Using eqs. 7.6 and 7.7 for $\sigma^{\uparrow\uparrow}$ and $\sigma^{\uparrow\downarrow}$ we get

$$\varepsilon = \frac{\exp(-n_o \times \sigma_o - n_o \times P_p P_t \sigma_{ss}) - \exp(-n_o \times \sigma_o + n_o \times P_p P_t \sigma_{ss})}{\exp(-n_o \times \sigma_o - n_o \times P_p P_t \sigma_{ss}) + \exp(-n_o \times \sigma_o + n_o \times P_p P_t \sigma_{ss})}$$

$$= \tanh(-n_o \times P_p P_t \sigma_{ss}) \quad . \qquad 7.12$$

Since σ_{ss} is usually small, we obtain

$$\varepsilon = -n_o \times P_p P_t \sigma_{ss}$$

from which we get

$$\sigma_{ss} = -\frac{\varepsilon}{n_o \times P_p P_t} = -\frac{1}{n_o \times P_p P_t} \frac{N^{\uparrow\uparrow} - N^{\uparrow\downarrow}}{N^{\uparrow\uparrow} - N^{\uparrow\downarrow}} \quad . \qquad 7.13$$

This also could be rewritten as

$$\sigma_{ss} = -\frac{A_z}{n_o \times P_t} \quad .$$

The code ECIS was used to calculate the values of σ_{ss} using our DOM and CCM for ^{27}Al and ^{59}Co. To do this we assume a completely polarized beam and target. Then eq. 7.8 becomes

$$\sigma_{ss} = \frac{1}{2}(\sigma^{\uparrow\uparrow} - \sigma^{\uparrow\downarrow}) = \frac{1}{2}[\sigma_{tot}(-V-V_{ss}) - \sigma_{tot}(-V+V_{ss})] \quad . \qquad 7.14$$

So the problem is reduced to calculating the total cross section for the spin-up and the spin-down orientations. This simple way of calculating σ_{ss} does not include the effect of the spin-orbit coupling and the spin-spin tensor forces. However, McAbee *et al.* [McA86] have shown that the effect of these terms is small.

7.3 Calculation of σ_{ss} Using the DOM and CCM

From calculations of the spin-spin total cross section with both the DOM and CCM for ^{27}Al, we found that both give a qualitatively good description of the data except for the datum at 7.6 MeV. The results are compared to the data of Gould *et al.* [Gou86] and Heeringa *et al.* [Hee89] in Figure 7.2. It can be seen that except for the

datum at 7.6 MeV for both the coupled channels and dispersive optical model calculation, the data are qualitatively reproduced with a surface real term having V_{ss} = 0.80 MeV, r_{ss} = 1.0 fm, and a_{ss} = 0.654 fm and no imaginary W_{ss}. It is also interesting to see that the calculated spin-spin cross section starts to decrease around 3 MeV, and crosses through zero around 2 MeV; this behavior is similar to the behavior of ^{59}Co spin-spin cross section. This behavior would be a good motive for future spin-spin measurements between 0-7 MeV. Lastly our predictions are in good agreement with McAbee's folding model predictions shown in Figure 7.3.

For ^{59}Co the fit to the spin-spin data using the CCM and the DOM led to a spin-spin potential of the same strength and geometry as the ^{27}Al spin-spin potential, namely V_{ss} = 0.80 MeV, r_{ss} = 1.0 fm, and a_{ss} = 0.654 fm. Figure 7.4 shows the prediction of σ_{ss} using the CCM and DOM. The experimental data at low energy has a compound nucleus contribution which was calculated by Thompson [Tho76] to be

$$\langle \sigma_{ss}^{CE} \rangle = C \frac{I}{2I+1} [\langle \rho(I+\tfrac{1}{2}) \rangle - \langle \rho(I-\tfrac{1}{2}) \rangle]. \qquad 7.15$$

Here σ_{ss}^{CE} is the compound-elastic spin-spin cross section, I is the target spin, and ρ is the level density. Since the level density decreases with J, then from eq. 7.15 we can see that $\langle \sigma_{ss}^{CE} \rangle$ is negative. Actually Thompson calculated the average σ_{ss}^{CE} between 0.58-1.43 MeV to be -129 mb.

It is sometimes helpful to compare volume integrals for potentials of different models. We calculated the volume integral of the spin-spin potential from the standard equation for surface potentials :

$$J_{ss}/A = 16 \pi R_{ss}^2 \; V_{ss} \; a_{ss} \left(1 + \frac{1}{3} \left[\frac{\pi \; a_{ss}}{R_{ss}} \right]^2 \right) / A \quad .$$

Substituting V_{ss} = 0.80 MeV, r_{ss} = 1.00 fm, and a_{ss} = 0.654 fm, we get

$$J_{ss}/A = 26.30\,[\ A^{-1/3} + \frac{1.41}{A}\ ]\ .$$

Therefore, for ^{27}Al , J_{ss}/A = 10.14 MeV fm^3, which is in good agreement with the McAbee *et al.* [McA86] prediction of 8 MeV fm^3. For ^{59}Co we get J_{ss}/A = 7.35 MeV fm^3.

We also investigated turning off the reorientation effect on σ_{ss} for ^{27}Al (Figure 7.5) and ^{59}Co (Figure 7.6). It is surprising that although the effect on σ_T of setting RME = 0 is similar for ^{27}Al and ^{59}Co (see Figures 6.8 and 6.18) there is a high sensitivity of σ_{ss} to this term in the case of ^{27}Al, but not for ^{59}Co. The reason for this must be some type of delicate interference effect in these CCM calculations.

One interesting observation that we noticed while working on the description of σ_{ss} for ^{27}Al and ^{59}Co is that the spin-spin cross section had a close relation to the derivative of the total cross section with respect to energy. We created a polynomial fit to the σ_T data and took the energy derivative of this function. Figures 7.7 and 7.8 show curves that represent this derivative of the total cross section multiplied by a factor of -0.50 for the two nuclei ^{27}Al and ^{59}Co, respectively. The data are compared to the experimental spin-spin cross section. This multiplication factor is related to the slope of the real central potential. We extended this straight forward derivative comparison to ^{93}Nb and a similar behavior was observed where this time $d\sigma/dE$ need to be multiplied by a factor of -0.30. This is shown in Figure 7.9. The physics behind the discovery of this derivative relationship is not understood. Before we leave this point we mention that one way to look at this phenomenon was suggested by our colleague in this work, Dr. J. P. Delaroche. From the definition of σ_{ss} (eq. 7.14), we can write:

$$\sigma_{ss} = \frac{1}{2}(\sigma^{\uparrow\uparrow} - \sigma^{\uparrow\downarrow})$$

$$= \frac{1}{2}[\sigma_{tot}(-V-V_{ss}, -W_D-W_{D_{ss}}, -W_v-W_{v_{ss}}) - \sigma_{tot}(-V+V_{ss}, -W_D+W_{D_{ss}}, -W_v+W_{v_{ss}})].$$

$$= V_{ss}\frac{\partial\sigma_{tot}}{\partial V} + W_{D_{ss}}\frac{\partial\sigma_{tot}}{\partial W_D} + W_{v_{ss}}\frac{\partial\sigma_{tot}}{\partial W_v}$$

where we assumed (for argument sake) that V and V_{ss} have the same form of radial dependence. Now, since

$$\frac{\partial\sigma_{tot}}{\partial V} = \frac{\partial\sigma_{tot}}{\partial E}\frac{\partial E}{\partial V}$$

$$\frac{\partial\sigma_{tot}}{\partial W_D} = \frac{\partial\sigma_{tot}}{\partial E}\frac{\partial E}{\partial W_D}$$

$$\frac{\partial\sigma_{tot}}{\partial W_v} = \frac{\partial\sigma_{tot}}{\partial E}\frac{\partial E}{\partial W_v},$$

we obtain

$$\sigma_{ss} = \frac{\partial\sigma_{tot}}{\partial E}\left[V_{ss}\left(\frac{\partial V}{\partial E}\right)^{-1} + W_{D_{ss}}\left(\frac{\partial W_D}{\partial E}\right)^{-1} + W_{v_{ss}}\left(\frac{\partial W_v}{\partial E}\right)^{-1}\right]$$

From our nucleon-nucleus potential we can calculate $\frac{\partial V}{\partial E}$, $\frac{\partial W_D}{\partial E}$, and $\frac{\partial W_v}{\partial E}$. This is where we stop at this writing. This whole approach to σ_{ss} was only recognized a few weeks ago and we are attempting to develop the next steps to investigate the power of this approach. It is apparent that there is some physical significance to this derivative "rule". One importance of our finding is that it may prove to be a very useful tool in planning experiments to measure the spin-spin interaction strength at other energies or for other non-zero spin nuclei.

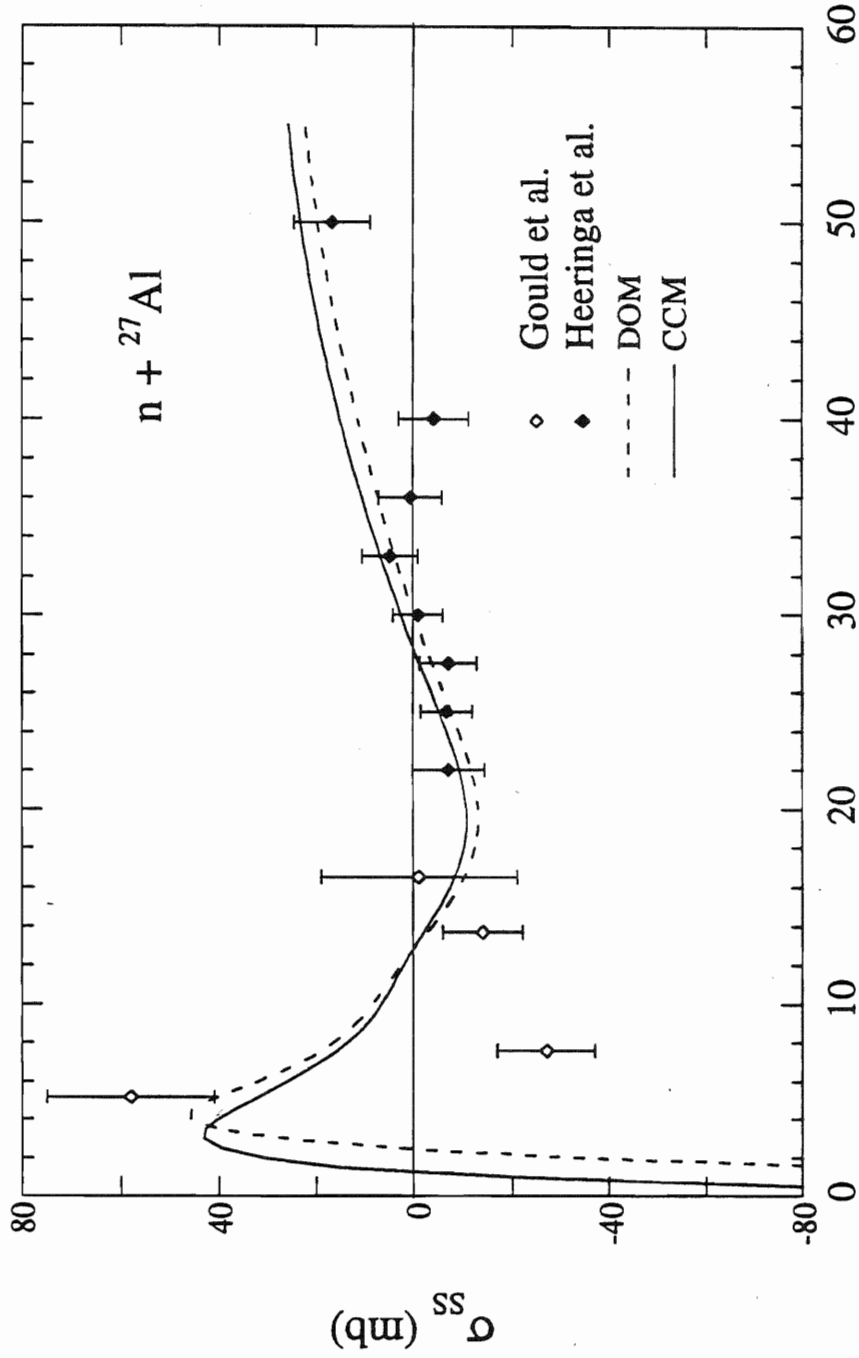

Figure 7.2. Spin-spin cross section calculations for ^{27}Al using the DOM and CCM.

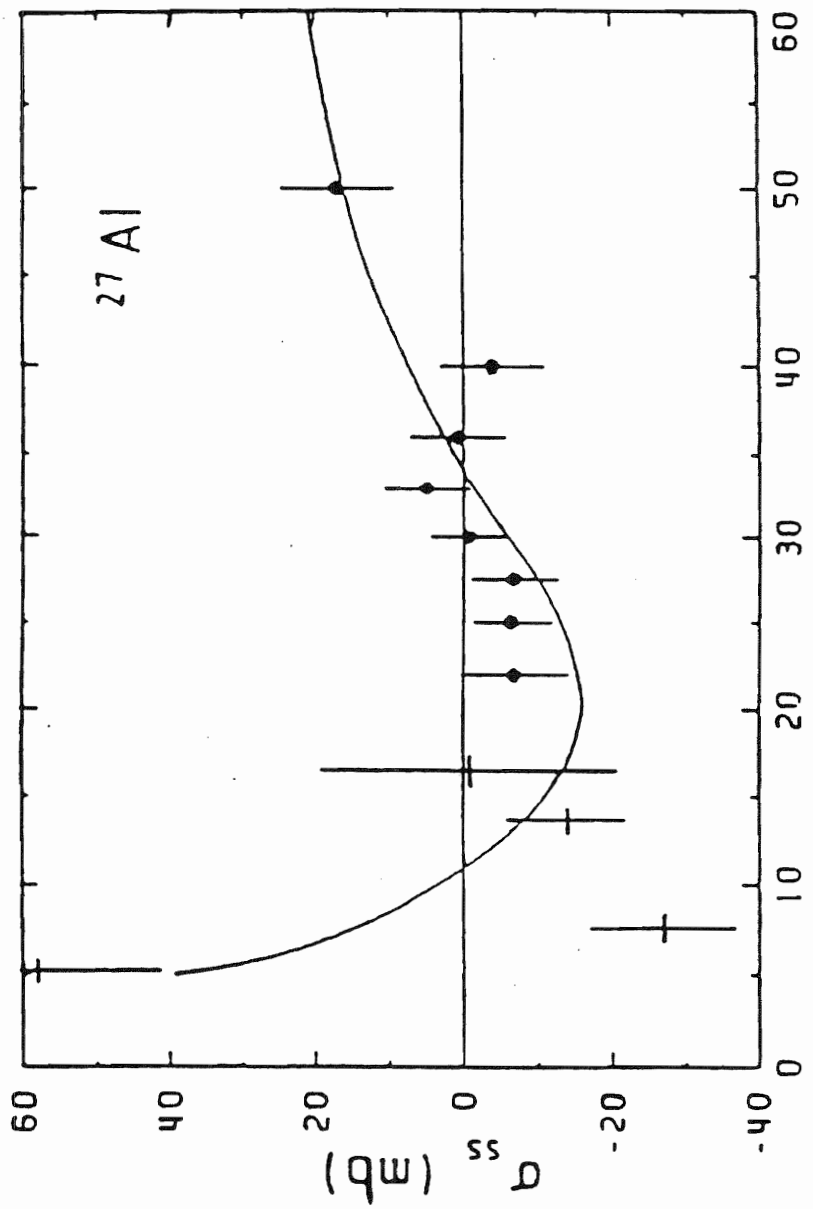

Figure 7.3. Comparisons of theoretical predictions of [McA86] with experimental σ_{ss}. Dots are for [Hee89] and crosses are for [Gou86].

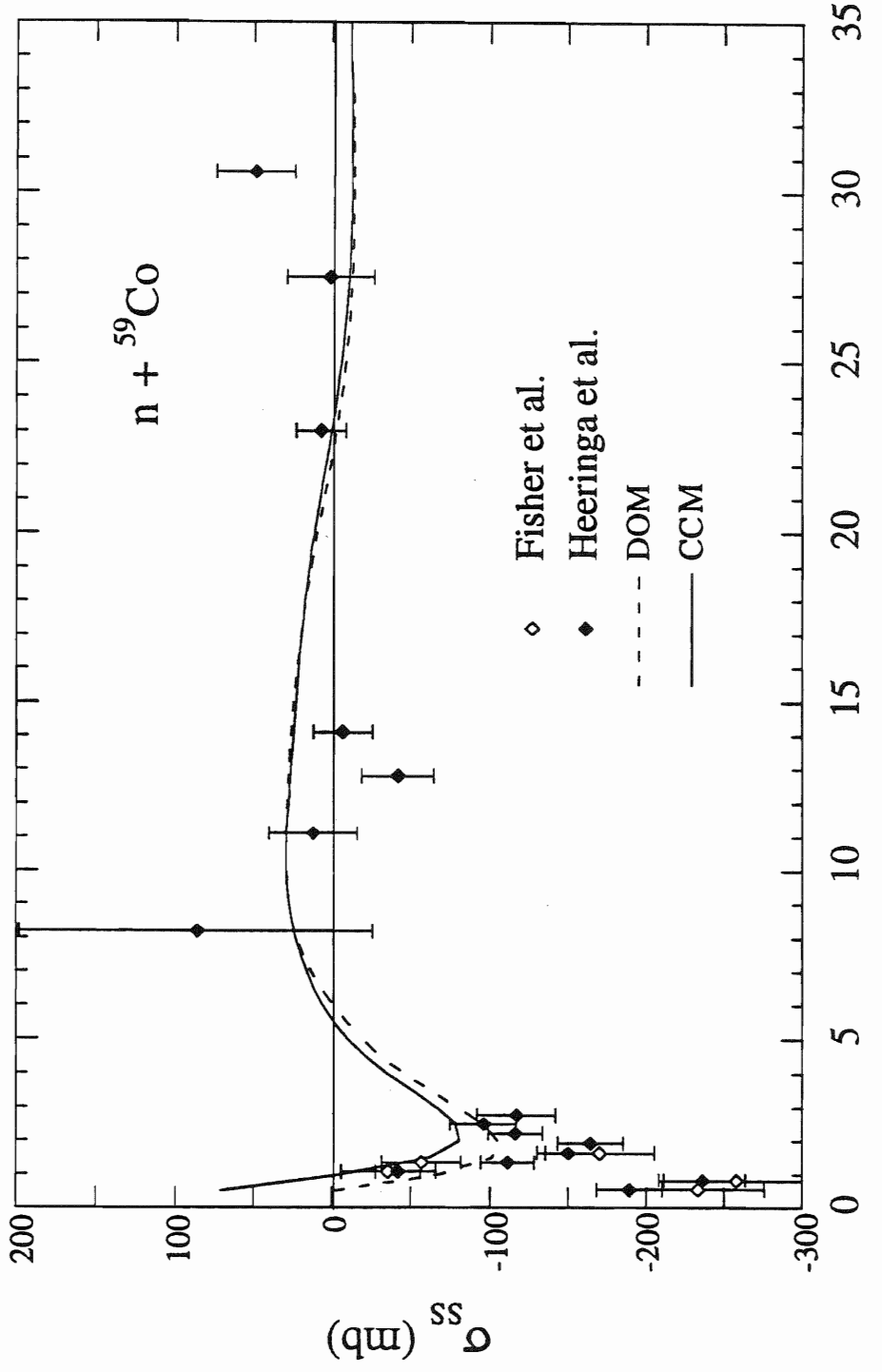

Figure 7.4. Spin-spin cross section calculations for ^{59}Co using the DOM and CCM.

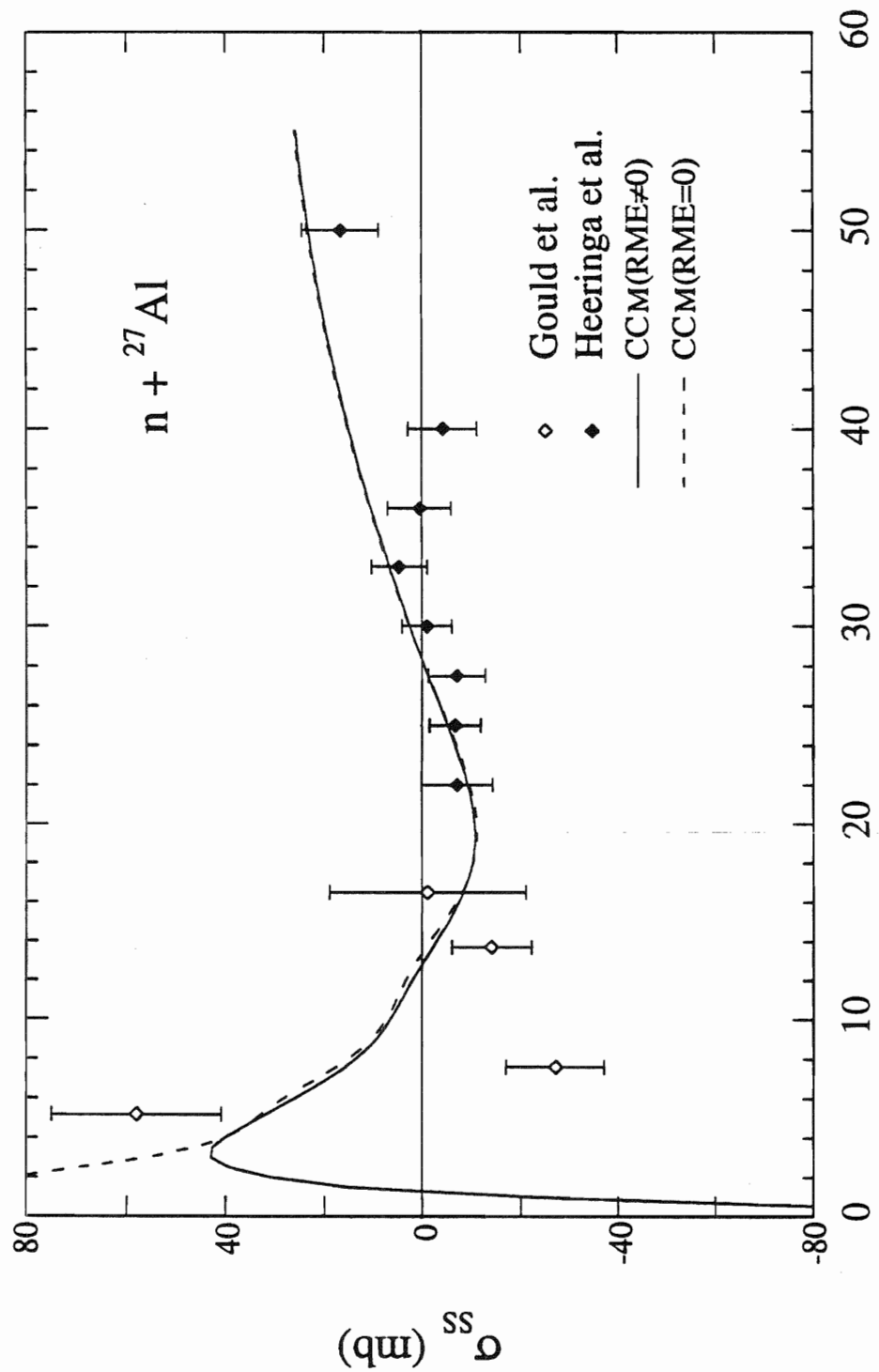

Figure 7.5. The effect of turning off the reorientation effect on σ_{ss} for ^{27}Al.

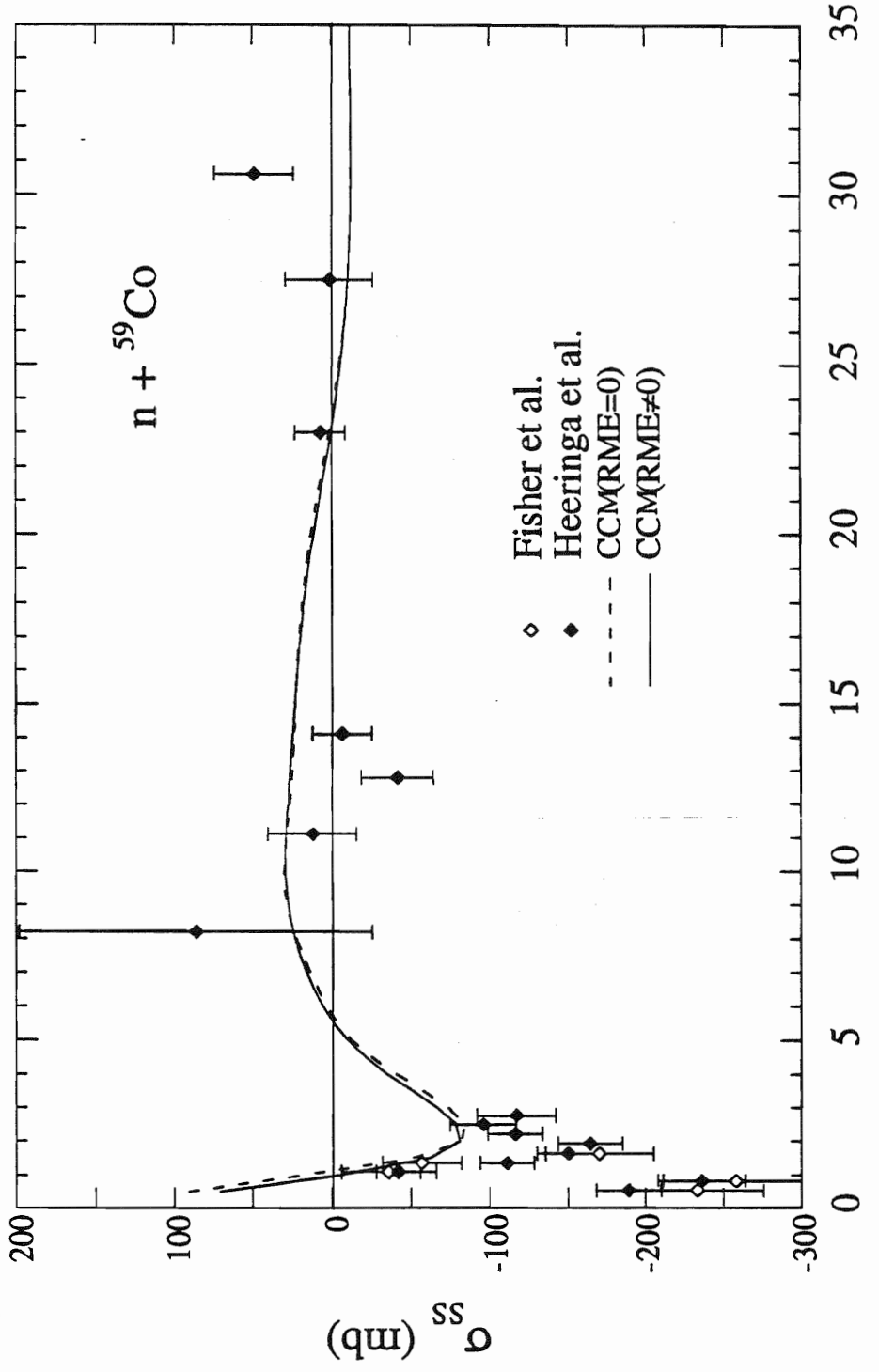

Figure 7.6. The effect of turning off the reorientation effect on σ_{ss} for ^{59}Co.

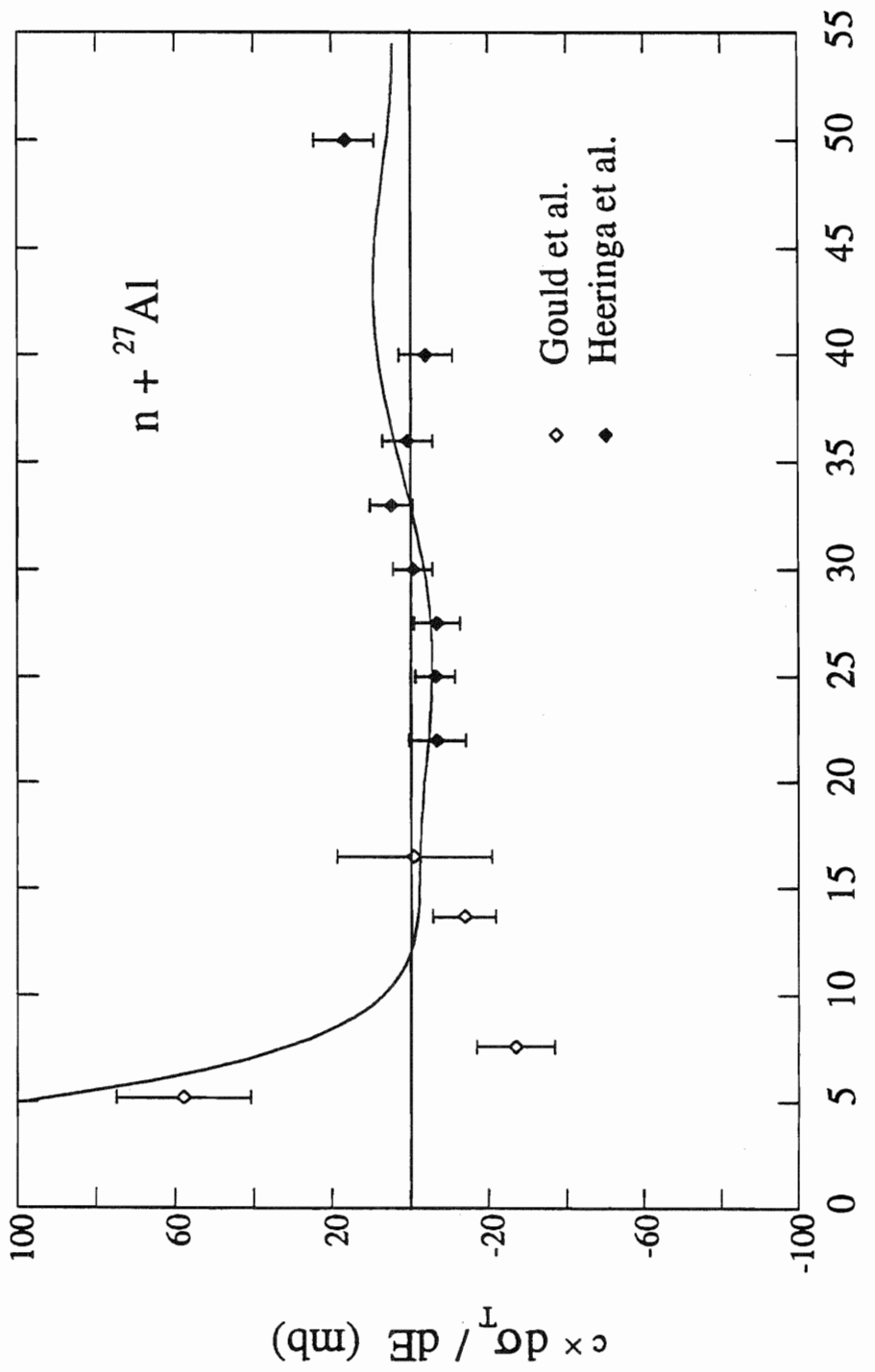

Figure 7.7. The derivative of the polynomial fit of the experimental total cross section for ^{27}Al compared with the experimental σ_{ss}.

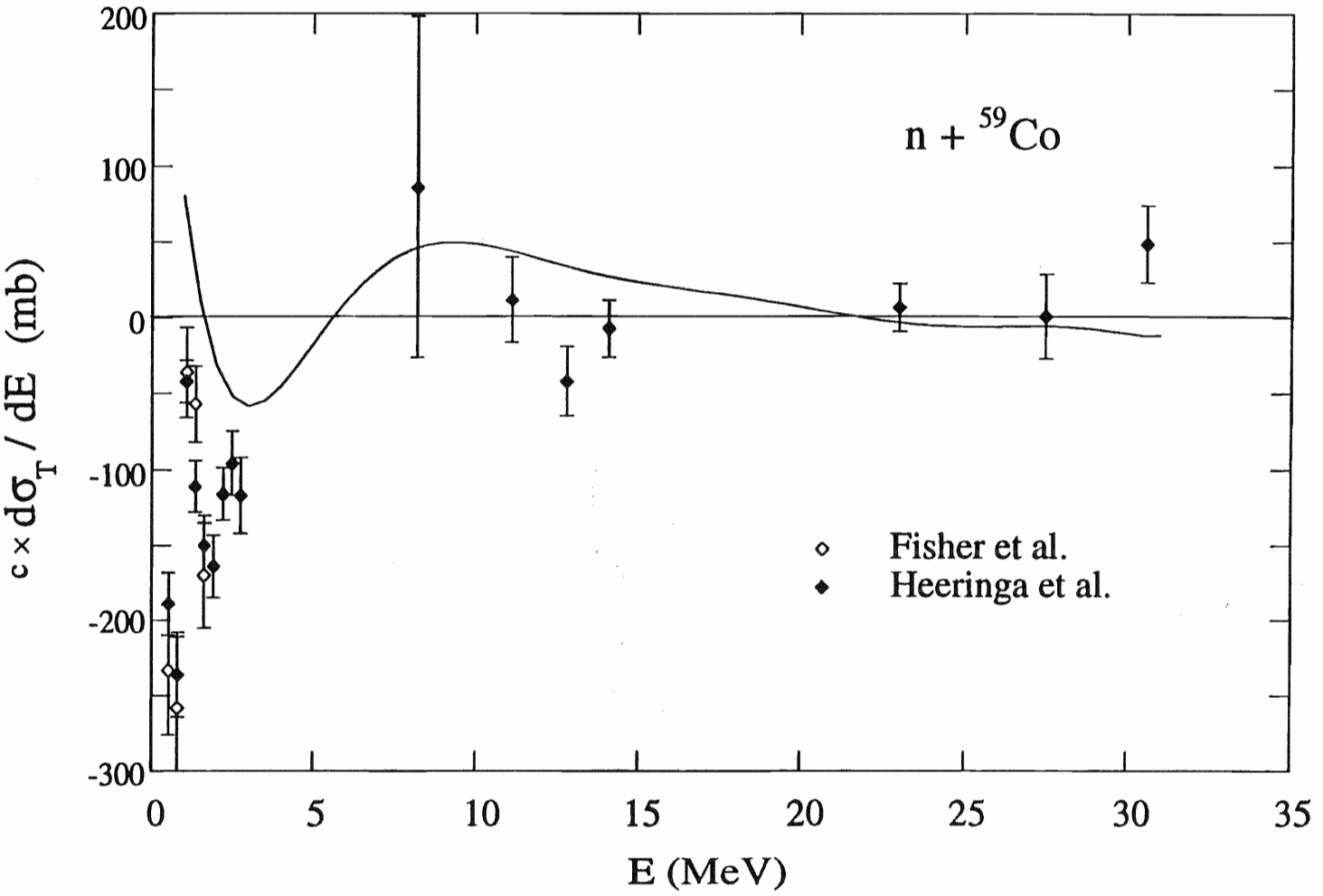

Figure 7.8. The derivative of the polynomial fit of the experimental total cross section for ^{59}Co compared with the experimental σ_{ss}.

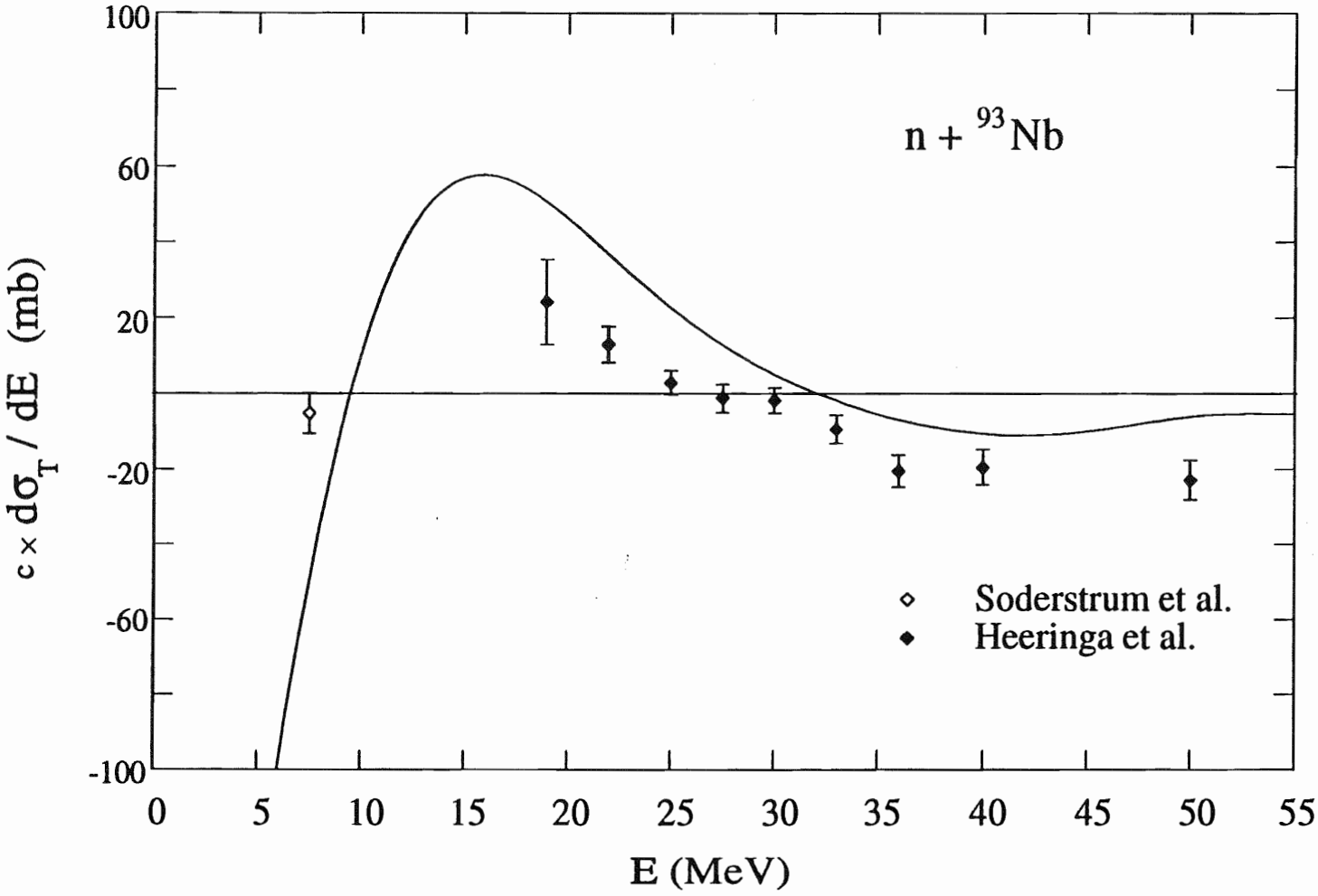

Figure 7.9. The derivative of the polynomial fit of the experimental total cross section for ^{93}Nb compared with the experimental σ_{ss}.

CHAPTER 8

SUMMARY AND CONCLUSIONS

Two main reasons motivated this study of the interaction of neutrons with the nuclei ^{27}Al and ^{59}Co. First was the need for a good nuclear model to describe measured data for the total and differential cross section and analyzing power for n + ^{27}Al and n + ^{59}Co in order to have a basis for interpreting the magnitude of the spin-spin cross section data. The second reason was to investigate the extension of the dispersion-relation optical model to deformed nuclei.

To accomplish these goals $\sigma(\theta)$ and $A_y(\theta)$ were measured for ^{27}Al and ^{59}Co at approximately 15.4 MeV. In addition, the $\sigma(\theta)$ was measured for ^{59}Co at 10, 12, 14, 17, and 19 MeV. Measurements were carried out using the time-of-flight facility at TUNL. Cross section measurements were conducted with a pulsed deuteron beam and the neutron source ^{2}H(d, n)^{3}He. Analyzing power measurements were done using a polarized deuteron beam produced by the new atomic beam polarized-ion source and the neutron source ^{2}H(d, n)^{3}He. The value of the neutron beam polarization was obtained using the calibration reaction ^{12}C(n, n).

Experimental data obtained for ^{27}Al and ^{59}Co were corrected for finite geometry, flux attenuation, and multiple scattering using the computer codes EFFIGY15 and JANE for $\sigma(\theta)$ and $A_y(\theta)$ corrections, respectively. The codes EFFIGY15 and JANE are basically Monte Carlo routines which simulate the experimental data. Our measurements for $\sigma(\theta)$ and $A_y(\theta)$ were consistent with the systematics of previously published data.

A large data base was compiled for ^{27}Al and ^{59}Co consisting of σ_T, $\sigma(\theta)$, and $A_y(\theta)$ over the energy range from about 0.5 to above 30 MeV. Adjustment for compound-nucleus contribution to $\sigma(\theta)$ below 11 MeV for ^{27}Al and below 8 MeV for ^{59}Co was done using the computer code OPSTAT.

Our corrected data base was then used to develop a dispersive optical model (DOM) for ^{27}Al and ^{59}Co. Although ^{27}Al and ^{59}Co are deformed nuclei and the DOM previously had been tested mainly for spherical nuclei, we did manage to describe the data quite well in general. However, there was a systematic problem describing σ_T below 10 MeV which we attribute to possible l-dependencies in the absorptive potential. For ^{27}Al the DOM model describes $\sigma(\theta)$ very well above 8 MeV except for a small discrepancy at the backward angles at 15.4, 18, and 26 MeV. However, below 8 MeV the model overestimates $\sigma(\theta)$ at forward angles by as much as 60%. For ^{27}Al the model describes the analyzing power data very well except between 65° - 90° where the model consistently overpredicted $A_y(\theta)$. Extending the DOM for ^{27}Al to the bound state region was successful in that it predicts the energy for the deeply bound 1s-state. For ^{59}Co we faced a similar problem fitting σ_T below 10 MeV; in addition, above 35 MeV the DOM slightly underestimates σ_T for the nearby nucleus ^{58}Ni which was compared due to lack of data for ^{59}Co in this region. For $\sigma(\theta)$ the DOM for ^{59}Co describes the data very well at all energies, except for a small discrepancy at the backward angles at 15.43, 16.88, and 18.86 MeV. Analyzing power data for ^{59}Co was generally well described by the DOM calculations except below 30° where the calculation underestimates the data. Extending the DOM for ^{59}Co to bound states was successful in that it does predict the energy of the deeply bound 1s-state. In general the DOM proved to be quite successful in describing these deformed nuclei except at energies below 8 MeV.

The failure of the DOM to describe the low energy data (below 8 MeV) led us to consider investigating the reorientation effect which is caused by the coupling of the ground state to itself. The CCM improved the description of the data for both ^{27}Al and ^{59}Co, although it did not completely eliminate the low energy σ_T problem for ^{27}Al and ^{59}Co.

One purpose of obtaining $A_y(\theta)$ data of this project was to sharpen our knowledge of the nucleon-nucleus spin-orbit interaction. Neither of the models (DOM or CCM) were able to give accurate fits to the data. In some angular regions the magnitudes of the data were overpredicted and in other regions underpredicted. Because there was no clear systematic trend, the spin-orbit parameters are still loosely defined. In particular, it was not possible to conclude whether the spin-orbit potential contains an imaginary component in the 10-20 MeV region where $A_y(\theta)$ exist. Searches with $W_{so} = 0$ and $W_{so} = 0.6$ MeV gave about the same χ^2 for the $A_y(\theta)$ data and both sets of calculations looked to give similar quality agreement. Therefore, we conclude that until the overall description of the data is improved with a new optical model parameterization, we are unable to limit the magnitude of W_{so} to a range smaller than $0 \leq W_{so} \leq 1.0$ MeV.

One of our main motivations for this work is to use our models to calculate the spin-spin cross section σ_{ss}. For ^{27}Al both of our models, DOM and CCM, give a qualitatively good description of the σ_{ss} data of Gould *et al.* [Gou86] and Heeringa *et al.* [Hee89] except for the datum at 7.6 MeV. This description was accomplished using a spin-spin real surface potential of +0.80 MeV and a geometry of $r_{ss} = 1.0$ fm and $a_{ss} = 0.654$ fm. For ^{59}Co we also obtained a good fit to the σ_{ss} data using both of our DOM and CCM, and surprisingly the same spin-spin potential parameters as used

for ^{27}Al. Our predictions do not reproduce the low energy data as well as the high energy because of compound-nucleus spin-spin contributions at low energy.

One interesting observation that we noticed while working on the description of σ_{ss} for ^{27}Al and ^{59}Co is that the reported spin-spin cross section values have a close relation to the derivative of the total cross section with respect to energy. To investigate this quantitatively, created a polynomial fit to the σ_T data and took the energy derivative of this function. We extended this approach to ^{93}Nb and a similar close behavior was observed. The discovery of this derivative relationship is not understood. It must be a consequence of the nature (strength, energy dependence, and form factor) of the U_{ss}. It is apparent that there is some physical significance to this derivative "rule". The practical importance of our finding might be that it may prove to be a very useful tool in planning the energy for conducting experiments to measure the strength of the spin-spin interaction at other energies or for other non-zero-spin nuclei.

Although the way we calculated the spin-spin cross section using the computer code ECIS is a good approximation for σ_{ss}, it is still important to incorporate the spin-spin interaction explicitly. This can be done with the computer code SPINSOR. We feel that aspects of the spin-spin cross section are not understood yet, like the low energy σ_{ss} for ^{27}Al and ^{93}Nb, as well as the derivative rule. Ultimately, the only way to resolve these issues fully will be to have more σ_{ss} data over a wide range of energies, but especially at low energy.

APPENDIX A

DIFFERENTIAL CROSS SECTION TABULATIONS

The differential cross section data in this appendix is tabulated and fitted using the computer code MACRO. The Legendre polynomials were used to fit the data according to the following equation:

$$\sigma(\theta, E) = \sum_{l=0} A_l(E)\, P_l(\cos\theta) = (\sigma_{int}/4\pi)\,[\alpha_0 + \sum_{l=1} (2l+1)\alpha_l(E) P_l(\cos\theta)]. \qquad A.1.$$

The parameters of this equation and the symbols used in the tables are defined as follows:

l-value	order of the Legendre polynomial in the expansion
A_l	the l th expansion coefficient of the Legendre polynomial expansion
ΔA_l	absolute uncertainty in $A_l(E)$
α_l	reduced expansion coefficients in ENDF/B-V form, defined to be: $\alpha_0 = 1$ $\alpha_l = A_l/A_0(2l+1)$
$\Delta\alpha_l$	absolute uncertainty in α_l
σ_{int}	integrated differential cross section over the 4π solid angle
θ_{lab}	experimental laboratory angle
$\sigma(\theta_{lab})$	normalized differential cross section as measured in the lab, before correction for multiple scattering, finite geometry, attenuation, and detector efficiency.
$\Delta\sigma_{lab}$	absolute error in $\sigma(\theta_{lab})$ which does not include uncertainties due to data normalization

$\sigma(\theta_{c.m.})$	corrected differential cross section in the center-of-mass. This cross section is corrected for multiple scattering, finite geometry, attenuation, and detector efficiency.
$\Delta\sigma_{c.m.}$	absolute error in the corrected cross sections which does not include uncertainties due to data normalization
%Dev.	percentage deviation of the calculated cross section from the experimental value
χ^2	the chi-square per point for the calculation at that angle
F-Test	integral probability $$P_F(F, \gamma_1, \gamma_2) = \int_F^\infty P_f(f, \gamma_1, \gamma_2)\, df$$ where γ_1 and γ_2 are the respective degrees of freedom
F-value or F_χ	$\frac{\chi^2_{n-1} - \chi^2_n}{\chi^2_n}(N - n - 1)$ where N is the number of data points, and n is the number of terms in the fit

The total cross section values for ^{27}Al and ^{59}Co are the averages over many data sources (see text for details). The calculated Wick's limit and its uncertainty are based on the used average total cross section. The zero degree cross sections are calculated from the fits to the data. The integrated differential cross sections σ_{int} is obtained by integrating the fits to the cross section data over 4π.

^{27}Al NEUTRON ELASTIC SCATTERING CROSS SECTIONS

Neutron Energy ± Energy Spread	15.431 ± 0.067 MeV
Excitation Energy J^{π}	0.000 MeV ($5/2^{+}$)
Total Cross Section	1.750 ± 0.035 barns
Integrated Cross Section	0.816 ± 0.007 barn
Calculated Wick's Limit	1392.62 ± 55.9 mb/sr
Zero Degree Cross Section	1345.29 ± 9.96 mb/sr
Normalization Uncertainty	3.00 %
Chi-square/degree-of-freedom	2.363

l-Value	A_l	ΔA_l	a_l	Δa_l	F-Value	F-Test
0	64.91	0.552	1.00000	0.00000	35.000	0.463
1	130.85	1.524	0.67193	0.00783	13.616	0.463
2	163.44	2.383	0.50357	0.00734	1.208	0.463
3	179.91	3.024	0.39594	0.00666	0.205	0.464
4	200.50	3.583	0.34318	0.00613	0.451	0.465
5	205.38	3.821	0.28763	0.00535	0.185	0.466
6	182.16	3.899	0.21586	0.00462	13.714	0.466
7	113.15	3.491	0.11621	0.00359	82.390	0.466
8	58.27	3.236	0.05280	0.00293	302.458	0.466
9	20.81	2.699	0.01687	0.00219	5.118	0.467
10	14.76	2.349	0.01082	0.00172	18.728	0.468
11	6.36	1.634	0.00426	0.00109	0.005	0.469
12	4.80	1.017	0.00296	0.00063	8.973	0.469

uncorrected			corrected			calculation		
θ_{lab}	$\sigma(\theta_{lab})$	$\Delta\sigma_{lab}$	$\theta_{c.m.}$	$\sigma(\theta_{c.m.})$	$\Delta\sigma_{c.m.}$	$\sigma(\theta_{c.m.})$	%Dev.	χ^2
18.0	469.18	4.44	18.5	633.96	11.47	640.80	-1.1	0.35
21.0	381.21	1.88	21.4	525.73	16.16	493.98	6.0	3.86
24.0	245.33	2.15	24.2	345.71	6.81	362.89	-5.0	6.36
27.0	193.10	0.79	27.0	279.66	10.29	252.56	9.7	6.93
30.0	110.25	2.14	29.9	165.33	6.81	165.07	0.2	0.00
33.0	64.32	0.80	32.7	99.44	4.33	99.83	-0.4	0.01
36.0	34.57	0.84	35.7	51.17	2.26	53.76	-5.1	1.31
39.0	23.28	0.79	39.3	26.80	1.27	24.80	7.4	2.48
42.0	18.02	0.20	43.6	16.67	0.47	16.67	0.0	0.00
45.0	19.00	0.66	47.4	22.68	1.28	24.61	-8.5	2.25
48.0	25.39	0.88	50.5	33.54	1.76	35.81	-6.8	1.68
52.0	38.27	0.53	54.3	51.34	1.13	50.22	2.2	0.98
56.0	47.46	0.99	58.1	63.69	1.41	61.23	3.9	3.01
60.0	48.07	0.93	61.9	64.75	1.32	66.45	-2.6	1.67
65.0	47.87	1.53	66.7	64.71	2.24	63.81	1.4	0.16
70.0	40.18	0.88	71.5	54.46	1.60	53.08	2.5	0.74
75.0	26.06	0.95	76.4	35.09	1.44	38.91	-10.9	7.06
80.0	20.42	0.45	81.4	26.88	0.79	26.12	2.8	0.92
85.0	13.94	0.19	86.6	17.66	0.32	17.70	-0.2	0.02
90.0	11.47	0.24	91.8	14.23	0.34	14.02	1.5	0.38
95.0	10.53	0.20	97.0	13.37	0.29	13.39	-0.2	0.01

100.0	10.52	0.09	102.0	13.76	0.14	13.85	-0.6	0.40
105.0	11.06	0.21	106.9	14.76	0.31	14.38	2.5	1.47
110.0	11.06	0.43	111.8	14.96	0.64	14.66	2.0	0.21
115.0	10.56	0.42	116.7	14.39	0.63	14.54	-1.0	0.06
120.0	9.93	0.32	121.6	13.53	0.47	13.99	-3.4	0.96
125.0	9.83	0.19	126.5	13.34	0.29	13.18	1.3	0.33
130.0	9.06	0.10	131.4	12.33	0.15	12.41	-0.7	0.30
135.0	9.17	0.22	136.2	12.58	0.35	11.81	6.1	4.99
140.0	7.73	0.18	141.0	10.66	0.28	11.10	-4.1	2.39
145.0	7.35	0.08	145.8	10.00	0.16	9.90	1.0	0.42
150.0	6.19	0.14	150.6	8.12	0.21	8.37	-3.0	1.34
154.0	6.16	0.14	154.6	7.84	0.20	7.69	2.0	0.56
155.0	6.09	0.14	155.7	7.75	0.23	7.73	0.3	0.01
160.0	7.48	0.10	160.7	9.91	0.15	9.93	-0.2	0.02

^{59}Co NEUTRON ELASTIC SCATTERING CROSS SECTIONS

Neutron Energy ± Energy Spread	9.953 ± 0.083 MeV
Excitation Energy J^{π}	0.000 MeV ($7/2^-$)
Total Cross Section	3.210 ± 0.066 barns
Integrated Cross Section	1.778 ± 0.019 barn
Calculated Wick's Limit	3081.39 ± 126.7 mb/sr
Zero Degree Cross Section	3202.99 ± 25.53 mb/sr
Normalization Uncertainty	3.00 %
Chi-square/degree-of-freedom	0.630

l-Value	A_l	ΔA_l	a_l	Δa_l	F-Value	F-Test
0	141.48	1.501	1.00000	0.00000	37.000	0.463
1	354.94	4.243	0.83623	0.01000	0.947	0.463
2	507.74	6.611	0.71774	0.00935	0.012	0.463
3	563.81	8.188	0.56928	0.00827	1.158	0.463
4	545.44	9.505	0.42834	0.00746	12.087	0.463
5	429.79	9.862	0.27616	0.00634	20.422	0.464
6	299.87	10.201	0.16304	0.00555	29.709	0.465
7	187.37	9.219	0.08829	0.00434	37.117	0.466
8	101.78	8.424	0.04232	0.00350	92.080	0.466
9	47.20	6.255	0.01756	0.00233	124.047	0.466
10	16.47	4.897	0.00554	0.00165	25.388	0.466
11	6.50	2.639	0.00200	0.00081	20.582	0.467
12	0.59	1.762	0.00017	0.00050	0.192	0.468

uncorrected			corrected			calculation		
θ_{lab}	$\sigma(\theta_{lab})$	$\Delta\sigma_{lab}$	$\theta_{c.m.}$	$\sigma(\theta_{c.m.})$	$\Delta\sigma_{c.m.}$	$\sigma(\theta_{c.m.})$	%Dev.	χ^2
18.0	794.08	7.80	17.9	1790.48	37.64	1835.86	-2.5	1.45
22.0	643.01	6.42	21.6	1446.95	35.78	1414.12	2.3	0.84
25.0	519.22	5.28	24.4	1155.51	33.06	1118.39	3.2	1.26
28.0	390.84	4.00	27.2	861.33	26.53	855.15	0.7	0.05
31.0	283.62	2.61	30.1	619.01	17.81	631.09	-2.0	0.46
35.0	192.88	1.72	33.8	408.37	14.35	396.57	2.9	0.68
39.0	115.64	1.11	37.6	227.88	8.99	230.99	-1.4	0.12
43.0	65.35	0.87	41.3	117.50	5.29	123.34	-5.0	1.22
47.0	38.52	0.81	45.1	61.31	4.07	59.51	2.9	0.20
51.0	21.17	0.36	49.1	25.09	1.80	24.59	2.0	0.08
55.0	13.18	0.35	53.9	8.57	1.05	8.21	4.2	0.12
59.0	8.93	0.19	59.6	5.42	0.57	5.67	-4.6	0.19
63.0	7.95	0.23	64.2	8.42	0.79	8.47	-0.6	0.00
66.0	7.95	0.22	67.2	10.84	0.74	10.86	-0.2	0.00
69.0	8.58	0.18	70.0	13.46	0.61	13.22	1.8	0.15
73.0	9.49	0.17	73.8	16.65	0.52	16.18	2.8	0.80
77.0	9.81	0.18	77.7	17.82	0.55	18.76	-5.3	2.95
81.0	11.36	0.19	81.5	20.94	0.59	20.74	0.9	0.11
85.0	11.98	0.20	85.4	22.39	0.60	21.99	1.8	0.43
89.0	11.97	0.21	89.3	22.19	0.63	22.38	-0.9	0.09

93.0	11.99	0.21	93.2	22.19	0.64	21.82	1.7	0.35
97.0	10.86	0.20	97.1	19.89	0.59	20.31	-2.1	0.51
101.0	9.91	0.19	101.0	17.88	0.56	18.06	-1.0	0.10
105.0	9.09	0.15	104.9	15.93	0.53	15.35	3.7	1.22
109.0	7.32	0.13	108.8	12.31	0.40	12.61	-2.5	0.57
113.0	6.57	0.18	112.8	10.47	0.50	10.27	1.9	0.15
122.0	5.10	0.16	122.0	7.55	0.43	7.53	0.2	0.00
126.0	4.83	0.15	126.2	7.21	0.42	7.31	-1.4	0.06
130.0	4.93	0.15	130.3	7.56	0.42	7.44	1.6	0.09
134.0	5.06	0.16	134.4	7.82	0.43	7.88	-0.8	0.02
138.0	5.49	0.18	138.5	8.70	0.49	8.78	-0.9	0.03
142.0	6.42	0.19	142.6	10.58	0.53	10.37	2.0	0.16
145.0	7.10	0.20	145.6	12.08	0.56	12.06	0.2	0.00
148.0	7.86	0.21	148.5	13.79	0.61	14.12	-2.4	0.28
152.0	9.57	0.20	152.4	17.31	0.61	17.14	1.0	0.08
156.0	10.93	0.21	156.2	20.11	0.62	20.11	0.0	0.00
160.0	12.12	0.32	160.0	22.49	0.87	22.53	-0.2	0.00

^{59}Co NEUTRON ELASTIC SCATTERING CROSS SECTIONS

Neutron Energy ± Energy Spread	11.944 ± 0.074 MeV
Excitation Energy J^{π}	0.000 MeV (7/2$^-$)
Total Cross Section	2.920 ± 0.059 barns
Integrated Cross Section	1.470 ± 0.017 barn
Calculated Wick's Limit	3059.84 ± 122.8 mb/sr
Zero Degree Cross Section	3103.11 ± 21.24 mb/sr
Normalization Uncertainty	3.00 %
Chi-square/degree-of-freedom	0.423

l-Value	A_l	ΔA_l	a_l	Δa_l	F-Value	F-Test
0	116.96	1.318	1.00000	0.00000	37.000	0.463
1	292.03	3.749	0.83226	0.01068	0.003	0.463
2	428.36	5.846	0.73246	0.01000	0.008	0.463
3	494.13	7.228	0.60352	0.00883	0.865	0.463
4	500.61	8.249	0.47557	0.00784	13.123	0.463
5	426.97	8.372	0.33186	0.00651	31.045	0.464
6	328.58	8.383	0.21609	0.00551	5.218	0.465
7	236.66	7.408	0.13489	0.00422	5.291	0.466
8	155.40	6.583	0.07815	0.00331	32.914	0.466
9	79.24	4.823	0.03565	0.00217	102.681	0.466
10	32.41	3.677	0.01320	0.00150	220.585	0.466
11	8.83	1.972	0.00328	0.00073	31.541	0.467
12	2.93	1.269	0.00100	0.00043	12.262	0.468

uncorrected			corrected			calculation		
θ_{lab}	$\sigma(\theta_{lab})$	$\Delta\sigma_{lab}$	$\theta_{c.m.}$	$\sigma(\theta_{c.m.})$	$\Delta\sigma_{c.m.}$	$\sigma(\theta_{c.m.})$	%Dev.	χ^2
18.0	724.79	7.30	17.7	1576.88	34.01	1613.28	-2.3	1.15
22.0	556.04	5.79	21.4	1212.34	34.49	1178.14	2.8	0.98
25.0	415.03	4.36	24.2	900.26	27.95	889.97	1.1	0.14
28.0	293.46	2.22	27.0	633.49	19.63	641.79	-1.3	0.18
31.0	204.69	2.04	29.8	441.40	15.10	441.45	0.0	0.00
35.0	122.49	1.20	33.6	249.03	9.19	247.88	0.5	0.02
39.0	69.88	0.78	37.4	129.23	5.52	125.70	2.7	0.41
43.0	36.57	0.53	41.5	55.85	2.45	58.54	-4.8	1.21
47.0	23.81	0.53	45.9	29.45	1.73	27.75	5.8	0.96
51.0	14.89	0.25	50.4	16.96	0.81	17.08	-0.7	0.02
55.0	11.09	0.27	54.6	12.98	0.84	12.81	1.4	0.04
59.0	7.65	0.15	58.6	9.22	0.48	9.49	-3.0	0.33
63.0	6.38	0.17	62.9	6.98	0.47	6.64	4.8	0.52
66.0	5.43	0.10	66.5	5.73	0.27	5.83	-1.6	0.12
69.0	5.66	0.10	70.1	7.20	0.33	7.02	2.5	0.31
73.0	6.43	0.12	74.4	10.40	0.46	10.78	-3.6	0.65
77.0	8.55	0.14	78.2	15.33	0.47	15.21	0.8	0.07
81.0	10.36	0.16	81.9	19.21	0.47	19.26	-0.2	0.01
85.0	11.85	0.13	85.6	22.15	0.36	22.06	0.4	0.06
89.0	12.32	0.16	89.4	22.96	0.43	23.04	-0.4	0.04

93.0	11.98	0.15	93.2	22.08	0.45	22.10	-0.1	0.00
97.0	10.97	0.16	97.0	19.80	0.49	19.64	0.8	0.10
101.0	9.35	0.15	100.9	16.33	0.46	16.37	-0.2	0.01
105.0	7.84	0.12	104.9	13.06	0.39	13.05	0.1	0.00
109.0	6.44	0.11	108.9	10.14	0.32	10.32	-1.8	0.33
113.0	5.77	0.10	113.0	8.65	0.29	8.56	1.0	0.09
117.0	5.41	0.10	117.2	7.96	0.28	7.78	2.2	0.41
122.0	5.06	0.13	122.4	7.61	0.34	7.89	-3.7	0.65
126.0	5.43	0.14	126.5	8.47	0.36	8.52	-0.5	0.01
130.0	5.81	0.14	130.5	9.39	0.38	9.46	-0.7	0.03
134.0	6.55	0.15	134.5	10.91	0.41	10.59	2.9	0.60
138.0	7.08	0.15	138.4	11.86	0.39	11.76	0.8	0.06
142.0	7.41	0.11	142.3	12.64	0.31	12.79	-1.2	0.23
148.0	7.98	0.17	148.1	13.70	0.45	13.85	-1.1	0.12
152.0	8.53	0.16	152.1	14.64	0.43	14.33	2.1	0.51
156.0	8.63	0.16	156.0	14.87	0.44	15.00	-0.9	0.09
160.0	9.37	0.17	159.9	16.26	0.44	16.26	0.0	0.00

^{59}Co NEUTRON ELASTIC SCATTERING CROSS SECTIONS

Neutron Energy ± Energy Spread	13.934 ± 0.069 MeV
Excitation Energy J^{π}	0.000 MeV (7/2$^-$)
Total Cross Section	2.700 ± 0.056 barns
Integrated Cross Section	1.267 ± 0.016 barn
Calculated Wick's Limit	3052.01 ± 127.4 mb/sr
Zero Degree Cross Section	2978.42 ± 19.69 mb/sr
Normalization Uncertainty	3.00 %
Chi-square/degree-of-freedom	0.715

l-Value	A_l	ΔA_l	a_l	Δa_l	F-Value	F-Test
0	100.86	1.239	1.00000	0.00000	38.000	0.463
1	248.51	3.524	0.82134	0.01165	3.123	0.463
2	360.45	5.524	0.71477	0.01095	1.070	0.463
3	427.06	6.827	0.60490	0.00967	0.013	0.463
4	447.37	7.766	0.49285	0.00856	6.432	0.463
5	410.04	7.788	0.36959	0.00702	33.001	0.463
6	336.28	7.699	0.25648	0.00587	2.860	0.464
7	265.49	6.721	0.17549	0.00444	0.508	0.465
8	197.64	5.940	0.11527	0.00346	6.957	0.466
9	118.16	4.398	0.06166	0.00230	78.876	0.466
10	49.92	3.394	0.02357	0.00160	194.951	0.466
11	14.16	1.878	0.00611	0.00081	107.395	0.466
12	2.49	1.167	0.00099	0.00046	5.709	0.467

uncorrected			corrected			calculation		
θ_{lab}	$\sigma(\theta_{lab})$	$\Delta\sigma_{lab}$	$\theta_{c.m.}$	$\sigma(\theta_{c.m.})$	$\Delta\sigma_{c.m.}$	$\sigma(\theta_{c.m.})$	%Dev.	χ^2
18.0	666.22	6.77	17.6	1408.33	37.00	1413.55	-0.4	0.02
22.0	451.53	4.66	21.2	976.96	28.72	980.47	-0.4	0.01
25.0	326.01	2.47	24.0	709.23	25.95	701.85	1.0	0.08
28.0	205.07	2.02	26.8	444.47	12.89	473.34	-6.5	5.02
31.0	151.10	1.58	29.6	324.10	12.98	299.29	7.7	3.65
35.0	77.48	0.85	33.5	143.68	5.57	143.74	0.0	0.00
39.0	42.44	0.54	37.9	62.49	2.12	61.96	0.8	0.06
43.0	28.91	0.46	42.7	37.35	1.21	37.35	0.0	0.00
47.0	23.53	0.53	47.1	35.42	1.39	35.32	0.3	0.01
51.0	18.41	0.28	50.9	32.74	0.91	33.21	-1.4	0.26
55.0	14.84	0.32	54.5	27.35	1.08	27.23	0.4	0.01
59.0	10.63	0.18	58.2	18.78	0.73	18.69	0.4	0.01
63.0	7.52	0.19	62.4	10.47	0.52	10.22	2.4	0.23
66.0	6.38	0.10	66.3	7.05	0.26	7.08	-0.4	0.01
69.0	6.61	0.11	70.3	9.02	0.49	9.25	-2.6	0.23
73.0	8.89	0.14	74.5	15.72	0.59	15.51	1.4	0.13
77.0	11.64	0.17	78.1	21.67	0.56	21.53	0.6	0.05
81.0	13.67	0.18	81.8	25.61	0.52	25.93	-1.3	0.39
85.0	14.95	0.15	85.4	27.86	0.42	27.61	0.9	0.35
89.0	14.17	0.19	89.1	26.15	0.52	26.31	-0.6	0.10

93.0	12.55	0.18	92.9	22.81	0.54	22.68	0.6	0.06
97.0	10.24	0.16	96.7	18.05	0.51	17.89	0.9	0.10
101.0	7.68	0.13	100.6	12.76	0.38	13.16	-3.2	1.14
105.0	6.31	0.11	104.8	9.59	0.28	9.53	0.6	0.05
109.0	5.45	0.10	109.1	7.82	0.23	7.65	2.1	0.51
113.0	5.05	0.10	113.4	7.43	0.23	7.52	-1.3	0.17
117.0	5.33	0.10	117.6	8.34	0.25	8.38	-0.6	0.04
122.0	5.91	0.15	122.5	9.75	0.36	9.76	-0.1	0.00
126.0	6.31	0.15	126.4	10.61	0.37	10.60	0.1	0.00
130.0	6.63	0.16	130.3	11.20	0.37	11.08	1.1	0.11
134.0	6.75	0.16	134.2	11.34	0.37	11.21	1.2	0.12
138.0	6.54	0.15	138.1	10.87	0.36	11.14	-2.6	0.59
142.0	6.77	0.16	142.1	11.14	0.37	11.02	1.1	0.12
145.0	6.71	0.16	145.1	11.01	0.37	10.94	0.6	0.03
148.0	6.43	0.15	148.0	10.54	0.37	10.90	-3.4	0.92
152.0	7.01	0.15	152.0	11.44	0.36	10.88	4.9	2.44
156.0	6.52	0.14	155.9	10.52	0.34	10.89	-3.5	1.14
160.0	6.90	0.14	159.9	11.04	0.35	10.94	0.9	0.08

^{59}Co NEUTRON ELASTIC SCATTERING CROSS SECTIONS

Neutron Energy ± Energy Spread	15.425 ± 0.069 MeV
Excitation Energy J^{π}	0.000 MeV ($7/2^-$)
Total Cross Section	2.560 ± 0.057 barns
Integrated Cross Section	1.202 ± 0.014 barn
Calculated Wick's Limit	3037.30 ± 135.0 mb/sr
Zero Degree Cross Section	3054.84 ± 16.96 mb/sr
Normalization Uncertainty	3.00 %
Chi-square/degree-of-freedom	1.628

l-Value	A_l	ΔA_l	a_l	Δa_l	F-Value	F-Test
0	95.62	1.075	1.00000	0.00000	33.000	0.463
1	231.35	3.056	0.80649	0.01065	7.686	0.464
2	330.83	4.774	0.69199	0.00999	2.147	0.465
3	398.52	5.897	0.59540	0.00881	1.184	0.466
4	430.46	6.669	0.50020	0.00775	2.175	0.466
5	412.05	6.649	0.39176	0.00632	9.750	0.466
6	354.66	6.533	0.28531	0.00526	2.460	0.466
7	293.86	5.726	0.20489	0.00399	2.200	0.467
8	239.05	5.090	0.14706	0.00313	1.421	0.468
9	160.45	3.886	0.08832	0.00214	53.080	0.469
10	75.59	3.104	0.03765	0.00155	128.605	0.469
11	25.35	1.882	0.01153	0.00086	69.712	0.470
12	7.06	1.169	0.00295	0.00049	21.945	0.471

uncorrected			corrected			calculation		
θ_{lab}	$\sigma(\theta_{lab})$	$\Delta\sigma_{lab}$	$\theta_{c.m.}$	$\sigma(\theta_{c.m.})$	$\Delta\sigma_{c.m.}$	$\sigma(\theta_{c.m.})$	%Dev.	χ^2
18.0	599.07	6.40	17.6	1245.80	31.94	1309.00	-5.1	3.92
21.0	447.13	4.63	20.3	945.12	26.60	969.79	-2.6	0.86
24.0	316.31	3.38	22.9	688.75	18.36	678.49	1.5	0.31
28.0	208.69	2.31	26.5	459.31	20.07	378.93	17.5	16.04
32.0	84.78	1.07	30.3	176.03	6.57	179.45	-1.9	0.27
37.0	41.29	0.44	36.1	54.57	1.79	53.69	1.6	0.24
39.0	34.16	0.39	38.8	40.45	1.00	41.06	-1.5	0.38
42.0	30.53	0.37	42.5	43.61	1.07	43.50	0.2	0.01
47.0	28.28	0.35	47.4	50.05	1.12	49.91	0.3	0.01
52.0	23.82	0.31	51.7	44.08	1.21	44.17	-0.2	0.00
57.0	16.21	0.25	56.2	30.07	1.04	29.45	2.1	0.35
62.0	9.92	0.19	61.3	13.95	0.57	13.58	2.7	0.43
65.0	7.90	0.10	65.3	8.76	0.31	9.11	-4.0	1.30
67.0	8.71	0.12	68.1	10.91	0.56	10.59	2.9	0.31
72.0	11.71	0.14	73.5	21.17	0.67	20.59	2.8	0.77
77.0	16.18	0.19	78.0	30.17	0.64	29.79	1.3	0.35
82.0	18.60	0.18	82.5	34.58	0.55	34.48	0.3	0.03
87.0	17.40	0.17	87.1	32.01	0.61	32.92	-2.9	2.26
92.0	14.10	0.29	91.8	25.55	0.83	26.17	-2.4	0.56
97.0	10.47	0.25	96.5	18.51	0.74	17.55	5.2	1.70

102.0	6.71	0.14	101.5	10.55	0.39	10.20	3.3	0.82
107.0	5.25	0.10	107.2	6.73	0.24	6.84	-1.6	0.20
112.0	5.34	0.07	112.8	8.06	0.24	8.18	-1.5	0.25
117.0	6.24	0.23	117.7	10.73	0.56	10.79	-0.5	0.01
122.0	7.17	0.12	122.4	12.71	0.28	12.39	2.5	1.30
127.0	7.03	0.13	127.1	12.36	0.31	12.38	-0.2	0.00
132.0	6.31	0.12	132.0	10.86	0.28	11.13	-2.5	0.94
137.0	5.89	0.23	137.0	9.90	0.52	9.75	1.6	0.09
142.0	5.57	0.09	142.1	9.21	0.21	9.13	0.9	0.15
147.0	5.53	0.10	147.1	9.17	0.22	9.23	-0.6	0.06
152.0	5.75	0.13	152.0	9.48	0.30	9.38	1.0	0.09
156.0	5.81	0.10	155.9	9.25	0.22	9.31	-0.7	0.10
160.0	6.06	0.13	160.0	9.23	0.27	9.18	0.5	0.03

^{59}Co NEUTRON ELASTIC SCATTERING CROSS SECTIONS

Neutron Energy ± Energy Spread	16.879 ± 0.108 MeV
Excitation Energy J^{π}	0.000 MeV ($7/2^-$)
Total Cross Section	2.470 ± 0.053 barns
Integrated Cross Section	1.091 ± 0.014 barn
Calculated Wick's Limit	3094.02 ± 132.2 mb/sr
Zero Degree Cross Section	2809.29 ± 18.02 mb/sr
Normalization Uncertainty	3.00 %
Chi-square/degree-of-freedom	3.770

l-Value	A_l	ΔA_l	a_l	Δa_l	F-Value	F-Test
0	86.85	1.139	1.00000	0.00000	38.000	0.463
1	203.81	3.247	0.78225	0.01246	21.925	0.463
2	283.70	5.111	0.65334	0.01177	5.103	0.463
3	340.78	6.341	0.56055	0.01043	2.122	0.463
4	373.66	7.182	0.47806	0.00919	4.769	0.463
5	365.21	7.191	0.38229	0.00753	4.144	0.463
6	329.40	6.997	0.29176	0.00620	0.225	0.464
7	286.37	6.052	0.21983	0.00465	4.765	0.465
8	243.34	5.252	0.16482	0.00356	0.010	0.466
9	171.92	3.911	0.10419	0.00237	42.256	0.466
10	85.78	3.112	0.04703	0.00171	102.199	0.466
11	29.95	1.898	0.01499	0.00095	50.877	0.466
12	8.53	1.219	0.00393	0.00056	12.331	0.467

uncorrected			corrected			calculation		
θ_{lab}	$\sigma(\theta_{lab})$	$\Delta\sigma_{lab}$	$\theta_{c.m.}$	$\sigma(\theta_{c.m.})$	$\Delta\sigma_{c.m.}$	$\sigma(\theta_{c.m.})$	%Dev.	χ^2
18.0	519.50	9.70	16.9	1219.58	37.58	1209.86	0.8	0.07
22.0	346.77	5.71	20.3	855.48	33.22	807.33	5.6	2.10
26.0	176.01	1.85	23.7	459.19	17.28	478.45	-4.2	1.24
29.0	110.22	1.84	26.4	281.60	13.35	286.26	-1.7	0.12
32.0	60.94	1.02	29.7	129.71	5.60	139.76	-7.8	3.22
35.0	42.74	0.76	33.9	54.64	1.57	54.06	1.1	0.14
39.0	32.42	0.55	39.7	47.94	1.66	47.32	1.3	0.14
43.0	33.78	0.35	43.9	64.41	1.20	63.72	1.1	0.33
47.0	35.29	0.54	47.3	70.73	1.75	68.94	2.5	1.04
51.0	29.41	0.44	50.6	60.10	1.55	63.71	-6.0	5.47
55.0	23.71	0.38	54.0	48.71	1.65	50.23	-3.1	0.84
59.0	16.47	0.28	57.7	31.26	1.15	32.35	-3.5	0.90
63.0	11.92	0.24	62.3	16.88	0.61	16.45	2.5	0.48
66.0	10.91	0.17	66.4	13.37	0.42	12.58	5.9	3.53
69.0	10.71	0.18	70.3	15.89	0.65	16.85	-6.0	2.20
73.0	12.80	0.23	74.6	23.54	0.83	25.63	-8.9	6.41
77.0	16.14	0.28	78.2	31.45	0.78	32.34	-2.8	1.30
81.0	17.91	0.34	81.7	35.28	0.90	35.70	-1.2	0.21
85.0	19.19	0.26	85.2	38.00	0.78	35.30	7.1	11.95
89.0	17.07	0.33	88.6	33.84	1.08	31.60	6.6	4.30
93.0	13.08	0.26	92.2	25.95	0.93	25.68	1.1	0.09

97.0	9.45	0.19	96.0	17.47	0.59	18.95	-8.5	6.40
101.0	8.30	0.18	100.3	12.91	0.50	12.71	1.6	0.16
105.0	6.16	0.14	105.1	8.67	0.32	9.08	-4.7	1.60
109.0	5.85	0.14	109.6	9.28	0.37	8.91	4.0	1.03
113.0	6.67	0.15	113.7	11.48	0.40	10.33	10.0	8.14
117.0	6.57	0.11	117.4	11.49	0.31	11.79	-2.7	0.99
122.0	6.94	0.19	122.1	12.13	0.49	12.52	-3.2	0.63
126.0	6.16	0.16	126.0	10.84	0.40	11.86	-9.4	6.61
130.0	6.10	0.18	129.7	10.85	0.47	10.43	3.9	0.79
134.0	5.31	0.11	133.6	9.32	0.31	8.88	4.6	1.94
138.0	5.00	0.09	137.7	8.18	0.24	7.79	4.8	2.82
142.0	4.36	0.13	142.0	6.78	0.31	7.59	-12.0	6.68
145.0	4.47	0.13	145.2	7.29	0.35	7.93	-8.8	3.37
148.0	5.05	0.14	148.2	8.76	0.36	8.38	4.4	1.13
152.0	5.44	0.14	152.0	9.60	0.38	8.82	8.1	4.23
156.0	5.46	0.14	155.9	8.68	0.35	9.02	-3.9	0.94
160.0	6.42	0.16	160.6	9.17	0.35	9.17	0.0	0.00

^{59}Co NEUTRON ELASTIC SCATTERING CROSS SECTIONS

Neutron Energy ± Energy Spread	18.862 ± 0.124 MeV
Excitation Energy J^{π}	0.000 MeV ($7/2^-$)
Total Cross Section	2.370 ± 0.049 barns
Integrated Cross Section	0.966 ± 0.011 barn
Calculated Wick's Limit	3183.23 ± 130.4 mb/sr
Zero Degree Cross Section	2635.99 ± 15.93 mb/sr
Normalization Uncertainty	3.00 %
Chi-square/degree-of-freedom	3.046

l-Value	A_l	ΔA_l	a_l	Δa_l	F-Value	F-Test
0	76.86	0.897	1.00000	0.00000	40.000	0.463
1	173.02	2.539	0.75031	0.01101	38.594	0.463
2	235.30	4.089	0.61225	0.01064	13.005	0.463
3	274.59	5.057	0.51034	0.00940	0.794	0.463
4	314.55	5.881	0.45469	0.00850	0.336	0.463
5	314.11	5.890	0.37150	0.00697	0.581	0.463
6	311.28	5.917	0.31152	0.00592	0.176	0.463
7	279.10	5.109	0.24207	0.00443	6.755	0.463
8	261.83	4.557	0.20037	0.00349	1.193	0.464
9	201.92	3.404	0.13826	0.00233	23.371	0.465
10	121.83	2.882	0.07548	0.00179	75.854	0.466
11	50.35	1.793	0.02848	0.00101	37.807	0.466
12	21.25	1.200	0.01106	0.00062	92.955	0.466

uncorrected			corrected			calculation		
θ_{lab}	$\sigma(\theta_{lab})$	$\Delta\sigma_{lab}$	$\theta_{c.m.}$	$\sigma(\theta_{c.m.})$	$\Delta\sigma_{c.m.}$	$\sigma(\theta_{c.m.})$	%Dev.	χ^2
18.0	436.24	6.98	16.5	1050.51	38.87	1039.80	1.0	0.08
21.0	279.38	8.56	18.9	731.78	27.12	743.97	-1.7	0.20
22.0	269.08	6.86	19.8	711.82	37.05	651.77	8.4	2.63
25.0	144.52	1.47	22.3	406.99	18.18	413.80	-1.7	0.14
39.0	61.35	1.02	26.3	140.98	6.44	165.52	-17.4	14.55
32.0	40.93	0.60	30.6	47.22	1.23	46.42	1.7	0.41
35.0	34.26	0.50	35.8	40.89	2.01	38.84	5.0	1.04
49.0	37.58	0.45	40.6	74.29	1.88	74.35	-0.1	0.00
43.0	43.07	0.51	43.8	89.56	1.43	90.17	-0.7	0.18
57.0	42.68	0.52	47.0	89.59	1.54	91.28	-1.9	1.20
51.0	36.90	0.46	50.3	78.93	1.93	79.16	-0.3	0.01
55.0	27.21	0.32	53.7	58.38	1.70	58.40	0.0	0.00
69.0	18.89	0.40	57.7	36.55	1.32	35.62	2.5	0.49
63.0	14.70	0.34	62.5	20.95	0.71	19.86	5.2	2.33
66.0	12.39	0.40	66.5	17.40	0.89	18.89	-8.6	2.78
79.0	13.93	0.23	70.1	23.62	0.70	23.94	-1.3	0.20
73.0	15.94	0.23	74.1	30.68	0.64	31.00	-1.1	0.26
87.0	17.60	0.26	77.7	34.69	0.73	35.39	-2.0	0.92
81.0	19.98	0.40	81.2	39.45	0.98	36.41	7.7	9.52
85.0	18.86	0.43	84.7	37.18	1.20	34.08	8.4	6.74

89.0	14.97	0.28	88.3	29.27	0.94	29.11	0.6	0.03
93.0	11.04	0.16	92.1	20.95	0.56	22.62	-7.9	8.68
97.0	8.79	0.16	96.0	15.66	0.51	15.86	-1.3	0.15
101.0	6.86	0.14	100.3	10.76	0.37	10.36	3.8	1.16
105.0	5.67	0.13	105.0	8.29	0.30	8.01	3.3	0.87
119.0	5.52	0.13	109.6	8.87	0.35	9.23	-4.1	1.03
113.0	6.53	0.12	113.7	11.78	0.33	11.75	0.3	0.01
117.0	6.88	0.13	117.4	13.28	0.34	13.56	-2.1	0.68
120.0	6.83	0.11	120.1	13.51	0.33	13.90	-2.9	1.41
122.0	7.23	0.15	121.8	14.45	0.42	13.59	5.9	4.19
126.0	6.21	0.13	125.2	12.56	0.43	11.84	5.7	2.80
130.0	4.53	0.09	128.8	8.79	0.32	9.01	-2.6	0.48
134.0	3.47	0.15	132.9	5.64	0.35	5.95	-5.6	0.80
138.0	3.23	0.13	137.7	4.49	0.26	4.34	3.2	0.29
142.0	2.89	0.11	142.4	4.76	0.29	4.98	-4.6	0.59
145.0	3.48	0.12	145.4	6.21	0.32	5.88	5.3	1.06
148.0	3.69	0.12	148.3	6.62	0.30	6.61	0.2	0.00
152.0	3.96	0.13	152.2	6.99	0.32	7.23	-3.4	0.56
156.0	4.51	0.14	156.1	8.34	0.36	8.16	2.2	0.25
160.0	5.23	0.15	159.6	10.49	0.38	10.53	-0.4	0.01

APPENDIX B

ANALYZING POWER TABULATIONS

The analyzing power data in this appendix is tabulated and fitted using the computer code MACRO. The fits are associated Legendre polynomials calculated from the product of analyzing powers and differential cross sections according to the following equation:

$$A_y(\theta, E) \times \sigma(\theta, E) = \sum_{l=1}^{n} B_l(E) \times P_l^1(\cos\theta).$$

l-value	order of the associated Legendre polynomial in the expansion
B_l	l th coefficient of the associated Legendre polynomial
ΔB_l	absolute uncertainty in $B_l(E)$
Ratio	$B_l(E)/B_1(E)$.
θ_{lab}	experimental lab. angle
$A_y(\theta_{lab})$	analyzing power as measured in the lab before correction
$\Delta A_y(\theta_{lab})$	absolute error of $A_y(\theta_{lab})$ which does not include normalization uncertainties
$\theta_{c.m.}$	reaction angle in the center-of-mass system
$A_y(\theta_{c.m.})$	corrected analyzing power in the center-of-mass. The analyzing power is corrected for multiple scattering, attenuation, and finite geometry.
$\Delta A_{y_{c.m.}}$	absolute error of $A_y(\theta_{c.m.})$ which does not include normalization uncertainties
Dev.	absolute deviation of the calculated analyzing power from the experimental value
χ^2	chi-square per point for the calculation at that angle

F-Test integral probability

$$P_F(F, \gamma_1, \gamma_2) = \int_F^{\infty} P_f(f, \gamma_1, \gamma_2)\, df$$

where γ_1 and γ_2 are the respective degrees of freedom

F-value or F_χ $\dfrac{\chi^2_{n-1} - \chi^2_n}{\chi^2_n} (N - n - 1)$

where N is the number of data points, and n is the number of terms in the fit

^{27}Al NEUTRON ELASTIC SCATTERING ANALYZING POWERS

Neutron Energy ± Energy Spread	15.425 ± 0.344 MeV
Excitation Energy J^{π}	0.000 MeV ($5/2^{+}$)
Normalization ± Calibration Error	1.00 ± 0.030
Chi-square/degree-of-freedom	1.109

l-Value	B_l	ΔB_l	Ratio	F-Value	F-Test
1	-7.9636	0.5868	1.0000	16.000	0.476
2	-9.1317	0.5910	1.1467	16.514	0.478
3	-4.5809	0.6631	0.5752	0.119	0.479
4	-3.4618	0.7441	0.4347	0.067	0.480
5	-5.0700	0.7269	0.6367	0.006	0.484
6	-5.2733	0.6454	0.6622	68.550	0.486
7	-1.6243	0.5504	0.2040	6.650	0.490
8	-0.7529	0.4561	0.0945	9.127	0.494
9	0.2603	0.3955	-0.0327	0.284	0.499
10	-0.0646	0.3271	0.0081	3.048	0.506
11	0.4075	0.2265	-0.0512	2.697	0.515

uncorrected			corrected			calculation		
θ_{lab}	$A_y(\theta_{lab})$	$\Delta A_{y_{lab}}$	$\theta_{c.m.}$	$A_y(\theta_{c.m.})$	$\Delta A_{y_{c.m.}}$	$A_y(\theta_{c.m.})$	Dev.	χ^2
25.0	-0.225	0.026	25.4	-0.227	0.027	-0.207	-0.020	0.55
30.0	-0.329	0.041	30.2	-0.331	0.043	-0.326	-0.004	0.01
35.0	-0.454	0.047	35.1	-0.479	0.051	-0.542	0.063	1.52
38.0	-0.616	0.057	38.3	-0.757	0.065	-0.737	-0.020	0.09
41.0	-0.490	0.054	42.3	-0.623	0.064	-0.611	-0.012	0.03
45.0	-0.204	0.059	47.3	-0.146	0.066	-0.120	-0.026	0.16
50.0	-0.056	0.036	52.3	-0.040	0.038	-0.055	0.016	0.17
60.0	-0.139	0.044	61.9	-0.140	0.045	-0.161	0.022	0.23
70.0	-0.335	0.037	71.6	-0.342	0.039	-0.323	-0.019	0.24
80.0	-0.535	0.055	81.6	-0.568	0.058	-0.566	-0.003	0.00
90.0	-0.357	0.071	91.9	-0.404	0.077	-0.436	0.033	0.18
102.0	0.270	0.058	103.9	0.307	0.061	0.345	-0.038	0.39
115.0	0.403	0.074	116.7	0.429	0.079	0.355	0.073	0.86
128.0	0.094	0.065	129.4	0.101	0.069	0.154	-0.052	0.58
140.0	0.002	0.091	141.0	0.000	0.097	-0.079	0.079	0.66

^{59}Co NEUTRON ELASTIC SCATTERING ANALYZING POWERS

Neutron Energy ± Energy Spread	15.273 ± 0.435 MeV
Excitation Energy J^{π}	0.000 MeV ($7/2^-$)
Normalization ± Calibration Error	1.00 ± 0.030
Chi-square/degree-of-freedom	0.935

l-Value	B_l	ΔB_l	Ratio	F-Value	F-Test
1	-7.2262	0.3829	1.0000	25.000	0.468
2	-3.7956	0.3627	0.5253	11.362	0.469
3	-0.1869	0.4311	0.0259	0.822	0.469
4	0.6578	0.4664	-0.0910	0.097	0.470
5	0.4730	0.4750	-0.0655	0.406	0.471
6	1.2166	0.4718	-0.1684	0.041	0.472
7	-0.3709	0.4613	0.0513	55.381	0.473
8	-3.9848	0.4461	0.5514	1.575	0.474
9	-3.8719	0.4256	0.5358	1.241	0.475
10	-3.3978	0.3839	0.4702	104.734	0.476
11	-1.2515	0.3224	0.1732	8.723	0.478
12	-0.8027	0.2685	0.1111	0.267	0.479
13	-0.6980	0.2498	0.0966	4.268	0.480
14	-0.3504	0.2179	0.0485	3.985	0.484
15	-0.0618	0.1078	0.0086	0.219	0.486

uncorrected			corrected			calculation		
θ_{lab}	$A_y(\theta_{lab})$	ΔA_{ylab}	$\theta_{c.m.}$	$A_y(\theta_{c.m.})$	$\Delta A_{yc.m.}$	$A_y(\theta_{c.m.})$	Dev.	χ^2
18.0	-0.037	0.009	17.4	-0.044	0.010	-0.030	-0.014	1.98
21.0	-0.005	0.014	19.8	-0.011	0.016	-0.017	0.005	0.11
24.0	0.043	0.018	22.2	0.041	0.021	0.004	0.037	3.26
27.0	0.047	0.027	24.6	0.045	0.031	0.038	0.007	0.05
31.0	0.117	0.027	28.1	0.153	0.033	0.112	0.041	1.51
35.0	0.086	0.019	32.5	0.217	0.025	0.241	-0.023	0.85
41.0	-0.171	0.024	40.8	-0.264	0.034	-0.267	0.002	0.00
45.0	-0.354	0.027	45.5	-0.519	0.038	-0.562	0.044	1.30
50.0	-0.608	0.028	49.7	-0.730	0.036	-0.688	-0.042	1.34
55.0	-0.698	0.029	53.6	-0.822	0.038	-0.813	-0.009	0.06
60.0	-0.697	0.034	58.2	-0.989	0.049	-1.013	0.024	0.24
65.0	-0.428	0.053	65.1	-0.589	0.078	-0.582	-0.007	0.01
75.0	-0.029	0.058	76.9	0.020	0.070	0.010	0.010	0.02
80.0	-0.205	0.058	80.9	-0.222	0.068	-0.161	-0.061	0.81
85.0	-0.262	0.034	85.0	-0.287	0.039	-0.312	0.025	0.41
95.0	-0.466	0.044	93.6	-0.540	0.053	-0.526	-0.014	0.07
105.0	-0.399	0.048	104.0	-0.555	0.066	-0.558	0.003	0.00
115.0	-0.071	0.044	115.8	-0.065	0.056	-0.064	-0.001	0.00
125.0	0.202	0.039	124.9	0.280	0.047	0.265	0.015	0.10
130.0	0.147	0.047	129.5	0.260	0.057	0.323	-0.063	1.22
135.0	0.126	0.050	134.3	0.267	0.062	0.198	0.069	1.23
145.0	-0.390	0.056	144.4	-0.593	0.069	-0.540	-0.054	0.60
150.0	-0.410	0.051	149.3	-0.652	0.064	-0.633	-0.019	0.09
154.0	-0.240	0.043	153.1	-0.417	0.053	-0.472	0.054	1.06

REFERENCES

[AlO92] M. A. AlOhali *et al.*, to be published (1992).

[Bri71] D. M. Brink and G. R. Satchler, Angular momentum, (Oxford Univ. Press, Oxford, 1971)

[Cle90] T. B. Clegg *et al.*, TUNL Rep. XXIX, 114 (1990).

[Coh58] B.L. Cohen and A.G. Rubbin, Phys. Rev. **111**, 1568 (1958).

[Das90] R.K. Das and R.W. Finlay, Phys. Rev. **C42**, 1013 (1990).

[Del88] J.P. Delaroche and W. Tornow, Phys. Lett. **B203**, 4 (1988).

[Del89] J.P. Delaroche *et al.*, Phys. Rev. **C39**, 391 (1989).

[ElK81] S.M. ElKadi, Ph.D. Dissertation, Duke University (1981).

[Fes58] H. Feshbach, Ann. Rev. Nucl. Sci. **8**, 49 (1958).

[Fis69] T.R. Fisher, D.C. Healey, and J.S. McCarthy, Nucl. Phys. **A130**, 609 (1969).

[Fis71a] T.R. Fisher, Phys. Lett. **35B**, 7 (1971).

[Fis71b] T.R. Fisher, H.A. Grench, D.C. Healey, J.S. McCarthy, D. Parks, and R. Whitney, Nucl. Phys. **A179**, 241 (1972).

[Fru84] S. Frullani *et al.*, Adv. in Nucl. Phys. **14** , 1 (1984).

[Gou86] C.R. Gould, D.G. Haase, L.W. Seagondollar, J.P. Soderstrum, K.E. Nash, M.B. Schneider, and N.R. Roberson, Phys. Lett. **57**, 2371 (1986).

[Gou88] C.R. Gould, N.R. Roberson, and W.J. Thompson, Phys. Rev. Lett. **60**, 2335 (1988).

[Gus82] P.P. Guss, Ph.D. Dissertation, Duke University (1982).

[Hau52] W. Hauser and H. Feshbach, Phys. Rev. **87**, 366 (1952).

[Hee76] W. Heeringa and H. Postma, Phys. Lett. **61B**, 350 (1976).

[Hee77] W. Heeringa, H. Postma, H. Dobiasch, R. Fischer, H.O. Klages, R. Maschuw, and B. Zeitnitz, Phys. Rev. **C16**, 1389 (1977).

[Hee83] W. Heeringa and H. Postma, Phys. Rev. **C5**, 2012 (1983).

[Hee89] W. Heeringa, H.O. Klages, Chr. Wölff, and R.W. Finlay, Phys. Rev. Lett. **63**, 2456 (1989).

[Hni87] V. Hnizdo and K.W. Kemper, Phys. Rev. Lett. **59**, 1982 (1987).

[Hod71] P.E. Hodgson, Nucl. Reactions, Oxford University Press, 1971.

[Hop71] J.C. Hopkins and G. Breit, Nucl. Data Tables **A9**, 137 (1971).

[How84] C.R. Howell, Ph.D. Dissertation, Duke University (1982).

[How88] C.R. Howell *et al.*, Phys. Rev. **C38**, 1552 (1988).

[Jeu83] J.P. Jeukene and C. Mahaux, Nucl. Phys. **A394**, 445 (1983).

[Joh87] C.H. Johnson, D.J. Horen, and C. Mahaux, Phys. Rev. **C36**, 2252 (1987).

[Joh88] C.H. Johnson and C. Mahaux, Phys. Rev. **C38**, 2589 (1988).

[Joh90] C.H. Johnson, Computer Code BOUNDSTATE, private communication (1990).

[Kob87] S. Kobayashi *et al.*, J. Phys. Soc. Jpn. **22**, 368 (1967).

[Kin70] W.E. Kinney and F.G. Perey, Nucl. Sci. Eng. **40**, 396 (1970).

[McA86] T.L. McAbee, Ph.D. dissertation, University of North Carolina at Chapel Hill, 1986.

[Mah83] C. Mahaux and H. Ngo, Nucl. Phys. **A410**, 271 (1983).

[Mah86] C. Mahaux and R. Sartor, Nucl. Phys. **A458**, 25 (1986).

[Mah87] C. Mahaux and R. Sartor, Nucl. Phys. **A468**, 193 (1987).

[Mah90] C. Mahaux and R. Sartor, Nucl. Phys. **A516**, 285 (1990).

[Mah91a] C. Mahaux and R. Sartor, Adv. in Nucl. Phys. **20** (1991).

[Mah91b] C. Mahaux and R. Sartor, Nucl. Phys. (1991) (in press).

[Mar71] P. Marmier and E. Sheldon, Phys. Nucl. and Part., Vol. II, (New York: Academic Press Inc., 1971).

[Mart87] Ph. Martin, Nucl. Phys. **A466**, 119 (1987).

[Mol64] P.A. Moldauer, Phys. Rev. **B135**, 64 (1964).

[Nag70] K. Nagamine, A. Uchida, and S. Kobayashi, Nucl. Phys. **A145**, 203 (1970).

[Ohl72] G.G. Ohlsen, Rep. Progr. Phys. **35**, 717 (1972).

[Ped86] R.S. Pedroni, Ph.D. Dissertation, Duke University (1986).

[Ped88] R.S. Pedroni *et al.*, Phys. Rev. **C38**, 2052 (1988).

[Per62] F. Perey and B. Buck, Nucl. Phys. **32**, 353 (1962).

[Rap78] J. Rapaport *et al.*, Nucl. Phys. **A296**, 95 (1978).

[Ray79] J. Raynal, Computer Code ECIS79 (unpublished).

[Rob88] M.L. Roberts, Ph.D. Dissertation, Duke University (1988).

[Rob91] M.L. Roberts *et al.* , Phys. Rev. **C44**, 2006 (1991).

[Sar80] R. Sartor and C. Mahaux, Phys. Rev. **C21**, 1546 (1980).

[Sat71] G.R. Satchler, Phys. Lett. **34B**, 37 (1971).

[Smi86] A.B. Smith, P.T. Guenther, and R.D. Lawson, Nucl. Phys. **A455**, 344 (1986).

[Tam65] T. Tamura, Rev. of Mod. Phys. **37**, 679 (1965).

[Tho76] W.J. Thompson, Phys. Lett. **62B**, 245 (1976).

[Tor87] W. Tornow, E. Woye, and R.L. Walter, J. Phys. G: Nucl. Phys. **13**, 177 (1987).

[Tor90] W. Tornow, Z. P. Chen, and J. P. Delaroche, Phys. Rev. **C42**, 693 (1990).

[Wei92] G.J. Weisel, Ph.D. Dissertation, Duke University (1992).

BIOGRAPHY

MAHMOUD MOHAAMUD NAGADI

Born: Jeddah, Saudi Arabia
February 20, 1956

Education: B. Sc., Physics, King Fahad University for Petroleum and Minerals (KFUPM), 1979
M. Sc., Physics, King Fahad University for Petroleum and Minerals (KFUPM), 1984

Positions: Graduate Assistant, 1979-1984

Memberships: American Physical Society

Contributed Abstracts, Papers/Talks Presented:

1. Influence of Including the Dispersion Relation in the OM Potential on the Magnitude of Extracted Spin-spin Potentials. M. Nagadi, R.L. Walter, W. Tornow, C.R. Howell, and J.P. Delaroche, Bull. of the Amer. Phys. Soc., **34** 1831 (1989).

2. Influence of Including the Dispersion Relation in the OM Potential on the Magnitude of Extracted Spin-Spin Potentials. M.M. Nagadi, J.P. Delaroche, C.R. Howell, W. Tornow, and R.L. Walter, contributed papers in 7th Int. Conf. on Pol. Phen. in Nucl. Phys., Paris 90, **47B** (1990).

3. The Dispersive Optical Model and Coupled Channel Model for n+^{27}Al and n+^{59}Co. M. Nagadi, R.L. Walter, W. Tornow, C.R. Howell, and J.P. Delaroche, Bull. of the Amer. Phys. Soc., **36** 2730 (1991).